THE NUMERICAL SIMULATION OF THIN FILM FLOW OVER HETEROGENEOUS SUBSTRATES

by

Mathieu Sellier

Submitted in accordance with the requirements for the degree of

Doctor of Philosophy

The University of Leeds

School of Mechanical Engineering

October 2003

ABSTRACT

Considerable progress in the understanding of thin film flow over surfaces has been achieved thanks to lubrication theory which enables the governing Navier-Stokes equations to be reduced to a more tractable form, namely a coupled set of partial differential equations. These are solved numerically since the flows of interest involve substrates containing heterogeneities in the form of wetting patterns and/or topography.

An efficient and accurate numerical method is described and used to solve two classes of problem: droplet spreading in the presence of wetting and topographic heterogeneities; gravity-driven flow of continuous thin liquid films down an inclined surface containing well defined topographic features. The method developed, employs a Full Approximation Storage (FAS) multigrid algorithm, is fully implicit and has embedded within it an adaptive time-stepping scheme that enables the same to be optimised in a controlled manner subject to a specific error tolerance.

Contact lines are ubiquitous in the context of droplet spreading and the well-known singularity which occurs there is alleviated by means of a disjoining pressure model. The latter allows prescription of a local equilibrium contact angle and three-dimensional numerical simulations reveal how droplets can be forced to either wet or dewet a region containing topography depending on the surface wetting characteristics. The growth of numerical instabilities, in the contact line region, which can lead to the occurrence of non-physical, negative film thicknesses is avoided by using a Positivity Preserving Scheme.

A range of two- and three-dimensional problems is explored featuring the gravity-driven flow of a continuous thin liquid film over a non-porous inclined flat surface containing topography. Important new results include: the quantification of the validity range of the lubrication approximation for step-up and step-down topographies; description of the "bow wave" triggered by localised topography and an explanation, in terms of the local flow rate, of the accompanying "downstream surge"; an assessment of linear superposition as a means of examining free surface response to topographies. In addition, the potential of local mesh refinement as a

means of reducing computational time is highlighted.

Finally, more complex liquids composed of a non-volatile resin dissolved in a solvent and allowed to evaporate are considered. An evaporation model based on the well-mixed approximation is utilised. Results show that localised topographies produce defects in dried continuous films which persist far downstream of the topography, while with respect to droplet motion, solvent evaporation is found to be responsible for contact line pinning and thus a reduction in spreading.

The following papers, based on sections of this thesis, have appeared or been accepted for publication.

1. **Gaskell P.H., Jimack, P.K., Sellier, M., Thompson, H.M. and Decré, M.** (2001) Numerical simulation of the spreading of droplets. In: *Proc. of the ECS'2001 (ed. J.-M. Buchlin & J. Anthoine)* Brussels, Belgium, pp 149-154.

2. **Gaskell P.H., Jimack, P.K., Sellier, M. and Thompson, H.M.** (2003) Gravity-driven flow of evaporating thin liquid films over substrates with topography. To appear in *Proc. of the ECS'2003* Fribourg, Switzerland.

3. **Gaskell P.H., Jimack, P.K., Sellier, M. and Thompson, H.M.** (2003) Efficient and accurate time adaptive multigrid simulations of droplet spreading. *Int. J. Num. Meth. Fluids* in press.

4. **Gaskell, P.H., Jimack, P.K., Sellier, M., Thompson, H.M. and Wilson, M.C.T.** (2003) Gravity-driven flow of continuous thin liquid films on non-porous substrates with topography. *J. Fluid Mech.* in press.

To my wife ...

ACKNOWLEDGEMENTS

I wish to express my deepest appreciation to my supervisors, Prof. P.H. Gaskell, Prof. P.K. Jimack and Dr. H.M. Thompson for giving me the opportunity to do this PhD and for their invaluable guidance, advice and encouragement throughout the course of this research work. The keen interest of Prof. M.M.J. Decré, his insightful comments and helpful suggestions deserve special mention. I also wish to thank Dr. M.C.T. Wilson for several insightful and useful discussions.

The financial support from the School of Mechanical Engineering and Philips Electronics is gratefully acknowledged. Without their support, the present work would not have been possible.

I would also like to thank my fellow PhD students in Room 344 of the School of Mechanical Engineering for providing a friendly working atmosphere.

Finally, my special thanks go to my family and my wife in particular for their love, support and encouragement during my extended studies.

Contents

List of Figures

List of Tables

NOMENCLATURE

A convention used throughout the thesis is that, unless otherwise stated, quantities in upper case are dimensional while those in lower case are dimensionless. The subscript "0" denotes characteristic quantities used for the nondimensionalisation. Variables with multiple definitions are clearly distinguished in the text by the context in which they are used.

A	Aspect ratio of the topography
Bo	Bond number
C_1, C_2, C_3, C_4, C_5	Coefficients in the lubrication approximation
Ca	Capillary number
c_s, c_0	Solvent concentrations
E, e	Evaporation rate
E_σ, E_d	Surface tension and disjoining pressure energies
G^i	Grid level i
g	Acceleration due to gravity (9.81 m/s^2)
H, H_0, h	Film thickness
h_r	Resin height
H^*, h^*	Precursor film thickness
	Dimensionless free surface perturbation profile
h_0	Droplet thickness at the centre of the droplet
L_0	Substrate extent
L_c	Capillary length
L_T, l_t	Streamwise topography extent
N	Measure of the normal component of gravity
N_{cyc}	Number of V-cycles
(n, m)	Exponents in the disjoining pressure function
n_{pre}, n_{post}	Number of pre and postsmoothing sweeps
P, P_0, p	Liquid pressure
Q_0	Inlet flow rate
R, R_0	Droplet radius

r	Radial coordinate in a cylindrical polar coordinate system
Re	Reynolds number
S, S_0, s	Topography height
T, T_0, t	Time
Tol	Error tolerance
U, V, W, U_0, u, v, w	Velocity components
V_d	Droplet volume
W_T, w_t	Spanwise topography extent
X, Y, Z, x, y, z	Cartesian coordinates
(x^*, y^*)	Dimensionless coordinate system centred on the topography in units of Capillary length
(x^+, y^+)	Dimensionless coordinate system in units of Capillary length
(X_1, Y_1), (x_1, y_1)	Coordinate of the bottom left corner of the topography
(X_T, Y_T), (x_t, y_t)	Coordinate of the centre of the topography

Greek letters

α	Tilt angle of the substrate
β	Extent of the substrate in multiples of the Capillary length
Δ	Mesh resolution
$\Delta t, \Delta t^{n+1}$	Time-step size
γ	Parameter controlling the steepness of the topography
ϵ	Aspect ratio of the film
μ, μ_0, $\tilde{\mu}$	Dimensional, scaling and dimensionless dynamic viscosities
Π, π	Disjoining pressure function
ρ	Density
σ, σ_0, $\tilde{\sigma}$	Dimensional, scaling and dimensionless surface tensions
Θ_0	Equilibrium contact angle
Θ_t	Coefficient in the temporal discretisation scheme
Ψ, ψ	Free surface height

Abbreviations

$\mathcal{ADI}$	Alternating Direction Implicit
CPU	Central Processing Unit
$\mathcal{FAS}$	Full Approximation Storage
FE	Finite Element
LTE	Local Truncation Error
$\mathcal{MLAT}$	Multilevel Adaptive Technique
ODE	Ordinary Differential Equation
$\mathcal{PPS}$	Positivity Preserving Scheme
$\mathcal{SS}$	Standard Scheme

Chapter 1

Introduction

Contents

1.1 Background

1.1.1 Coating flows

Often unnoticed, thin liquid films frequently appear in nature and as part of many manufacturing process. For example, they feature in the human body in the form of tear films in the eye or as a protective linning in the lungs (Oron *et al.* (1997)). Industrial applications include, for instance, the deposition of coatings and inks, direct patterning of functional layers during microchip production, spreading of pesticides and the flow of oil in heat exchangers and the coating of paper (de Gennes (1985), Peurrung and Graves (1993)). Coated films can be composed of a single or several superimposed layers. Photosensitive film is a typical application combining many layers of light-sensitive emulsions, dye-forming and image-modifying chemicals. When part of a manufacturing process, the deposited liquid film is generally subsequently dried or cured to leave a solid layer on the substrate. The function of this layer might be to protect, simply decorative or even to record information.

A familiar film deposition process is that of decorative painting. This may seem quite a simple example, however it requires a good understanding of the underlying physics and control of the governing parameters. A paint too thin will lead to poor coverage of the surface area while one too thick will be difficult to apply. If the surface tension is too low, it may lead to a poor levelling of the painted layer leaving "brush-marks". Another well studied cause of non-uniformity in painted layer is the solutal Marangoni effect resulting from composition variations of the paint giving rise to surface tension gradients (Overdiep (1986), Evans *et al.* (2000)).

This already rather long list of undesired effects is a consequence of considering the fluid properties only but of course, the overall homogeneity of the substrate will also strongly affect the quality of the coated film. For example, a small speck of dust or topographic feature on a surface is known to deform a coated free surface over distances orders of magnitude greater than the size of the submerged defect itself (Pozrikidis and Thoroddsen (1991), Gaskell *et al.* (2004)). Also, when the paint is applied on curved substrates, the liquid layer is known to thin at outside corners

and thicken at inside ones (Weidner *et al.* (1996)).

Coating imperfections may also arise when a substrate's chemical composition is heterogeneous, yielding wettability variations. The appearance of "reticulation" (formation of a defect pattern) resulting from non-uniform wettability has been studied by Schwartz *et al.* (2000) and Podgorski *et al.* (1999) who explored the formation of dry patches on an inclined non-wettable surface.

The number of mechanisms that may lead to poor quality coating or complete failure of the film deposition process, even for a basic application such as painting, illustrates and highlights the difficulty faced by the coating engineer. Moreover industrial applications usually involve multiple interconnected coating passes and demand concerning coating quality and high speed application for productivity reasons is continually being pushed to the limit. Hence, the question that coating engineers often have to answer is: What is the optimal operating window for a given coating device? In other words, what are the optimal parameters to achieve a successful film deposition of prescribed thickness, free of instability and at the highest possible speed?

The answer to these questions lies essentially in the theory of fluid mechanics. In the pioneering work of Landau and Levich (1942), a rigorous mathematical analysis of the viscous, surface tension and static pressure forces in liquid film deposition, as it occurs in dip coating, was derived. The theoretical approach adopted by these authors proved that significant insight into interfacial phenomena and valuable predictive relationships could be obtained by formal analysis. However, until approximately three decades ago, the development of new coating technologies outpaced the research in this area and the understanding was mostly empirical (Ruschak (1985)). Since then, the growing scientific interest, the availability of more advanced mathematical methods and more potent computers have enabled substantial progress in understanding the governing principles underpinning the application of thin liquid coatings. An exhaustive review of the history of coating science is given in Kistler and Schweizer (1997).

Of course, the motivation behind a better understanding of liquid film deposition

and coatings in general is not only to avoid the different failure modes exposed previously but also to achieve a desired goal. The recent invention of self-cleaning glass* for windows is a good example of successful research in the coating area. A durable, long-lasting coating is fused into the glass at high temperatures during the manufacturing process. The coating uses the sun's ultraviolet light to break down and loosen organic dirt and causes water to sheet off of the surface, so that rain or a light water spray can easily rinse the loosened dirt away with minimal spotting and streaking.

In microfluidic applications there is a growing interest in selectively coating or "inking" chemically patterned surfaces for use as chemical microreactors. The study of Darhuber *et al.* (2000(a)) explores how this could be achieved in the context of dip coating. In Schwartz and Eley (1998), the effect of wettability contrasts on the spreading of a droplet was investigated and later extended by Gaskell *et al.* (2003) to account for the presence of a topography. For inkjet printing, the requirement is that the impact of droplets is as small and focused as possible. Sometimes, instead of requiring a smooth, level dried coated layer, the goal might be to produce an effect such as the hammer tone finish often produced for metallic substrates.

From a fluid mechanics point of view, coating processes develop as a balance between viscous and surface tension forces; in some configurations, other body forces such as centrifugal of thermocapillary forces may also be relevant to drive the flow. Coating flows generally share a number of characteristic features regardless of the specific application:

- They are low Reynolds number flows so that the effect of inertia can often be ignored and are therefore referred to as *creeping flows*. An additional consequence is the absence of turbulence which is particularly convenient for modelling purposes.

- They have at least one *free surface* and for multi-layer coating, internal interfaces. When the fluid is bounded by two free surfaces, it is called a *free film*.

*url: http://www.ppg.com/gls_residential/gls_sunclean/faq.htm

- They possess *static* and *dynamic contact lines*, the latter when liquid displaces a gas (usually air) from a solid web or substrate.

- They are small scale flows because of their thin nature which make them prone to long-range interaction forces.

Although the Navier-Stokes equations, dictating the motion of fluids, have been known for more than two centuries and result from basic conservation considerations, exact analytical solutions are scarce and restricted to simple geometry and parameter ranges. The presence of a free surface and a dynamic contact line are additional complicating features of coating flows. Because the location of the free surface is unknown *a priori*, it needs to be determined during the solution process like the other dependent variables namely the velocity and pressure field. Moreover since the boundary conditions that apply at such an interface are highly nonlinear, it is crucial to be able to represent them accurately. In fact, it is this requirement that proved to be the major obstacle to the analysis of coating systems and it was only with the advent of powerful computers in the early 1980's, when Finite Element methods for coating flows were being developed at the University of Minnesota (Kistler and Scriven (1983)), that expert users were first able to explore the effect of process operating parameters on the flow.

Since then, various other numerical methods have been developed to track interfaces. They include the boundary-element method, the marker-and-cell method, the volume-of-fluids method or the phase field method - see Scardovelli and Zaleski (1999) for a complete review. The free surface difficulty is "technical" in the sense that although solutions are difficult to find, the governing equations are known. In contrast, the difficulty associated with the dynamic contact line is theoretical because the exact nature of the flow in its vicinity is still a matter of dispute due to the breakdown of the usual no-slip boundary condition between the liquid and the substrate at the contact line (Huh and Scriven (1971)). There is a clear mismatch between the continuum description of the liquid in the Navier-Stokes equations and the molecular scale of the contact line region. Because several instabilities in coating flows are linked to the presence of a dynamic contact line, it is essential for any

predictive model to capture accurately its macroscopic effects. Several approaches to relieve this singularity are discussed in Chapter 2.

1.1.2 The thin film approximation

In spite of these complicating features, significant progress has been possible by taking advantage of the creeping nature of coating flows, the usual small ratio of the typical film thickness and the characteristic length in the substrate direction. Under these assumptions, the flow field is nearly rectilinear, the streamlines being almost parallel to the substrate. An analysis of the leading order terms in the Navier-Stokes equations reveal that the evolution of the film can be described by a coupled set of second order partial differential equations in terms of the film thickness and the pressure across the film, or equivalently by a single fourth order partial differential equation in terms of the film thickness alone (Myers (1998)). These equations are often called the lubrication approximation because of the similarity they have with the equation first derived by Reynolds (1886) to calculate the pressure in lubricated slipper bearings.

The lubrication approximation, also referred to as the long-wave approximation, reduces considerably the complexity of the free boundary problem by effectively transforming the initial problem, where the velocity and pressure are unknown fields in a three-dimensional fluid domain, to one where the film thickness and depth-averaged pressure are unknown variables depending on the substrate location only. A clear drawback of this approximation is therefore the impossibility to have multivalued film thickness. For coating applications, this formulation is particularly convenient because the film thickness and overall shape of the free surface are normally the key factors to assess the quality of the deposited film. Nevertheless, from a knowledge of the film thickness and the pressure, the velocities can also be inferred if necessary.

Although much more tractable than the Navier-Stokes equations, the lubrication equations still represent a considerable challenge when it comes to solving them either analytically or numerically. Firstly, they are highly non-linear equations and can only be linearised in a few particular cases. Furthermore, the lubrication equa-

tions are degenerate in the sense that the coefficient of the highest derivative tends to zero as the film thickness approaches zero (Myers (1998)). This issue is most severe when a dynamic contact line is present since the film thickness decreases as the contact line is approached leading to a change in the intrinsic nature of the governing equations. This is a consequence of the contact line paradox mentioned above: the incompatibility between the no-slip condition and the dynamic contact line. Thus, although the lubrication approximation simplifies the representation of the free-surface, it does not releave the singularity at the contact line.

Another complicating feature of the lubrication approximation is that the maximum principle which guarantees that the solution is bounded from above and below by its initial data is not applicable (Bertozzi (1998)). This means that given a strictly positive initial profile, the film thickness can change sign leading to unrealistic negative film thicknesses. This lack of positivity-preserving property can have disastrous consequences when numerical solutions are sought, yielding possible instabilities and eventually blow-up of the solution.

Finally, the lubrication approximation, like any other approximation, is only valid within a certain parameter range. Although experience suggests that it is robust and has a tendency to deliver good results (in agreement with experiment) in parameter regimes on the outer limits of the expected range of validity (O'Brien and Schwartz (2002)), the limited applicability of the lubrication approximation needs to be kept in mind and the validity window quantified whenever possible. Under certain conditions, usually involving further assumptions, a simplified geometry or taking advantage of the presence of symmetry, analytical treatment is possible. In which case, valuable insight can be gained on the asymptotic behaviour of the liquid film, on its stability or its possible self-similar properties. The available mathematical methods for thin film flows have recently been reviewed by Kistler and Schweizer (1997) and Myers (1998).

1.1.3 Focus of the present work

The lubrication approximation is the basis of the work presented in this thesis and is derived formally in Chapter 2. More specifically, the lubrication approximation is applied to two quite different flow conditions: droplet spreading and gravity-driven continuous thin liquid films in the constant flux configuration on heterogeneous substrates. The study of the former is relevant to inkjet printing for example when the droplet has impacted on the substrate but also from a more general point of view as a "benchmark" problem for dynamic wetting. The latter, which consists of a liquid film on an inclined plane, occurs in some regions of slide and curtain coating. Heterogeneities considered are of two kinds: wettability patterns and/or topographic features. These might be desired, in order to achieve selective coating, or unwanted such as a speck of dust on the substrate.

The presence of heterogeneities introduces singularities in the lubrication approximation and a numerical approach as a means of solution is almost inevitable. In order to capture accurately the liquid film behaviour in the vicinity of a singularity such as a wetting line for instance, fine computational mesh resolution is necessary. For example, when modelling a dynamic contact line assuming that a precursor film precedes it (see Chapter 2), the mesh resolution in the wetting line region needs to be of the same order as the precursor film thickness as discussed by Bertozzi (1998). If the flow is unidirectional or axisymmetric, i.e. the lubrication approximation only depends on one spatial coordinate and the time, fine mesh resolution in the singularity region can be achieved at little computational cost (by today's standard). Many local mesh refinement algorithms are available and "relatively" easy to implement (Bertozzi (1995)). For multidimensional situations the problem becomes more severe and complex, and much more computationally intensive. Quoting Schwartz and Eley (1998), "Resolution of wetting-layer thickness in the nanometre range is not possible for multidimensional problems; nor is it practically possible to resolve substrate variations on the micron scale, in macroscopic simulations".

Hence, one of the main thrusts of the work presented in this thesis is to apply existing numerical techniques and develop new ones to improve the efficiency, robustness and

accuracy of numerical methods applied to the lubrication approximation. The scope of this thesis is however not purely numerical since the resultant numerical schemes are notably applied to industrially relevant coating flows but also to interesting features associated with the spreading of a droplet and the flow of a gravity-driven film over a substrate with wettability patterns and/or topographic features.

In order to obtain a discrete analogue of the lubrication approximation, the Finite Difference method is certainly the most popular (Weidner *et al.* (1997), Diez and Kondic (2002)) although the Finite Element method was the one used by Peurrung and Graves (1991) and Grun and Rumpf (1998). Efficiency in solving the set of non-linear algebraic equations resulting from the discretisation process can be improved in different ways. Firstly, explicit time marching methods for which the solution at a given time step depends exclusively on the solution at the previous time step are known to impose a stringent upper bound on the size of possible time increments in order to avoid instability (Bertozzi (1998)). Explicit schemes were used in the "early days" of numerical simulation of the lubrication approximation by Schwartz (1989) and Stillwagon and Larson (1990) but they become obsolete when fine mesh resolution is required due to their poor numerical efficiency. This lead Schwartz and co-workers to develop a semi-implicit numerical scheme for which the solution at a given time step depends only "moderately" on the one at the previous time step (Moriarty and Schwartz (1993), Weidner *et al.* (1997)). These authors used an alternating-direction-implicit ($\mathcal{ADI}$) technique to solve the discrete analogue of the lubrication approximation. These techniques use alternating sweeps in each direction so that only a banded system of equation needs to be solved to update the solution. The approach of Schwartz and co-workers presented a great enhancement since time increments can be as much as a factor 10^5 larger than the characteristic maximum step for stability of the explicit method. Nevertheless, the numerical scheme adopted by them is still partly explicit and since a formal stability analysis, such as that of Von Neumann, of the numerical scheme is impossible because of its non-linear nature, its stability cannot be guaranteed. Furthermore, the convergence rate of $\mathcal{ADI}$ schemes, although very good, is not optimal in the sense that it is not independent of the number of unknowns - Trottenberg (2001).

Accordingly, the tack followed in this thesis builds on earlier research performed in the Engineering Fluid Mechanics Research group at the University of Leeds (Daniels *et al.* (2000)) and consists of using a fully-implicit numerical scheme and multigrid solver which is known for its optimal efficiency (Trottenberg (2001)). Because the scheme is fully implicit, the method is stable. The idea of multigrid techniques in concise terms is to smooth the whole spectrum of the error components on a hierarchy of computational grids with variable mesh densities. The principles of multigrid methods are introduced in Chapter 3.

Other than Daniels *et al.* (2000), no reported attempt to apply Mutilgrid techniques to the lubrication approximation have been found in the literature however they have been used successfully in a related area of research: elastohydrodynamic lubrication (Ehret *et al.* (1997), Goodyer (2001)). The governing equations in elastohydrodynamic lubrication (EHL) bear resemblance with the lubrication approximation because they result from the same basic assumptions first stated by Reynolds (1886). However, the fluid domain in EHL applications is bounded by two solid surfaces which are in relative movement and therefore differs from the free surface flow of interest.

The benefits of being able to use larger time increments in numerical simulations should not however be at the cost of a poorer accuracy. This is another area where progress is possible. The implementation of an adaptive time stepping procedure should allow the optimal time step to be inferred automatically and combine efficiency and accuracy. As a consequence, small/large time increments should be automatically selected when the solution varies rapidly/slowly. Most previously reported adaptive time stepping schemes in the context of the lubrication approximation rely on some "empirical" criteria such as the rate of change of the numerical solution (Schwartz *et al.* (2000), Bielarz and Kalliadasis (2003)) to choose a suitable time step and make no attempt to optimise a guess for the next time increment, which may lead to unnecessary failure of the solution at that time step.

In contrast, the adaptive time stepping scheme developed and described in Chapter 3 bases time increment selection on an a robust estimate of the local truncation error so that the unavoidable accumulation of error at each time step remains bounded

and does not lead to an inaccurate solution at a given time. A further important efficiency gain is the use of local mesh refinement. Because, regions requiring fine resolution generally represent a small portion of the total computational domain, the possibility to tune the mesh density accordingly can result in significant savings in computational time.

For the one-dimensional lubrication approximation, Bertozzi (1995) implemented successfully a local mesh refinement algorithm. In the two-dimensional case, Diez and Kondic (2002) proposed a numerical scheme to allow calculations on nonuniform grids but at the cost of a lower order of accuracy. A further advantage of the multigrid method used in this work is that it naturally extends to allow local mesh refinement as demonstrated in the landmark work of Brandt (1977). Although this was not the main focus of this thesis, sample results will be shown to reveal the potential of such methods. Finally, the Positivity Preserving Scheme derived by Zhornitskaya and Bertozzi (2000) is implemented in the present work since it enhances considerably the robustness of the numerical scheme by preventing the occurrence of unphysical film thicknesses even on under-resolved computational grids. In fact, this scheme proves to be essential to capture the motion of wetting lines over topographic features.

An additional motivation for the work contained in this thesis are the experimental results recently obtained by Decré and Baret (2003) concerning the flow of gravity-driven thin liquid films over a square trench topography located on an inclined plane. These results provide a rare opportunity to validate the numerical prediction of flow in a three-dimensional fluid domain and to obtain a quantitative estimate of the validity of the lubrication approximation.

1.2 Outline of the thesis

The next two chapters are essentially descriptive. In Chapter 2, by expanding the Navier-Stokes equation in terms of the small aspect ratio of the film, and retaining the leading order terms, a formal derivation of the lubrication approximation is presented. The scalings relevant to the flow configurations of interest, i.e. droplet

spreading and gravity-driven thin liquid films, are then introduced and the range of the various associated dimensionless groups is given. For compactness, the lubrication approximation is presented in a general form with coefficients that need prescribing depending on the flow conditions. A review of the possible approaches to handle the singularity at a dynamic contact line follows, with particular emphasis on the disjoining pressure model adopted in this work and as used extensively by Schwartz and co-workers - Schwartz and Eley (1998) and Schwartz (1998).

Chapter 3 is devoted to a description of the numerical approach used to solve the lubrication approximation. After an introductory discussion, going in depth into the numerical difficulties associated with the lubrication approximation and the history of multigrid methods, the spatial and temporal discretisations are detailed together with the adaptive time stepping procedure and Positivity Preserving Scheme. The Full Approximation Storage ($\mathcal{FAS}$) form of the multigrid method, which is well suited to non-linear problems, is outlined in a pseudo-code formalism along with the necessary modifications to implement the Multi-Level Adaptive Technique ($\mathcal{MLAT}$) which enables local mesh adaptivity.

Chapter 4 is concerned with the validation and evaluation of the performance of the proposed numerical schemes. This necessary stage is achieved by applying the methods to differential equations with known analytical solutions. The adaptive time stepping scheme is first applied to an ordinary differential equation for which the analytical solution is known and of the same form as Tanner's closed form solution for the film thickness of an axisymmetrically spreading droplet (Tanner (1979)). The results establish the ability of the scheme to give a good estimate of the local truncation error and therefore a good guess of the optimal time increment. Then, the accuracy and performance of the combination of the adaptive time stepping scheme with the multigrid algorithm are assessed by considering solutions of the transient heat diffusion equation. The adaptive time stepping scheme is tested under conditions for which the heat transfer coefficient varies rapidly with time. The final results of this chapter investigate the benefits of using local mesh refinement in a region where the heat transfer coefficient varies discontinuously. Overall, Chapter 4 provides insight to and establishes clearly the benefits of the proposed numerical

methods before applying them with confidence to the lubrication approximation.

Chapters 5, 6 and 7 focus on solving numerically the lubrication approximation. Chapter 5 concentrates on droplet spreading. Initially, the efficiency of the numerical method is investigated by performing a parametric study of the convergence history of the numerical solutions and, importantly, results are compared with previously reported data. Results are found to obey Tanner's law of spreading (Tanner (1979)) when the droplet is far from equilibrium and to agree well with the results of Schwartz and Eley (1998). The numerical results are further validated in the extreme case where the spreading of the droplet is induced mostly by gravity. A self-similar solution first derived by Nakaya (1974) is available in this case. The effect of the disjoining pressure on the spreading behaviour of droplets is also explored by comparing solutions for a fully and a partially wetting droplet. The chapter concludes by presenting simulations for a range of new problems including droplet spreading over heterogeneous substrates.

In Chapter 6, gravity-driven thin liquid films over topographies are considered. Firstly, flow over step-up, step-down topographies and trenches are investigated. For these cases, the cross flow invariance implies that the flow is effectively two-dimensional and solutions to the full Navier-Stokes equations were possible using the Finite Element method, Wilson (2003), which enables the effect of inertia to be quantified. Moreover, the comparison of the lubrication approximation and Navier-Stokes results for a range of inlet flow rates and step heights provides a quantitative picture of the range of validity of the lubrication approximation. With a clearer idea on the accuracy of the lubrication approximation, flow over localised topographies giving rise to three-dimensional free surface disturbances is investigated. The numerical results for the flow over a square trench are found to be in excellent agreement with the experimental results published recently by Decré and Baret (2003) and show the characteristic "horseshoe"-shaped "bow wave". Additional results concerning the effects of the spanwise aspect ratio and the normal component of gravity are presented. Moreover, by comparing the solution of "equal-but-opposite" topographies the suggestion of Decré and Baret (2003) that the free surface response can be inferred by means of the linear superposition principle is assessed, Gaskell

et al. (2003(b)). Finally, the benefit of using local mesh adaptivity is demonstrated and interesting features are revealed when the inlet flow rate varies periodically. The latter results relate to, and extend, the recently published study of Bielarz and Kalliadasis (2003).

In the penultimate chapter the lubrication approximation is extended to account for evaporation in a binary mixture composed of a solvent and a resin. Assuming that only the solvent is allowed to evaporate and that the well-mixed approximation is applicable, the conservation law governing the solvent concentration is derived. The well-mixed approximation simply states that the solvent diffusion is rapid enough so that it is uniform across the liquid layer (Howison *et al.* (1997)). The implementation of this additional equation in the multigrid algorithm is then described emphasizing the flexibility of multigrid methods to incorporate additional physics. With a rheology of the binary mixture that depends on the local solvent fraction, results are shown for the two flow configurations of interest: droplet spreading and a gravity-driven thin liquid film.

The thesis concludes with a short chapter summarizing the work presented and suggesting extensions and avenues for future research.

Chapter 2

Model description

Contents

2.1 Introduction

As emphasised in the introduction, the modelling of free-surface flows presents a considerable theoretical and computational challenge. For the flows of interest in this thesis, the fluid domain is bounded by a non-porous substrate and a free-surface. The former may be flat or exhibit asperities of height S with respect to the origin of the coordinate system - see Figure 2.1. In the context of thin liquid films, the small aspect ratio, ϵ, of the characteristic film thickness, H_0, and the characteristic length in the streamwise direction, L_0, may be exploited to reduce the general governing Navier-Stokes equations to a more tractable pair of second order nonlinear partial differential equations in terms of the film thickness, H, and the pressure across the film, P.

In this chapter the time-dependent lubrication approximation for a three-dimensional fluid domain is derived following the same formalism as Williams (1998) and the different scalings resulting from various driving forces are introduced. The disjoining pressure model adopted to describe contact line regions is then explained followed by a derivation of the various energies associated with each force in play.

2.2 Governing equations

In a three-dimensional Cartesian coordinate system (X, Y, Z) attached to the substrate inclined at an angle α to the horizontal, where X denotes the down-slope coordinate, Y, the cross-slope coordinate and Z the coordinate normal to the substrate (see Figure 2.1), the conservation of momentum and mass for an incompressible, isothermal Newtonian fluid with constant viscosity, μ, yield the following time-dependent Navier-Stokes equations, viz.

$$\rho\left(\frac{\partial \underline{U}}{\partial T} + \underline{U}.\nabla\underline{U}\right) = -\nabla P + \mu\nabla^2\underline{U} + \rho\underline{\hat{g}}\,, \tag{2.1}$$

$$\nabla.\underline{U} = 0\,, \tag{2.2}$$

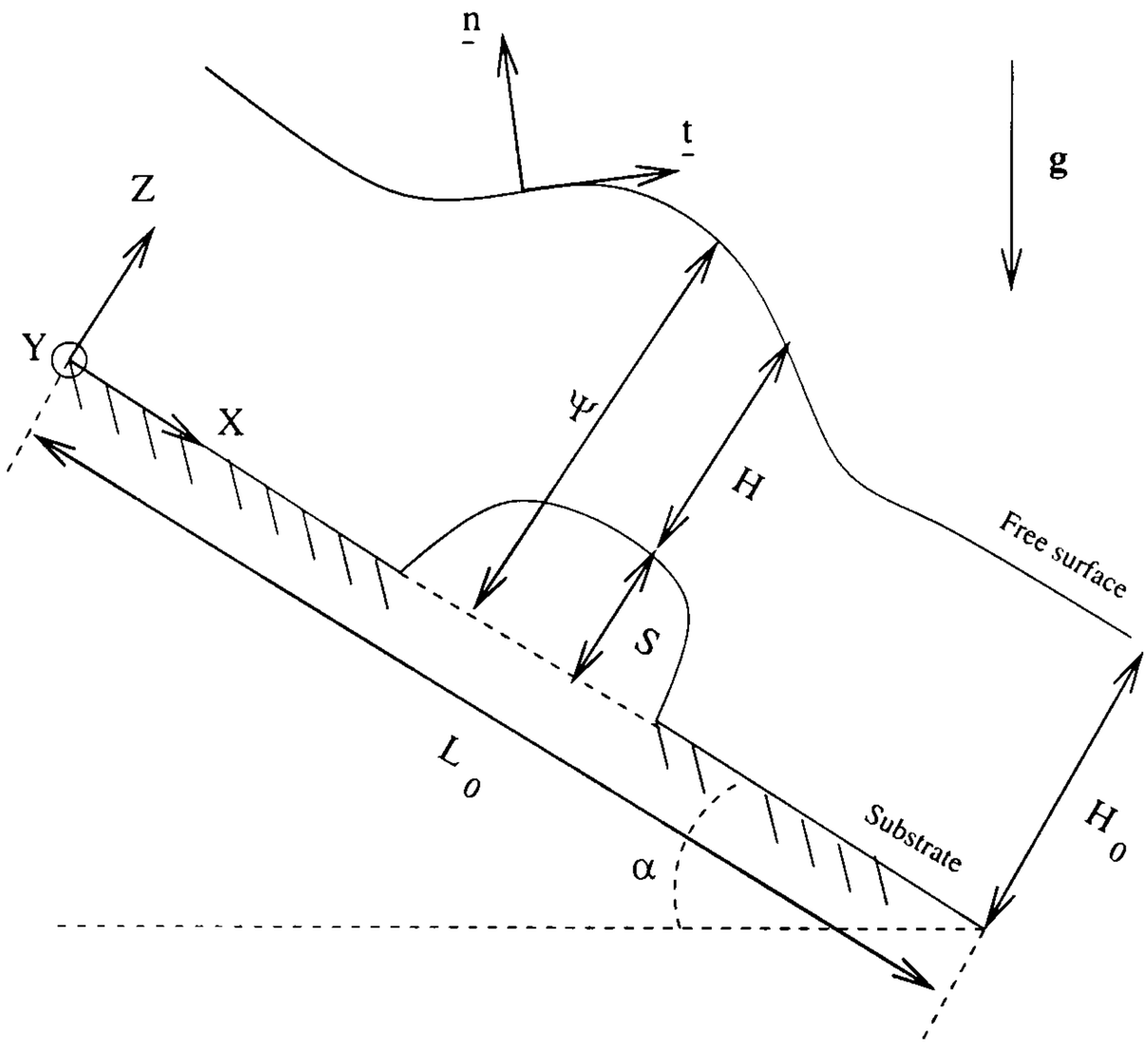

FIGURE 2.1: Sketch of the geometry and notations.

where $\underline{U} = (U, V, W)$ is the fluid velocity, T is the time and $\underline{\hat{g}} = g(\sin\alpha, 0, -\cos\alpha)$ is the acceleration due to gravity. Following Stillwagon and Larson (1990), the non-porous substrate surface is described by the topography function $S(X, Y)$ and the fluid is subject to the no-slip and no-penetration boundary condition along this surface, viz.

$$U = V = W = 0 \quad \text{on} \quad Z = S(X, Y)\ . \tag{2.3}$$

The free-surface is located at $\Psi(X, Y, T) = S(X, Y) + H(X, Y, T)$ and the kinematic boundary condition there requires that

$$\frac{\partial \Psi}{\partial T} + U\frac{\partial \Psi}{\partial X} + V\frac{\partial \Psi}{\partial Y} = W \quad \text{on} \quad Z = \Psi(X, Y, T)\ . \tag{2.4}$$

Since the topography function $S(X, Y)$ is not a function of time, eq. (2.4) is equivalent to

$$\frac{\partial H}{\partial T} + U\frac{\partial \Psi}{\partial X} + V\frac{\partial \Psi}{\partial Y} = W \quad \text{on} \quad Z = \Psi(X, Y, T)\ . \tag{2.5}$$

which using eq. (2.2) and Liebnitz' Rule* may be rewritten as

$$\frac{\partial H}{\partial T} + \frac{\partial}{\partial X}\left(\int_S^\Psi U dz\right) + \frac{\partial}{\partial Y}\left(\int_S^\Psi V dz\right) = 0 \,. \tag{2.6}$$

The proof of the equivalence of the integral and differential forms of the kinematic boundary condition is reported in Appendix B. Considering the normal and tangential stress at the free-surface provides additional boundary conditions. The components of the stress tensor for a Newtonian fluid are

$$\Sigma_{ij} = -P\delta_{ij} + \mu\left(\frac{\partial U_i}{\partial X_j} + \frac{\partial U_j}{\partial X_i}\right) \,. \tag{2.7}$$

Providing the air above the liquid film exerts negligible shear stress on the free-surface, the continuity of the tangential stress states that

$$\underline{t}.\underline{\underline{\Sigma}}.\underline{n} = 0 \quad \text{on} \quad Z = \Psi(X,Y,T) \,. \tag{2.8}$$

The normal stress must balance the capillary pressure resulting from the constant surface tension σ and the disjoining pressure $\Pi(H)$ caused by long-range intermolecular forces, accordingly

$$\underline{n}.\underline{\underline{\Sigma}}.\underline{n} = \sigma\kappa + \Pi(H) \quad \text{on} \quad Z = \Psi(X,Y,T) \,, \tag{2.9}$$

where κ is the free-surface curvature given by the sum of principal curvatures in the orthogonal directions. Following Kistler and Schweizer (1997), the curvature is given by

$$\kappa = \frac{\frac{\partial^2\Psi}{\partial X^2}\left[1+\left(\frac{\partial\Psi}{\partial Y}\right)^2\right] + \frac{\partial^2\Psi}{\partial Y^2}\left[1+\left(\frac{\partial\Psi}{\partial X}\right)^2\right] - 2\frac{\partial^2\Psi}{\partial Y\partial X}\frac{\partial\Psi}{\partial Y}\frac{\partial\Psi}{\partial X}}{\left[1+\left(\frac{\partial\Psi}{\partial Y}\right)^2+\left(\frac{\partial\Psi}{\partial X}\right)^2\right]^{3/2}} \,. \tag{2.10}$$

---

*Liebnitz' Rule: Given $f(x,z)$, $a(x)$ and $b(x)$, where f and $\frac{\partial f}{\partial x}$ are continuous in x and z, and a and b are differentiable functions of x,

$$\int_a^b \frac{\partial f}{\partial x} dz = \frac{\partial}{\partial x}\left(\int_a^b f dz\right) + f(x,a)\frac{\partial a}{\partial x} - f(x,b)\frac{\partial b}{\partial x}$$

The detail and importance of the disjoining pressure term in droplet spreading flows is discussed later - see §2.5.2.

The normal vector to the free-surface $\underline{n}$ pointing outward is

$$\underline{n} = \frac{(-\Psi_X, -\Psi_Y, 1)}{\left({\Psi_X}^2 + {\Psi_Y}^2 + 1\right)^{1/2}} , \tag{2.11}$$

and the tangential vectors at the free-surface in the X and Y directions are respectively

$$\underline{t}_X = \frac{(1, 0, \Psi_X)}{\left(1 + {\Psi_X}^2\right)^{1/2}} \quad \text{and} \quad \underline{t}_Y = \frac{(0, 1, \Psi_Y)}{\left(1 + {\Psi_Y}^2\right)^{1/2}} . \tag{2.12}$$

Combining eqs. (2.9) and (2.11) yield

$$-P + \frac{2\mu}{\Delta^2}[U_X\left({\Psi_X}^2 - 1\right) + V_Y\left({\Psi_Y}^2 - 1\right) + \left(U_Y + V_X\right)\Psi_Y\Psi_X - \left(U_Z + W_X\right)\Psi_X - \left(W_Y + V_Z\right)\Psi_Y] = \sigma\kappa + \Pi(H) \text{ on } Z = \Psi(X, Y, T) , \tag{2.13}$$

where $\Delta = \left(1 + {\Psi_X}^2 + {\Psi_Y}^2\right)^{1/2}$. Similarly, substituting eq. (2.12) in eq. (2.8) yields the following two equations

$$\mu[\left(1 - {\Psi_X}^2\right)\left(U_Z + W_X\right) + 2\left(W_Z - U_X\right)\Psi_X - \left(U_Y + V_X\right)\Psi_Y - \left(W_Y + V_Z\right)\Psi_X\Psi_Y] = 0 \quad \text{on} \quad Z = \Psi(X, Y, T) , \tag{2.14}$$

$$\mu[\left(1 - {\Psi_Y}^2\right)\left(V_Z + W_Y\right) + 2\left(W_Z - V_Y\right)\Psi_Y - \left(V_X + U_Y\right)\Psi_X - \left(W_X + U_Z\right)\Psi_X\Psi_Y] = 0 \quad \text{on} \quad Z = \Psi(X, Y, T) . \tag{2.15}$$

Equations (2.1), (2.6), (2.13), (2.14) and (2.15), along with inflow and outflow boundary conditions, describe the hydrodynamics of thin films.

In the next section, scalings are introduced and the lubrication approximation corresponding to the leading-order terms of the asymptotic expansion of the governing equations in terms of ϵ is presented.

2.3 The lubrication approximation

The choice of scaling is not unique and depends on the type of flow under consideration. In the present work two, quite different, flows are investigated:

- droplet spreading;
- the gravity-driven flow of continuous thin liquid films.

For the first, a commonly used set of scalings (Schwartz and Eley (1998), Schwartz (1998)) is

$$P_0 = \frac{\sigma\epsilon}{L_0}, \quad U_0 = \frac{L_0}{T_0}, \quad T_0 = \frac{\mu L_0}{\sigma\epsilon^3} . \tag{2.16}$$

T_0 is proportional to that derived by Orchard (1962) for the levelling of surface disturbances and H_0, L_0 are the characteristic droplet thickness and extent of the substrate, respectively.

For the second, a natural choice of characteristic film thickness is that for the case of fully developed thin film flow down an inclined plane with constant flux, Q_0, per unit width (Aksel (2000)), viz.

$$H_0 = \left(\frac{3\mu Q_0}{\rho g \sin\alpha}\right)^{1/3} , \tag{2.17}$$

while following Bertozzi and Brenner (1997), L_0 is chosen to be proportional to the capillary length, L_c, viz

$$L_0 = \beta L_c \quad \text{where} \quad L_c = \left(\frac{\sigma H_0}{3\rho g \sin\alpha}\right)^{1/3} = \frac{H_0}{(6Ca)^{1/3}} . \tag{2.18}$$

Here, $Ca = \frac{\mu U_0}{\sigma}$, is the capillary number expressing the ratio of viscous stresses to that of surface tension. Note that the present definition of the capillary length differs from the usual definition ($L_c = \sqrt{\sigma/\rho g}$) and is sometimes referred to as the dynamic capillary length (Decré and Baret (2003)). The characteristic velocity U_0 is taken to be the surface velocity of the fully developed film, namely

$$U_0 = \frac{3Q_0}{2H_0} . \tag{2.19}$$

Constants	Droplet spreading.	Gravity-driven thin film.
C_1	$\frac{Bo\sin\alpha}{\epsilon}$	2
C_2	$Bo\cos\alpha$	$\frac{2}{\beta}6^{1/3}Ca^{1/3}cot\alpha$
C_3	1	$\frac{6}{\beta^3}$
C_4	1	0

TABLE 2.1: Definition of the constants C_1, C_2, C_3 and C_4 for the two types of flow.

The characteristic pressure and time scale are respectively $P_0 = \frac{\rho g L_0 \sin\alpha}{2}$ and $T_0 = \frac{L_0}{U_0}$.

Introducing either set of scalings in equations (2.1), (2.13), (2.14) and (2.15), and retaining the leading-order terms (those up to $O(\epsilon^2, \epsilon^2 Re)$) gives, in $s(x,y) \leqslant z \leqslant \psi(x,y,t)$,

$$\frac{\partial^2 u}{\partial z^2} = \frac{\partial p}{\partial x} - C_1 \,, \tag{2.20}$$

$$\frac{\partial^2 v}{\partial z^2} = \frac{\partial p}{\partial y} \,, \tag{2.21}$$

$$\frac{\partial p}{\partial z} = -C_2 \,, \tag{2.22}$$

with boundary conditions,

$$u = v = w = 0 \qquad \text{on} \qquad z = s(x,y,t) \,, \tag{2.23}$$

$$\frac{\partial u}{\partial z} = \frac{\partial v}{\partial z} = 0 \qquad \text{on} \qquad z = \psi(x,y,t) \,, \tag{2.24}$$

$$p = -C_3 \nabla^2 \psi - C_4 \Pi(h) \qquad \text{on} \qquad z = \psi(x,y,t) \,. \tag{2.25}$$

The lower case notation denotes dimensionless variables defined by,

$$h(x,y,t) = \frac{H}{H_0}, \quad \psi(x,y) = \frac{\Psi}{H_0}, \quad s(x,y) = \frac{S}{H_0}, \quad (x,y) = \frac{(X,Y)}{L_0}, \quad z = \frac{Z}{H_0}, \quad p(x,y,t) = \frac{P}{P_0}, \quad (u,v,\epsilon w) = (U,V,W)\frac{1}{U_0}, \quad t = \frac{T}{T_0} \,. \tag{2.26}$$

The scaling-dependent constants, C_1, C_2, C_3 and C_4, are as reported in Gaskell *et al.* (2003(a)), Gaskell *et al.* (2003(b)) and summarised in Table 2.1. Because of the absence of wetting lines for gravity-driven thin liquid films, the disjoining pressure term can be neglected, thus $C_4 = 0$. $Bo = \frac{\rho g L_0^2}{\sigma}$ is the Bond number measuring the

relative importance of gravitational to surface tension forces within such flows.

Equations (2.20) and (2.21) are integrated twice with respect to z over the film thickness ($s \leqslant z \leqslant \psi$) subject to the above boundary conditions to yield

$$u = \left(\frac{\partial p}{\partial x} - C_1\right)(z-s)\left(\frac{1}{2}(z-s) - h\right) , \tag{2.27}$$

$$v = \left(\frac{\partial p}{\partial y}\right)(z-s)\left(\frac{1}{2}(z-s) - h\right) . \tag{2.28}$$

The time-dependent lubrication equations are obtained by combining eqs. (2.27) and (2.28) with the dimensionless counterpart of eq. (2.6),

$$\frac{\partial h}{\partial t} = \frac{\partial}{\partial x}\left[\frac{h^3}{3}\left(\frac{\partial p}{\partial x} - C_1\right)\right] + \frac{\partial}{\partial y}\left[\frac{h^3}{3}\left(\frac{\partial p}{\partial y}\right)\right] . \tag{2.29}$$

Integrating eq. (2.22) with respect to z and setting the integration constant using eq. (2.25), yields the pressure field throughout the droplet/film,

$$p = -C_3\nabla^2\psi - C_4\Pi(h) + C_2(\psi - z) . \tag{2.30}$$

The form of eq. (2.29) ensures that the z dependence in eq. (2.30) has no influence on the evolution of the droplet/film thickness and it is therefore omitted from subsequent analysis. Previous studies reviewed in Oron *et al.* (1997) have substituted eq. (2.30) into eq. (2.29) to yield the fourth order time-dependent lubrication equations purely in terms of the droplet height/film thickness, h. However in the present work it is found to be advantageous to solve the lubrication equations as the two coupled nonlinear equations for h and p, eqs. (2.29) and (2.30) respectively, since the second order differential operators are simpler to discretise and to incorporate in the Full Approximation Storage multigrid solver - see Chapter 3.

The terms multiplying each constants C_1, C_2, C_3 and C_4 correspond to the various forces in play. C_1 and C_2 are associated with the components of the gravity tangent and normal to the substrate respectively, C_3 with the surface tension and C_4 with the disjoining pressure. The literature reports situations where the domination of one term with respect to the others allows an analytical solution to be found. For

example, for surface tension-driven droplet spreading, only the surface tension term will differ from zero providing the droplet if far from equilibrium and Schwartz and Eley (1998) derived a similarity solution for the droplet profile which takes the following form:

$$h = t^{-1/5} f\left(\frac{r}{t^{1/10}}\right) , \tag{2.31}$$

where f is the solution of a third-order nonlinear ordinary differential equation and r is the radial coordinate in a cylindrical coordinate system. If, in turn, the spreading is driven mostly by the normal component of gravity, the dominating term will be $C_2(\psi - z)$ in eq. (2.30) and neglecting the other terms, Nakaya (1974) was able to extract a self-similar solution. This solution is described in detail in Chapter 5 since it is used for validation purposes.

For viscous flow down a slope, the similarity solution found by Huppert (1982) states that for long-time, $h(x,t)$ behaves like $\left(\frac{x}{t}\right)^{1/2}$ providing the flow is driven by the tangential component of the gravity only.

2.4 Governing parameters

2.4.1 Gravity-driven flow of continuous thin liquid films

Motivated by the experimental work of Decré and Baret (2003), many of the results presented in subsequent chapters focus on the continuous flow of a 100 μm thick water film down a plane inclined at 30^o. Liquid properties are taken as $\mu = 0.001$ Pa s. $\rho = 1000$ kg m^{-3} and $\sigma = 0.07$ N m^{-1} and the substrate extends over 100 capillary length ($\beta = 100$). Table 2.2 summarises the associated scalings and dimensionless groups. The constant $Ca^{1/3} \cot\alpha$, appearing in C_2, which measures the relative importance of the normal component of gravity (Bertozzi and Brenner (1997)), is more commonly referred to N in the literature and this notation is adopted from here onwards.

A wide range of gravity-driven flow over topography is investigated in Chapters 6 and 7. When comparing with Decré and Baret (2003), topographies typically extend

Scalings, dimensionless groups	Equation	Value
Q_0	$Q_0 = \frac{{H_0}^3 \rho g \sin\alpha}{3\mu}$	1.635×10^{-6} m^2/s
U_0	$U_0 = \frac{3Q_0}{2H_0}$	2.452×10^{-2} m/s
L_c	$L_c = \left(\frac{\sigma H_0}{3\rho g \sin\alpha}\right)^{1/3}$	7.8×10^{-4} m
L_0	$L_0 = \beta L_c$	7.8×10^{-2} m
T_0	$T_0 = \frac{L_0}{U_0}$	3.18 s
P_0	$P_0 = \frac{\rho g L_0 \sin\alpha}{2}$	1.913×10^2 Pa
ϵ	$\epsilon = \frac{H_0}{L_0}$	1.28×10^{-3}
Ca	$Ca = \frac{\mu U_0}{\sigma}$	3.5×10^{-4}
N	$N = Ca^{1/3} \cot\alpha$	1.2×10^{-1}

TABLE 2.2: The value of scalings and dimensionless groups for the flow of a 100 μm thick water film down a plane inclined at 30^o.

over $1.54L_c$ (1.2 mm) in the streamwise direction with a spanwise length ranging from $1.54L_c$ to $7.7L_c$ (1.2 mm to 6 mm) and a depth equal to $0.25H_0$ (25 μm). The extent of the topography is chosen to be of the same order as the capillary length in order to test the potential nonlinear effects (Decré and Baret (2003)). Indeed, as discussed by Stillwagon and Larson (1990) and further developed in Kalliadasis *et al.* (2000), when the ratio of topography extent and the capillary length is small, the free surface tends to respond to the topography as a localised, singular perturbation, whereas large values of this ratio lead to well separated non-interacting step-up or -down.

2.4.2 Droplet spreading

The choice of characteristic droplet thickness, H_0, and substrate extent, L_0, is not arbitrary. It is defined with respect to a reference state of the droplet. The reference state as defined in Schwartz (1998) is a stationary paraboloidal droplet with central height H_0 and base radius R_0 located at the centre of a square, flat substrate of extent L_0, characterised by a constant equilibrium contact angle Θ_0. Within the small slope assumption, the contact angle satisfies $\Theta_0 \sim 2H_0/R_0$ (Schwartz and Eley (1998)) showing that, for a given equilibrium contact angle, H_0 and R_0 can not be chosen independently. In a cylindrical polar coordinate system centred on

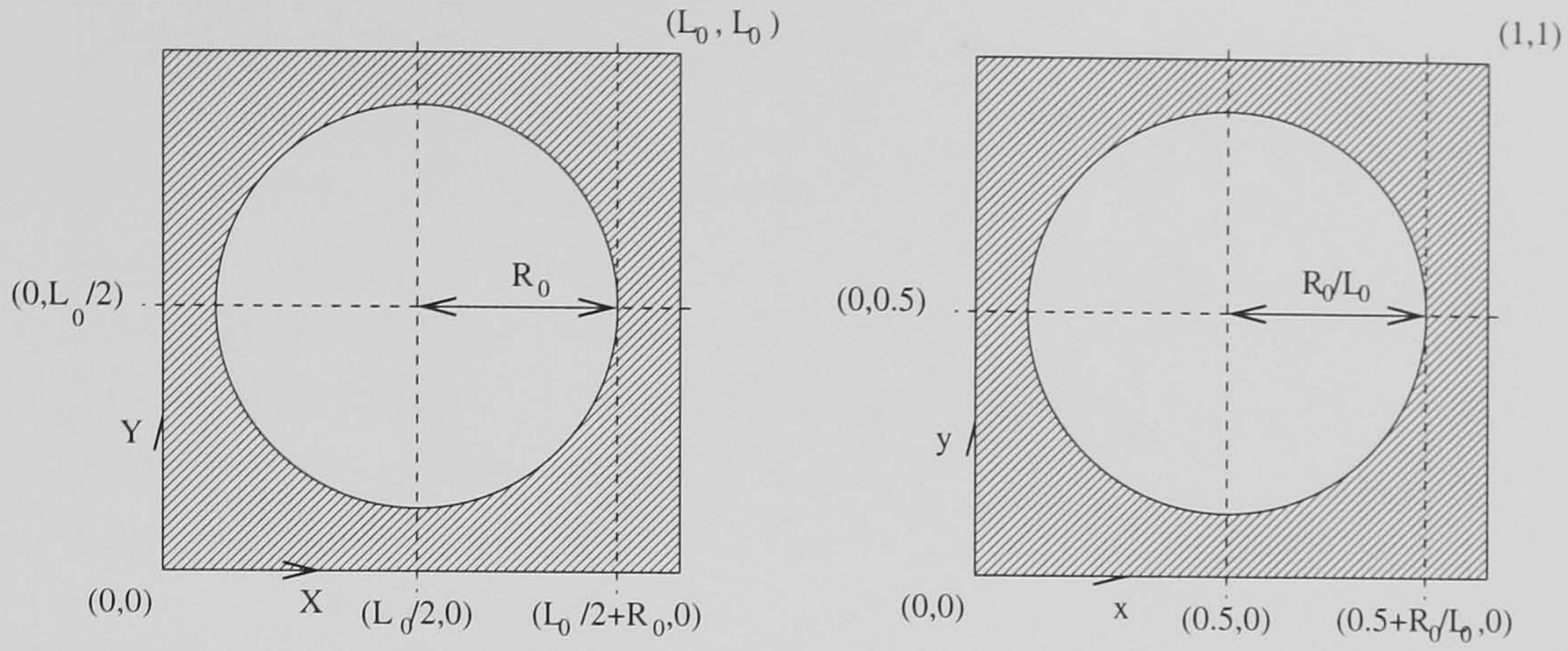

FIGURE 2.2: Footprint of a reference droplet (white disk) on the substrate in physical (Figure (**a**)) and dimensionless (Figure (**b**)) coordinate systems.

the symmetry axis of the droplet, the reference droplet profile is given by

$$H(R) = max\left(H_0\left(1-\left(\frac{R}{R_0}\right)^2\right), H^*\right) , \tag{2.32}$$

where H^* is the precursor film thickness which will be discussed in depth in the next section. The substrate extent L_0 is chosen so that the droplet base diameter D_0 satisfies $D_0 = 2R_0 = \frac{3}{4}L_0$. This choice of scaling ensures that the substrate is large enough to capture the expansion of the droplet from its initial state to the reference (or equilibrium) state and avoid interferences between the contact line and the boundary of the substrate. For clarity, Figure 2.2 shows the footprint of the reference droplet on the substrate in both physical and dimensionless coordinate systems. The reference droplet profile in terms of dimensionless variables is

$$h(r) = max\left(1-\left(\frac{r}{R_0/L_0}\right)^2, h^*\right) = max\left(1-\frac{64}{9}r^2, h^*\right) , \tag{2.33}$$

where r is the distance from the centre of the substrate $(x, y) = (0.5, 0.5)$. In subsequent numerical results, initial droplet profiles are paraboloids with central height H_i and radius R_i. The volume of the initial paraboloidal droplet V_d satisfies $V_d = \frac{\pi}{2}H_i{R_i}^2$ and its conservation imposes that

$$\frac{\pi}{2}H_i{R_i}^2 = \frac{\pi}{2}H_0{R_0}^2 . \tag{2.34}$$

Scalings, dimensionless groups	Equation	Value
L_0	$L_0 = \frac{8}{3}R_0$	2.667×10^{-3} m
H_0	$H_0 = \frac{\Theta_0 R_0}{2}$	8.727×10^{-5} m
ϵ	$\epsilon = \frac{H_0}{L_0}$	3.272×10^{-2}
P_0	$P_0 = \frac{\sigma\epsilon}{L_0}$	8.59×10^{-1} Pa
T_0	$T_0 = \frac{\mu L_0}{\sigma\epsilon^3}$	1.089 s
U_0	$U_0 = \frac{L_0}{T_0}$	2.449×10^{-3} m/s
Bo	$Bo = \frac{\rho g {L_0}^2}{\sigma}$	9.997×10^{-1}

TABLE 2.3: The value of scalings and dimensionless groups for the spreading of a droplet of characteristic base radius 1 mm and equilibrium contact angle 10^o.

Thus, the initial droplet profile will be given by

$$H(R) = max\left(H_i\left(1 - \left(\frac{R}{R_i}\right)^2\right), H^*\right) , \tag{2.35}$$

and taking as an example $H_i = 5H_0$ yields the following dimensionless counterpart of eq. (2.35),

$$h(r) = max\left(5\left(1 - \frac{320}{9}r^2\right), h^*\right) . \tag{2.36}$$

A more quantitative picture is achieved by taking a particular example. Consider a water droplet at equilibrium on a flat, horizontal substrate with a base radius of 1 mm and an equilibrium contact angle of 10^o. Keeping the water properties identical to those defined in the previous section, Table 2.3 summarises the scalings and dimensionless groups. Note that because of the small-slope assumption in the derivation of the lubrication approximation and the parabolic velocity profile, the range of possible equilibrium contact angle is restricted to small values. To the best of the author's knowledge, a quantitative estimate of the limiting equilibrium contact angle beyond which the lubrication approximation is no longer valid has never been attempted.

2.5 Contact lines

Contact, or wetting, lines are ubiquitous in the context of droplet spreading and as such the means by which the same are modelled in terms of the lubrication

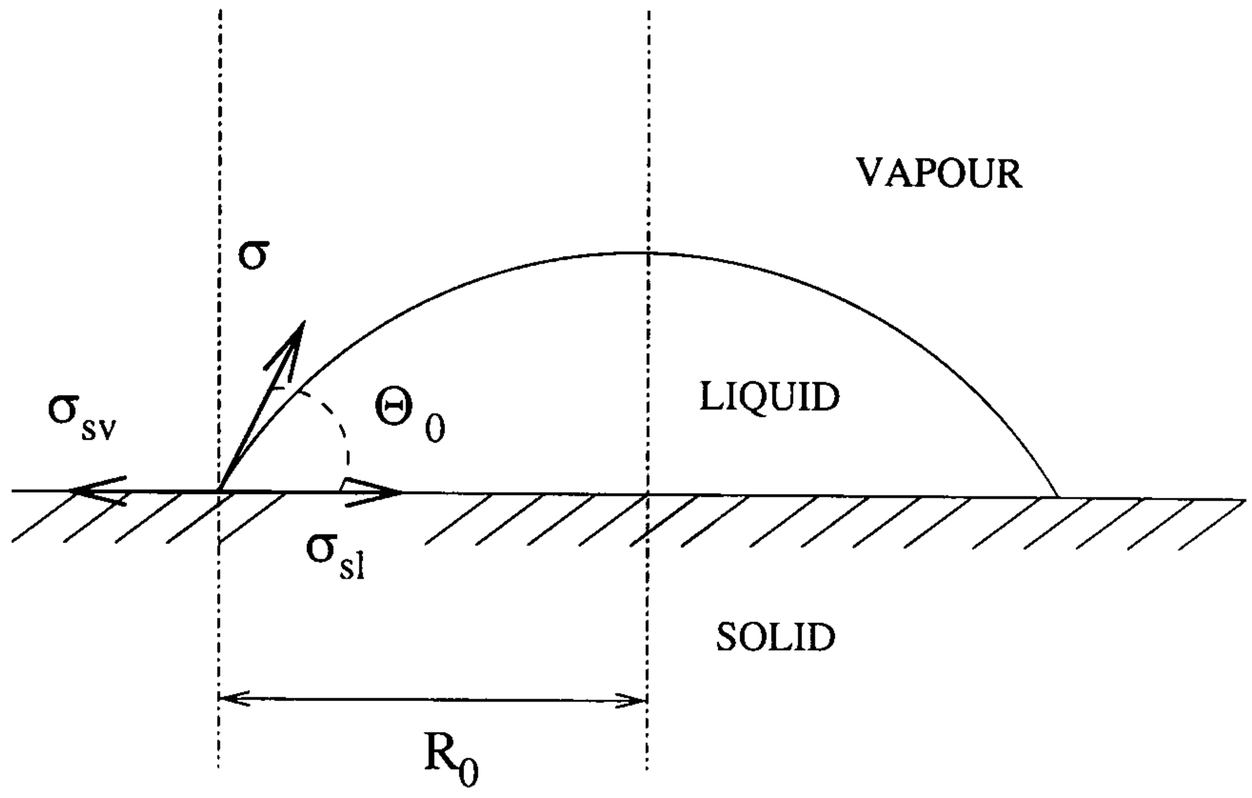

FIGURE 2.3: Droplet at equilibrium with corresponding surface energies (force per unit length).

approximation is discussed below.

2.5.1 Static wetting

Definitions

The wetting or non-wetting of a solid by a liquid is governed by the surface energies between the solid and the vapour phase, σ_{sv}, the solid and the liquid phase, σ_{sl}, and the liquid and vapour phases, σ. A force balance at the contact line, see Figure 2.3, defined as the triple juncture of the solid-vapour, solid-liquid and liquid-vapour interface, yield the well-known Young equation (Adamson (1982)):

$$\cos\Theta_0 = \frac{\sigma_{sv} - \sigma_{sl}}{\sigma}\,, \tag{2.37}$$

where Θ_0 is the equilibrium contact angle (see Figure 2.3). Following the definitions of Law (2001), when $0^o < \Theta_0 < 90^o$, the substrate is *partially wetted* by the liquid while when $90^o < \Theta_0 < 180^o$ the substrate is *partially dried* by the liquid. In the limit when $\Theta_0 = 0$, the liquid is said to *completely wet* the substrate while at the opposite extreme, when $\Theta_0 = 180^o$, we have *complete drying* of the substrate by the liquid.

Throughout this thesis, it is assumed that the value of the equilibrium contact angle

is known and fixed for a particular solid/liquid/vapour system, although it should be noted that the value of the equilibrium contact angle is not necessarily unique for a particular solid/liquid/vapour system. For example, little droplets can remain stuck on inclined surfaces showing that, despite the equilibrium state of the droplet, different values of the equilibrium contact angle can coexist along the contact line: large ones at the front and smaller ones at the rear. This phenomenon, known as *contact angle hysteresis*, is not explored in this work.

Quéré (2002) reviews various mechanisms which affect wetting. These include sharp edges on the substrate where the singularity of the solid slope leaves the contact angle undetermined, chemical discontinuities at the surface where the contact angle can fluctuate between its value on one side of the boundary to its value on the other. The roughness of the substrate is also known to influence the wetting by increasing the hysteresis (the range of possible contact angle).

2.5.2 Dynamic wetting

The contact line paradox

Problems arise when the contact line is in motion, i.e. a liquid for example spreads to displace air. The dynamics of a contact line are still a matter of intense research and no universally agreed description of the underlying physics is available to date. The difficulty arises from the incompatibility between the usual no-slip condition at the solid-liquid interface and the moving contact line leading to a multivalued velocity field. This paradox was formally reported by Huh and Scriven (1971) as they found that a logarithmically divergent force would be required to displace the contact line leading them to the vivid conclusion that "*not even Heracles could sink a solid*". Ever since, there have been two main approaches to alleviate this singularity:

1. allowing for a small amount of slippage effective at small scales in the the contact line region (slip-model);

2. introduction of a very thin precursor film ahead of the contact line maintained

in equilibrium by long-range intermolecular forces (disjoining pressure model).

These methods are reviewed by Oron *et al.* (1997) and by Bertozzi (1998). Blake and Haynes (1969), for example, proposed a molecular-kinetic theory to describe the macroscopic behaviour of the wetting line by considering the overall statistics of the individual molecular displacements which occur within the three-phase zone. However, this approach is not considered in this thesis.

Slip-model

Typically, slip at the wetting line is introduced by replacing the no-slip boundary condition by

$$U = \lambda \frac{\partial U}{\partial Z} \ , \tag{2.38}$$

at the substrate. Here λ represents the *slip length* and is numerically small so that the slip is negligible except near the contact line where $\frac{\partial U}{\partial Z}$ is large. In addition to the slip condition, Greenspan and Mc Cay (1981) argued that a constitutive law relating the dynamic contact angle also called apparent contact angle, Θ, to the contact line speed, U_{cl}, is required in order to obtain a well-posed mathematical model. The experimental and theoretical studies of Dussan V. (1979) showed that this constitutive law takes the form,

$$U_{cl} = K_a(\Theta - \Theta_a)^m \ , \quad \Theta > \Theta_a \ , \tag{2.39}$$

$$U_{cl} = -K_r(\Theta_r - \Theta)^m \ , \quad \Theta < \Theta_r \ , \tag{2.40}$$

where K_a, K_r and m are positive constants and Θ_a, Θ_r are the advancing and receding contact angle respectively. Using this approach for a completely wetting axisymmetric droplet ($\Theta_a = 0$) driven purely by surface tension and with $m = 1$, Greenspan (1978) found that the base radius of the droplet $R(T)$ satisfies a power law of the form:

$$R \sim T^q \ , \tag{2.41}$$

with $q = \frac{1}{4}$. Ehrhard and Davis (1991) took $m = 3$ instead leading to $q = \frac{1}{10}$ in good agreement with the experimental results of Tanner (1979). The success of

this approach is however restricted to configurations with a high degree of symmetry (O'Brien and Schwartz (2002)) and the extension to spreading problems with complex wettability patterns is not straightforward. For this reason, the disjoining pressure model detailed in the next section was adopted.

The disjoining pressure model

The disjoining pressure model relies on the assumption that a very thin precursor film precedes the contact line so that the film effectively spreads on a prewetted surface. The presence of this precursor film has been reported experimentally for various solid/liquid/vapour systems when the liquid completely wets the solid. A review of these experiments can be found in de Gennes (1985). The asymptotic thickness, H^*, of the precursor film depends on the interaction potential for a particular solid/liquid/vapour system and is constrained by the stability criteria discussed by Mitlin (1994). Outside of this stability window, a uniform film cannot exist and dewetting of the substrate leading to the formation of holes occurs. It is generally thought that H^* lies in the range of 1 to 100 nm (Schwartz and Eley (1998), Ehrhard and Davis (1991)). From an hydrodynamic point of view, the presence of this precursor film releases the singularity at the contact line and Deryagin (1955) was the first to suggest that the gradients in disjoining pressure resulting from long-range interaction forces may be responsible for the motion of contact lines. The difficulty associated with this model is the need to derive the exact form of the disjoining pressure for each particular solid/liquid/vapour system, although Teletzke (1983) was able to derive a disjoining pressure term applicable to most fluid-solid systems. By including molecular, electrostatic and structural forces, he found that the disjoining pressure could be written as

$$\Pi(H) = \sum_{1}^{4} \frac{A_n}{H^n} \,, \tag{2.42}$$

although, the constants A_n are still system-dependent.

Following Schwartz (1998), the form of the disjoining pressure adopted for the

present work is taken to be

$$\Pi(H) = B\left[\left(\frac{H^*}{H}\right)^n - \left(\frac{H^*}{H}\right)^m\right] , \tag{2.43}$$

where B, n and m are positive constant with $n > m > 1$. The first and second terms on the right-hand side of eq. (2.43) characterise the liquid-solid attraction and liquid-solid repulsion respectively. In the literature, various pairs of exponents (n, m) have been used. The pair $(9, 3)$ corresponding to attractive, *Van der Waals*, and repulsive, *hard sphere*, potentials was used by Mitlin and Petviashvili (1994), while Churaev and Sobolev (1995) and Teletzke (1983) used the pair $(3, 2)$. Figure

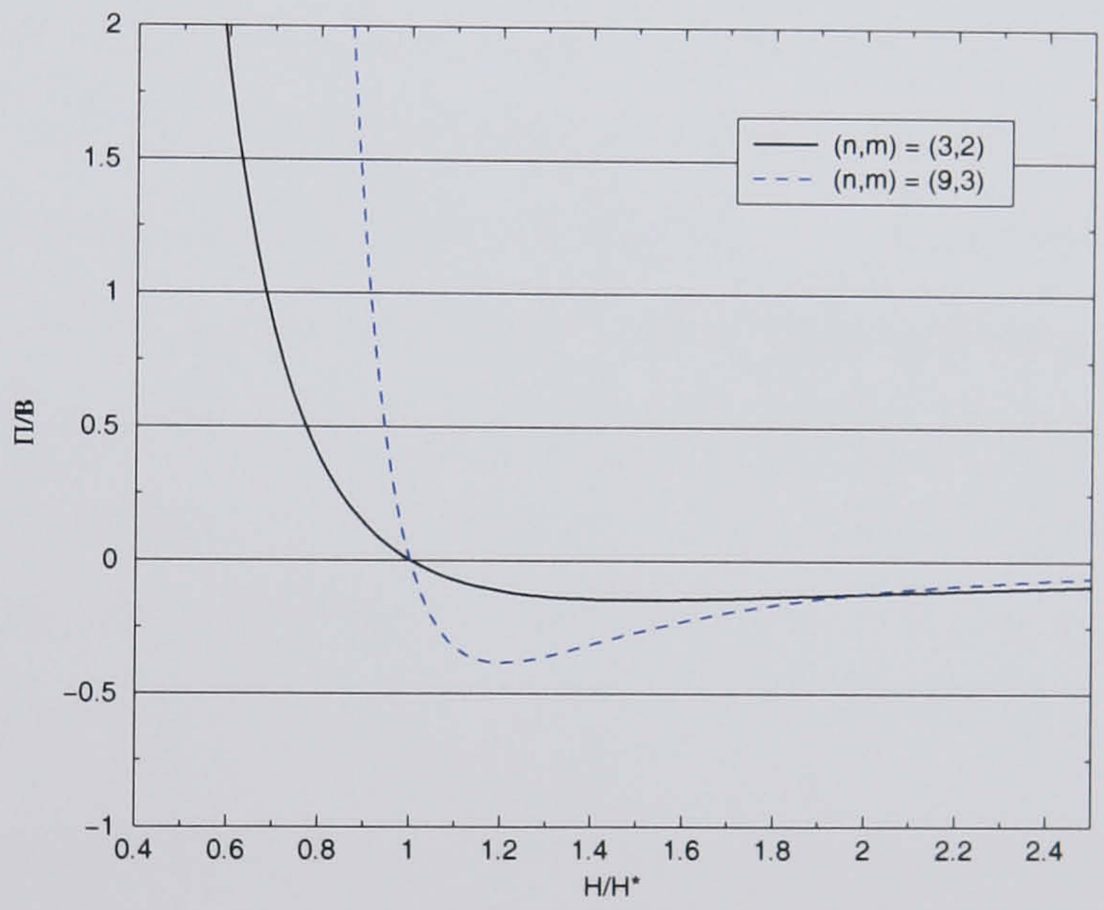

FIGURE 2.4: Normalised disjoining pressure for $(n, m) = (3, 2)$ and $(n, m) = (9, 3)$.

2.4 shows the form of the normalised disjoining pressure with the pairs of exponents $(3, 2)$ and $(9, 3)$. These curves reveal a single stable energy minimum at the precursor film thickness H^* since if $H < H^*$, the positive pressure will tend to restore the film thickness to H^* while if $H > H^*$, the negative pressure will have the same effect.

In Schwartz's approach the constant B is obtained by performing a force balance in the contact line region when the contact line is at equilibrium, and to assume that B remains constant even when the contact line is in motion. The calculations, detailed in Schwartz (1998) and reported in Appendix A, yield

$$B = \frac{(n-1)(m-1)}{H^*(n-m)}\sigma(1-\cos\Theta_0) \approx \frac{(n-1)(m-1)}{2H^*(n-m)}\sigma{\Theta_0}^2 , \tag{2.44}$$

where the small-argument approximation to $\cos\Theta_0$ is used for the approximate equality. Using the scalings defined in the previous section for droplet spreading, the dimensionless counterpart of eqs. (2.43) and (2.44) is

$$\Pi(h) = \frac{(n-1)(m-1)(1-\cos\Theta_0)}{h^*(n-m)\epsilon^2}\left[\left(\frac{h^*}{h}\right)^n - \left(\frac{h^*}{h}\right)^m\right], \tag{2.45}$$

or

$$\Pi(h) = \frac{(n-1)(m-1){\Theta_0}^2}{2h^*(n-m)\epsilon^2}\left[\left(\frac{h^*}{h}\right)^n - \left(\frac{h^*}{h}\right)^m\right], \tag{2.46}$$

when the small-argument approximation to $\cos\Theta_0$ is used. The former form of the disjoining pressure (eq. (2.45)) is the one used in this thesis. However, it is interesting to note that, in the latter form of the disjoining pressure (eq. (2.46)), the ratio ${\Theta_0}^2/\epsilon^2$ can be merged by taking further advantage of the small-slope approximation. Remembering that $\Theta_0 = 2H_0/R_0$, $\epsilon = H_0/L_0$ and $R_0 = 3L_0/8$, the ratio ${\Theta_0}^2/\epsilon^2$ is constant and equal to 256/9. This additional simplification is made in Schwartz and Eley (1998) and Schwartz (1998) offering the advantage of solving governing equations which are independent of the choice of the reference state. It should be noted that Schwartz and co-workers use R_0 as the in-plane characteristic length in which case, ${\Theta_0}^2/\epsilon^2 = 4$.

By imposing a spatially dependent value of the equilibrium contact angle, Θ_0 in eq. (2.45), complex wettability patterns may be reproduced. A drawback of this model is that the choice of H^* is arbitrary and the spreading rate depends on its value. Thicker precursor films tend to over predict the spreading rate. However, for small enough H^*, Schwartz (1998) was able to predict closely the rate of expansion for water droplets on glass in agreement with the experimental results of Lelah and Marmur (1981).

Interestingly, the dynamic contact line stability analysis performed by Spaid and Homsy (1995) showed that the features of the free surface are relatively independent of the choice of contact line model. Furthermore, their stability results using both contact line models agree quantitatively when the slip length, λ, is numerically equal to the precursor film thickness, H^*. From a computational point of view, the benefit of using the disjoining pressure model was also outlined in Hocking (1992)

and further emphasised in Diez *et al.* (2000) where it was shown that larger time increments were achievable, hence reducing the total computational time. This computational benefit motivates further the choice of the disjoining pressure model in the present work.

2.6 Domain boundary conditions

The solution to equations (2.29) and (2.30) is sought on a square domain with $(x, y) \in \Omega = (0, 1) \times (0, 1)$ and in order to obtain a well-posed mathematical problem, boundary conditions are necessary at the substrate boundary. Two types of boundary condition have been applied in this work depending on the problem considered.

1. For droplet spreading, symmetry boundary conditions are imposed at the edge of the substrate, viz

$$\frac{\partial p}{\partial n} = \frac{\partial h}{\partial n} = 0 \,, \tag{2.47}$$

where n is the normal to the substrate boundary. As explained in the previous section, the parameters are chosen so that all of the spreading occurs within the domain so that the effect of the boundary conditions is very weak.

2. For gravity-driven thin liquid films in the constant flux configuration, the boundary conditions result from the assumptions that the flow is fully developed upstream and downstream, that is:

$$h(x = 0, y) = 1 \,, \ \frac{\partial h}{\partial x}|_{x=0} = 0 \ \text{ and } \ \frac{\partial h}{\partial x}|_{x=1} = \frac{\partial p}{\partial x}|_{x=1} = 0 \,, \tag{2.48}$$

and choosing

$$\frac{\partial p}{\partial y}|_{y=0} = \frac{\partial p}{\partial y}|_{y=1} = 0 \ \text{ and } \ \frac{\partial h}{\partial y}|_{y=0} = \frac{\partial h}{\partial y}|_{y=1} = 0 \,, \tag{2.49}$$

along the boundary parallel to the mainstream flow insures, according to eq. (2.28), a zero flux in the direction normal to the boundary.

2.7 Energy considerations

In this section, the expression of the energies associated with each driving force is reported for later use. Much insight about the dominant driving forces during the motion of thin films is gained by monitoring the corresponding energy variations. For example, the energy budget applied to a droplet spreading, freely and spontaneously, on a homogeneous substrate states that the rate of viscous dissipation is equal to the rate of decrease of the energy stored in the form of surface tension and disjoining energy. Since the viscous dissipation is proportional to the square of the speed of motion, rapid decrease of the potential (or stored) energy corresponds to episodes of rapid motion.

Different methods purely based on energy balance have been developed to investigate droplet spreading and thin film flows. For example, the "Overall Energy Balance" (OEB) method proposed by Gu and Li (1998) successfully reproduced the dynamics of silicon liquid droplets spreading on a soda-lime glass plate after the adjustment of a single parameter. Darhuber *et al.* (2001) calculated static equilibrium ink surface profile with SURFACE EVOLVER which is an energy minimisation software tool that computes liquid equilibrium conformations given the volume, geometric boundary conditions, and surface energies associated with the liquid-air, liquid-solid, and air-solid interface (Brakke (1992)).

In the cases considered throughout this thesis, the three different forces which contribute to the total potential energy of the system are the surface tension, the disjoining pressure and gravity. Those energies are found by considering the work done for a very small displacement of the free surface and then integrating over the whole surface area. Each component of the energy is written in integral form (Schwartz and Eley (1998)) as follows

1. Surface tension energy, E_σ

$$E_\sigma = \frac{\sigma}{2} \int \int \bigtriangledown H . \bigtriangledown H \, dA \, , \tag{2.50}$$

where dA denotes an elementary surface area.

2. Disjoining pressure energy, E_d

$$E_d = \frac{\sigma}{2} \int \int {\Theta_0}^2 \left[1 + \frac{m-1}{n-m} \left(\frac{H^*}{H} \right)^{n-1} - \frac{n-1}{n-m} \left(\frac{H^*}{H} \right)^{m-1} \right] \, dA \, , \quad (2.51)$$

which for the pair of exponent $(3, 2)$ takes the simpler form

$$E_d = \frac{\sigma}{2} \int \int \Theta_0^2 \left(1 - \frac{H^*}{H} \right)^2 \, dA \, . \quad (2.52)$$

3. Energy associated with the normal component of the gravity, $E_\perp$

$$E_\perp = \frac{1}{2} \rho g \cos \alpha \int \int \left(H^2 - H^{*2} \right) \, dA \, . \quad (2.53)$$

4. Energy associated with the tangential component of the gravity, $E_{||}$

$$E_{||} = \rho g \sin \alpha \int \int X (H - H^*) \, dA \, . \quad (2.54)$$

In the following, all the energies will be made dimensionless by scaling with respect to$\pi \sigma h_0^2$.

Chapter 3

Solution procedure

Contents

3.1 Introduction

Within its validity range, the lubrication approximation derived in the previous chapter provides a robust tool to investigate thin film flows with the benefit of reducing considerably the number of unknowns (U, V, W, P and H for the Navier-Stokes equations against h and p for the lubrication approximation). Despite this simplification, analytical solutions not requiring further assumptions are scarce and restricted to two-dimensional or axisymmetric configurations. A review of the possible analytical approaches can be found in Myers (1998). In the absence of general analytical treatment, the governing equations have to be solved numerically.

There are, however, several major computational obstacles to overcome to successfully solve the lubrication equations (eqs. (2.29) and (2.30)), principally due to the stiffness introduced by surface tension and the need to resolve short length scales close to wetting lines. These features lead to impractical restrictions on the choice of stable time increments, Δt, when explicit time stepping numerical schemes are employed, $\Delta t < O(\Delta^4)$ in terms of the spatial resolution Δ, Bertozzi (1998). Several authors have eased the severe restriction on time step noted above by employing semi-implicit schemes incorporating alternating-direction implicit ($\mathcal{ADI}$) algorithms which, for three-dimensional flows, use alternating sweeps in each direction so that only banded systems of equations need be solved at each time step, Weidner *et al.* (1997). These schemes, often referred to as *time-splitting*, Christov *et al.* (1997), have been used widely by Schwartz and co-workers to analyse a range of problems including, for example, that due to the effects of substrate curvature and surface tension gradients on the thinning of a coating on a curved substrate (Weidner *et al.* (1996)), droplet motions on heterogeneous substrates with materials having widely different equilibrium contact angles (Schwartz and Eley (1998), Schwartz (1998)) and gravity- and surface shear stress-driven thin coating flows (Eres *et al.* (2000)).

An additional difficulty comes from the fact that accurate representation of the wetting line and, in particular, avoidance of negative film thicknesses in their vicinity requires that the spatial resolution should be of the same order of magnitude as h^*. Because the precursor film is so thin (in the range of 1 to 100 nm), it is

currently not feasible to use realistic h^* in the computations. For example, for a droplet of typical thickness 1 mm and a 100 nm thick precursor film, a spatial resolution of order 10^{-4} would be necessary which is achievable for two-dimensional simulation but still out of reach without local mesh refinement for three-dimensional calculations. This and related issues are discussed in detail by Bertozzi (1998) and have led to the development of new numerical schemes which ensure that the film thickness remains positive without requiring excessive mesh refinement near wetting lines, Zhornitskaya and Bertozzi (2000). Furthermore, as mentioned in the previous chapter, h^* is the principal determinant of spreading rate, Schwartz (1998), so that the inability to use a sufficiently small h^* in computations leads to a systematic over-prediction of spreading rate. However, this difficulty can normally be compensated for by using an analytic correction, Schwartz and Eley (1998).

In contrast to employing time-splitting to solve the time dependent lubrication equations, the present work utilises a fully implicit multigrid approach.

The key advantage of multigrid methods is the efficiency. Fedorenko (1964) was the first to establish the optimal efficiency of the method as he proved that for the standard five-point finite difference discretisation of the Poisson equation on a square computational domain, the work required to reach a given precision is $O(N)$, where N is the total number of unknowns. By comparison, $\mathcal{ADI}$ schemes require $O(Nlog(N)log(\epsilon))$ operations, where ϵ is a stopping criterion (Trottenberg (2001)).

The pioneering work of Brandt (1977) provided a practical framework for the multigrid technique and he developed the $\mathcal{FAS}$ version of multigrid for nonlinear partial differential equations. His work also outlined the principle of mesh adaptivity, another important feature of multigrid techniques. In the meantime, Hackbusch (1981) developed a formal framework giving rigorous convergence proofs.

Ever since, multigrid techniques have been applied to increasingly difficult systems of partial differential equations and are now commonly used to solve the discretised equations arising from a wide variety of flow problems - see for example Spitaleri and Corinaldesi (1997), Chou (2000), Liao and Mashayek (2001) - for which major improvements in efficiency and robustness are now being achieved, Thomas *et al.*

(2003). Multigrid techniques have also been applied with success in an area of research related to thin film flows: elastohydrodynamic lubrication (Ehret *et al.* (1997), Goodyer (2001)).

In this chapter, spatial and temporal discretisation are first introduced with a particular emphasise on the Positivity Preserving Scheme ($\mathcal{PPS}$) derived by Zhornitskaya and Bertozzi (2000) and our own adaptive time-stepping scheme, Gaskell *et al.* (2003(a)). The implementation of the Full Approximation Storage ($\mathcal{FAS}$) variant of the multigrid method for nonlinear equations, Brandt (1982), is then described along with the treatment of boundary conditions.

3.2 Spatial discretisation

Problems are solved on a square computational domain with $(x, y) \in \Omega = (0, 1) \times (0, 1)$ using the multigrid approach described below. The finest grid level (i.e the actual grid on which the solution is desired) has $(2^{k_f} + 1)$ nodes in each direction so that the spatial co-ordinates of its grid points are given by $x_i = \frac{(i-1)}{2^{k_f}}$ and $y_j = \frac{(j-1)}{2^{k_f}}$ in terms of the fine grid density parameter k_f. In this work $k_f \in [6, 10]$ corresponding to grids at the finest level with between 65 and 1025 nodes in each direction. For clarity, Figure 3.1 shows a typical cell of the mesh centred on the vertex (i, j).

Equations (2.29) and (2.30) are approximated spatially using central differences as in Weidner *et al.* (1997) or Kondic and Diez (2001), leading to the following second order accurate discretisations

$$\frac{\partial h_{i,j}}{\partial t} = \frac{1}{\Delta^2}\left[\frac{h^3}{3}|_{i+\frac{1}{2},j}\,(p_{i+1,j} - p_{i,j}) - \frac{h^3}{3}|_{i-\frac{1}{2},j}\,(p_{i,j} - p_{i-1,j}) + \right.$$
$$\left.\frac{h^3}{3}|_{i,j+\frac{1}{2}}\,(p_{i,j+1} - p_{i,j}) - \frac{h^3}{3}|_{i,j-\frac{1}{2}}\,(p_{i,j} - p_{i,j-1})\right] -$$
$$C_1 h_{i,j}^2 \left(\frac{h_{i+1,j} - h_{i-1,j}}{2\Delta}\right) + O(\Delta^2)\,, \tag{3.1}$$

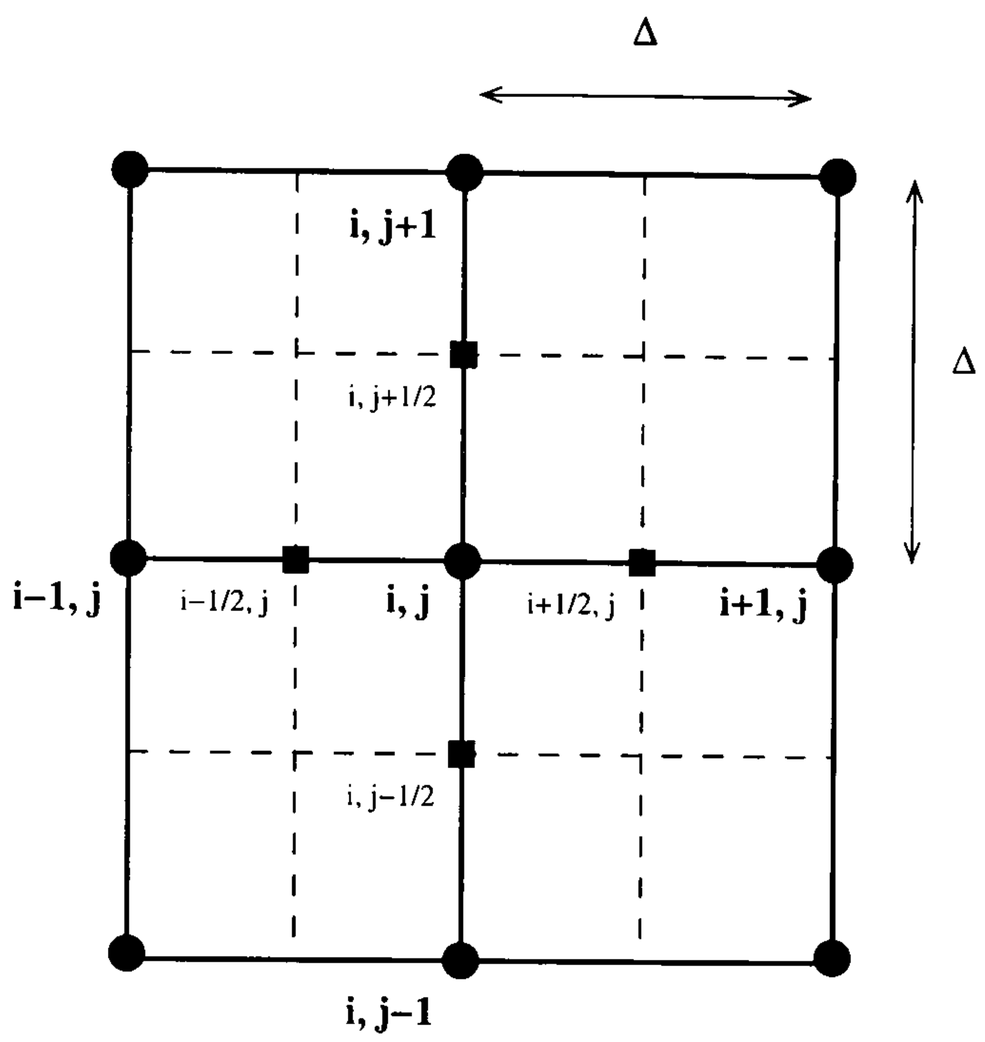

FIGURE 3.1: A typical cell of the mesh centred on the vertex (i, j).

$$p_{i,j} + \frac{C_3}{\Delta^2}\Big[(h_{i+1,j} + s_{i+1,j}) + (h_{i-1,j} + s_{i-1,j}) + (h_{i,j+1} + s_{i,j+1}) + (h_{i,j-1} + s_{i,j-1}) - 4(h_{i,j} + s_{i,j})\Big] + C_4 \frac{(n-1)(m-1)(1-\cos\Theta_e)}{h^*(n-m)\epsilon^2} \times \left[\left(\frac{h^*}{h_{i,j}}\right)^n - \left(\frac{h^*}{h_{i,j}}\right)^m\right] - C_2(h_{i,j} + s_{i,j}) + O(\Delta^2) = 0\,, \tag{3.2}$$

for any interior point (i,j) in the computational domain, where $\Delta = 2^{-k_f}$ is the spatial increment. Two different schemes have been used for the mid-point interpolation of the prefactors $\Gamma(h) = \frac{h^3}{3}$ in eq. (3.1). The first one, and the most commonly used, is referred to the Standard Scheme ($\mathcal{SS}$) in Kondic and Diez (2001) and simply consists of a linear interpolation of the pre-factor between the two neighbouring nodes, viz

$$\frac{h^3}{3}|_{i\pm\frac{1}{2},j} = \frac{1}{2}\left(\frac{h^3}{3}|_{i\pm1,j} + \frac{h^3}{3}|_{i,j}\right)\,, \tag{3.3}$$

$$\frac{h^3}{3}|_{i,j\pm\frac{1}{2}} = \frac{1}{2}\left(\frac{h^3}{3}|_{i,j\pm1} + \frac{h^3}{3}|_{i,j}\right)\,. \tag{3.4}$$

The second one, based on the work of Zhornitskaya and Bertozzi (2000). is a Posit-

ivity Preserving Scheme ($\mathcal{PPS}$). Their study proved rigorously the consistency and stability of this scheme along with its positivity preserving nature even on underresolved grids. The $\mathcal{PPS}$ is defined as follows

$$\frac{h^3}{3}|_{i+\frac{1}{2},j} = \frac{h_{i+1,j} - h_{i,j}}{g_{i+1,j} - g_{i,j}} \,, \tag{3.5}$$

where $g' = \frac{1}{\Gamma(h)}$, which gives

$$\frac{h^3}{3}|_{i+\frac{1}{2},j} = \frac{2}{3}\frac{h_{i,j}^2 h_{i+1,j}^2}{h_{i+1,j} + h_{i,j}} \,, \tag{3.6}$$

$$\frac{h^3}{3}|_{i,j+\frac{1}{2}} = \frac{2}{3}\frac{h_{i,j}^2 h_{i,j+1}^2}{h_{i,j+1} + h_{i,j}} \,, \tag{3.7}$$

in agreement with Diez and Kondic (2002). Similar expressions can easily be found for the other pre-factors.

Solving eqs. (3.1) and (3.2) in the entire computational domain is equivalent to solving simultaneously a set of $(2^{k_f} + 1)^2$ nonlinear ordinary differential equations where the time, t, is the independent variable. The choice of temporal discretisation is critical to the success and efficiency of the solution procedure and the next section describes the approach adopted.

3.3 Temporal discretisation

Ideally, time-stepping schemes for the numerical solution of time-dependent flows should be both *efficient* and *accurate*. The former ensures that small time steps are avoided when the solution varies slowly while the latter should enable the error to be controlled throughout the solution process. Most previous numerical studies of lubrication-type flows have focussed on increasing the efficiency of the solution and, in particular, overcoming the stability requirement for explicit schemes that the time step Δt should be $O(\Delta^4)$ - an impractical restriction when even moderate spatial resolution is employed. The use of *time-splitting* algorithms is a clear improvement as time steps several orders of magnitude larger than $O(\Delta^4)$ can be used successfully. A standard temporal discretisation scheme is the so-called Θ_t-scheme, as used by

Diez and Kondic (2002) for example, defined as

$$h_{i,j}^{n+1} - \Theta_t \Delta t^{n+1} F(h_{i,j}^{n+1}, p_{i,j}^{n+1}, h_{i\pm1,j}^{n+1}, p_{i\pm1,j}^{n+1}, h_{i,j\pm1}^{n+1}, p_{i,j\pm1}^{n+1}) =$$
$$h_{i,j}^{n} + (\Theta_t - 1)\Delta t^{n+1} F(h_{i,j}^{n}, p_{i,j}^{n}, h_{i\pm1,j}^{n}, p_{i\pm1,j}^{n}, h_{i,j\pm1}^{n}, p_{i,j\pm1}^{n}) , \qquad (3.8)$$

where $F(h_{i,j}, p_{i,j}, h_{i\pm1,j}, p_{i\pm1,j}, h_{i,j\pm1}, p_{i,j\pm1})$ corresponds to the right-hand side of equation (3.1), $0 \leq \Theta_t \leq 1$, and the superscript n denotes data at the n^{th} time step. Here, $\Theta_t = 0$ gives the forward Euler scheme (explicit, $O(\Delta t^{n+1})$), $\Theta_t = 1$ equates to the backward Euler scheme (implicit, $O(\Delta t^{n+1})$), and $\Theta_t = \frac{1}{2}$ yields the Crank-Nicholson scheme (implicit, $O((\Delta t^{n+1})^2)$). Throughout the thesis, $\Theta_t = \frac{1}{2}$ has been used.

The use of these schemes alone give little control as to accuracy and it is only recently that an estimate of the local truncation error has been used to test whether the equations are being solved to a specified error tolerance, Diez and Kondic (2002) and Kondic and Diez (2001). Their scheme, however, does not attempt to optimise the time step for a given error tolerance.

Hence, the goal of the present section is to address this issue and provide an efficient alternative to existing schemes by using time-stepping based on local error estimates from an implicit, second order method which reduces to Heun's method, Chapra and Canale (1998), in the case of a fixed time step. This uses an estimate of the local truncation error, obtained from the difference between this solution and an explicit predictor, to increase the time step in a controlled manner whilst at the same time minimising the computational expense associated with repeated time step failure.

The predictor stage is fully explicit, second order accurate in time and proceeds by solving

$$h_{i,j_{Predict}}^{n+1} = \beta^2 h_{i,j}^{n-1} + \left(1 - \beta^2\right) h_{i,j}^{n} + \Delta t^{n+1}(1+\beta) F(h_{i,j}^{n}, p_{i,j}^{n}, h_{i\pm1,j}^{n}, p_{i\pm1,j}^{n}, h_{i,j\pm1}^{n}, p_{i,j\pm1}^{n}) , \qquad (3.9)$$

where $\beta = \frac{\Delta t^{n+1}}{\Delta t^{n}}$. As demonstrated in Appendix C, the local truncation error (LTE)

for the predictor stage is given by

$$(LTE_{Predict})_{i,j} = \frac{\left(\Delta t^{n+1}\right)^2 \Delta t^n (1+\beta)}{6} \frac{\partial^3 h_{i,j}}{\partial t^3}|_{t=t_p} \ , \tag{3.10}$$

where the third derivative term is evaluated at a time $t_p \in (t_n, t_{n+1})$. The solution stage consists of solving eq. (3.8) with $\Theta_t = \frac{1}{2}$ for which the local truncation error is

$$(LTE)_{i,j} = \frac{-1}{12}(\Delta t_{n+1})^3 \frac{\partial^3 h_{i,j}}{\partial t^3}|_{t=t_c} \ , \ t_c \in (t_n, t_{n+1}) \ . \tag{3.11}$$

As described in Chapra and Canale (1998), the assumption that the third order derivative term varies only a small amount over the time step enables the local truncation error to be estimated as

$$(LTE)_{i,j} = \frac{-1}{1+2\left(\frac{1+\beta}{\beta}\right)} \left(h_{i,j}^{n+1} - h_{i,jPredict}^{n+1}\right) \ . \tag{3.12}$$

Following Dormand (1996), this expression is used to obtain an estimate of the overall truncation error by finding its Euclidean norm, $\|LTE\|$, which is then used to specify the next time step, Δt^{n+2}, via

$$\Delta t^{n+2} = 0.9 \Delta t^{n+1} \left(\frac{Tol}{\|LTE\|}\right)^{\frac{1}{3}} , \tag{3.13}$$

if $\|LTE\| \leqslant Tol$, whereas if $\|LTE\| > Tol$ the iteration is restarted with half the current time step.

The implicit system of algebraic equations (3.2) and (3.8) are solved at each time step using the $\mathcal{FAS}$ multigrid method described below.

3.4 The Full Approximation Storage ($\mathcal{FAS}$) multigrid algorithm

The key idea of multigrid is to use a simple iterative technique as a smoother, not as a solver, to reduce high frequency errors on the computational grid while lower frequency errors are smoothed out on a succession of coarser computational grids. A

hierarchy of grids is defined, G^0, G^1,...,G^L say, where the grid spacing is halved from one grid to the next and where G^0 denotes the coarsest grid and G^L the finest. The

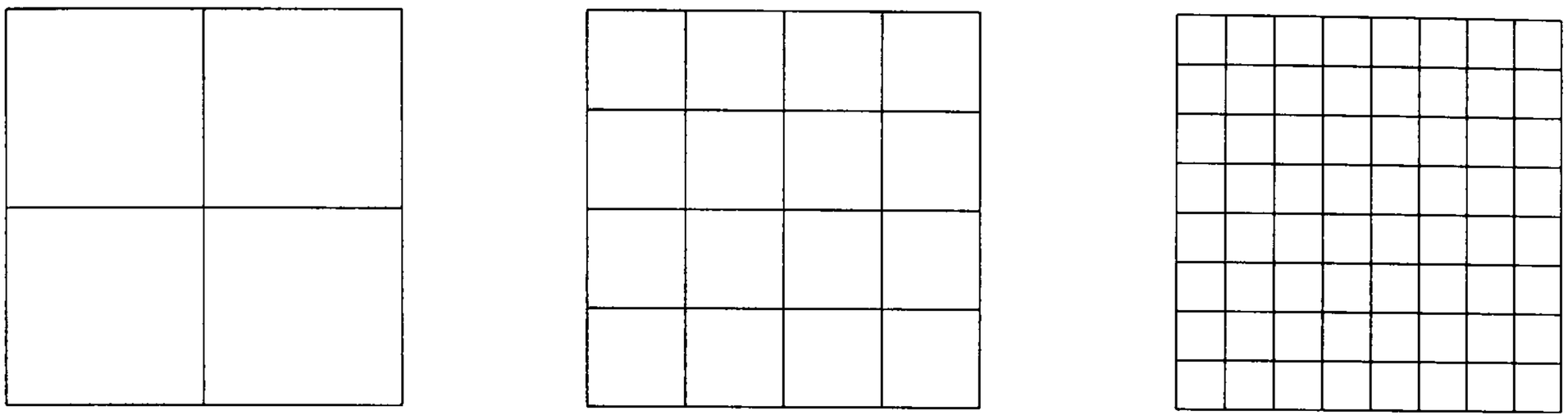

FIGURE 3.2: Hierarchy of grids showing 3 grid levels (G^0, G^1 and G^2) with $k_c = 1$ and $L = 2$.

coarsest grid level G^0 has $(2^{k_c} + 1)$ nodes in either direction so that the finest grid level G^L, i.e. the one on which the final solution is actually desired, has $(2^{k_f} + 1)$ nodes in either direction in terms of the fine grid parameter introduced above, where $k_f = L + k_c$. Figure 3.2 illustrates the grid hierarchy for three grid levels (G^0, G^1 and G^2) with $k_c = 1$ and $L = 2$. Note that the grid spacing associated with each grid level G^k is uniform and equal in both directions and simply given by $\Delta^k = \frac{1}{2^{k+k_c}}$.

The nonlinear discretised equations (3.2) and (3.8) are solved using a combination of the Full Approximation Storage ($\mathcal{FAS}$) method and Full Multigrid technique, Brandt (1982) and Wesseling (1992). Figure 3.3 illustrates the structure of the solution process for four grid levels. An important advantage of this technique is that an initial guess to the solution at a given level is provided by the interpolation of the solution on the next coarser level. At all but the coarsest level a fixed number of V-cycles (N_{cyc}) are applied. At the coarsest level an exact nonlinear solver may be applied or a large number of smoothing iterations may be taken: this work uses the former approach, based on Newton's method. At the very beginning of the full multigrid cycle the solution from the previous time step is used to provide a starting point for the multigrid procedure. In order to explain clearly the steps taken during a single V-cycle, the governing equations (3.2) and (3.8), at the grid level k, may be

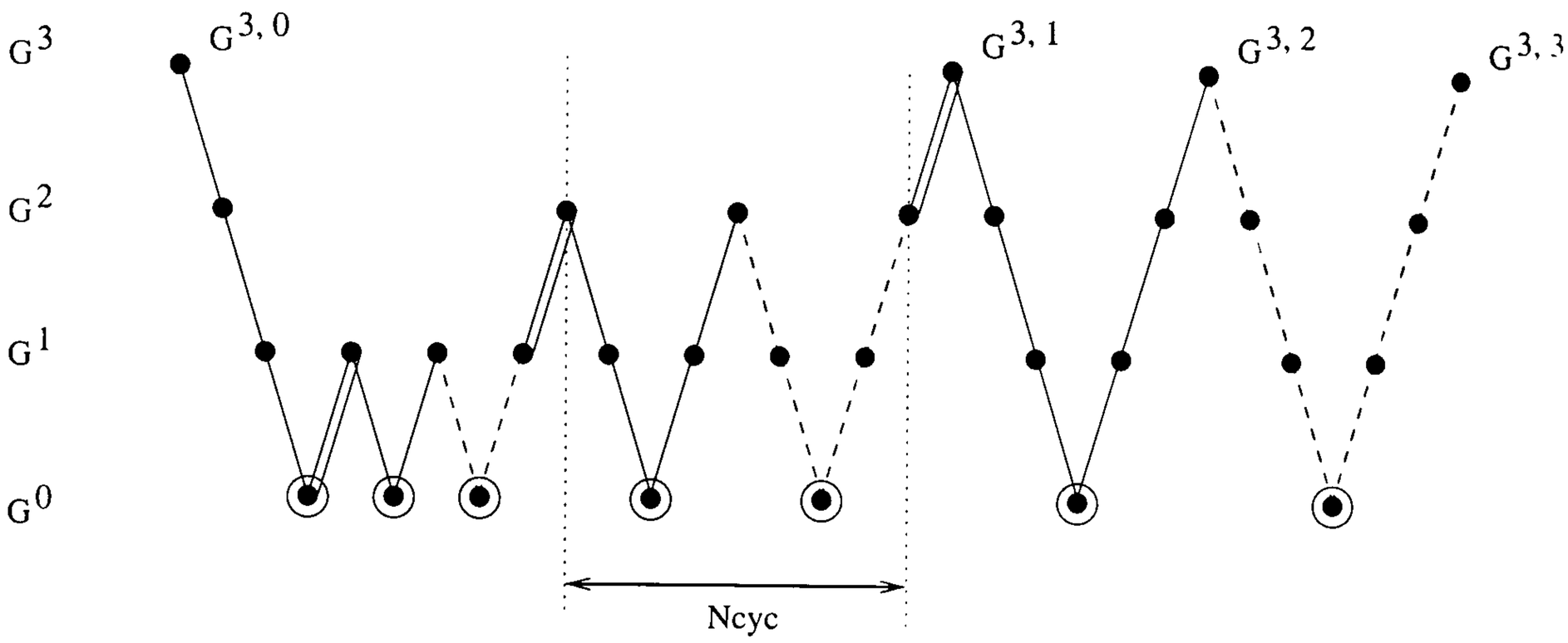

FIGURE 3.3: Description of the Full Multigrid technique for 4 grid levels.

rewritten in the following way:

$$\mathcal{L}_k^h\left(\underline{h}_k^{n+1}, \underline{p}_k^{n+1}\right) = f_k^h\left(\underline{h}_k^n, \underline{p}_k^n\right), \tag{3.14}$$

$$\mathcal{L}_k^p\left(\underline{h}_k^{n+1}, \underline{p}_k^{n+1}\right) = 0, \tag{3.15}$$

where the film thicknesses and pressure at the n^{th} time step t^n are known and are given by $\underline{h}_k^n = \{h_{ij_k}^n\}$ and $\underline{p}_k^n = \{p_{ij_k}^n\}$, and f_k^h corresponds to the right-hand side of eq. (3.8).

Given $\underline{h0}_k^{n+1}$ and $\underline{p0}_k^{n+1}$ as an initial guess to the solution of equations (3.14) and (3.15), the computed values after completion of the V-cycle are: $\underline{h1}_k^{n+1}$ and $\underline{p1}_k^{n+1}$. Each V-cycle within the solution process may be defined in a recursive way using precisely the same pseudo-code formalism as in Trottenberg (2001):

In functional notation this V-cycle from level k may be written as

$$\left(\underline{h1}_k^{n+1}, \underline{p1}_k^{n+1}\right) = FASCYC\left(k, \underline{h0}_k^{n+1}, \underline{p0}_k^{n+1}, f_k^h, f_k^p, n_{pre}, n_{post}\right).$$

The function FASCYC may be broken down into three distinct stages:

1. *Presmoothing stage:*

   - Apply n_{pre} times a Red-Black Gauss-Seidel scheme to a linearised form of equations (3.14) and (3.15) so that, in functional notation:

$$\left(\widetilde{\underline{h_0}_k}^{n+1}, \widetilde{\underline{p_0}_k}^{n+1}\right) = RELAX^{n_{pre}}\left(\underline{h_0}_k^{n+1}, \underline{p_0}_k^{n+1}, f_k^h, f_k^p\right) .$$

2. *Coarse grid correction stage:*

   - Compute the defects:

$$d_k^h = f_k^h - \mathcal{L}_k^h\left(\widetilde{\underline{h_0}_k}^{n+1}, \widetilde{\underline{p_0}_k}^{n+1}\right) , \; d_k^p = f_k^p - \mathcal{L}_k^p\left(\widetilde{\underline{h_0}_k}^{n+1}, \widetilde{\underline{p_0}_k}^{n+1}\right) .$$

     (Note that in our problem, from equation (3.15), $f_L^p = 0$. However this is not the case in general for $k < L$, as shown below.)

   - Restrict the defect to the next coarse grid level using a half-weighting restriction operator, R_k^{k-1}:

$$d_{k-1}^h = R_k^{k-1}\left(d_k^h\right) , \; d_{k-1}^p = R_k^{k-1}\left(d_k^p\right) .$$

   - Restrict $\widetilde{\underline{h_0}_k}^{n+1}$ and $\widetilde{\underline{p_0}_k}^{n+1}$ in the same way:

$$\widetilde{\underline{h_0}_{k-1}}^{n+1} = R_k^{k-1}\left(\widetilde{\underline{h_0}_k}^{n+1}\right) , \; \widetilde{\underline{p_0}_{k-1}}^{n+1} = R_k^{k-1}\left(\widetilde{\underline{p_0}_k}^{n+1}\right) .$$

   - Compute the right-hand side at the next coarser level:

$$f_{k-1}^h = d_{k-1}^h + \mathcal{L}_{k-1}^h\left(\widetilde{\underline{h_0}_{k-1}}^{n+1}, \widetilde{\underline{p_0}_{k-1}}^{n+1}\right) , \; f_{k-1}^p = d_{k-1}^p + \mathcal{L}_{k-1}^p\left(\widetilde{\underline{h_0}_{k-1}}^{n+1}, \widetilde{\underline{p_0}_{k-1}}^{n+1}\right) . \tag{3.16}$$

   - Compute an approximate solution $\underline{\widehat{w}}_{k-1}^h, \underline{\widehat{w}}_{k-1}^p$ of the coarse grid equation on G^{k-1}:

$$\mathcal{L}_{k-1}^h\left(\underline{w}_{k-1}^h, \underline{w}_{k-1}^p\right) = f_{k-1}^h , \tag{3.17}$$

$$\mathcal{L}_{k-1}^p\left(\underline{w}_{k-1}^h, \underline{w}_{k-1}^p\right) = f_{k-1}^p . \tag{3.18}$$

     If k=1: find the exact solution using the coarse grid solver (see below).

     If k>1: solve eqs. (3.17) and (3.18) by performing the $\mathcal{FAS}$ cycle using $\widetilde{\underline{h_0}_{k-1}}^{n+1}$ and $\widetilde{\underline{p_0}_{k-1}}^{n+1}$ as an initial approximation:

$$\left(\underline{\widehat{w}}_{k-1}^h , \underline{\widehat{w}}_{k-1}^p\right) = FASCYC\left(k-1, \widetilde{\underline{h_0}_{k-1}}^{n+1}, \widetilde{\underline{p_0}_{k-1}}^{n+1}, f_{k-1}^h, f_{k-1}^p, n_{pre}, n_{post}\right) .$$

- Compute the corrections:

$$\underline{\widehat{v}}^h_{k-1} = \underline{\widehat{w}}^h_{k-1} - \underline{\widetilde{h_0}}^{n+1}_{k-1}\,,\ \underline{\widehat{v}}^p_{k-1} = \underline{\widehat{w}}^p_{k-1} - \underline{\widetilde{p_0}}^{n+1}_{k-1}\,.$$

- Interpolate the corrections using the bilinear interpolation operator, I^k_{k-1}:

$$\underline{\widehat{v}}^h_k = I^k_{k-1}\left(\underline{\widehat{v}}^h_{k-1}\right)\,,\ \underline{\widehat{v}}^p_k = I^k_{k-1}\left(\underline{\widehat{v}}^p_{k-1}\right)\,.$$

- Compute the corrected approximation on G^k:

$$\underline{h_{0c}}^{n+1}_k = \underline{\widetilde{h_0}}^{n+1}_k + \underline{\widehat{v}}^h_k\,,\ \underline{p_{0c}}^{n+1}_k = \underline{\widetilde{p_0}}^{n+1}_k + \underline{\widehat{v}}^p_k$$

3. *Postsmoothing stage:*

   - Apply n_{post} times the relaxation scheme:

$$\left(\underline{h_1}^{n+1}_k\,,\ \underline{p_1}^{n+1}_k\right) = RELAX^{n_{post}}\left(\underline{h_{0c}}^{n+1}_k, \underline{p_{0c}}^{n+1}_k, f^h_k, f^p_k\right).$$

The relaxation scheme consists of one step of a Newton iteration solved with a fixed number of sweeps (n_{pre} or n_{post}) of Red-Black Gauss-Seidel. The linearised form of equations (3.14) and (3.15) is obtained by computing the local Jacobian only, so that each relaxation sweep (in the pre-smooth stage for example) proceeds by solving:

$$\frac{\partial \mathcal{L}^h_k}{\partial h^{n+1}_{ij_k}}\Delta h + \frac{\partial \mathcal{L}^h_k}{\partial p^{n+1}_{ij_k}}\Delta p = f^h_k - \mathcal{L}^h_k\left(\underline{h_0}^{n+1}_k, \underline{p_0}^{n+1}_k\right)\,, \tag{3.19}$$

$$\frac{\partial \mathcal{L}^p_k}{\partial h^{n+1}_{ij_k}}\Delta h + \frac{\partial \mathcal{L}^p_k}{\partial p^{n+1}_{ij_k}}\Delta p = f^p_k - \mathcal{L}^p_k\left(\underline{h_0}^{n+1}_k, \underline{p_0}^{n+1}_k\right)\,, \tag{3.20}$$

for Δh and Δp. Hence a new approximation to the solution is given by: $\widetilde{h_{0i,j_k}}^{n+1} = h^{n+1}_{0i,j_k} + \Delta h\,,\ \widetilde{p_{0i,j_k}}^{n+1} = p^{n+1}_{0i,j_k} + \Delta p\,.$

At the coarsest level (G^0, k=1), the discretised equations are solved using a Newton iteration scheme. The iteration is defined in terms of the Jacobian matrices:

$$\underline{\underline{A}} = \frac{\partial \mathcal{L}^p_0}{\partial \underline{p}^{n+1}_0},\ \underline{\underline{B}} = \frac{\partial \mathcal{L}^p_0}{\partial \underline{h}^{n+1}_0},\ \underline{\underline{C}} = \frac{\partial \mathcal{L}^h_0}{\partial \underline{p}^{n+1}_0},\ \underline{\underline{D}} = \frac{\partial \mathcal{L}^h_0}{\partial \underline{h}^{n+1}_0}. \tag{3.21}$$

Given $\underline{w}^h_0, \underline{w}^p_0$ as first approximations to solutions of the coarse grid equations (3.17) and (3.18), then increments to $\underline{w}^h_0, \underline{w}^p_0$, $\underline{\Delta w}^h_0$ and $\underline{\Delta w}^p_0$ respectively, are obtained by

solving the linearised Newton iteration equations:

$$\underline{\underline{A}}\,\underline{\Delta w}_0^p + \underline{\underline{B}}\,\underline{\Delta w}_0^h = f_0^p - \mathcal{L}_0^p\left(\underline{w}_0^h, \underline{w}_0^p\right) , \tag{3.22}$$

$$\underline{\underline{C}}\,\underline{\Delta w}_0^p + \underline{\underline{D}}\,\underline{\Delta w}_0^h = f_0^h - \mathcal{L}_0^h\left(\underline{w}_0^h, \underline{w}_0^p\right) . \tag{3.23}$$

Solutions of these equations are obtained as follows. Setting $\underline{\Delta w}_0^h = \underline{0}$ in (3.22), an initial approximation to $\underline{\Delta w}_0^p$ is: $\underline{\Delta w}_0^{p'} = \underline{\underline{A}}^{-1}\left(f_0^p - \mathcal{L}_0^p\left(\underline{w}_0^h, \underline{w}_0^p\right)\right)$, while the equation for $\underline{\Delta w}_0^h$ is obtained by eliminating $\underline{\Delta w}_0^p$ from equations (3.22) and (3.23), viz

$$(\underline{\underline{D}} - \underline{\underline{C}}\,\underline{\underline{A}}^{-1}\underline{\underline{B}})\underline{\Delta w}_0^h = f_0^h - \mathcal{L}_0^h\left(\underline{w}_0^h, \underline{w}_0^p\right) - \underline{\underline{C}}\underline{\Delta w}_0^{p'} . \tag{3.24}$$

Equation (3.24) is solved to yield $\underline{\Delta w}_0^h$ and $\underline{w}_0^h, \underline{w}_0^p$ are updated according to $\underline{w}_0^h \rightarrow \underline{w}_0^h + \underline{\Delta w}_0^h$ and $\underline{w}_0^p \rightarrow \underline{w}_0^p + \underline{\Delta w}_0^{p'} - \underline{\underline{A}}^{-1}\underline{\underline{B}}\underline{\Delta w}_0^h$ respectively. The iteration proceeds until the norm $\frac{\sqrt{|f_0^p - \mathcal{L}_0^p(\underline{w}_0^h, \underline{w}_0^p)|^2 + |f_0^h - \mathcal{L}_0^h(\underline{w}_0^h, \underline{w}_0^p)|^2}}{n}$, where n is the number of unknowns in one direction, is sufficiently small. In this work it is found that a relative reduction in the residual of just 10^{-3} (compared to the initial residual from the solution at the previous time step) is sufficient, however much greater accuracies are easily obtainable if required.

3.5 Treatment of the boundary conditions

The boundary conditions described in the previous chapter (eqs. (2.47), (2.48) and (2.49)) are all Neumann conditions apart from the upstream boundary condition for gravity-driven thin film flow which is a Dirichlet condition.

A first approach to implement the Neumann boundary conditions was to introduce "*ghost nodes*" outside the computational domain as denoted by □ shapes in Figure 3.4. The idea is then to solve eqs. (3.2) and (3.8) on the boundary nodes (∘ in Figure 3.4) as for any interior node (• in Figure 3.4) while the extra unknowns introduced at the ghost nodes are found by solving a discrete analog of the Neumann boundary conditions. For example, imposing a zero film thickness and pressure gradient along the "*west boundary*" imposes the following extra set of equations to be satisfied at

the ghost nodes

$$\frac{p_{1,j} - p_{0,j}}{\Delta} = 0 \quad \text{and} \quad \frac{h_{1,j} - h_{0,j}}{\Delta} = 0 \quad \text{for} \quad 1 \leq j \leq (2^{k_f} + 1) \,. \tag{3.25}$$

when backward differencing is used. The index $i = 1$ denotes boundary nodes while $i = 0$ denotes ghost nodes. Analogous expressions can be found for the north, south and east boundaries. The advantage of this approach is the ease of implementation

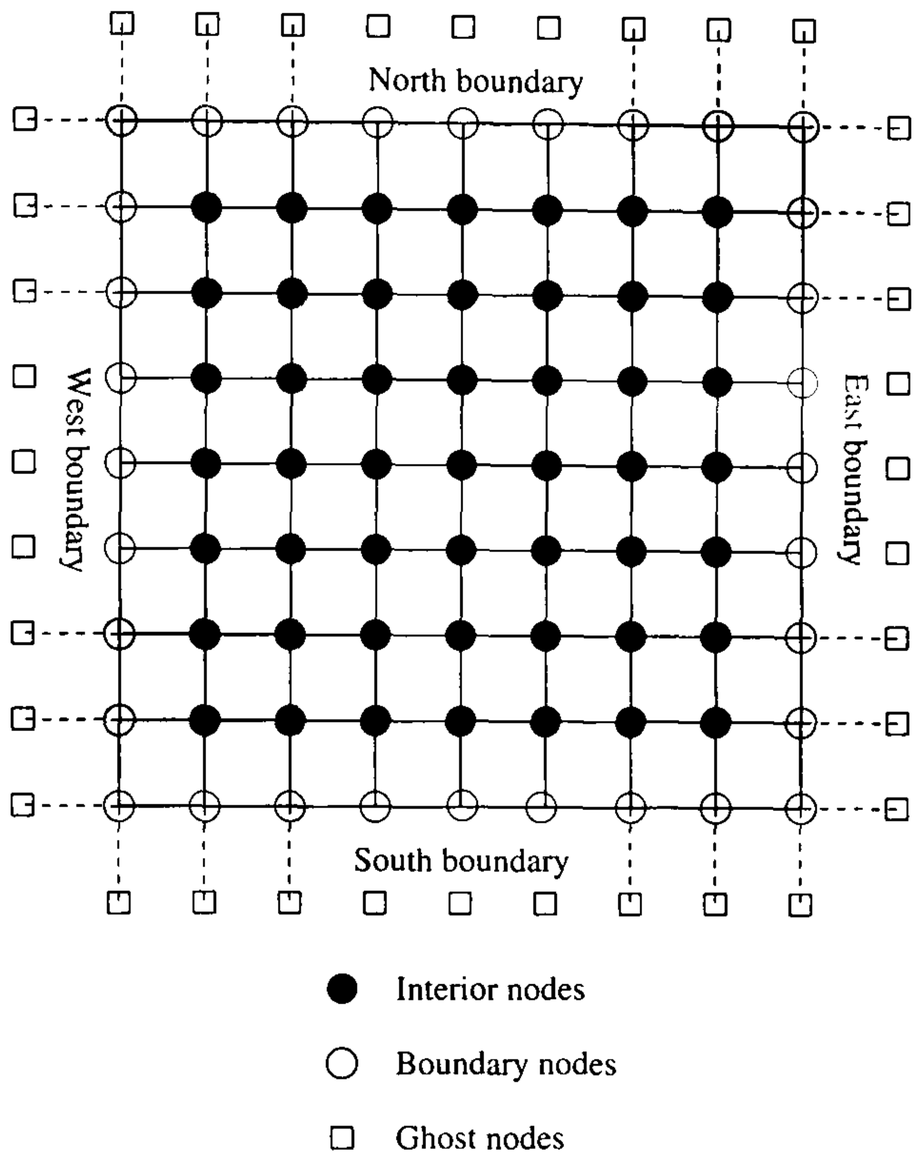

FIGURE 3.4: Computational grid with "*ghost nodes*".

as the same discrete equations need to be solved at boundary and interior nodes. However, the introduction of ghost nodes and corresponding extra set of discrete equations destroys the structure of the Jacobian matrix $\underline{\underline{A}}$ in the sense that this matrix becomes non-diagonal when the additional equations at the ghost nodes are included with a consequent increase in the computational work for the calculation of $\underline{\underline{A}}^{-1}$ in eq. (3.24). For the droplet spreading results presented in Chapter 5, this treatment of the boundary condition was implemented.

Alternatively, the Neumann boundary condition can be eliminated. The procedure consists in eliminating from eqs. (3.2) and (3.8) the unknowns lying outside the computational domain using a discrete analog of the Neumann boundary condition.

For example, along the west boundary, the zero film thickness and pressure gradient imposes that

$$\frac{p_{2,j} - p_{0,j}}{2\Delta} = 0 \quad \text{and} \quad \frac{h_{2,j} - h_{0,j}}{2\Delta} = 0 \quad \text{for} \quad 1 \leq j \leq (2^{k_f} + 1) \,. \tag{3.26}$$

Therefore, along the *west boundary*, $p_{0,j}$ and $h_{0,j}$ may be eliminated and replaced by $p_{2,j}$ and $h_{2,j}$ respectively. In contrast to the previous approach, the governing equations at boundary nodes will now differ slightly from those at interior nodes but because no additional equations are introduced the Jacobian matrix $\underline{\underline{A}}$ corresponds to the identity matrix. The inversion of $\underline{\underline{A}}$ required in eq. (3.24) is therefore trivial reducing the total computational work. This treatment of the boundary condition was used for the case of gravity-driven thin films.

In order to impose a constant film thickness at the inlet boundary for gravity-driven thin liquid films (eq. (2.48)), eq. (3.8) is simply replaced by

$$h_{1,j} - 1 = 0 \quad \text{for} \quad 1 \leq j \leq (2^{k_f} + 1) \,. \tag{3.27}$$

3.6 Local mesh refinement

The need for fine spatial resolution is often restricted to a relatively small portion of the computational domain where a singularity occurs or strong gradients of the solution are expected. For example, in the presence of a contact line, Bertozzi (1998) mentions that the spatial resolution should be of the same order of magnitude as the precursor film thickness. The mesh density should also increase when flow over steep topography is considered in order to capture accurately the substrate variations. In order to minimise the computational work, ideally the mesh should only be refined locally where required. Despite the obvious potential of local mesh adaptivity to handle the multi-scale physics in thin film flows and in particular dynamic contact lines, studies using such techniques are very scarce. Bertozzi (1995) developed a very efficient self similar adaptive mesh scheme achieving local resolution of order 2^{-65} to investigate finite time singularities when a thin film dewets and forms a "*hole*". However, her approach is restricted to one-dimensional computational domains. In

principle, there are two types of adaptive approaches, Trottenberg (2001):

- *predefined refinement* corresponding to grid structures where the refinement is determined in advance;
- *self-adaptive refinement* for which grid refinement is carried out dynamically during the solution process.

The multilevel adaptive method for hurricane track prediction discussed by Fulton (1997) is a good example of the latter approach. In this thesis, only the former approach has been developed. It should be stressed at this point that local mesh refinement is not the main thrust of the work in this thesis. Most of the results presented in subsequent chapters are obtained on uniform meshes. Nevertheless, the sample results obtained with local mesh refinement highlight the potential of such methods and call for further development.

For two- or three-dimensional computations, a major difficulty faced by local mesh adaptivity methods is the data structure. Complex tree structures are often necessary to handle the data structure in the context of Finite Element methods. In contrast, local mesh refinement is fully compatible with the multigrid structure as the solution is achieved through a hierarchy of computational grids. The idea is to have finer grid levels only covering the part of the domain where refinement is desired. In this work, the Multilevel Adaptive Technique ($\mathcal{MLAT}$) first introduced by Brandt (1977) was implemented. The reason for this choice is that the concepts of the standard multigrid technique can be relatively easily extended to account for mesh refinement. Prior to describing the technique, notations are introduced. The grid hierarchy is now defined by $\left(G^0, G^1, .., G^L, G^{L+1}, G^{L+2}, .., G^{L+L'}, G^{L+L'+1}, G^{L+L'+2}, ..\right)$. Again, the mesh resolution doubles from one grid to the next but while the grids $G^0, G^1, .., G^L$ cover the entire computational domain ("*global grids*"), $G^{L+1}, G^{L+2}, .., G^{L+L'}$ only cover a portion of it and $G^{L+L'+1}, G^{L+L'+2}, ..,$ a portion of this portion. Figure 3.5 illustrates the grid hierarchy for $L = 0$ and $L' = 1$.

Each grid is recursively defined by the indices of its "*south-west*" and "*north-east*" corners, (I_{sw}, J_{sw}) and (I_{ne}, J_{ne}) respectively, on the coarser grid level ("*parent*

grid"). For convenience, the local indices (i, j) on each grid vary from $(0, 0)$ to (i_{ne}, j_{ne}) where $i_{ne} = 2(I_{ne} - I_{sw})$ and $j_{ne} = 2(J_{ne} - J_{sw})$. For the example given on Figure 3.5, $(I_{sw}, J_{sw}) = (1, 1)$, $(I_{ne}, J_{ne}) = (3, 3)$ and $(i_{ne}, j_{ne}) = (4, 4)$. But the non-global grids don't all have to have the same number of points, as in this example.

The solution is sought on the "*composite grid*" which is the composition of each individual grid. Composite grids are denoted by $\left(\widehat{G}^0, \widehat{G}^1, .., \widehat{G}^L, \widehat{G}^{L+1}, \widehat{G}^{L+2}, .., \widehat{G}^{L+L'}, \widehat{G}^{L+L'+1}, \widehat{G}^{L+L'+2}, ..\right)$ as shown on Figure 3.5.

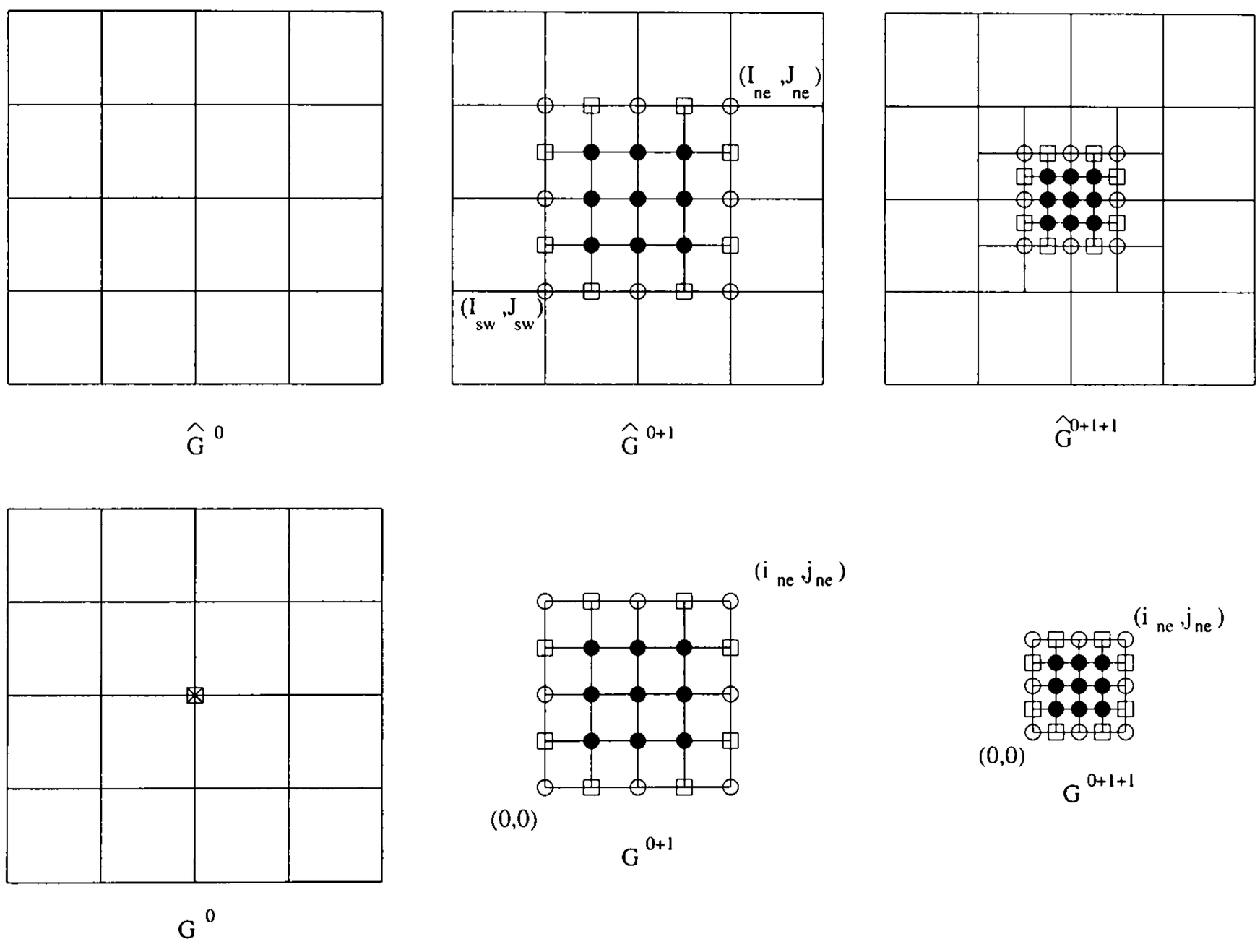

FIGURE 3.5: Grid hierarchy with 2 concentric local refinements. The upper three meshes are the composite grids, $\widehat{G}^0$, $\widehat{G}^{0+1}$ and $\widehat{G}^{0+1+1}$. The lower three meshes represent each grid level, G^0, G^{0+1} and G^{0+1+1}.

The main components of the multigrid technique described in §3.4 remain identical. Of course, the grid transfer operators (interpolation and restriction) are modified so that data is transfered only in the region where the grids overlap. The smoothing stage is unchanged for interior nodes on any grid (denoted by • shapes on the grid G^{0+1} in Figure 3.5 for example). If the grid only covers a subregion of the computational domain, the boundary nodes common to that grid and its parent

grid (denoted by ∘ shapes on the grid G^{0+1} in Figure 3.5) are treated as Dirichlet boundary conditions, i.e., the value of the unknowns at those points is equal to the value on the coarser level. Standard linear interpolation is used to compute the value of the unknowns at the remaining boundary nodes sometimes referred to "*hanging nodes*" (denoted by □ shapes on the grid G^{0+1} in Figure 3.5). An essential modification to the multigrid algorithm is that the right-hand side is only modified according to eqs. (3.16) on the coarse grid points common to interior points on the "*child grid*" (⊠ on grid G^0 on Figure 3.5).

Chapter 4

Validation of the numerical method

Contents

4.1 Introduction

The main goal of the present chapter is to develop a knowledge of the behaviour of the proposed numerical method when applied to well understood and widely documented problems and to develop an appreciation of their robustness and the computational benefits.

The adaptive time-stepping scheme is first applied to an ordinary differential equation (ODE) for which the corresponding analytical solution is known, and is of the same form as Tanner's closed form solution for film thickness at the centre of an axisymmetrically spreading droplet, Tanner (1979). The combination of the adaptive time-stepping scheme with the multigrid method described in the previous chapter is then used to solve the two-dimensional transient heat diffusion equation. The parabolic nature of this second-order partial differential equation makes it an ideal candidate to assess the numerical method since the lubrication equations (eqs. (2.29) and (2.30)) form a fourth-order parabolic equation when combined. Furthermore, the availability of analytical solutions for the transient heat-equation means that the accuracy of numerical solutions may be assessed easily.

Severe tests of the behaviour of the adaptive time-stepping scheme were carried out by imposing a strongly time-dependent diffusivity. The chapter ends with some results for the solution of the two-dimensional steady-state heat equation with a step-change in diffusivity modelled using local mesh refinement.

4.2 A first order ODE with constant coefficients

The accuracy of the estimate of the Local Truncation Error (LTE). equation (3.12), is first demonstrated by comparing it with the true local error for solution of the following ODE

$$\frac{dh}{dt} + \frac{1}{5}\frac{h}{t} = 0 \ , \quad h(t_0) = h_0 \ . \tag{4.1}$$

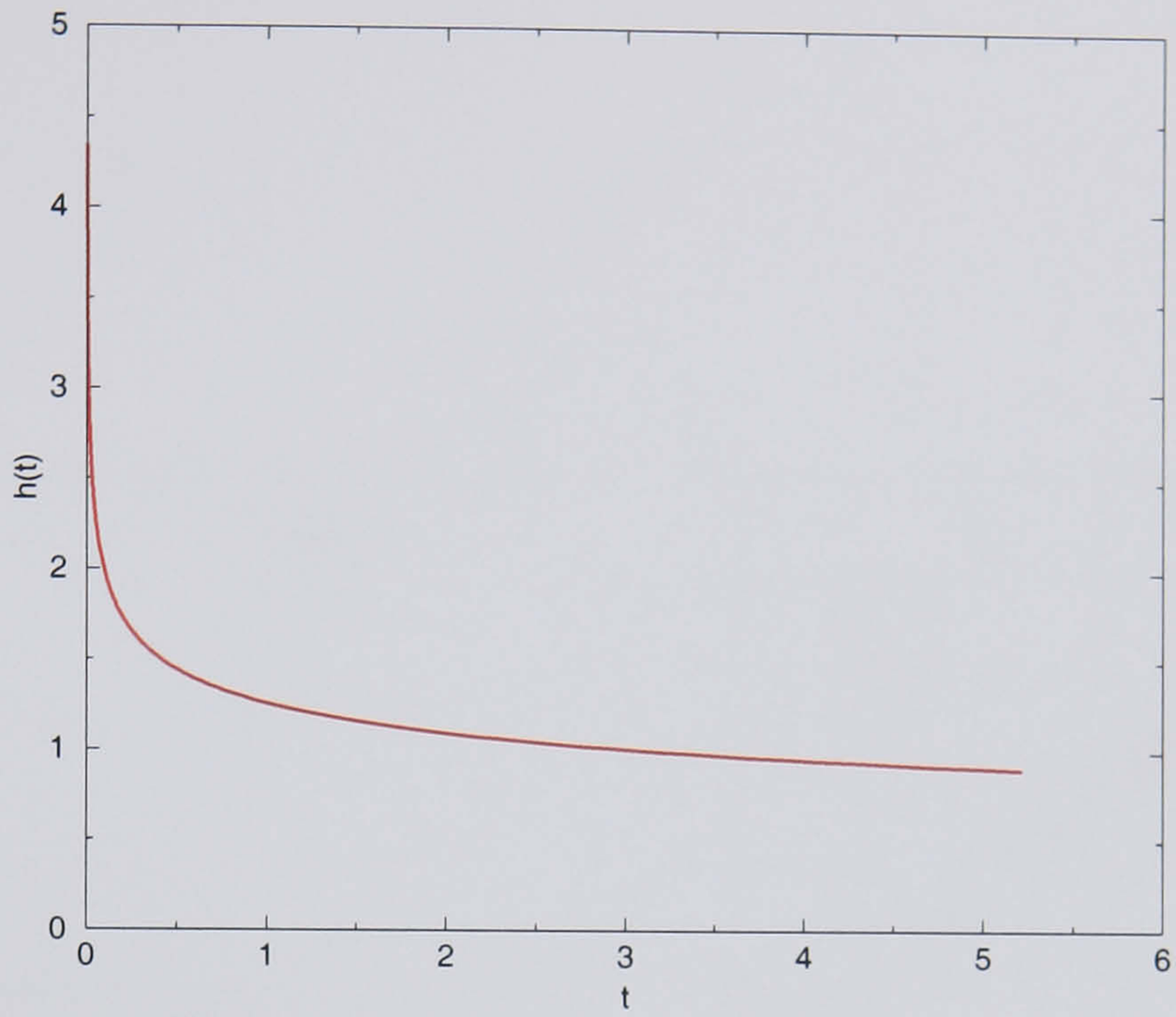

FIGURE 4.1: Analytical solution of equation (4.1) for the initial condition $h(t_0 = 10^{-3}) = 5$.

The analytical solution of this equation,

$$h(t) = h_0 \left(\frac{t_0}{t}\right)^{0.2} , \tag{4.2}$$

is of exactly the same form as Tanner's Law (1979) for film thickness at the centre of an axisymmetrically spreading droplet. Figure 4.1 shows the analytical solution for the initial condition $h(t_0 = 10^{-3}) = 5$. The numerical solution of equation (4.1) is obtained by applying the adaptive time-stepping scheme described in §3.3. The function F in eqs. (3.8) and (3.9) however take a much simpler form given by

$$F(h^n, t^n) = -\frac{1}{5}\frac{h^n}{t^n} . \tag{4.3}$$

If h^n is the numerical solution of equation (4.1) obtained at time t^n, then the true local truncation error of the scheme over the next time step, LTE_{theo}, is the difference between h^{n+1}, the numerical solution obtained at time t^{n+1}, and the corresponding analytical solution for the same initial condition $h(t^n) = h^n$, namely $h^n(t^n/t^{n+1})^{0.2}$. Figure 4.2(**a**) demonstrates that the estimate consistently over predicts the true error since $\frac{LTE_{num}}{LTE_{theo}} > 1$ and that decreasing the tolerance increases the accuracy of the estimate to the extent that for $Tol < 10^{-4}$ the estimated local

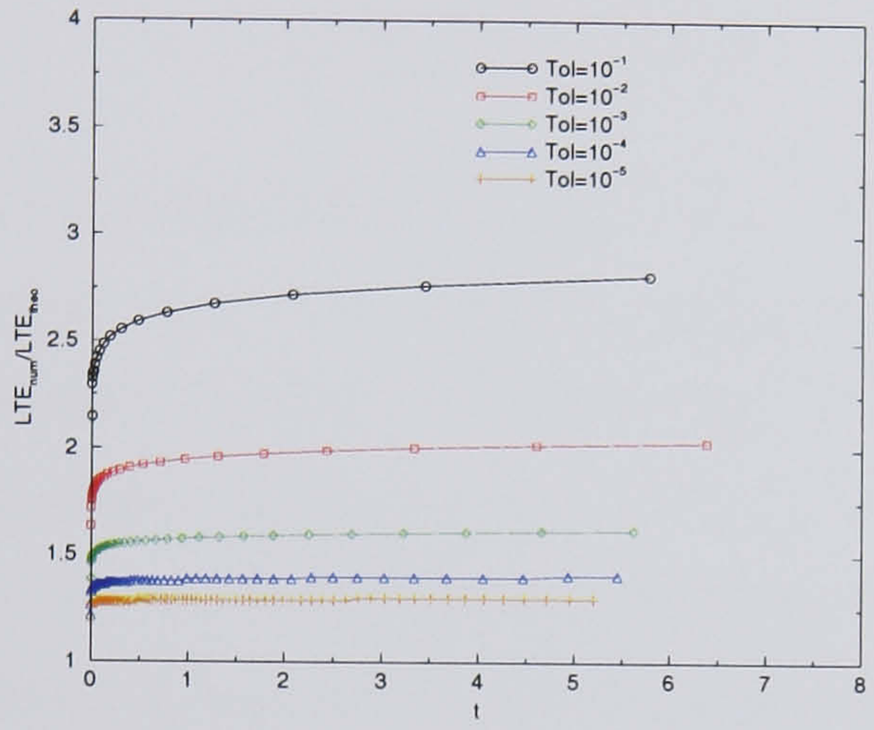

(**a**) Ratio of the estimated Local Truncation Error, LTE_{num}, to the true local error, LTE_{theo}, as a function of time for various tolerances.

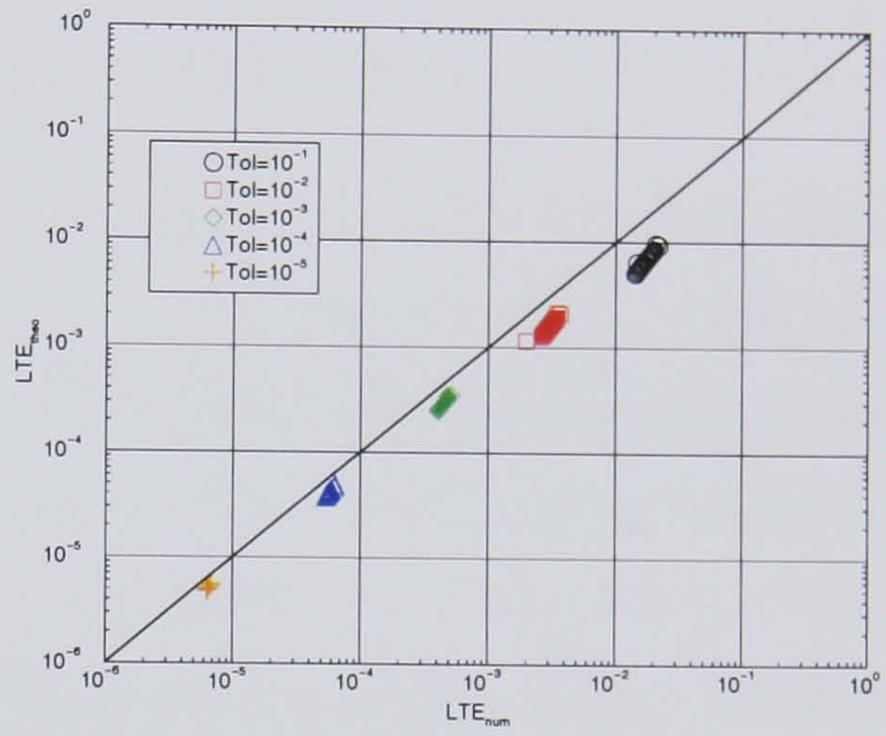

(**b**) Log-log map of the points (LTE_{num},LTE_{theo}) at each time step for various tolerances.

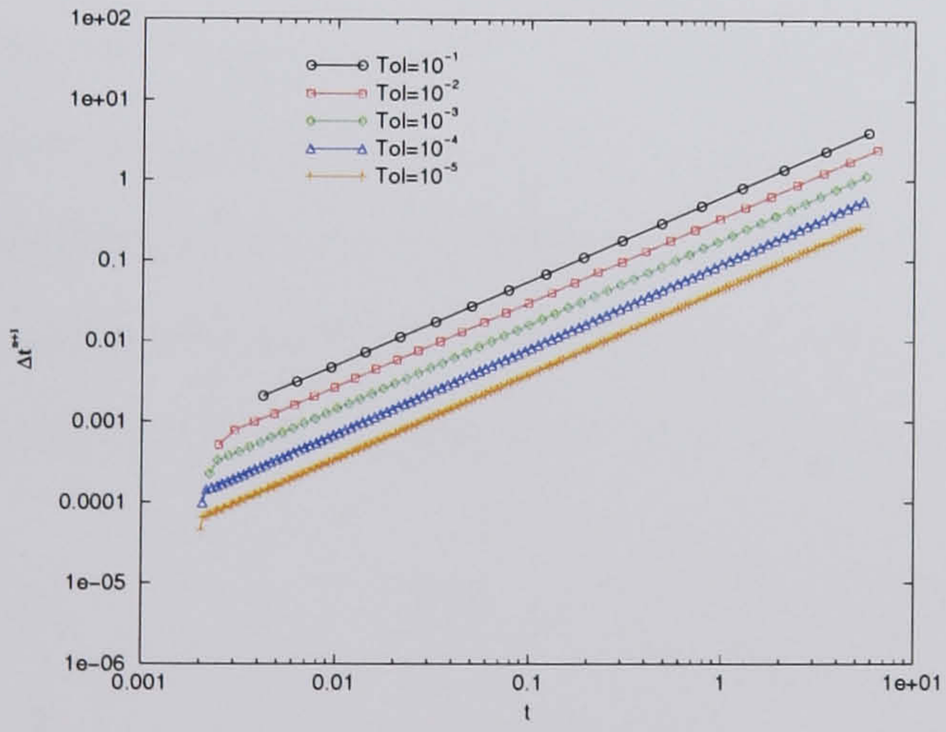

(**c**) Log-log graph showing the evolution of the time step Δt^{n+1} as a function of time for various tolerances.

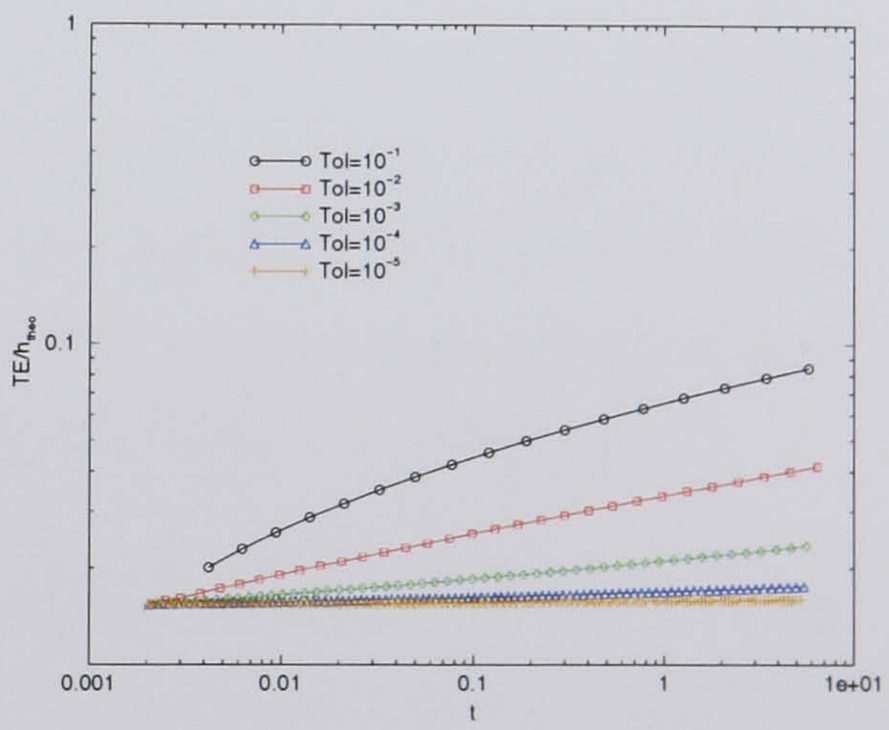

(**d**) Log-log graph of the normalised total error (TE) as a function of time for various tolerances.

FIGURE 4.2: Accuracy of the Local Truncation Error estimate and performance of the adaptive time-stepping scheme applied to the ODE (eq. (4.1)).

Tol	β
10^{-1}	1.6
10^{-2}	1.3
10^{-3}	1.15
10^{-4}	1.075
10^{-5}	1.045

TABLE 4.1: Values of $\beta = \frac{\Delta t^{n+1}}{\Delta t^n}$ for various tolerances.

error is within 30% of its true value. The over prediction of the true local error is better than under prediction since it will err on the side of caution, whilst the almost fixed ratio of the true and estimated errors ensures that the step size will be controlled reliably. The log-log map of the points (LTE_{num},LTE_{theo}) at each time step (Figure 4.2(**b**)) illustrates the previous conclusions in a different way as the groups of points corresponding to different tolerances come closer to the "*identity line*" corresponding to $LTE_{num} = LTE_{theo}$ (black solid line on Figure 4.2(**b**)) as the tolerance decreases. Figure 4.2(**b**) also confirms that the time-stepping scheme ensures that the local truncation error is kept below the prescribed tolerance.

The next figure, 4.2(**c**), shows the evolution of the time step, Δt^{n+1}, with time. Interestingly, all curves have a slope very close to one regardless of the value of the tolerance. A closer look at the ratio of two successive time-steps, $\beta = \frac{\Delta t^{n+1}}{\Delta t^n}$, explains this feature. For a given tolerance, this ratio is almost constant and reported in Table 4.1. Considering β constant, the time, t^{n+1}, after n iterations is

$$t^{n+1} = \Delta t^0 \left(1 + \beta + \beta^2 + \beta^3 + \ ... \ + \beta^n\right) \ , \tag{4.4}$$

which, in terms of a geometric series formula, may be rewritten as

$$t^{n+1} = \Delta t^0 \left(\frac{1 - \beta^{n+1}}{1 - \beta}\right) \ . \tag{4.5}$$

Replacing $\Delta t^0 \beta^{n+1}$ by Δt^{n+1} yields

$$\Delta t^{n+1} = (\beta - 1) t^{n+1} + \Delta t^0 \ . \tag{4.6}$$

The form of equation (4.6) explains why the gradient of the curves on the log-log

graph on Figure 4.2(**c**) is approximately equal to one for all tolerances.

The ultimate goal in controlling the local truncation error is to obtain a numerical solution as close as possible to the solution of the continuous problem defined by (4.1) for the least possible amount of work. The accumulation of local truncation error inevitably degrades the numerical solution but the control of the local truncation error should limit this discrepancy. This is exactly what can be seen in Figure 4.2(**d**) which shows the normalised total error (often referred to as global error), $\frac{|h(t^n)-h^n|}{h(t^n)}$, as a function of time. For large tolerances, the total error increases as the numerical solution proceeds but for small enough tolerances ($Tol \leq 10^{-4}$), the total error increases only very slowly as time increases which is an attractive feature of the time-adaptive scheme. Equally significantly, we see that by controlling the local truncation error via the Tol parameter it is possible to control the total error successfully, which is the ultimate goal of local truncation error control.

4.3 Solution of the transient, two-dimensional heat diffusion equation

4.3.1 Governing equation, discretisation and brief description of the solution procedure

The combination of the multigrid algorithm described in the previous chapter with the adaptive time-stepping scheme is next applied to the transient two-dimensional heat diffusion equation, namely

$$\frac{\partial u}{\partial t} = \frac{\partial}{\partial x}\left(C(x,y,t)\frac{\partial u}{\partial x}\right) + \frac{\partial}{\partial y}\left(C(x,y,t)\frac{\partial u}{\partial y}\right) \ , \tag{4.7}$$

for $(x,y) \in \Omega = (0,1) \times (0,1)$ and $t > 0$. $C(x,y,t)$ is the diffusivity in $m^2 s^{-1}$ and $u(x,y,t)$ the temperature. Equation (4.7) is solved subject to the following initial and boundary conditions

$$u(x,0,t) = u(x,1,t) = 0\ ,$$

$$u(0,y,t) = u(1,y,t) = 0\ ,$$

$$u(x,y,0) = xy(x-1)(y-1)\ .$$

Equation (4.7) is discretised in space using central differences on a square computational domain leading to

$$\begin{aligned}\frac{\partial u_{i,j}}{\partial t} = \frac{1}{4\Delta^2}\Big[&u_{i+1,j}\left(C_{i+1,j} - C_{i-1,j} + 4C_{i,j}\right) - \\ &u_{i-1,j}\left(C_{i+1,j} - C_{i-1,j} - 4C_{i,j}\right) + u_{i,j+1}\left(C_{i,j+1} - C_{i,j-1} + 4C_{i,j}\right) - \\ &u_{i,j-1}\left(C_{i,j+1} - C_{i,j-1} - 4C_{i,j}\right) - 16C_{i,j}u_{i,j}\Big] + O(\Delta^2)\ ,\end{aligned} \tag{4.8}$$

for any interior point (i,j). This form of the discretisation naturally appears when expanding the spatial partial derivatives in eq. (4.7). Notations are identical to those given in §3.2. The only modification to the time-adaptive scheme described in §3.3 is the function F in eqs. (3.8) and (3.9) which will now correspond to the right-hand side of eq. (4.8). For comparison purposes, results are also obtained using the backward Euler scheme ($\Theta_t = 1$ in eq. (3.8)).

The discretisation of eq. (4.7) introduces an additional source of numerical error to the local truncation error discussed in the previous section, that due to spatial discretisation. In order to obtain a reliable and efficient time-stepping scheme, the spatial error should dominate the local truncation error, Shampine (1994). However, reducing the local truncation error much below the spatial discretisation error constitutes a waste of computational time. A goal of this section is therefore to determine, through numerical experiments, the appropriate values for the tolerance, Tol, in order to satisfy these constraints.

The system of algebraic equations defined by eqs. (4.8) is solved with the combined Full Approximation Storage ($\mathcal{FAS}$) method and the Full Multigrid technique described in §3.4. The only two components of the algorithm that change are the relaxation scheme and the coarse grid solver. The relaxation stage consists of a Red-

Black Gauss-Seidel scheme which proceeds by updating the values of $u_{i,j}^{n+1}$ according to the following equation:

$$u_{i,j}^{n+1}{}_{new} = \frac{1}{1+\frac{4\Theta_t\Delta_t^{n+1}C_{i,j}}{\Delta^2}}\Bigg[f_k + \frac{\Theta_t\Delta_t^{n+1}}{4\Delta^2}\Big(u_{i+1,j}^{n+1}{}_{old}\left(C_{i+1,j}-C_{i-1,j}+4C_{i,j}\right) - u_{i-1,j}^{n+1}{}_{old}\left(C_{i+1,j}-C_{i-1,j}-4C_{i,j}\right) + u_{i,j+1}^{n+1}{}_{old}\left(C_{i,j+1}-C_{i,j-1}+4C_{i,j}\right) - u_{i,j-1}^{n+1}{}_{old}\left(C_{i,j+1}-C_{i,j-1}-4C_{i,j}\right)\Big)\Bigg] , \tag{4.9}$$

where f_k at the finest grid level is the right-hand side of eq. (3.8) with the aforementioned modification to the function F. The following results were all obtained with two presmoothing and postsmoothing stages ($n_{pre} = n_{post} = 2$) and five V-cycles at the intermediate and finest grid levels ($N_{cyc} = 5$). Because the coarsest grid level, G^0, is a 3x3 one, and the boundary conditions are of Dirichlet type, the coarse grid solver is trivial as only one unknown needs to be solved for at the centre of the computational domain $(x, y) = (0.5, 0.5)$.

4.3.2 Results with $C = 1$

The case with diffusivity $C = 1$ can be solved using the separation of variables method (see Appendix D), which yields

$$u(x,y,t) = \frac{16}{\pi^6}\sum_{n=1}^{\infty}\sum_{m=1}^{\infty}\frac{1-(-1)^n}{n^3}\frac{1-(-1)^m}{m^3}\sin(n\pi x)\sin(m\pi y)\exp(-\alpha_{nm}t) , \tag{4.10}$$

with

$$\alpha_{nm} = n^2\pi^2 + m^2\pi^2 .$$

Numerical results are compared with this analytical solution which is shown in Figure 4.3 calculated with $n_{max} = m_{max} = 20$ in eq. (4.10) at $t = 0.1$. Figure 4.4(**a**) shows the maximum relative total error defined as $max\left(\left|\frac{u(x_i,y_j,0.1)-u_{i,j}^{n+1}}{u(x_i,y_j,0.1)}\right|\right)$ as a function of the tolerance. All curves display the same trend. Initially, a decrease in the tolerance successfully increases the accuracy of the numerical solution as the maximum relative total error decreases. All the curves then reach a "*saturation threshold*" beyond which a further decrease in the tolerance degrades the numerical

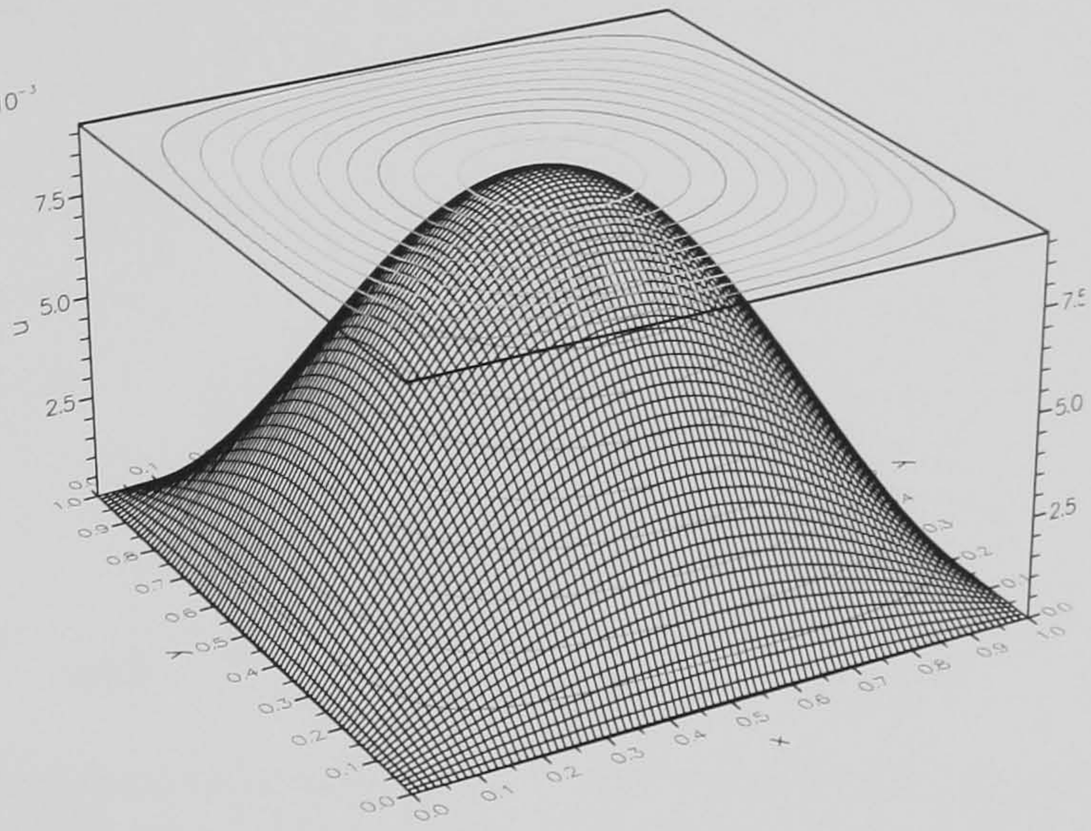

FIGURE 4.3: Analytical solution of the transient two-dimensional heat equation (eq. (4.7)) with unit diffusivity at $t = 0.1$.

solution as shown by the increase of the maximum relative total error. This threshold depends on the grid resolution. For example, when numerical solutions are sought on a 33x33 grid, the optimal tolerance is around 5×10^{-3} while on a 257x257 grid it is in the region of 5×10^{-4}. This feature is clearly a result of the spatial discretisation error which is much larger on a 33x33 grid than on a 257x257 grid (around $8^2 = 64$ larger since the spatial error is $O(\Delta^2)$). The spatial discretisation error will therefore start to dominate over the local truncation error for larger tolerances on a 33x33 grid than on a 257x257 grid. Next, Figure 4.4(**b**) shows how substantial increase in the time-step can be achieved on a 129x129 mesh while consistently keeping the local truncation error below the prescribed tolerance ($Tol = 10^{-4}$ in that case).

Tables 4.2 and 4.3 show the total computational time for the simulation to reach the final time $t = 0.1$ for the adaptive time-stepping scheme and the backward Euler method with fixed time-steps, respectively. Runs were performed on a SG Origin 200 with a MIPS R10000, 180 MHz processor running with the IRIX operating system. On all but the 33x33 mesh, the adaptive time-stepping scheme outperforms the backward Euler scheme, i.e., greater accuracy is achieved in less CPU time. For example, on a 257x257 mesh, the adaptive time-stepping scheme with a tolerance of

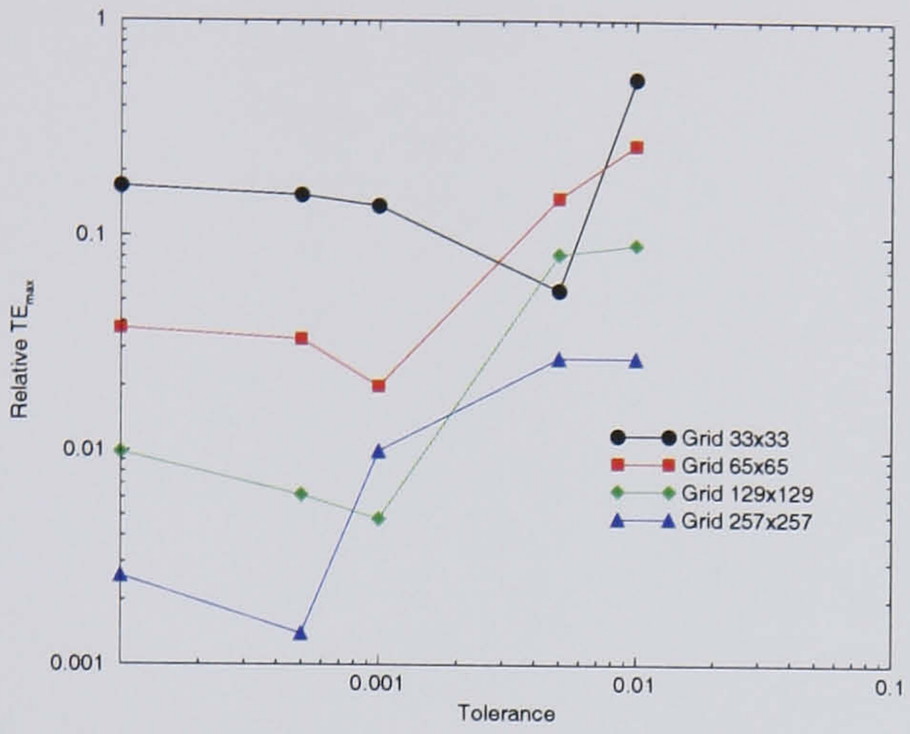

(**a**) Effect of the tolerance on the maximum relative total error at $t = 0.1$ for various mesh densities.

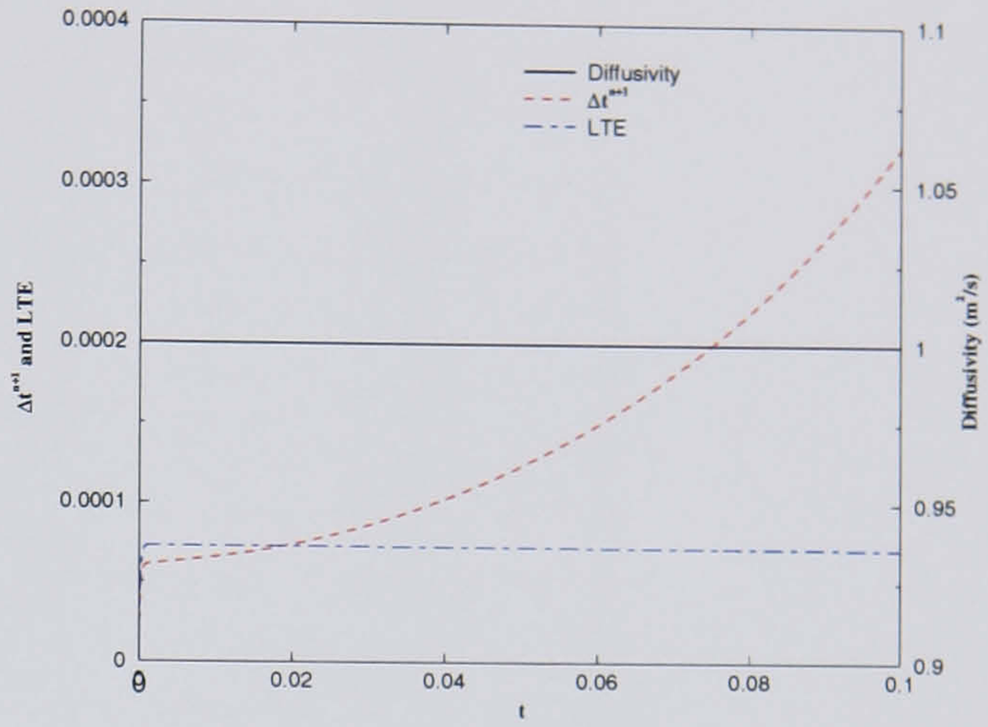

(**b**) Variation of the time-step and the Local Truncation Error with time for a unit diffusivity.

FIGURE 4.4: Performance of the adaptive time-stepping scheme applied to the transient two-dimensional heat equation (eq. (4.7)).

Grid	Tolerance	CPU time (s)	Relative TE_{max}	N_{tot}
G^4: 33x33	10^{-2}	1.059	0.54	25
G^4: 33x33	5.10^{-3}	1.287	0.056	34
G^4: 33x33	10^{-3}	3.062	0.138	105
G^4: 33x33	5.10^{-4}	5.17	0.155	193
G^4: 33x33	10^{-4}	16.334	0.17	893
G^5: 65x65	10^{-2}	4.43	0.265	26
G^5: 65x65	5.10^{-3}	5.327	0.15	34
G^5: 65x65	10^{-3}	15.276	0.02	105
G^5: 65x65	5.10^{-4}	27.72	0.033	193
G^5: 65x65	10^{-4}	95.46	0.037	893
G^6: 129x129	10^{-2}	23.133	0.091	35
G^6: 129x129	5.10^{-3}	25.19	0.082	39
G^6: 129x129	10^{-3}	70.209	0.0048	105
G^6: 129x129	5.10^{-4}	128.9	0.0062	193
G^6: 129x129	10^{-4}	550.95	0.0098	893
G^7: 257x257	10^{-2}	128.4	0.027	59
G^7: 257x257	5.10^{-3}	137.37	0.027	61
G^7: 257x257	10^{-3}	296.26	0.01	107
G^7: 257x257	5.10^{-4}	567.9	0.0014	193
G^7: 257x257	10^{-4}	2519.37	0.0026	893

TABLE 4.2: Efficiency and accuracy of the adaptive time-stepping scheme applied to the transient two-dimensional heat equation (eq. (4.7)) for various grid levels and tolerances.

Grid	Δt^{n+1}	CPU time (s)	Relative TE_{max}
G^4: 33x33	10^{-2}	0.712	1.18
G^4: 33x33	10^{-3}	2.8	0.095
G^4: 33x33	10^{-4}	13.205	0.025
G^5: 65x65	10^{-2}	2.853	1.05
G^5: 65x65	10^{-3}	11.734	0.014
G^5: 65x65	10^{-4}	91.512	0.027
G^6: 129x129	10^{-2}	11.98	1.01
G^6: 129x129	10^{-3}	48.826	0.029
G^6: 129x129	10^{-4}	560.6	0.008
G^7: 257x257	10^{-2}	47.814	1.011
G^7: 257x257	10^{-3}	206.6	0.032
G^7: 257x257	10^{-4}	2581.5	0.003

TABLE 4.3: Efficiency and accuracy of the backward Euler scheme applied to the transient two-dimensional heat equation(eq. (4.7)) for various grid levels and time step sizes.

5.10^{-4} gives a better accuracy than the backward Euler scheme with fixed time-steps equal to 10^{-4} in just a fifth of the total computational time.

4.3.3 Results with spatial- and time-dependent diffusivity

The ability of the adaptive time-stepping scheme to cope with steep changes in the diffusivity is now tested by imposing the following two spatial- and time-dependent diffusivities

$$C_{i,j} = 10 \left| \cos\left(\frac{12t\pi}{t_f}\right) \right| u_{i,j}^{n-1} \quad \text{with} \quad t_f = 0.1 \ , \tag{4.11}$$

$$C_{i,j} = \exp^{-t} - \exp^{-1000t} \ . \tag{4.12}$$

Numerical solutions are obtained on a 129x129 mesh with a tolerance of 10^{-4}.

The cyclic variation of the diffusivity defined by eq. (4.11) can be seen on Figure 4.5(**a**) for $(x, y) = (0.5, 0.5)$. The evolution of the time-step closely mirrors the evolution of the diffusivity: when the diffusivity peaks the time-step is lowest and vice-versa. This behaviour is expected as large diffusivity is associated with rapid changes in the solution and therefore, smaller time-steps are required in order to maintain the accuracy of the numerical solution. Figure 4.5(**a**) also confirms the validity of the adaptive time-stepping as the local truncation error in invariably

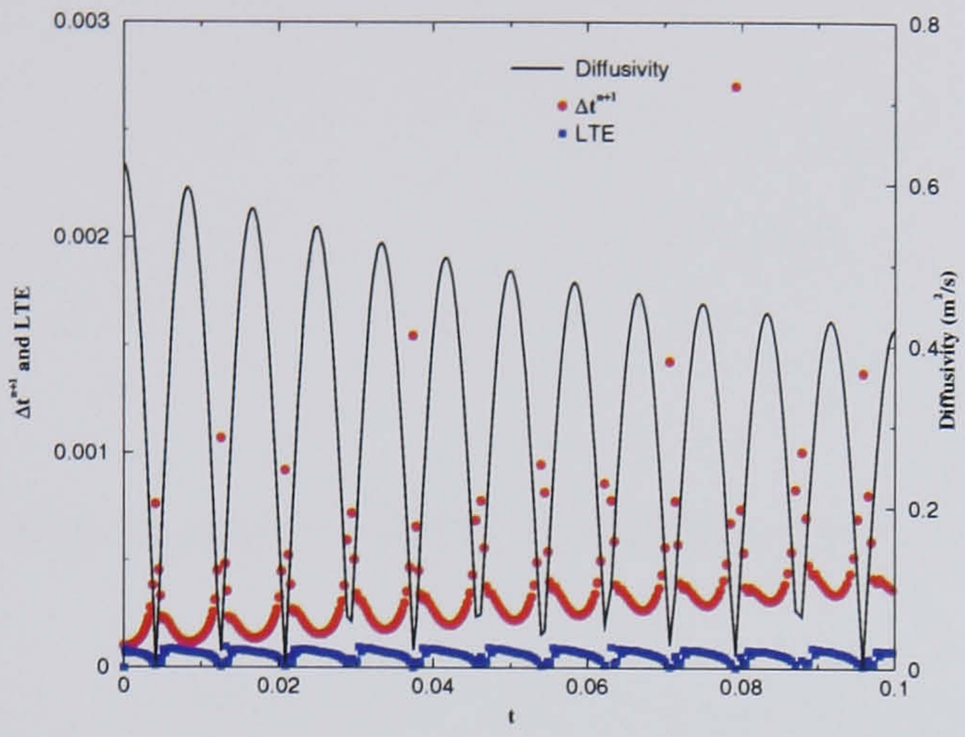

(**a**) Variation of the time-step and the Local Truncation Error with time for a diffusivity defined by eq. (4.11).

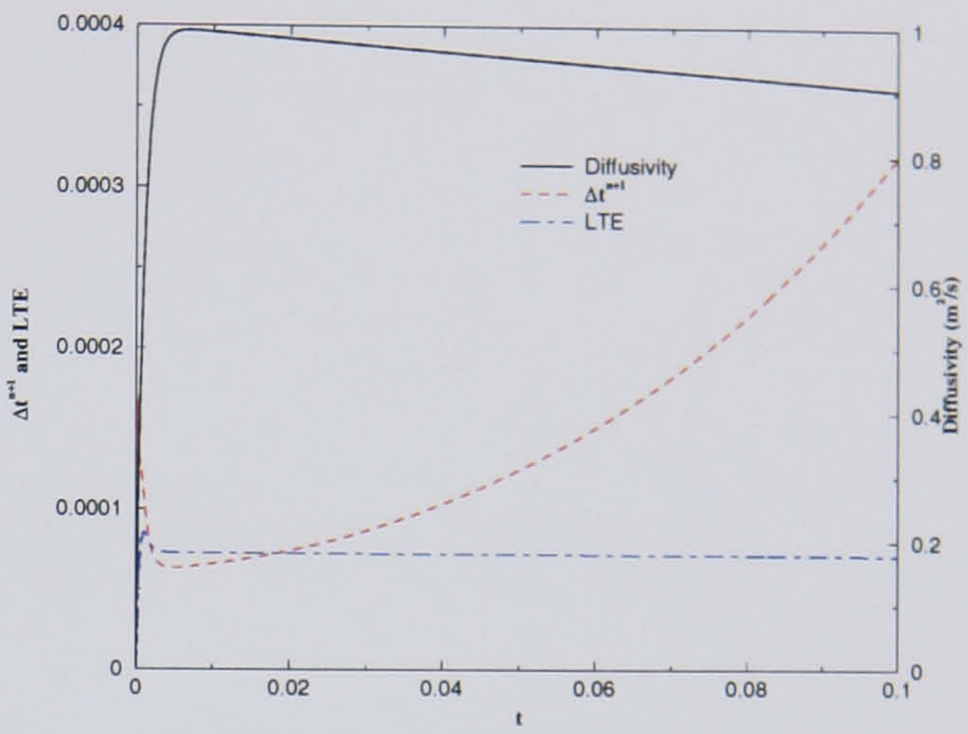

(**b**) Variation of the time-step and the Local Truncation Error with time for a diffusivity defined by eq. (4.12).

FIGURE 4.5: Variation of the time-step and the Local Truncation Error for strongly spatial- and time-dependent diffusivity in the transient two-dimensional heat equation (eq. (4.7)).

kept below the tolerance. In Figure 4.5(**b**), the very steep initial increase of the diffusivity due to the first exponential term in eq. (4.12) is accompanied by a sharp decrease of the time-step. The time-step then steadily increases as the diffusivity slowly decays. Again, the local truncation error plotted on Figure 4.5(**b**) is bounded at all times by the tolerance, Tol.

Having outlined the robustness of the proposed numerical scheme and the computational benefits of the time-stepping adaptivity, the next section focuses on another form of adaptivity which is also important to improve the efficiency of numerical schemes: local mesh refinement.

4.4 Local mesh refinement and the steady-state two-dimensional heat equation

The Multilevel Adaptive Technique $\mathcal{MLAT}$ described in §3.6 was implemented to solve the steady-state counterpart of the two-dimensional heat equation (eq. (4.7))

subject to the following boundary conditions

$$u(x,0) = 0 \quad \text{and} \quad u(x,1) = 1 \,,$$
$$u(0,y) = u(1,y) = 0 \,.$$

A step change is imposed to the x-independent diffusivity so that $C(y)$ satisfies

$$\begin{aligned} C(y) &= C_0 \quad \text{for} \quad y < y_s - \frac{\gamma}{2} \,, \\ C(y) &= \Delta C_0 \left[-2 \left(\frac{y - (y_s - \frac{\gamma}{2})}{\gamma} \right)^3 + 3 \left(\frac{y - (y_s - \frac{\gamma}{2})}{\gamma} \right)^2 \right] + C_0 \\ &\qquad \text{for} \quad y_s - \frac{\gamma}{2} < y < y_s + \frac{\gamma}{2} \,, \\ C(y) &= C_0 + \Delta C_0 \quad \text{for} \quad y > y_s + \frac{\gamma}{2} \,, \end{aligned} \tag{4.13}$$

where ΔC_0 and y_s are the amplitude and the y-coordinate of the step-change respectively and γ controls the steepness of the step. An obvious advantage of this "*benchmark*" problem is that the region where local mesh refinement is required is known prior to solving the governing equation. This region encompasses the computational domain where the diffusivity changes steeply. Numerical solutions are obtained on a variety of composite grids and compared with the solution on a uniform 513x513 grid in order to assess the potential computational savings, the correct implementation of the $\mathcal{MLAT}$ and its accuracy. The contours of temperature for the uniform 513x513 grid with $y_s = 0.5$, $C_0 = 0.01$, $\Delta C_0 = 0.1$ and $\gamma = 0.01$ are shown in Figure 4.6. The discontinuity of the partial derivative of the temperature in the y-direction can clearly be seen on that figure at $y = 0.5$.

Composite grids are defined so that the local spatial resolution in the region where the diffusivity faces a step change is the same as that on the uniform grid, i.e, $\Delta = 2^{-9}$.

Two types of refinement were considered. The first consists of a unique mesh refinement delimited by A=(0,0.34375) and D=(1,0.65625) in Figure 4.7, performed at a particular grid level. For the second, also illustrated in Figure 4.7, a first refinement again delimited by A and D is followed by a second refinement enclosed in the first

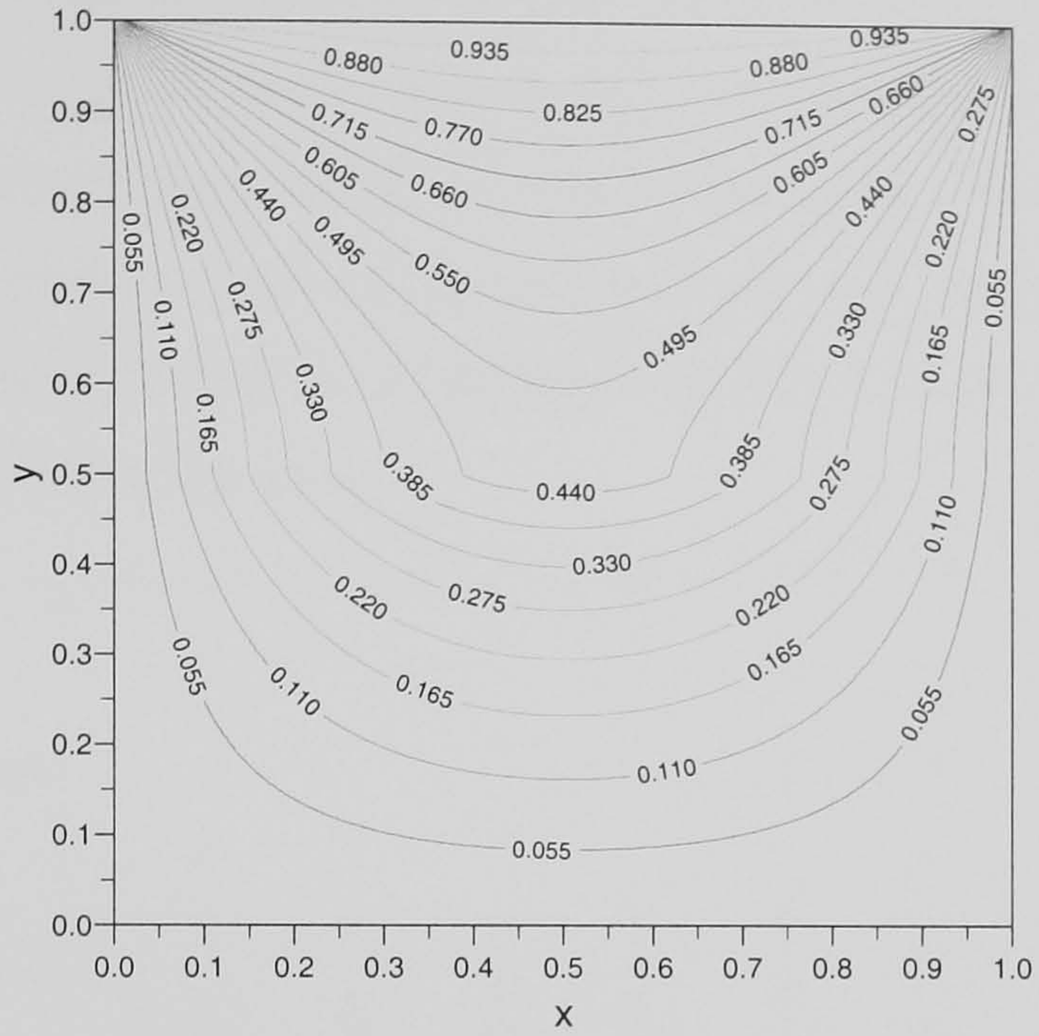

FIGURE 4.6: Contours of temperature for the numerical solution of the steady-state two-dimensional heat equation on a uniform 513x513 grid with a step change in the diffusivity defined by eq. (4.13) with y_s=0.5, C_0=0.01, ΔC_0=0.1 and γ=0.01.

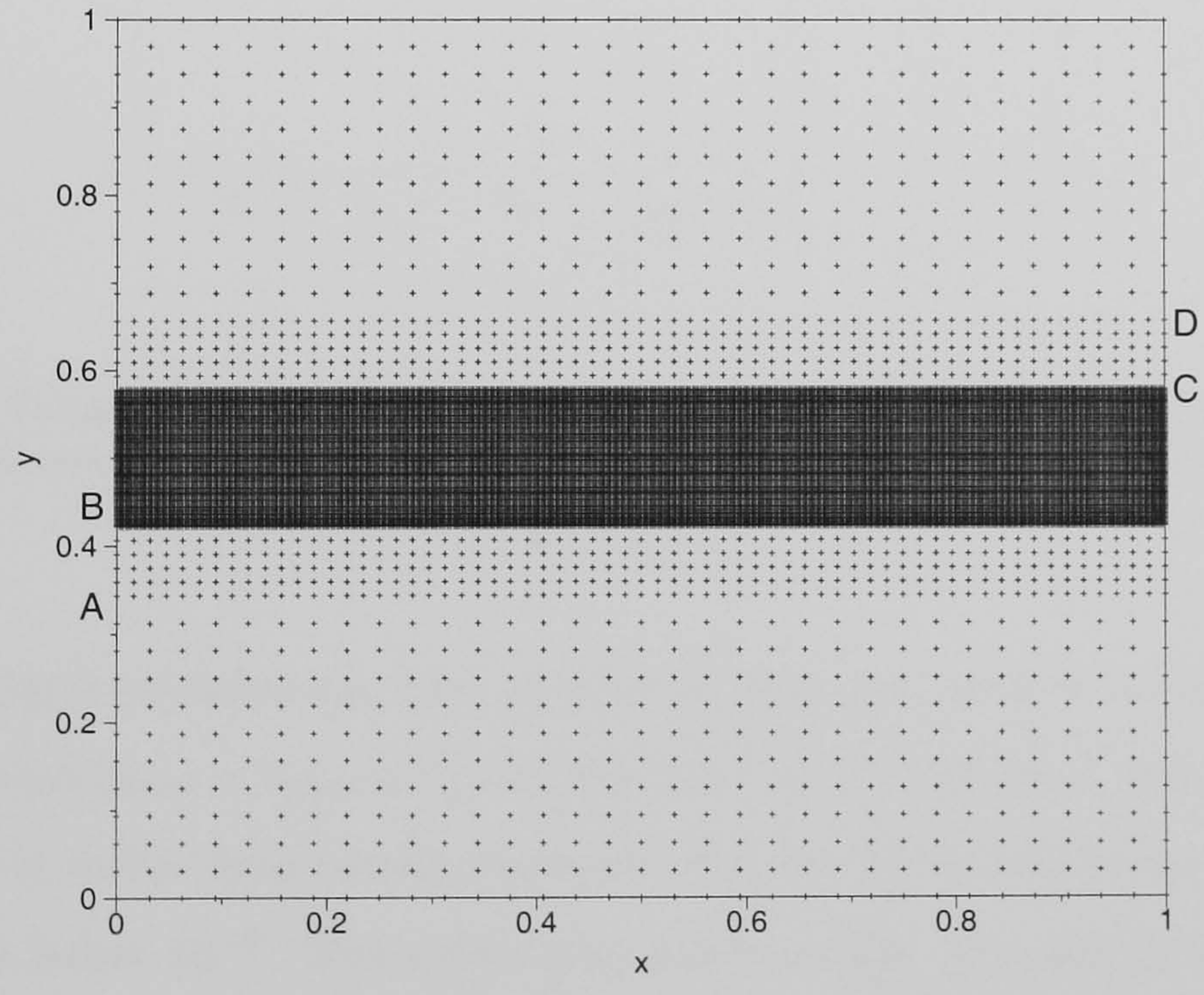

FIGURE 4.7: Composite grid $\widehat{G}^{2+1+3}$.

one, delimited by B=(0,0.421875) and C=(1,0.578125) and performed at a finer grid level. Of course, by varying the positions of the points A, B, C, D and the grid levels at which the refinement is performed, an infinite number of composite grids can be

built. The goal of this section however is not to find the optimal composite grid but to demonstrate the potential of the technique. Seven composite grids in total were considered and the corresponding variation of the mesh density in the y-direction for each of these grids is shown in Figure 4.8, along with the number of grid points. Grids are denoted according to the notation introduced in §3.6 and the coarse grid level G^0 is invariably a 9x9 grid.

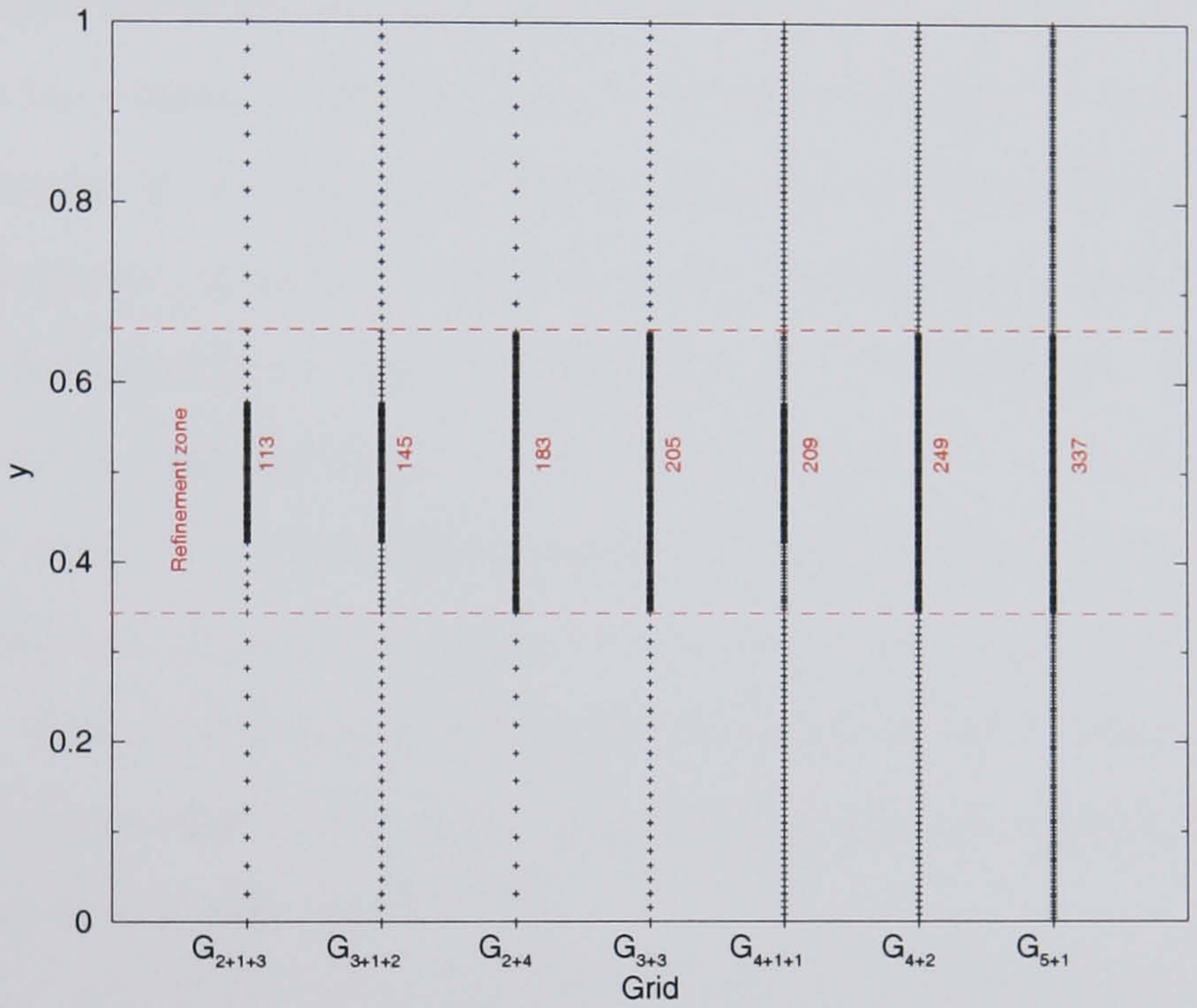

FIGURE 4.8: Variation of the mesh density in the y-direction for the composite grids considered. Grids are shown in ascending order of the total number of mesh-points in the y-direction.

All the multigrid calculations were performed with two presmoothing and posts-moothing stages ($n_{pre} = n_{post} = 2$) and the number of V-cycles at the intermediate and finest grid varies dynamically to ensure that the Euclidean norm of the residual decreases below 10^{-8}. The coarse-grid solver simply proceeds by applying the steady-state counterpart of the Red-Black Gauss-Seidel scheme defined by eq. (4.9) until convergence.

The correct implementation of the $\mathcal{MLAT}$ can be judged by looking at Figures 4.9 and 4.10 showing the temperature profile in the y-direction at $x = 0.5$ on the uniform and composite grids. In Figure 4.9 the profiles are obtained for composite grids having only one mesh refinement (grid $\widehat{G}^{2+4}$, $\widehat{G}^{3+3}$, $\widehat{G}^{4+2}$ and $\widehat{G}^{5+1}$), while

Figure 4.10 shows numerical results on composite grids with two concentric mesh refinements (grid $\widehat{G}^{2+1+3}$, $\widehat{G}^{3+1+2}$ and $\widehat{G}^{4+1+1}$). At first glance, the profiles are almost undistinguishable and only a by zooming into the discontinuity region (shown in the encapsulated graphs in Figures 4.9 and 4.10) is the difference between the uniform and composite grid results revealed to be no more than 0.25%. Not surprisingly the "*worst*" but still acceptable accuracy is for the composite grids $\widehat{G}^{2+4}$ and $\widehat{G}^{2+1+3}$. On those two grids, the first mesh refinement is performed on G^2, the 33x33 grid, which is too coarse to provide a very accurate Dirichlet boundary condition for boundary nodes of the child grid. Better accuracy is achieved by performing the first mesh refinement on finer grid levels at the cost of larger computational time (indicated in the caption of Figures 4.9 and 4.10). For example, when the local mesh refinement is performed on G^5, the 257x257 grid, the numerical solution on the composite grid, $\widehat{G}^{5+1}$, lies almost exactly on the uniform grid solution. The CPU time is reduced by approximately 45% in that case compared to the uniform grid solution. When two levels of refinement are used the CPU time decrease even further to the extent that a reduction of almost an order of magnitude is achieved when the solution is sought on $\widehat{G}^{2+1+3}$.

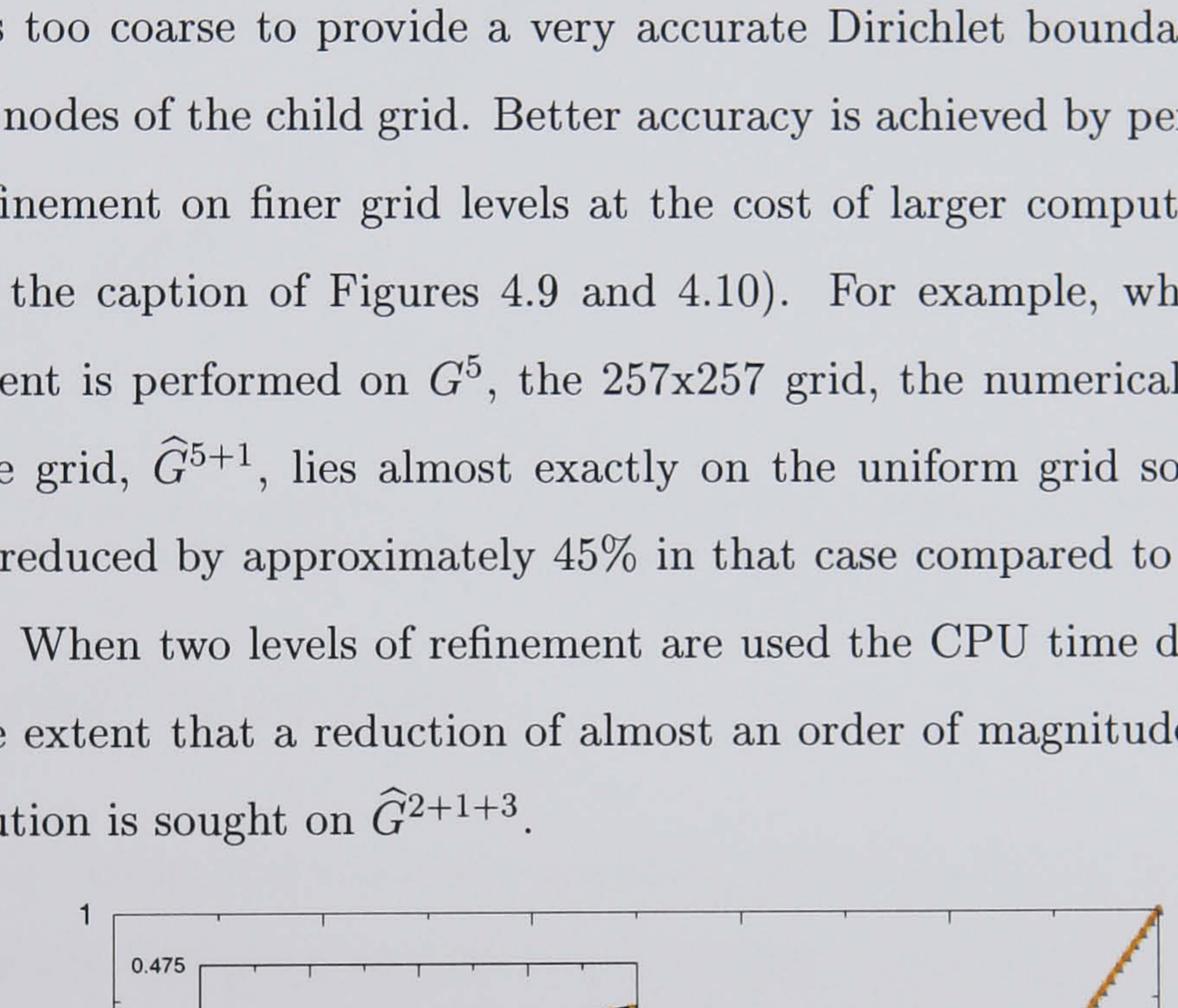

FIGURE 4.9: Temperature profiles at $x = 0.5$ obtained on a uniform and various composite grids with local mesh refinement at one grid level.

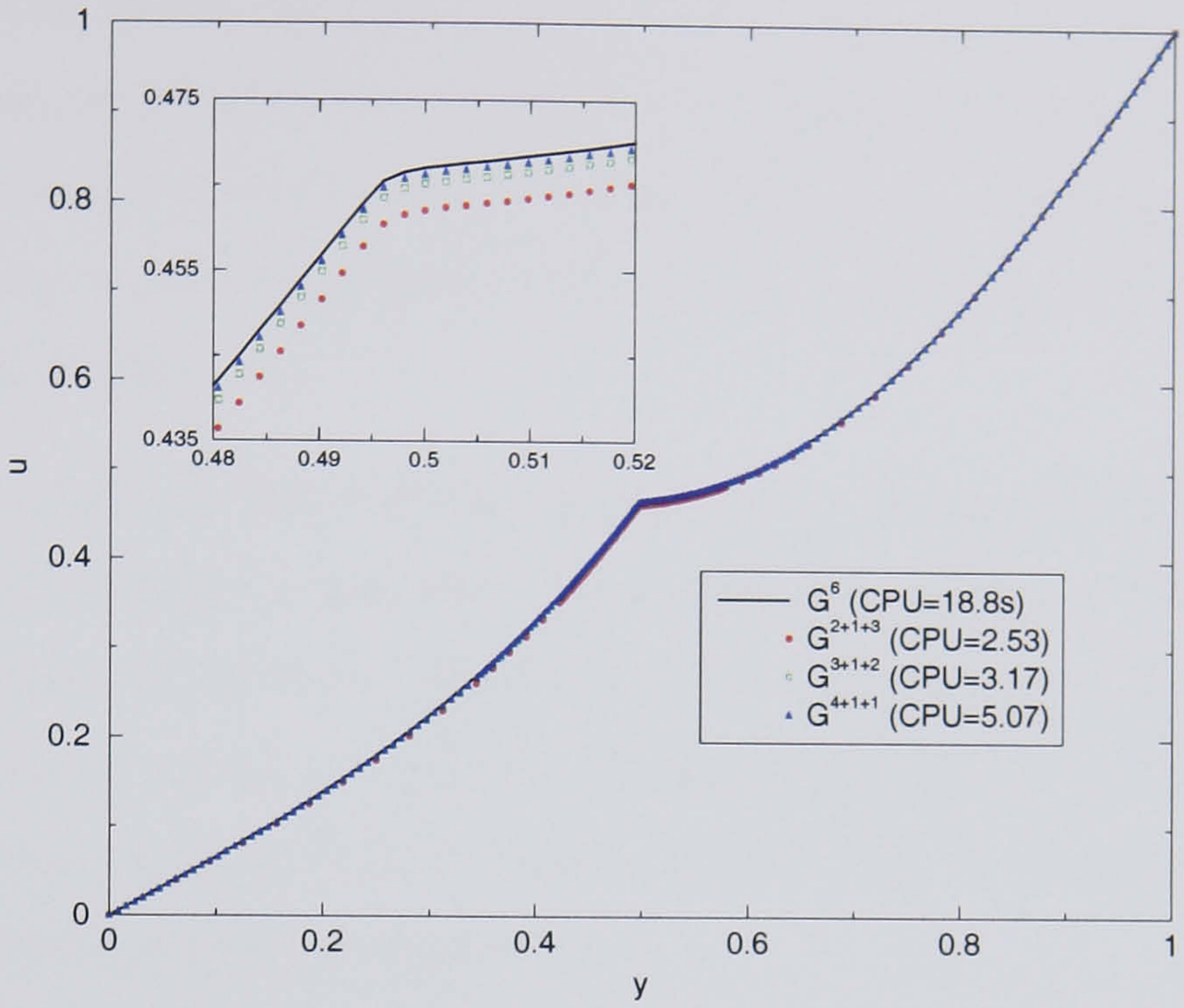

FIGURE 4.10: Temperature profiles at $x = 0.5$ obtained on a uniform and various composite grids local mesh refinement at two grid levels.

4.5 Concluding remarks

Based upon the results of this chapter, a number of conclusions can be drawn. The proposed adaptive time-stepping scheme successfully controls the local truncation error as shown by the comparison with the true local error for the solution of the ODE, eq. (4.1).

When applied to the transient two-dimensional heat equation, this scheme outperforms the backward Euler scheme as better accuracy can be achieved in significantly less computational time. However, the tolerance needs to be prescribed carefully. If the value of this tolerance is too large, the accumulation of the local truncation error at each time-step degrades the numerical solution leading to potentially large total error as shown by Figure 4.2(**d**). On the other hand, if this tolerance is smaller than a "*saturation threshold*", the interference of spatial discretisation error spoils slightly the benefit of controlling the local truncation error and the accuracy of the numerical solution decreases a little (see Figure 4.4(**a**)). The value of the optimal tolerance decreases when solutions are sought on finer and finer meshes. Finally, the application of the $\mathcal{MLAT}$ to the steady-state heat-equation with a step-change

in the diffusivity shows that the computational time can be reduced by almost an order of magnitude when two concentric local mesh refinements are performed without significant loss of accuracy. Of course, even greater computational savings can be achieved if the singularity is local instead of spanning through the whole computational domain.

No attempt is made in this work to combine adaptivity in time with adaptivity in space but this would be the next natural step to enhance the efficiency of the numerical method. In particular, mesh refinements could be applied to regions where the local truncation error is the greatest. Building on the better understanding and greater confidence in the proposed numerical schemes, the next chapters focus on a range of thin film spreading problems.

Chapter 5

Droplet spreading

Contents

5.1 Introduction

The focus of this chapter is the efficient numerical solution of flows involving droplet spreading through the use of the fully-implicit, time-adaptive multigrid algorithm described in Chapter 3. Such flows are of enormous significance in many branches of science and commerce, industrial applications including, for example, the deposition of coatings and inks, direct patterning of functional layers during microchip production, spreading of pesticides and the flow of oil in heat exchangers (de Gennes (1985), Peurrung and Graves (1993)). The same also arise in other diverse areas of science ranging from biology, where they form membranes on mammalian lungs and tear films in the eye, to geology where they feature in lava flows (Oron *et al.* (1997)). Most previous theoretical studies of droplet spreading have been restricted to flow on flat homogeneous substrates and have focussed on the accurate representation of the dynamic contact line. Various approaches to the latter have been proposed including, for example, fluid slip models (Greenspan (1978), Ehrhard and Davis (1991)), models with precursor films (Schwartz and Eley (1998), Glasner (2003)), diffuse interface models (Pismen and Pomeau (2000)) or chemical activation (Blake and Haynes (1969)) but no single model has had universal acceptance. Despite these efforts, the models invariably rely on the adjustment of at least one parameter.

Possibly because the dissipation mechanism in the contact line region is unclear, studies exploring industrially relevant spreading problems with complex wettability patterns and substrate features are few. Schwartz and co-workers have chosen to tackle such problems numerically using the lubrication approximation combined with the disjoining pressure model adopted here. Schwartz and Eley (1998) explored the spreading of a droplet on an heterogeneous substrate composed of two different materials having widely different equilibrium contact angles. The specific geometry they considered is a uniform substrate upon which lies a cross of higher contact angle material. In order to support the numerical results, they performed an experiment consisting in monitoring a droplet of glycerin spreading on a glass slide upon which a cross of Teflon tape was applied. In spite of the fact that the equilibrium contact angles of the glycerin on glass and Teflon (38^0 and 114^0 respectively) are far too large

for the lubrication approximation to be applicable, their numerical results revealed good qualitative agreement. The break-up of the droplet in four satellite droplets in the four quadrants delimited by the cross was remarkably well reproduced by the simulation. In Schwartz (1998), spreading over heterogeneous substrates with periodic arrays of high contact angle patches was investigated and revealed that the droplet can find different stable positions, depending on the previous history of motion, for large wettability contrast.

Darhuber and co-workers also devoted many studies to the equilibrium shape of liquid microstructures on chemically heterogeneous substrates. Using a combination of experiment and simulations, the latter relying on total energy minimisation, they investigated the selective deposition of liquids on hydrophilic regions, chemically defined on a hydrophobic surface, by means of dip coating in Darhuber *et al.* (2000(a)). Darhuber *et al.* (2000(b)) examined morphological aspects of microfluidic droplets deposited on flat but chemically patterned substrates having hydrophilic and hydrophobic regions. They explored a range of wettability patterns, volumes and surface energies and found that the computed droplet conformations closely resemble those obtained experimentally. A drawback of the total energy minimisation method used by these authors is that only equilibrium conformations can be computed leaving the droplet dynamics unknown.

The recent development of Lattice Boltzmann models also deserves a special mention. They bridge the gap between the traditional continuum approach and molecular dynamics and are therefore well suited to probing the behaviour of fluids on mesoscopic length scales. Because Lattice Boltzmann models incorporate a diffuse interface, the singularity at the contact line is removed. However, the limitation of a diffuse interface is that it is difficult to model large domains because of the magnitude of the computational demand (Briant *et al.* (2002)). In Dupuis *et al.* (2003), the ability of the Lattice Boltzmann approach to model the spreading of a droplet on a substrate comprising hydrophilic and hydrophobic stripes is demonstrated.

Finally, the experimental work of Cubaud (2001) covers a wide range of flows on substrates having wetting heterogeneities. Flows with topographic and wettability heterogeneities considered at the end of this chapter has recently been studied,

Gaskell *et al.* (2003(a)).

In the context of the lubrication approximation, most previous numerical approaches utilised a semi-implicit Alternating Direction Implicit ($\mathcal{ADI}$) scheme to solve the discretised governing equations (Weidner *et al.* (1997), Bielarz and Kalliadasis (2003)). Developed originally for second-order elliptic and parabolic systems, the $\mathcal{ADI}$ technique uses alternating sweeps in each direction and only a banded system of equations needs to be solved to update the discrete values. For higher order elliptic equations, Yanenko (1971) developed a version of the $\mathcal{ADI}$ technique called "time-splitting" which was first exploited by Schwartz and co-workers to solve the discrete counterpart of the lubrication approximation. In contrast to employing time-splitting to solve the time dependent lubrication equations, the present work utilises a fully implicit multigrid approach.

In his chapter, the efficiency and accuracy of the numerical method are first demonstrated by comparison with a series of analytical and previously-reported numerical results for spreading flows. The spontaneous motion of a droplet over a cross of poorly wetting material is then considered and results show good qualitative agreement with those of Schwartz and Eley (1998). Next, the effect of the disjoining pressure on the wetting behaviour of droplets is explored by comparing numerical solutions for partially and completely wetting droplets. Finally, new results are presented which show how the method can be readily applied to simulate flows over substrates with topographic and/or wettability inhomogeneities. All solutions were obtained using the multigrid approach described above with the Positivity Preserving Scheme described in 3.2 where the coarsest grid level G^0 is 17x17.

Figure 5.1 is a schematic diagram of the flow of a droplet, $H(X, Y, T)$, over a topographic feature, $S(X, Y)$, of amplitude S_0 and lengths L_T and W_T with respect to the reference coordinates (X, Y), on a substrate inclined at an angle α to the horizontal. Its aspect ratio $A = W_T/L_T$.

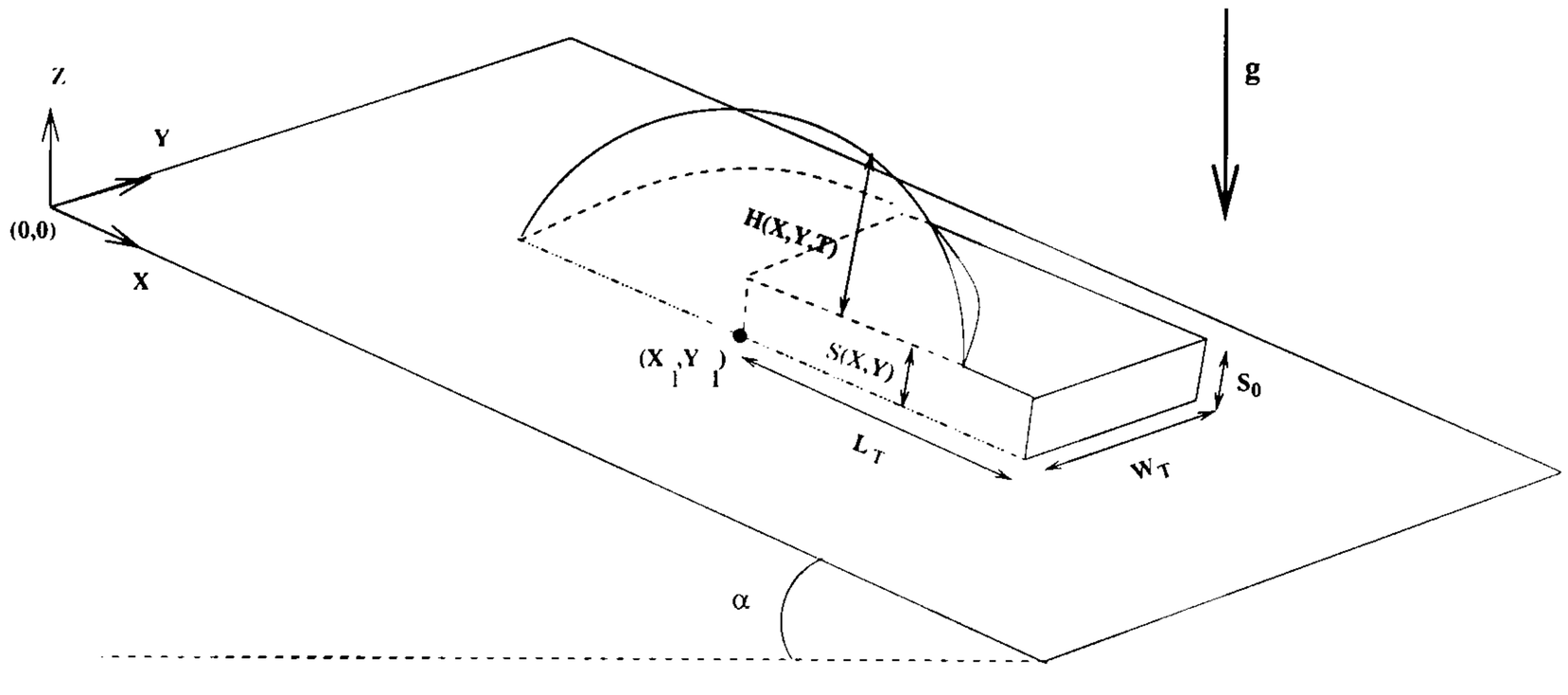

FIGURE 5.1: Schematic snap-shot of the flow of a droplet, $H(X, Y, T)$, over a topography, $S(X, Y)$, on a substrate inclined at an angle α to the horizontal, showing a section through the droplet, in the $X - Z$ plane and the parameters defining the topography.

5.2 Numerical efficiency

The efficiency of the multigrid and time-stepping procedures are demonstrated by considering droplet spreading on a horizontal substrate for a partially wetting system where the equilibrium contact angle $\Theta_0 > 0$ and the effects of gravity are neglected ($Bo = 0$). For the particular case of a spreading axisymmetric droplet, centred initially at $(x, y) = (0.5, 0.5)$, the film thickness at the droplet centre, $h_0(t)$, is given by Tanner (1979),

$$h_0(t) = \frac{K}{t^\beta} \quad \text{for } t > 0, \tag{5.1}$$

where K and β ($= 0.2$) are spreading constants, a result later verified by experiments of Lelah and Marmur (1981) which found $0.16 \leqslant \beta \leqslant 0.32$. The axisymmetric lubrication equations for this problem were subsequently solved numerically by Schwartz and Eley (1998) using time-splitting. They investigated the influence of the precursor film thickness h^* on the spreading rate parameters K and β in equation (5.1). Here, this flow is studied by solving the lubrication equations (2.29) and (2.30) for the particular case of $\epsilon = 0.005$, $(n, m) = (3, 2)$, with the initial droplet profile given by equation (2.36). An equilibrium contact angle of $\Theta_0 = 1.53^o$ was chosen so that $h_0(t) \to 1$ at large times. Note that, apart from the initial profile, no axisymmetry is imposed in the three-dimensional numerical solutions reported here.

The following sequence of figures elucidates the effect of the multigrid parameters on the convergence of the solutions by plotting the relative residuals at the finest grid level, which are defined as the ratio of the residual at the finest grid level after a given number of fine grid V-cycles compared to the initial residual at the beginning of the time step.

The effect of the number of V-cycles (N_{cyc}) at intermediate grid levels ($0 < k < L$) on the relative residuals where the finest grid level is 129x129 (i.e. $L = 3$) and the fixed (for this comparison) time step is 10^{-9} is shown in Figure 5.2(**a**). It clearly demonstrates the benefit of using at least one V-cycle at the intermediate level as the relative residuals are reduced by almost two orders of magnitude compared to the case where no intermediate V-cycle is used. More than one V-cycle does not improve noticeably the convergence of the solution at the finest level in these calculations, however using a higher order interpolation scheme for the Full Multigrid interpolation (such as bicubic interpolation instead of bilinear interpolation) might increase the benefit of using more intermediate V-cycles.

The initial increase in relative residuals is due to the fact that at the beginning of the solution process the initial guess, which corresponds to the solution at the previous time step, satisfies (3.15) exactly since the right-hand side of equation (3.15) does not change. Thus, after a first cycle, despite a reduction of the residuals for equation (3.14), the residuals of equation (3.15) can only increase. The magnitude of this initial increase in relative residuals is critical to the success of the solution procedure and therefore a larger number of presmoothing sweeps is performed for the first V-Cycle ($n_{pre} = 4$) while two presmoothing sweeps only are found to be sufficient for subsequent V-cycles. The parameter n_{post} is set to 2 regardless of the cycle number.

The effect of the grid size at the finest level is explored next for a fixed number of intermediate V-cycles ($N_{cyc} = 3$) and $\Delta t^{n+1} = 10^{-9}$. Figure 5.2(**b**) shows that for all grids with L ranging from 3 (129x129) to 5 (513x513) the ratio of consecutive residuals after the completion of each V-cycle is effectively independent of the finest grid level. Closer analysis of the data reveals that this ratio takes a value of approximately 1/20. Figure 5.2(**c**) shows that (fixed) time step size has little effect on

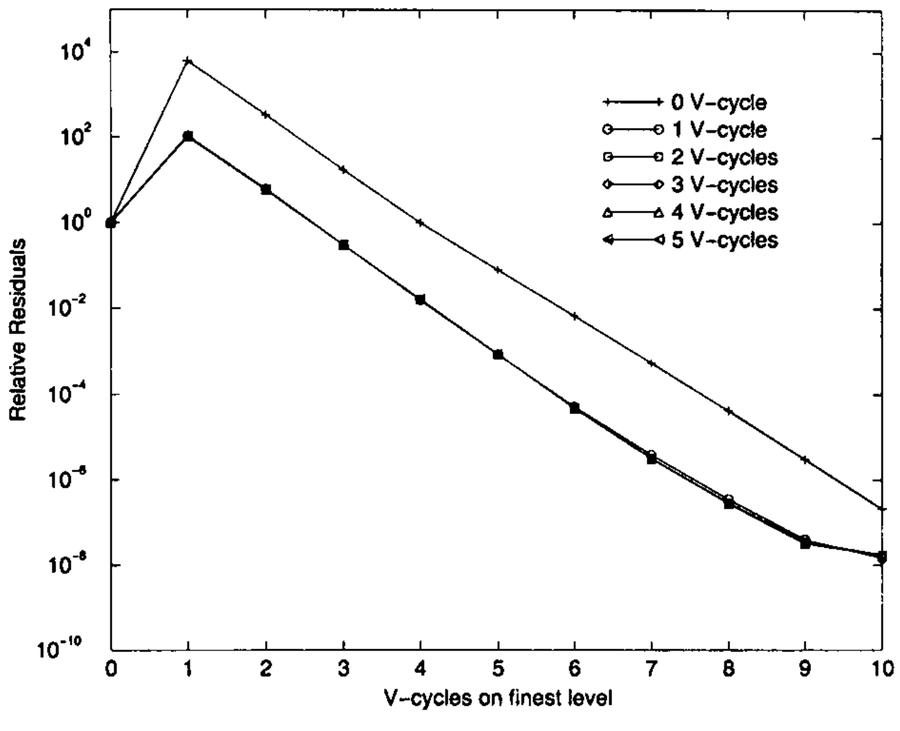

(a) Effect of the number of V-cycles (N_{cyc}) at the intermediate grid levels on the convergence history. The finest grid level, G^3, is 129x129 and $\Delta t^{n+1} = 10^{-9}$.

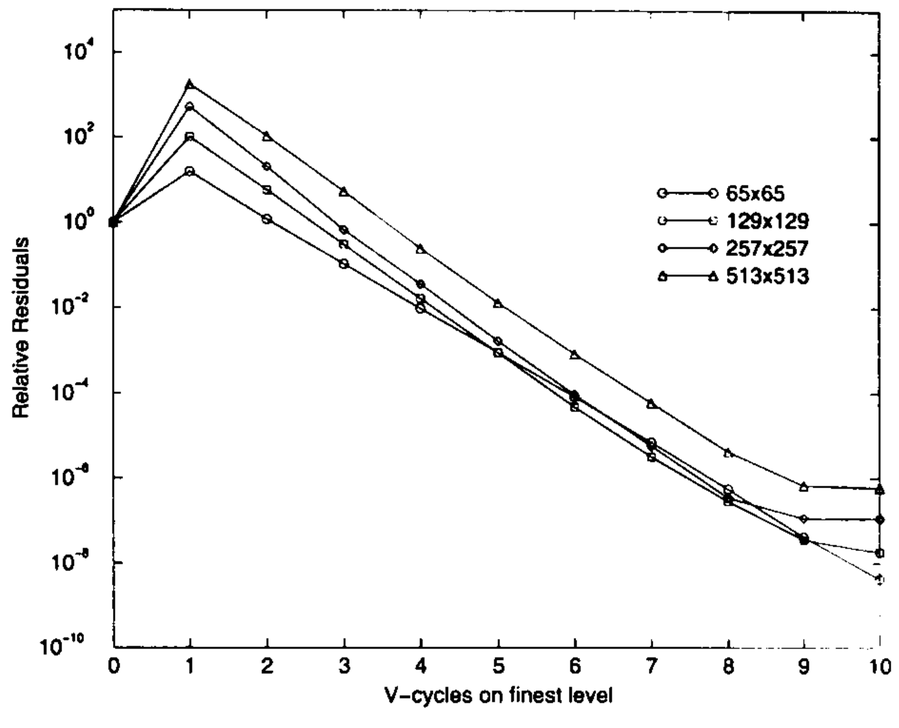

(b) Effect of the finest grid level on the convergence history with $N_{cyc} = 3$ and $\Delta t^{n+1} = 10^{-9}$.

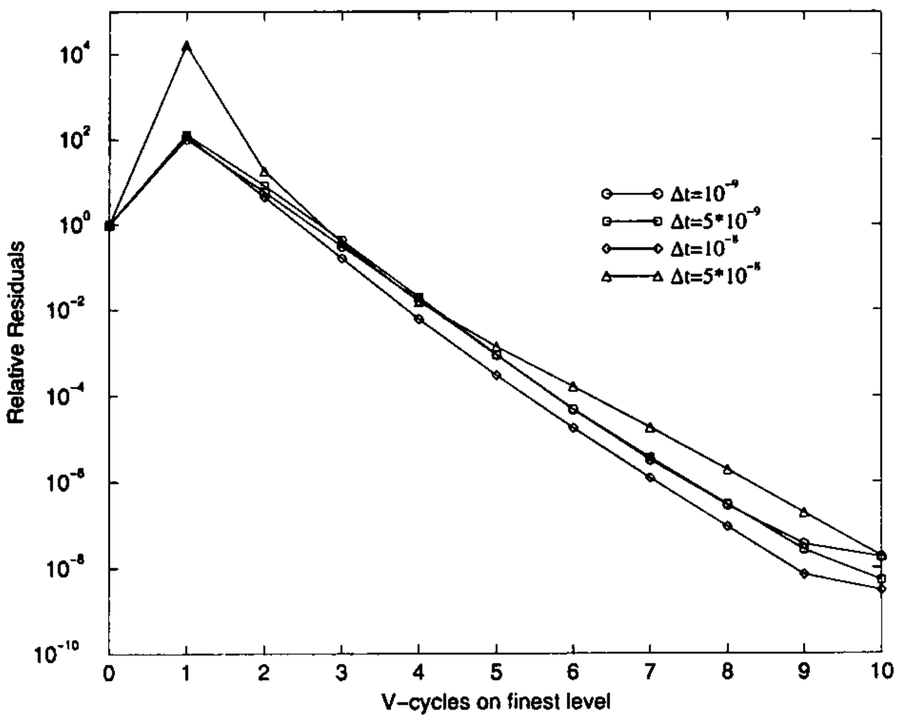

(c) Effect of time step on the convergence history with $N_{cyc} = 3$ and the finest grid level, G^3, is 129x129.

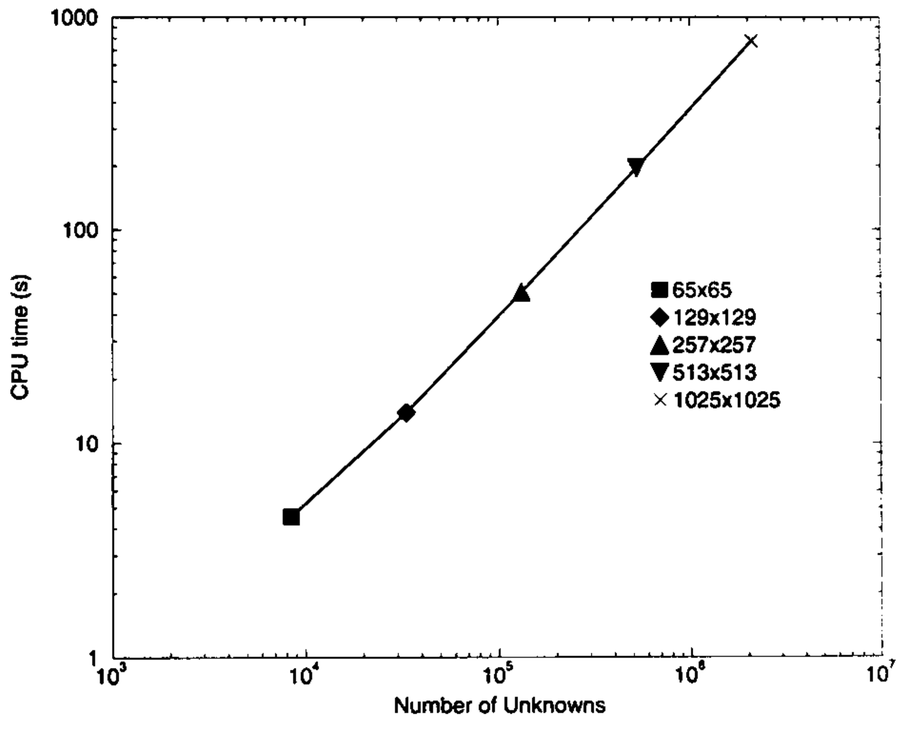

(d) Dependence of CPU time as a function of the total number of unknowns with $Tol = 10^{-4}$.

FIGURE 5.2: (**a**), (**b**), (**c**): Effect of multigrid parameters on the convergence history of solutions. (**d**): Dependence of CPU time for a typical time step as a function of the total number of unknowns. Flow conditions: partially wetting droplet with $Bo = 0$, $\epsilon = 0.005$, $\Theta_0 = 1.53^o$, $h^* = 0.04$ and $(n, m) = (3, 2)$

the convergence history until a threshold value $\Delta t_{max} = 5 \times 10^{-8}$ is reached. The initial increase in relative residuals becomes steeper and above this threshold value the solution procedure fails. This limiting value of the time step depends on both the mesh density and how advanced the solution is: as finer and finer grids are used, Δt_{max} decreases and at later times, Δt_{max} increases. This limiting time step is not related to some stability issue but to the ability of the coarse grid solver to converge to the exact solution. Indeed, at the coarsest level, the Newton iteration scheme does not guarantee the convergence to the exact solution if the initial guess is poor. Using a globally convergent method such as the Newton method with a backtracking algorithm would undoubtedly improve the robustness of the solver. Note that these calculations are for very early times where the spreading motion is most active and the demands on the multigrid solver are most severe. An additional advantage therefore of the adaptive time-stepping scheme described previously is that the time-step selected is always smaller than this limiting time step since no restart of the solution procedure is ever necessary. In light of the above, all subsequent results were obtained using 5 V-cycles at each level. Although clearly over-cautious, this has only a small additional computational cost since most of the computational time is spent performing cycles at the finest level.

Figure 5.2(**d**) shows how the CPU time for a typical time step depends on grid density and demonstrates that one of the most important potential advantages of multigrid methods, namely that CPU time varies linearly (i.e. the slope of the line in Figure 5.2(**d**) ≈ 1) with the total number of unknowns, is achieved by the solver. As noted above, when allied to ever-increasing computational power, this feature of the solver is particularly important when small-scale phenomena need to be simulated efficiently and accurately.

Figure 5.3(**a**) illustrates how the time step varies as a function of h^*, showing that when the effects of the choice of initial profile become negligible, the time-stepping scheme enables substantial efficiency gains to be realised. Furthermore the value of h^* has only a marginal influence, in the sense that the larger h^* values permit larger time steps to be used near the equilibrium state. Interestingly, in this log-log graph the variation of the time-step appears to mirror the evolution of the droplet

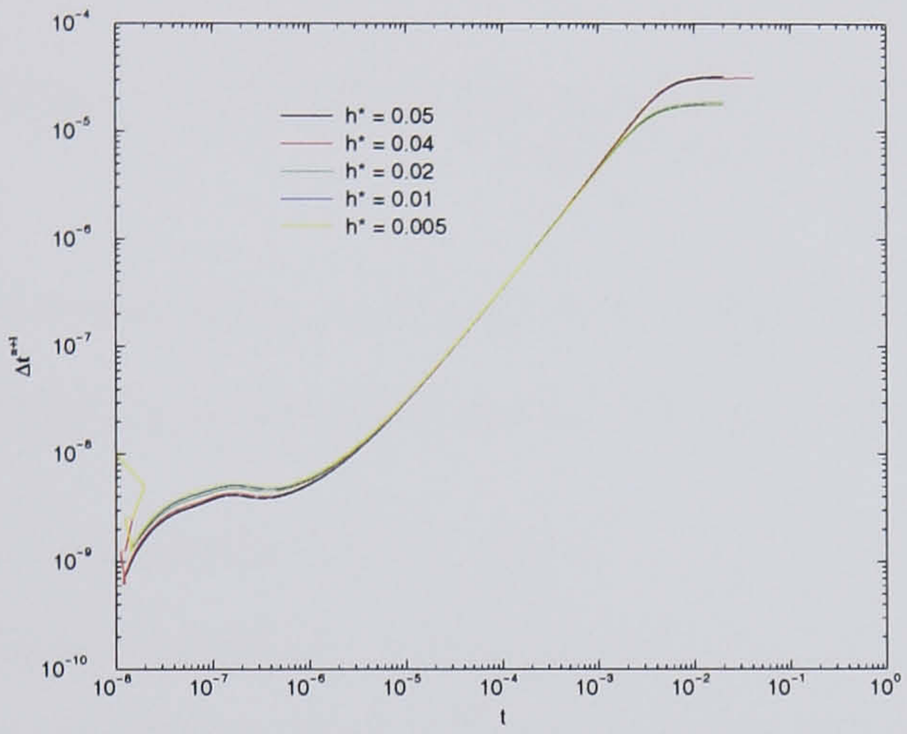

(**a**) Effect of precursor film thickness h^* on time step evolution. The finest grid level is G^4, i.e. 257x257.

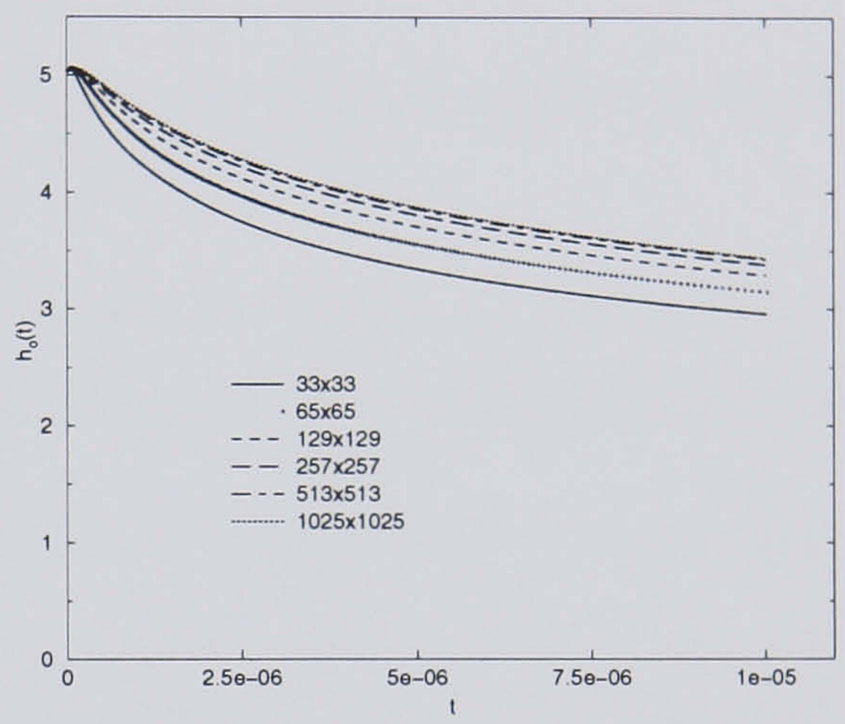

(**b**) Multigrid solutions of the droplet thickness at the centre of a partially wetting droplet as a function of time and grid density with $h^* = 0.04$.

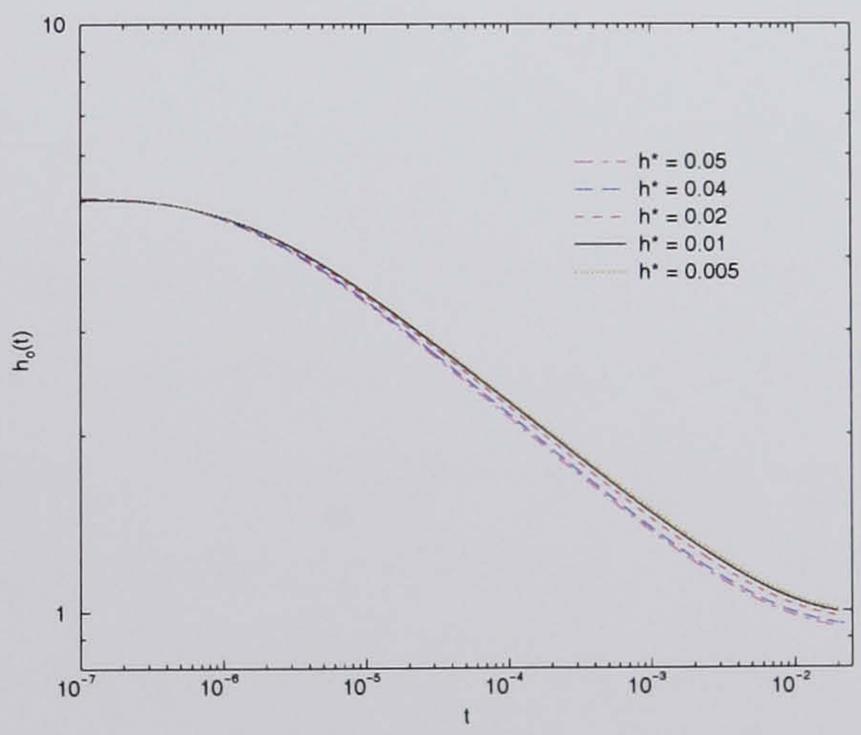

(**c**) Multigrid solutions of the droplet thickness at the centre of a partially wetting droplet as a function of time and precursor film thickness h^*. The finest grid level is G^4, i.e. 257x257.

FIGURE 5.3: Simulation parameters for (**a**), (**b**), (**c**): $Bo = 0$, $\epsilon = 0.005$, $(n, m) = (3, 2)$, $\Theta_0 = 1.53^o$ and $Tol = 10^{-4}$

h^*	K	β	Rescaled K
0.05	0.353	0.196	0.615
0.04	0.362	0.194	0.627
0.02	0.385	0.191	0.661
0.01	0.407	0.187	0.691
0.005	0.41	0.187	0.696

TABLE 5.1: The effect of precursor film thickness h^* on spreading rate parameters obtained using a 257x257 grid with $Tol = 10^{-4}$.

thickness shown in Figure 5.3(**c**). When the droplet thickness at its centre decreases according to Tanner's power law, the time step increases also following a power law.

In a technical report, Gresho and Kay (2002) discuss an adaptive time-stepping scheme based on a similar idea to the one presented in §3.3. The main difference between their scheme and the present one is in the predictor stage, which uses a second-order Adams-Bashforth method. Applied to diffusion and advection-diffusion problems they established that the scheme was also adequate to "follow the physics" and qualified the scheme as "a candidate best method in the context of low order finite element approximation in space". In the light of their experience, the adaptive time-stepping scheme used here also appears to "follow the physics".

The accuracy of the solutions is considered next. Figure 5.3(**b**) investigates the effect of grid size on the droplet thickness $h_0(t)$ for simulations where $h^* = 0.04$ and $Tol = 1 \times 10^{-4}$, where Tol is the specified error tolerance. It shows that the solution converges with respect to the spatial discretisation as the grid is progressively refined; the solutions on the three finest grid levels differing by only approximately 1%. The influence of the precursor film thickness h^* is shown next, in Figure 5.3(**c**), where solutions are obtained with a finest grid level of 257x257 and the adaptive time stepping with $Tol = 10^{-4}$. It shows that after an initial phase the droplet thickness $h_0(t)$ obeys the expected power law relationship $h_0(t) = K/t^\beta$ where the coefficients K and β are shown in Table 1. Figure 5.3(**c**) reveals that, at a given time, the thinner the precursor film thickness, the larger the droplet thickness at its centre. Note that, owing to a different time scaling in the present study, in order to compare these results with those of Schwartz and Eley (1998) the K values must be multiplied by the factor $0.059^{-\beta}$. The β values are found to be close to the expected

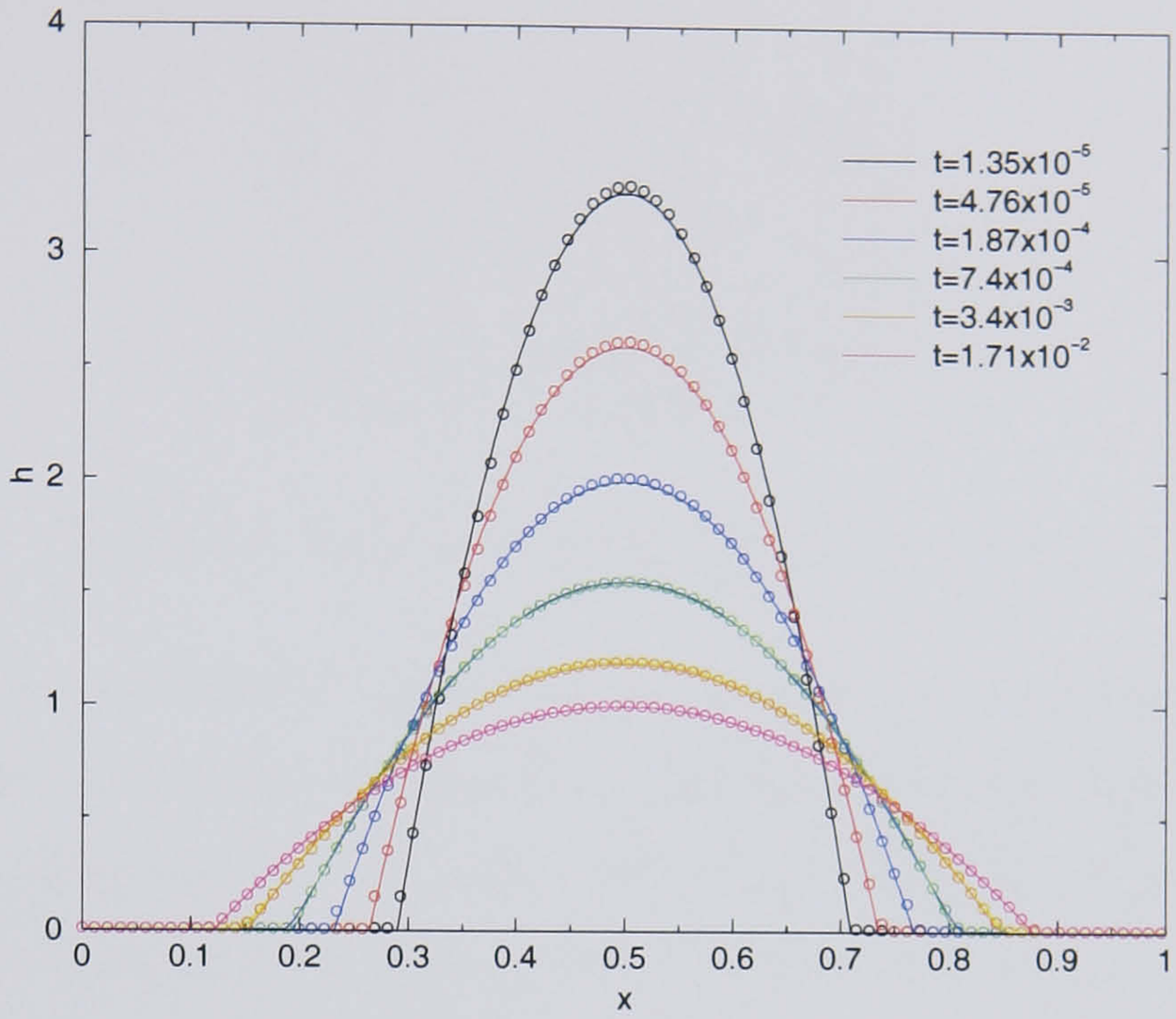

FIGURE 5.4: Droplet free surface profiles (symbols) and fitted parabolas (solid lines) at different times for $h^* = 0.01$.

value of 0.2, Tanner (1979), and the values of K also compare well with the values $K = 0.61$ ($h^* = 0.05$) and 0.68 ($h^* = 0.005$) obtained by Schwartz and Eley (1998).

Due to the form of the curvature term in eq. (2.30) which only involves second order spatial derivatives, it can be anticipated that the initially paraboloidal droplet will retain its paraboloidal shape during the spreading. This is confirmed by Figure 5.4 where the droplet free surface profiles at different times are fitted with parabolas for $h^* = 0.01$. The fitted parabolas satisfy the following equation

$$h(x) = A_0(x - 0.5)^2 + A_1 \ , \tag{5.2}$$

and the values of the constants A_0 and A_1 are reported in Table 5.2. The self-similarity of the droplet shape confirms the idea of Tanner (1979) that the spreading consists of a succession of steady states. After each elementary displacement of the contact line, surface tension is strong enough to restore the droplet to its energy minimizing shape (a paraboloid in our case).

Having established that the droplet remains paraboloidal during the spreading and that the thinner the precursor film thickness, the larger the droplet thickness at its

t	A_0	A_1
1.35×10^{-5}	-74.38	3.268
4.76×10^{-5}	-46.75	2.591
1.87×10^{-4}	-27.75	1.995
7.4×10^{-4}	-16.49	1.54
3.4×10^{-3}	-9.32	1.189
1.71×10^{-2}	-6.96	1.003

TABLE 5.2: Value of the fitting constants for eq. (5.2).

centre, it can be concluded in virtue of the conservation of the droplet volume that, at a given time, the thinner the precursor film thickness, the smaller the droplet radius. Hence, as previously mentioned, thinner precursor films slow the motion of the contact line down because of the increasing viscous dissipation.

5.3 Influence of the disjoining pressure on the spreading behaviour

In the contact line model employed, the disjoining pressure is responsible for the partially wetting behaviour of the droplet. The goal of this section is an attempt to shed some light on how the disjoining pressure affects spreading by comparing numerical results for completely and partially wetting droplets. The flow conditions are identical to those defined in the previous section, i.e. negligible gravity ($Bo = 0$), $\epsilon = 0.005$, $(n, m) = (3, 2)$, $h^* = 0.01$. The spreading of the droplet develops as a balance between the surface tension which tends to reduce the droplet's curvature and viscous stresses which resist its motion. For the partial wetting case, the small but non-zero equilibrium contact angle is $\Theta_0 = 1.53^o$ while for the complete wetting case, $\Theta_0 = 0$ by definition. Again, numerical solutions are obtained on a 257x257 grid with $Tol = 10^{-4}$ and the initial profile given by equation 2.36.

Figure 5.5(**a**) shows that the effect of disjoining pressure only becomes important in the later stage of spreading as curves showing the droplet thickness at the centre ($h_0(t)$) for the partially and completely wetting droplets are indistinguishable up to a dimensionless time of approximately 2×10^{-4}. Beyond this time, while h_0 carries on

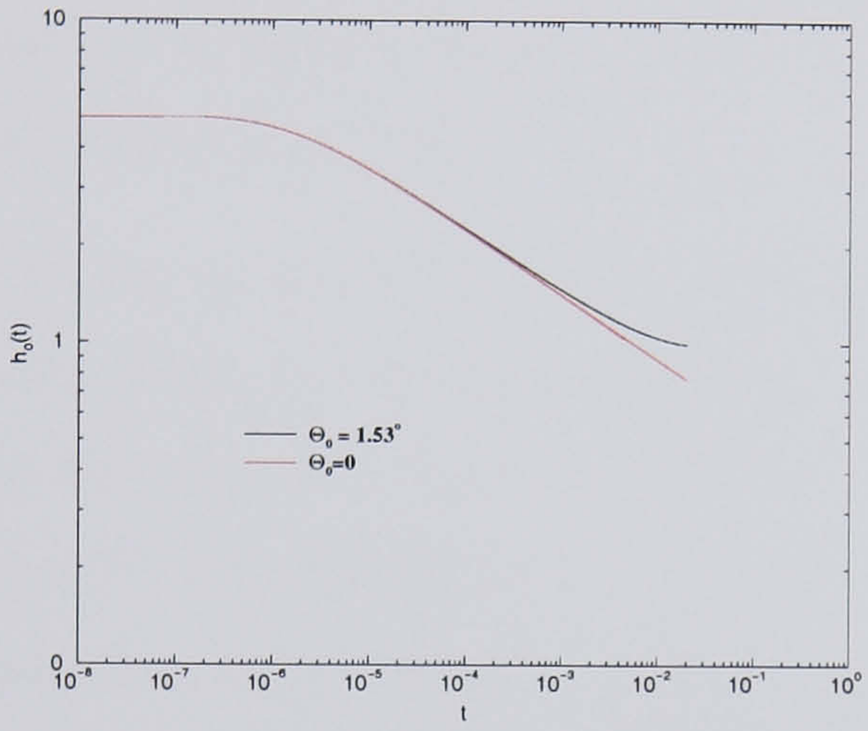

(**a**) Variation of the droplet thickness at the centre of a partially and a completely wetting droplet with time.

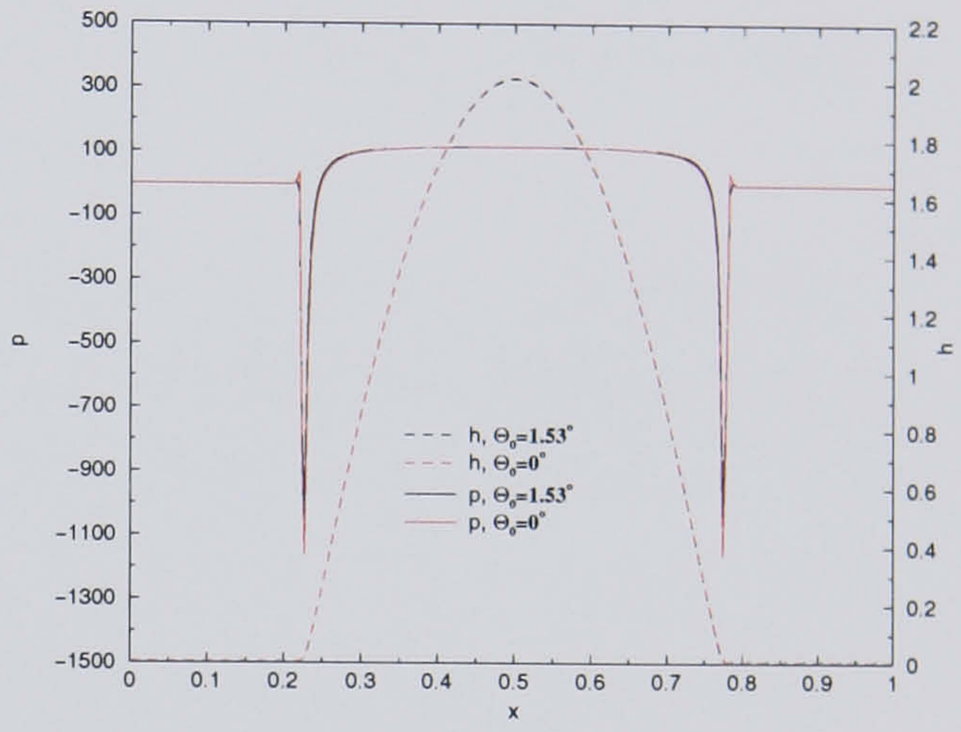

(**b**) Droplet thickness and pressure profile along $y = 0.5$ at $t = 1.76 \times 10^{-4}$ for a partially and a completely wetting droplet.

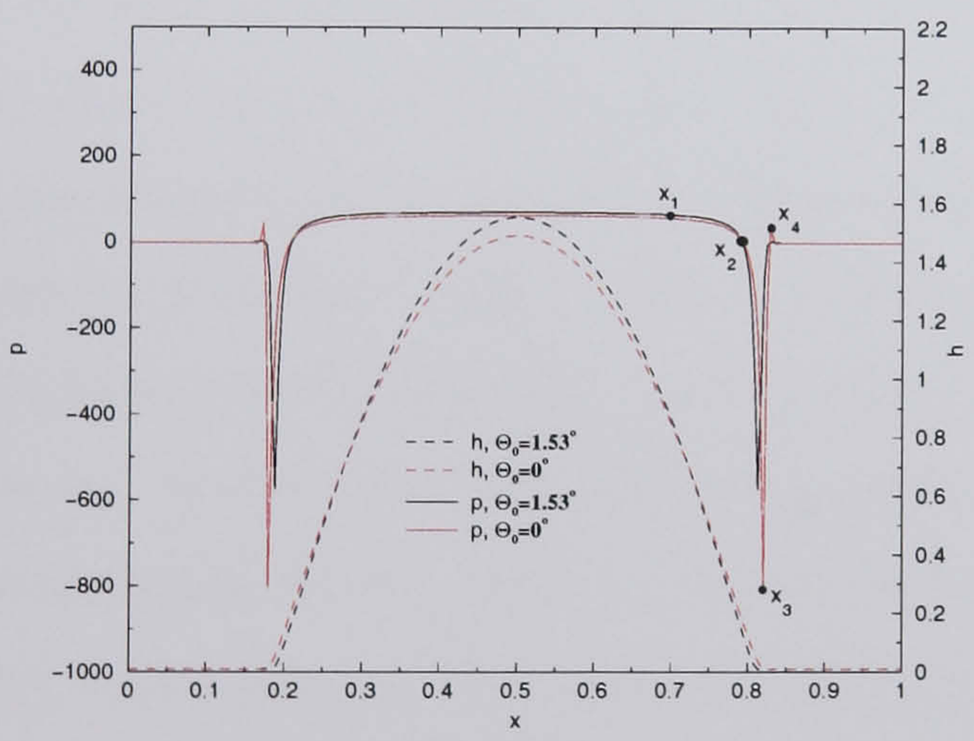

(**c**) Droplet thickness and pressure profile along $y = 0.5$ at $t = 7.85 \times 10^{-4}$ for a partially and a completely wetting droplet.

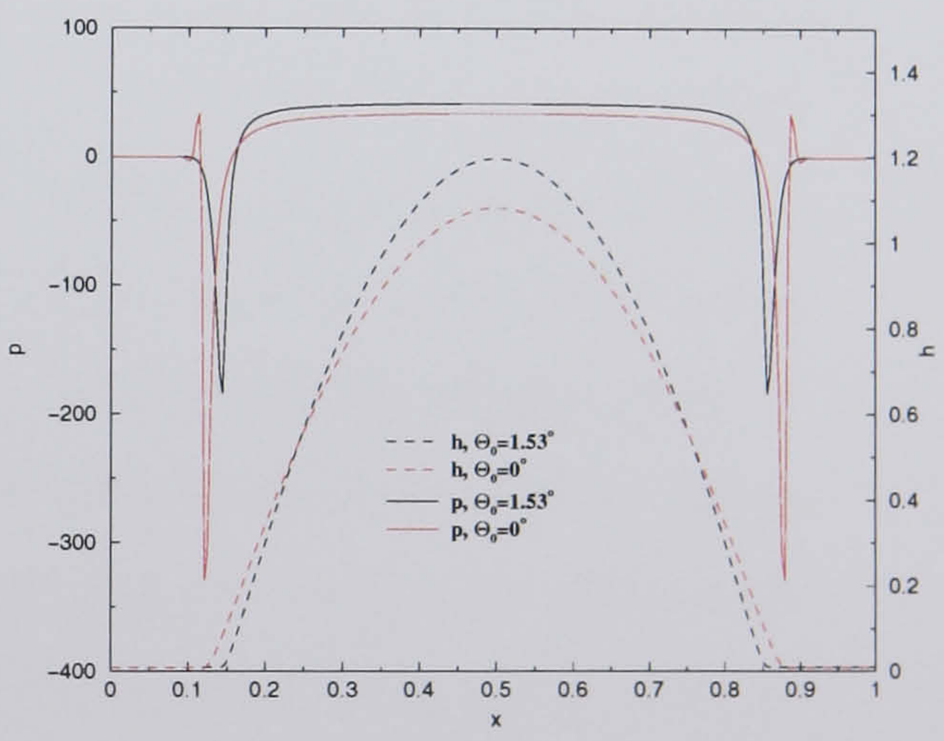

(**d**) Droplet thickness and pressure profile along $y = 0.5$ at $t = 3.8 \times 10^{-3}$ for a partially and a completely wetting droplet.

FIGURE 5.5: Droplet thickness and pressure for a partially and a completely wetting droplet ($\Theta_0 = 1.53^o$ and $\Theta_0 = 0$ respectively). Simulation parameters: $Bo = 0$, $\epsilon = 0.005$, $(n, m) = (3, 2)$, $h^* = 0.01$, $Tol = 10^{-4}$ and 257x257 grid.

decreasing for the completely wetting droplet, according to equation (5.1), it starts to level off and finally reaches a plateau at $h_0 = 1$ for the partially wetting droplet. Figure 5.5(**b**) confirms that for $t < 2 \times 10^{-4}$, the effect of disjoining pressure is negligible since the droplet thickness and pressure profiles along $y = 0.5$ are almost identical at $t = 1.76 \times 10^{-4}$. For times larger than 2×10^{-4}, significant differences appear in the droplet thickness and pressure profiles, as shown in Figures 5.5(**c**), 5.5(**d**), as discussed below.

Due to the axisymmetry of the droplet, profiles are symmetric with respect to $x = 0.5$, thus the description will focus on $x \geq 0.5$ where the droplet motion is in the direction of increasing x. The x-coordinate of the main features of the pressure profile are denoted by x_1, x_2, x_3, x_4 on Figure 5.5(**c**). For the partially and completely wetting droplets the pressure across the film is positive and decreases slowly from $x = 0.5$ to $x = x_1$. In this range of the x-coordinate, the value of the pressure is slightly higher in the partial wetting case because the contact line is not so advanced as in the complete wetting case, yielding larger values of the curvature in the bulk of the droplet. From $x = x_1$ to $x = x_3$, the pressure across the film experiences a sharp decrease and becomes negative at $x = x_2$. This change of sign in the pressure across the film corresponds to the inflection point highlighted in the analysis of Tanner (1979). Figures 5.5(**c**) and 5.5(**d**) reveal that the effect of the disjoining pressure is to reduce substantially the amplitude of the pressure drop at $x = x_3$. Furthermore, because in the case of complete wetting the contact line is further advanced, the minimum is shifted towards larger x. At $x = x_3$, which coincides with the contact line region, the free surface curvature changes rapidly from its value in the bulk of the droplet to its value in the precursor film leading to a sharp increase in the pressure. For the completely wetting droplet, the pressure peaks at $x = x_4$ where it is positive and then decays toward zero. In the partial wetting case, this peak is considerably reduced when $t = 7.96 \times 10^{-4}$ and completely disappears when $t = 3.8 \times 10^{-3}$.

These differences in the pressure profiles when the droplet completely or partially wets the substrate are accompanied by rather different behaviour of the free surface profiles in the contact line region. Zooming into the contact line region as shown

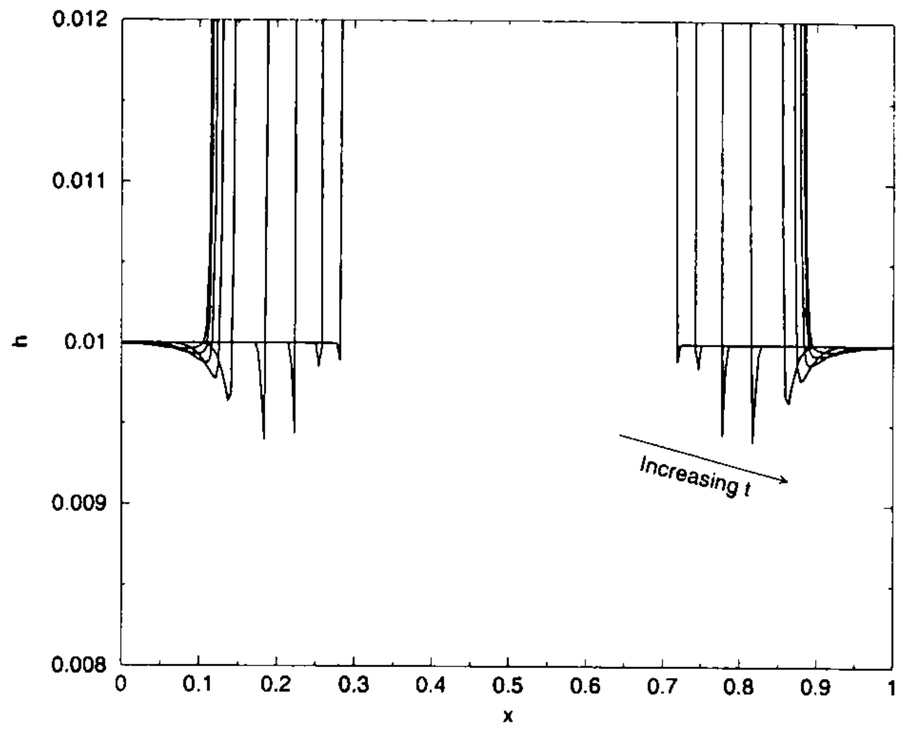

(**a**) Magnification of the contact line region for the partially wetting droplet along $y = 0.5$.

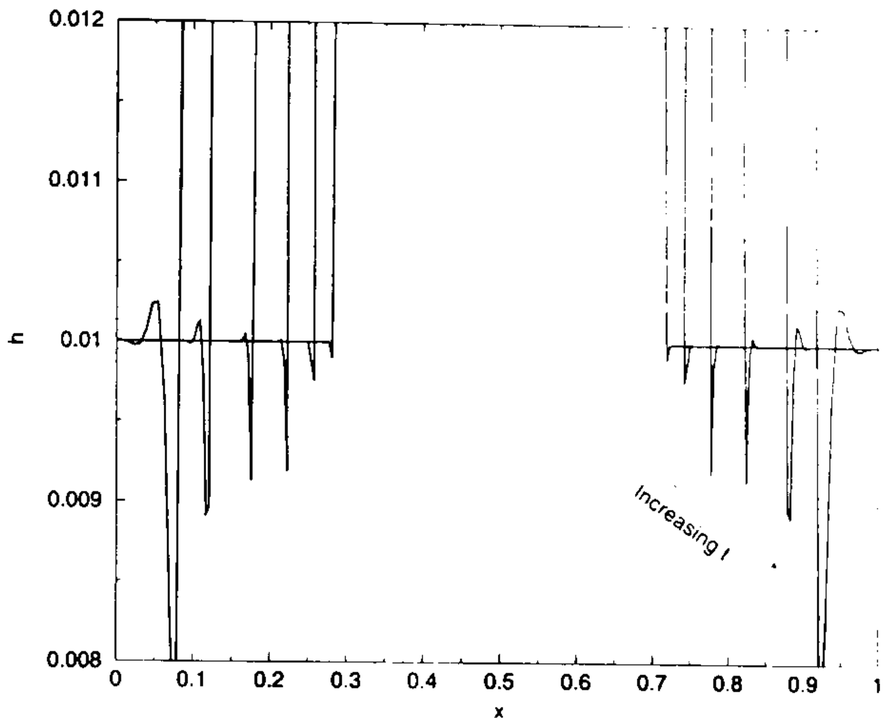

(**b**) Magnification of the contact line region for the completely wetting droplet along $y = 0.5$.

FIGURE 5.6: Magnification of the contact line region for a partially and completely wetting droplets ($\Theta_0 = 1.53^o$ and $\Theta_0 = 0$ respectively). Simulation parameters: $Bo = 0$, $\epsilon = 0.005$, $(n, m) = (3, 2)$, $h^* = 0.01$, $Tol = 10^{-4}$ and 257x257 grid.

in Figures 5.6(**a**) and 5.6(**b**), reveals that oscillations develop ahead of the contact line when the droplet completely wets the substrate. As pointed out by Bretherton (1961), the interfacial profile of a meniscus advancing over a pre-wet film has a minimum thickness. This result is confirmed by the presence of the depression ahead of the apparent contact line shown in Figure 5.6(**b**). This depression appears to grow in amplitude and to diverge as the contact line advances which could lead to the formation of a singularity at later times. This result seems counter-intuitive as in the absence of disjoining pressure, surface tension alone should tend to reduce the curvature of the free surface and prevent the occurrence of singularities. The reliability of the numerical results at such small length scale in the precursor film region might be questionable.

These oscillations can also be observed during the initial stage of the spreading in the case of partial wetting but they are of smaller amplitude and are damped in the final stage due to the effects of the disjoining pressure. The disappearance of these *ripples* ahead of the contact line was also observed by Hirasaki and Yang (2000) and attributed to the disjoining pressure.

From the knowledge of the droplet thickness and pressure, it is easy to calculate the

free surface velocity according to equation (2.27). Figure 5.7 shows the free surface velocity along $y = 0.5$ at different times. When the droplet completely wets the substrate, the free surface velocity changes sign twice. This is most obvious in Figure 5.7(**d**) where, for increasing x, the free surface velocity is first positive, then negative and finally positive again. Although the lubrication approximation does not allow recirculation flows, these sign changes in the surface velocity suggest the presence of recirculations having the pattern shown in Figure 5.8. In fact, the recirculation in the bulk of the droplet is expected and has been observed experimentally, Yarnold (1938), Veretennikov *et al.* (1998).

In contrast, the literature does not report recirculations in the precursor film. A likely reason is that the possibility to generate recirculations at length scales on the order of the nanometre seems doubtful. Nevertheless, the possible presence of these recirculations is a natural explanation for the decrease in film thickness observed in the precursor film ahead of the contact line (Bretherton (1961)) since the counter-rotating recirculations would tend to pull the free surface downward. Further away from the contact line, the recirculations have the opposite effect and create a slight bump in the free surface. When the droplet only partially wets the substrate, the disjoining pressure appears to reduce gradually this *back-flow* as the amplitude of the negative part of the free surface velocity tends towards zero. These results and observations suggest that recirculations play a role in the wetting behaviour of droplets. By preventing the formation of the recirculations in the precursor film, the disjoining pressure causes the droplet to stop spreading when the dynamic contact angle reaches its equilibrium value. It is worth noting however that the presence of the precursor film in the case of partial wetting is a matter of dispute and that the observed behaviour could be model-specific since the disjoining pressure model is only one of a number of possible wetting models.

Finally, the contrast between partially and completely wetting droplets is highlighted by monitoring the variations of the energies defined in §2.7. Figure 5.9 shows that in the partial wetting case, the increasing disjoining pressure energy balances exactly the decreasing surface tension energy at $t \sim 2\times10^{-3}$. The corresponding total energy decreases and reaches a minimum in the later stages of the spreading when the

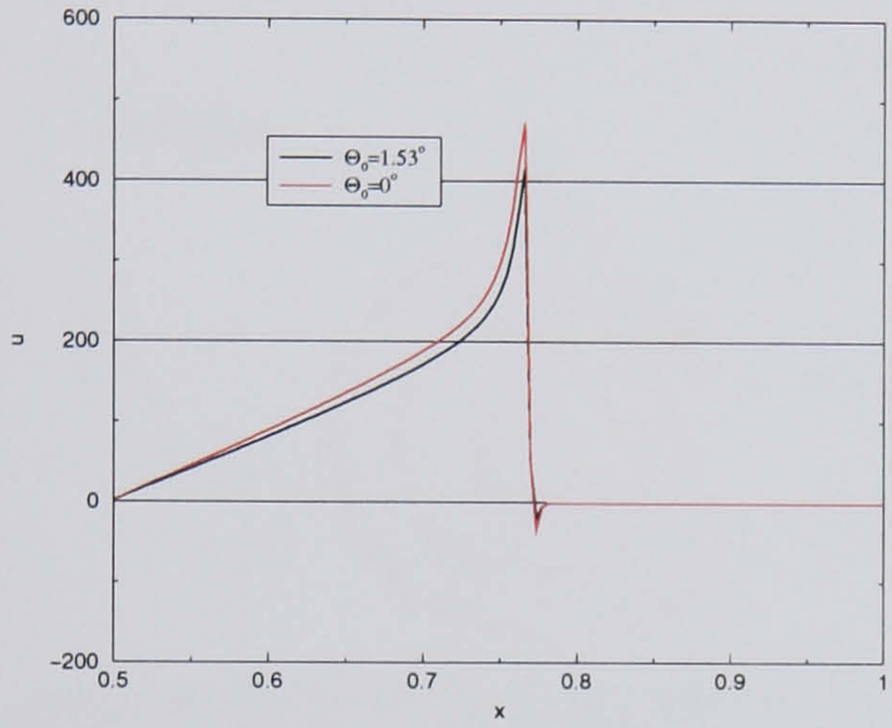

(**a**) Free surface velocity along $y = 0.5$ at $t = 1.76 \times 10^{-4}$.

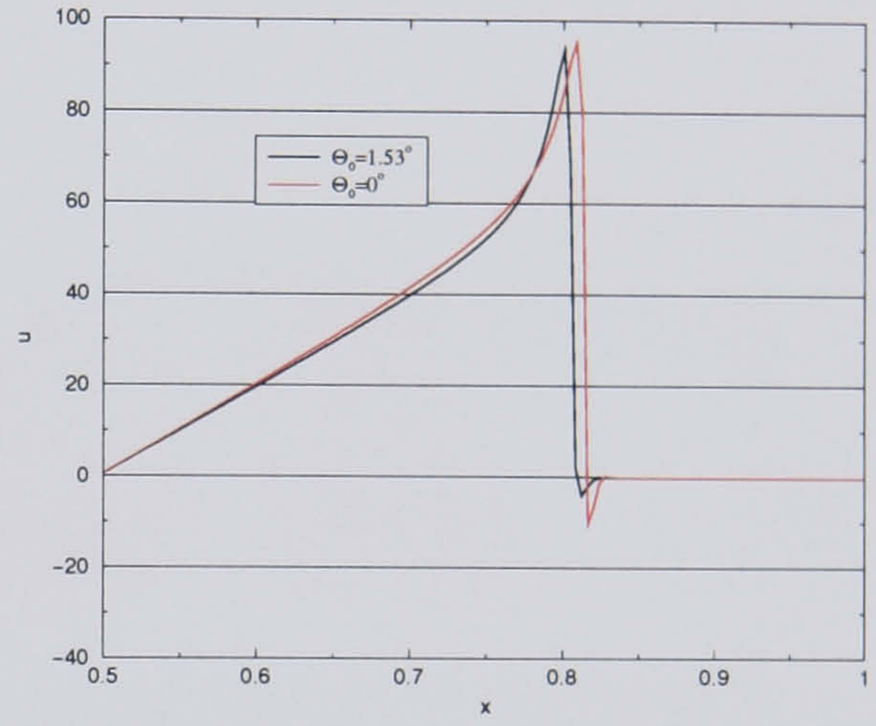

(**b**) Free surface velocity along $y = 0.5$ at $t = 7.85 \times 10^{-4}$.

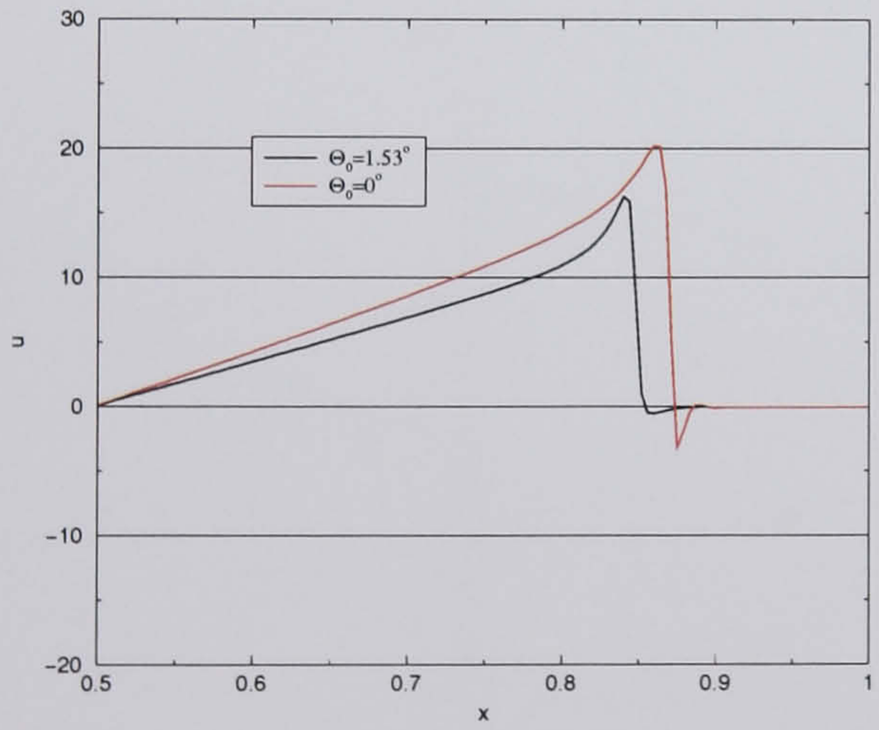

(**c**) Free surface velocity along $y = 0.5$ at $t = 3.8 \times 10^{-3}$.

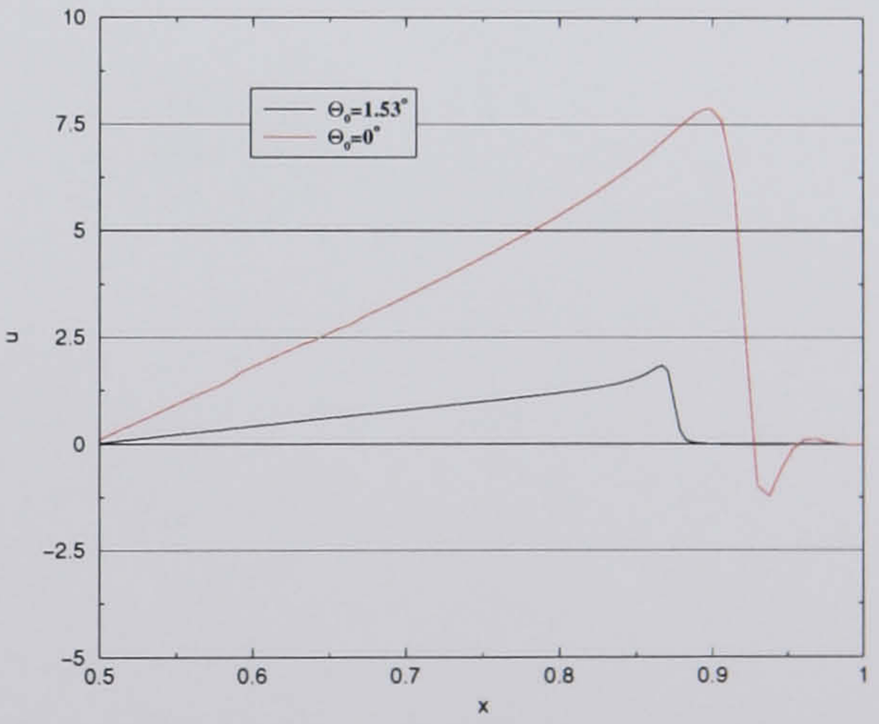

(**d**) Free surface velocity along $y = 0.5$ at $t = 0.1$.

FIGURE 5.7: Free surface velocity at various times for a partially and completely wetting droplets ($\Theta_0 = 1.53^o$ and $\Theta_0 = 0$ respectively). Simulation parameters: $Bo = 0$, $\epsilon = 0.005$, $(n, m) = (3, 2)$, $h^* = 0.01$, $Tol = 10^{-4}$ and 257x257 grid.

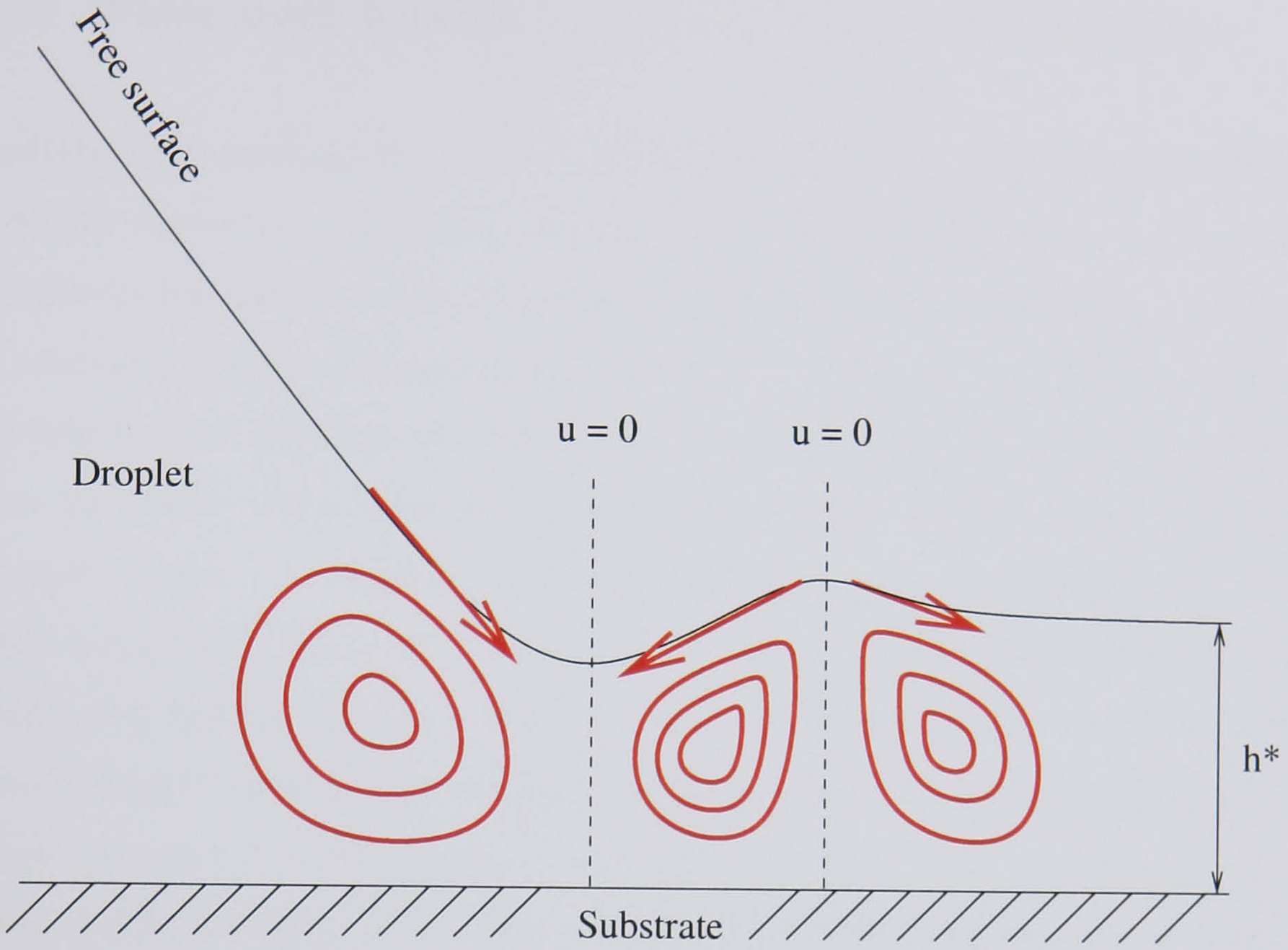

FIGURE 5.8: Suggested pattern of recirculations in the contact line region.

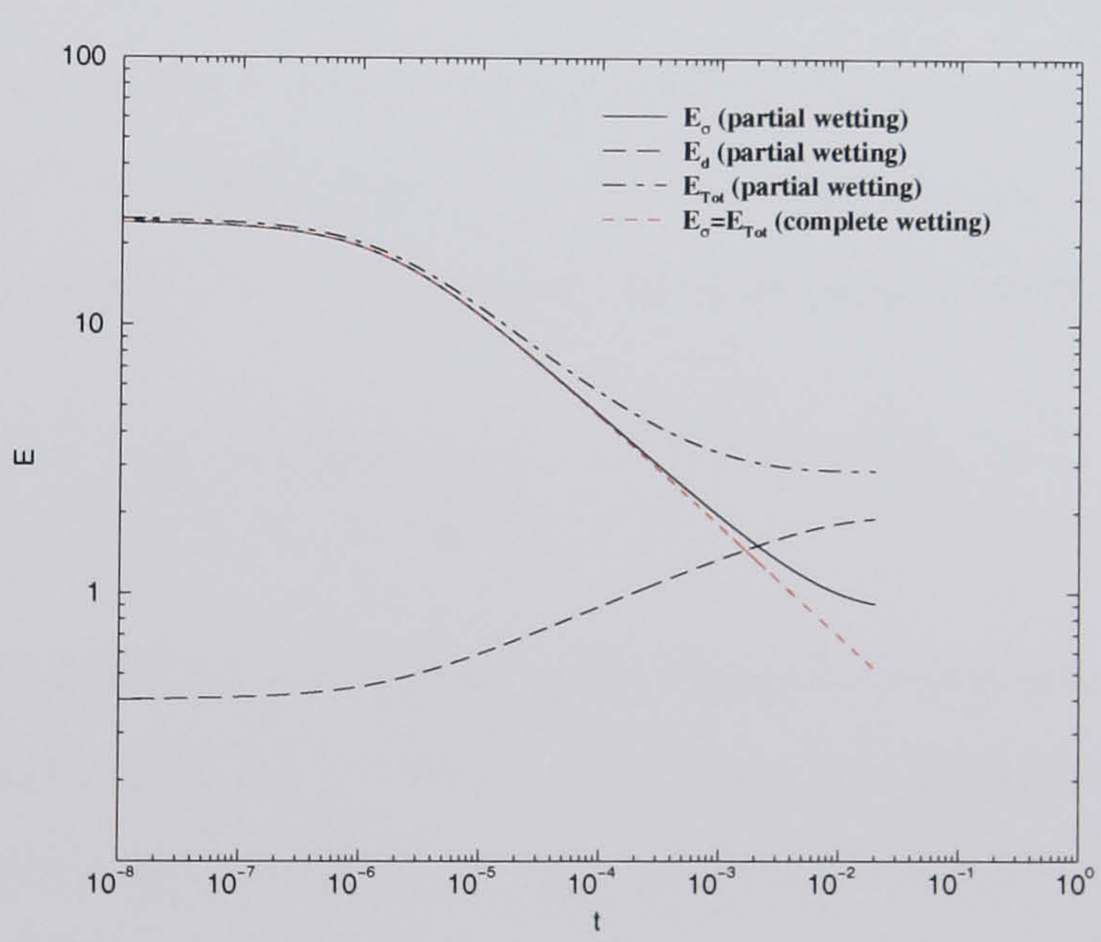

FIGURE 5.9: Variations in surface tension, disjoining pressure and total energy with time for the partially and completely wetting droplets.

droplet approaches its equilibrium configuration. On the other hand, for complete wetting, because the spreading is driven by surface tension only, the total energy is simply equal to the surface tension energy. This monotonically decreases and does so until the droplet effectively becomes a flat thin film.

5.4 Flow over a cross-shaped wetting heterogeneity

Following Schwartz and Eley (1998), numerical simulations have been performed for a droplet moving on a substrate composed of two different materials. The wettability pattern consists of a cross of poorly wetting ($\Theta_0 = 6.87^o$) material on a substrate of otherwise uniform wettability, $\Theta_0 = 1.53^o$. The combined experimental and numerical study of Schwartz and Eley (1998) reveals that the droplet located initially near the centre of the cross spontaneously moves and that the strong wettability contrast causes it to break-up into four smaller droplets lying in the four quadrants delimited by the cross. This change in topology of the droplet is particularly demanding numerically and makes this flow a good test of the numerical scheme presented in Chapter 3. The results presented are for the case of negligible gravity ($Bo = 0$) and $\epsilon = 0.005$, $(n, m) = (3, 2)$ and $h^* = 0.04$. The vertical strip of the cross is delimited by $x = 0.4$ and $x = 0.49375$ while the horizontal one is confined between $y = 0.4$ and $y = 0.49375$, in agreement with Schwartz and Eley (1998). A steep arctangent function was used to smoothly increase the equilibrium contact angle from its value on the substrate to its value on the cross and calculations were performed on a 257x257 grid with $Tol = 10^{-4}$. The droplet, initially centred at $(x, y) = (0.5, 0.5)$, is given by the following initial parabolic profile,

$$h(r) = max\left(2\left(1 - \frac{128}{9}r^2\right), h^*\right) . \tag{5.3}$$

The contours of droplet thickness are shown in Figure 5.10 and display the behaviour reported by Schwartz and Eley (1998). Note that the definition of the problem implies that the plane defined by $y = x$ is a symmetry plane and the contours of droplet thickness confirm that the numerical results respect this symmetry.

The initially connected contact line recedes along the strips of the cross (Figure 5.10 (**b**)) and merges at the centre of the cross causing the formation of a first satellite droplet (Figures 5.10 (**c**) and 5.10 (**d**)). Because the droplet is initially positioned off-centre with respect to the cross and the proportion of liquid initially covering the bottom-left quadrant is the lowest, this first satellite droplet is small. Figure 5.10

(**d**) shows that after the break-up of the droplet, the strongly distorted contact line relaxes and moves rapidly towards the upper-right quadrant. In Figure 5.10 (**e**), the receding contact line splits the remaining droplet further into three satellite droplets, leading to the final configuration of four droplets one in each of the four quadrants delimited by the cross, Figure 5.10 (**f**). Interestingly, the liquid "pumped" from the cross because of the strong wettability contrast causes the maximum droplet thickness to increase in the upper-right quadrant (Figures 5.10 (**e**) and 5.10 (**f**)). Figure 5.11, showing the free surface at $t = 2.33 \times 10^{-3}$, illustrates very clearly the four satellite droplets separated by the cross of poorly wetting material.

After the breaking-up, each droplet carries on its motion independently and, as noted by Schwartz and Eley (1998) tends towards a more circular shape in order to reduce its surface tension energy. This is most clearly observed for the small droplet in the bottom-left quadrant. The associated free surface and disjoining pressure energies are plotted in Figure 5.12(**a**) and reveal three regions of steeper gradient corresponding, according to Schwartz and Eley (1998), to the rapid contraction of the contact line, followed by the separation of the first satellite droplet and the simultaneous separation of the other two droplets from the bulk. These rapid variation in total energy match precisely the local minima of the time step shown in Figure 5.12(**b**). Thus, each disconnection of a satellite droplet is associated with a decrease of the time step. This result supports further the idea that the adaptive time-stepping scheme suitably captures the physics by reducing the time step when rapid changes in the solution occur.

5.5 Large Bond Number spreading of an axisymmetric droplet

Comparison is now made between numerical predictions and corresponding analytical solutions for the case of axisymmetric spreading flow of a completely wetting droplet over a horizontal substrate when gravitational effects dominate over surface tension ones, so that the Bond number, Bo, is large. In this case the lubrication equations for the droplet thickness h can be reduced to the following second-order

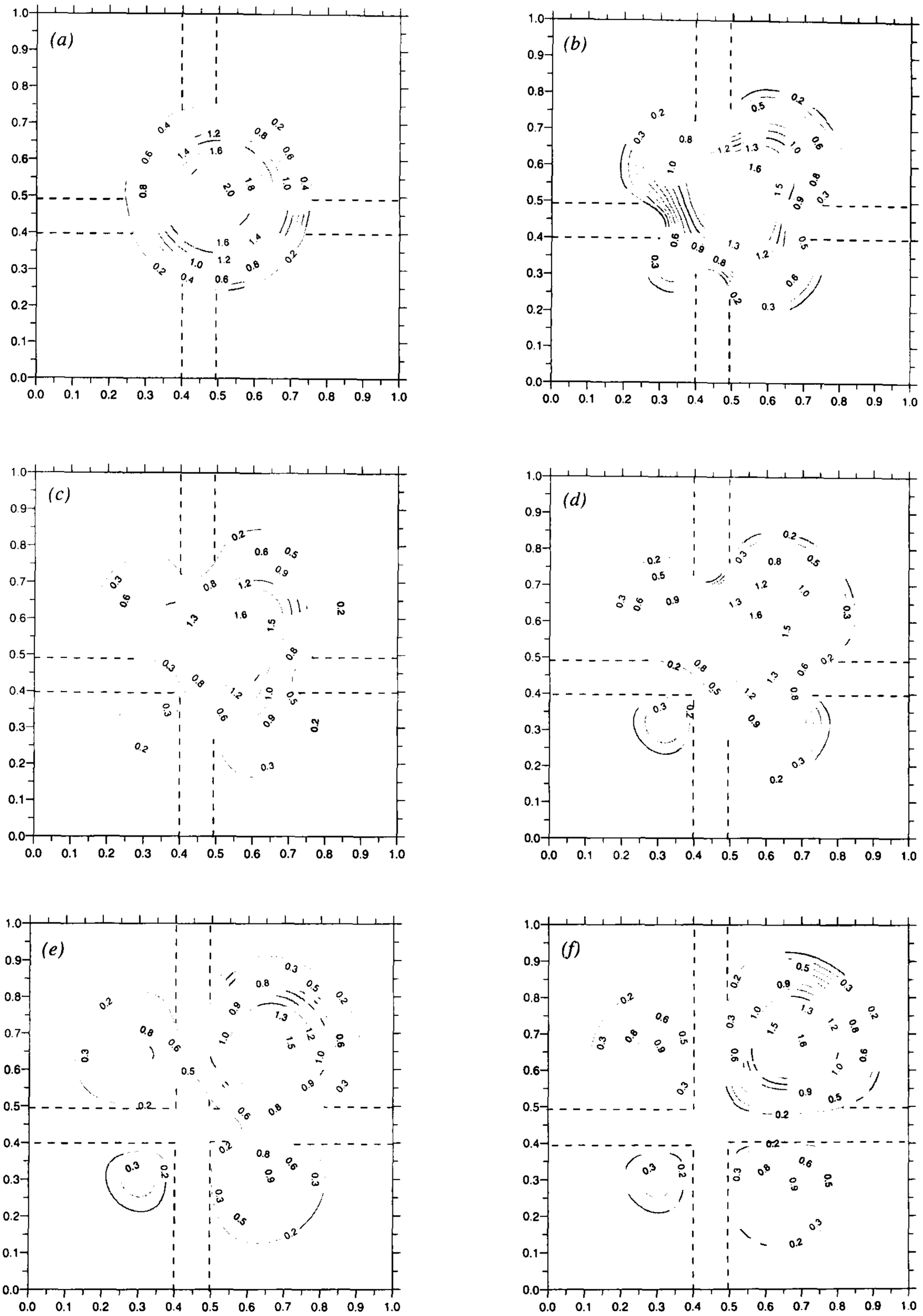

FIGURE 5.10: Contours of droplet thickness for the spreading of a droplet over a cross of poorly wetting material at different times: (**a**) t=4.8×10^{-6}, (**b**) t=6.5×10^{-4}, (**c**) t=1.25×10^{-3}, (**d**) t=1.3×10^{-3}, (**e**) t=2.17×10^{-3}, (**f**) t=2.33×10^{-3}.

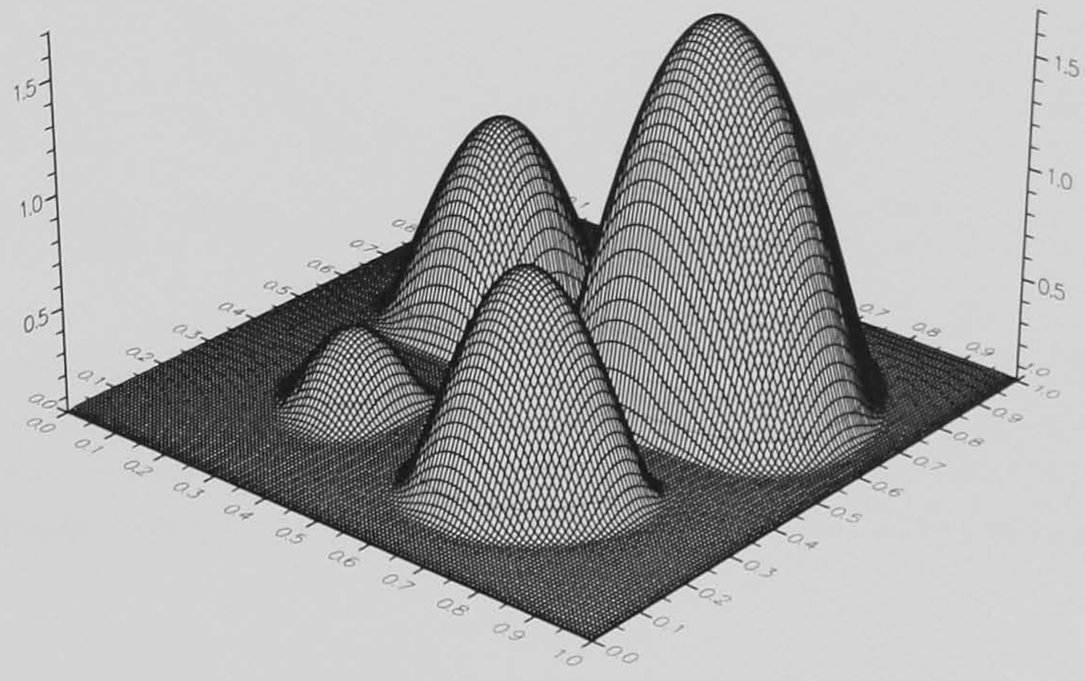

FIGURE 5.11: Free surface profile for the spreading of a droplet over a cross of poorly wetting material, at $t = 2.33 \times 10^{-3}$.

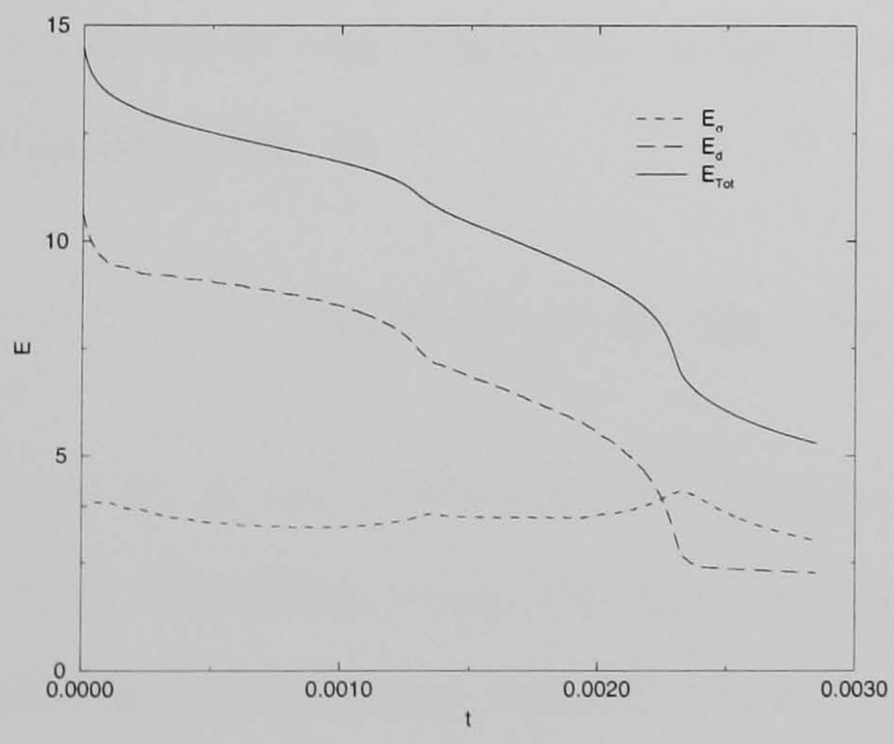

(**a**) Energy variation.

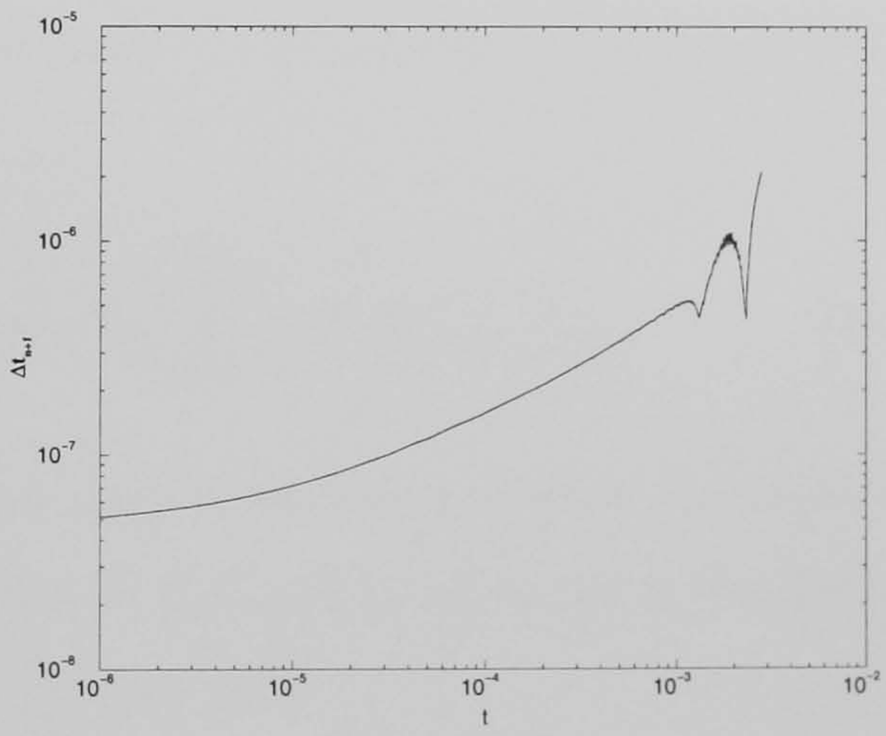

(**b**) Variation of the time step.

FIGURE 5.12: Energy and time step variation for the spreading of a droplet over a cross of poorly wetting material.

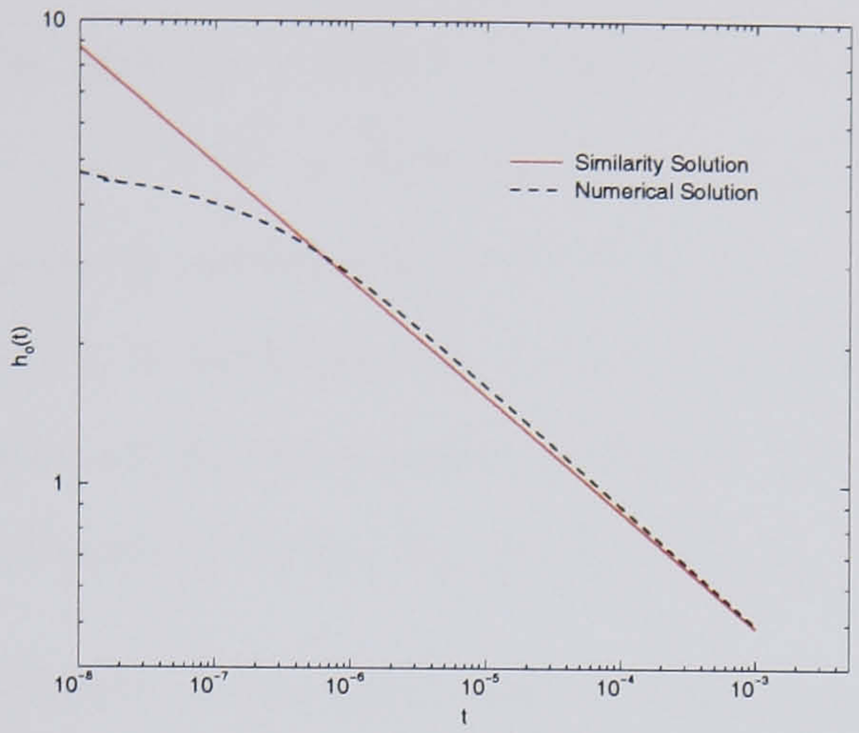

(**a**) Droplet thickness at the centre of a completely wetting droplet $h_0(t)$: comparison between the numerical predictions and the similarity solution (5.6).

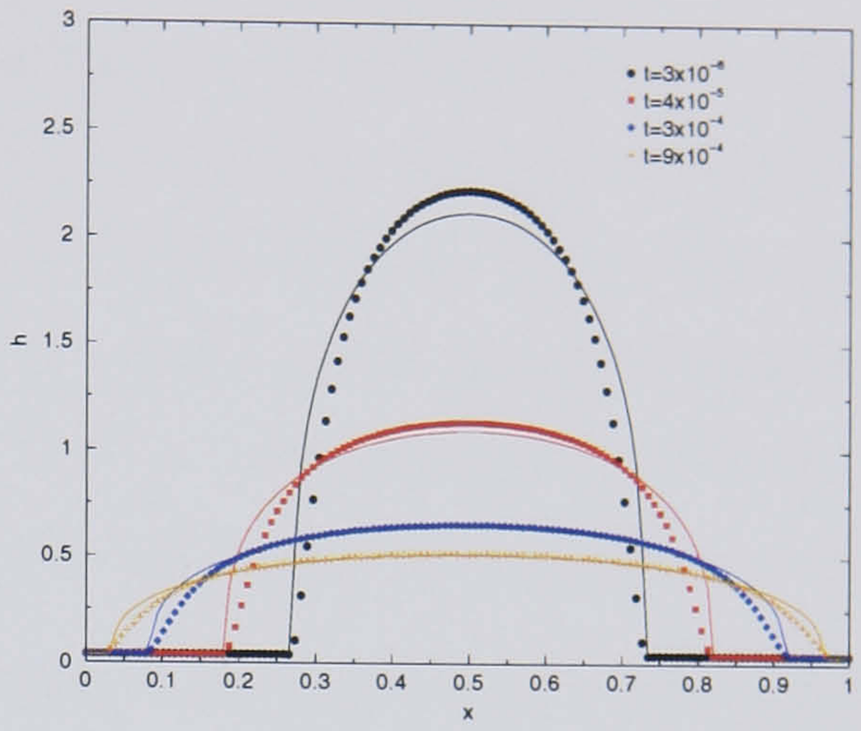

(**b**) Cross-sectional thickness profiles across a completely wetting droplet: comparison between numerical predictions (symbols) and the similarity solution (5.6).

FIGURE 5.13: Simulation parameters for (**a**), (**b**): $Bo = 1066$, $V_d = 0.261$, finest grid level equals 129x129 and $Tol = 2.5 \times 10^{-3}$

p.d.e. for axisymmetric flow

$$\frac{\partial h}{\partial t} = \frac{Bo}{3r}\frac{\partial}{\partial r}\left[rh^3\frac{\partial h}{\partial r}\right] , \tag{5.4}$$

in terms of r, the radial distance from the centre of the substrate $(x, y) = (0.5, 0.5)$.

The idealised case where the initial droplet profile is in the form of a Dirac delta function, given by

$$h(r, t = 0) \;=\; 0 \quad \text{for } r > 0 \text{ and } \; 2\,\pi \int_0^\infty \; rh \; dr \;=\; V_d, \tag{5.5}$$

where V_d is the volume of the droplet, has been analysed previously in Nakaya (1974). The latter study showed that equation (5.4) could be solved analytically by defining the similarity variable $\xi = r\left(\frac{3}{BoV_d{}^3 t}\right)^{\frac{1}{8}}$, to yield

$$h(\xi) = 0.753\left(\frac{V_d}{t\;Bo}\right)^{\frac{1}{4}}\left(0.799 - \xi^2\right)^{\frac{1}{3}} \; . \tag{5.6}$$

Figure 5.13(**a**) compares numerical predictions of the droplet thickness at its centre,

$h_0(t)$, as a function of time with the similarity solution (5.6) for the case $Bo = 1066$ and $V_d = 0.261$. The former are obtained on a 129x129 grid with $Tol = 2.5 \times 10^{-3}$, $h^* = 0.04$ and, since the droplet completely wets the substrate, the disjoining pressure term (2.45) is zero. The simulation uses the initial profile (2.36) since it is both sharply peaked and mimics, to some extent, the initial conditions in the analytical solution whilst at the same time guaranteeing that $h_0(t)$ changes substantially before the droplet flows out of the computational domain ($0 \leqslant r \leqslant \frac{\sqrt{2}}{2}$).

As expected, the agreement between the simulation and similarity solution is initially poor (for $t < 3 \times 10^{-7}$), due to the differences between the initial conditions in the two solutions, but improves at later times and eventually becomes very good beyond this initial phase where the maximum film thickness $h_0(t)$ decreases in proportion to $t^{-\frac{1}{4}}$ at later times. Similar agreement is also seen in Figure 5.13(**b**), which shows the development of the thickness profile across the droplet, where the agreement at later times is very good everywhere except near the contact line. The latter discrepancies are caused by the small, but non-zero, surface tension in the simulations which acts to reduce curvature in its vicinity.

5.6 Droplets spreading over topography

The remaining results concern examples of the flow of droplets over topographic features which have not been studied before. These results were obtained with the $\mathcal{PPS}$ (see §3.2) and the coarsest grid level G^0 is 17x17. Consider first the previous problem of axisymmetric flow of a completely wetting droplet at high Bond number extended to the case of a completely enveloped circular topography. It can be shown that the similarity solution (5.6) for the flow in the absence of a topography is only slightly modified by such a presence since the governing equation (5.4) simply becomes

$$\frac{\partial h}{\partial t} = \frac{Bo}{3r}\frac{\partial}{\partial r}\left[rh^3\frac{\partial(h+s)}{\partial r}\right], \tag{5.7}$$

where $s = s(r)$ is the topographic profile. Since $s(r)$ does not vary with time it is easy to show that the similarity solution with a topography is given by

$$h(\xi) = 0.753 \left(\frac{V_d}{t\ Bo} \right)^{\frac{1}{4}} \left(0.799 - \xi^2 \right)^{\frac{1}{3}} \ - \ s(r)\ , \tag{5.8}$$

where, once again, $\xi = r \left(\frac{3}{Bo {V_d}^3 t} \right)^{\frac{1}{8}}$.

The topography $s(r)$ is given by

$$s(r) \ = \ s_0 \ \left(\frac{T(r) \ - \ T(\frac{\sqrt{2}}{2})}{T(0) \ - \ T(\frac{\sqrt{2}}{2})} \right), \tag{5.9}$$

where s_0 is its height and, following Stillwagon and Larson (1988), $T(r)$ is an arctangent function

$$T(r) \ = \ tan^{-1} \left(\frac{\pi}{2\gamma} \ \left(1 - \frac{r}{r_t} \right) \right), \tag{5.10}$$

where the parameter γ controls the steepness of the topography and r_t is its radius.

Figure 5.14 shows a comparison between numerical predictions of the droplet thickness (h) profile across the film and the similarity solution (5.8) for the particular case of a topography with $s_0 = 0.2$, $\gamma = 0.2$ and $r_t = 0.1$, the former having been obtained with a finest grid level of 129x129, $Tol = 2.5 \times 10^{-3}$ and $h^* = 0.04$. As in the related case without a topography, results are obtained for the case $Bo = 1066$ and $V_d = 0.261$ while the droplet thickness profile (2.36) is modified so that the initial free surface profile is the same in both cases, i.e.

$$h + s = max \left(5 \left(1 - \frac{320}{9} r^2 \right), s(r) + h^* \right). \tag{5.11}$$

The figure shows similar behaviour to that reported in Figure 5.13(**b**) for the case without a topography.

Next, droplet spreading over substrates containing three-dimensional, rectangular topographies is explored. The extent of the topography is specified with respect to the reference point $(x_1, y_1) = \frac{(X_1, Y_1)}{L_0}$ as indicated in Figure 5.1. Following Peurrung and Graves (1993) the topography $s(x, y)$ is defined in terms of transformed co-

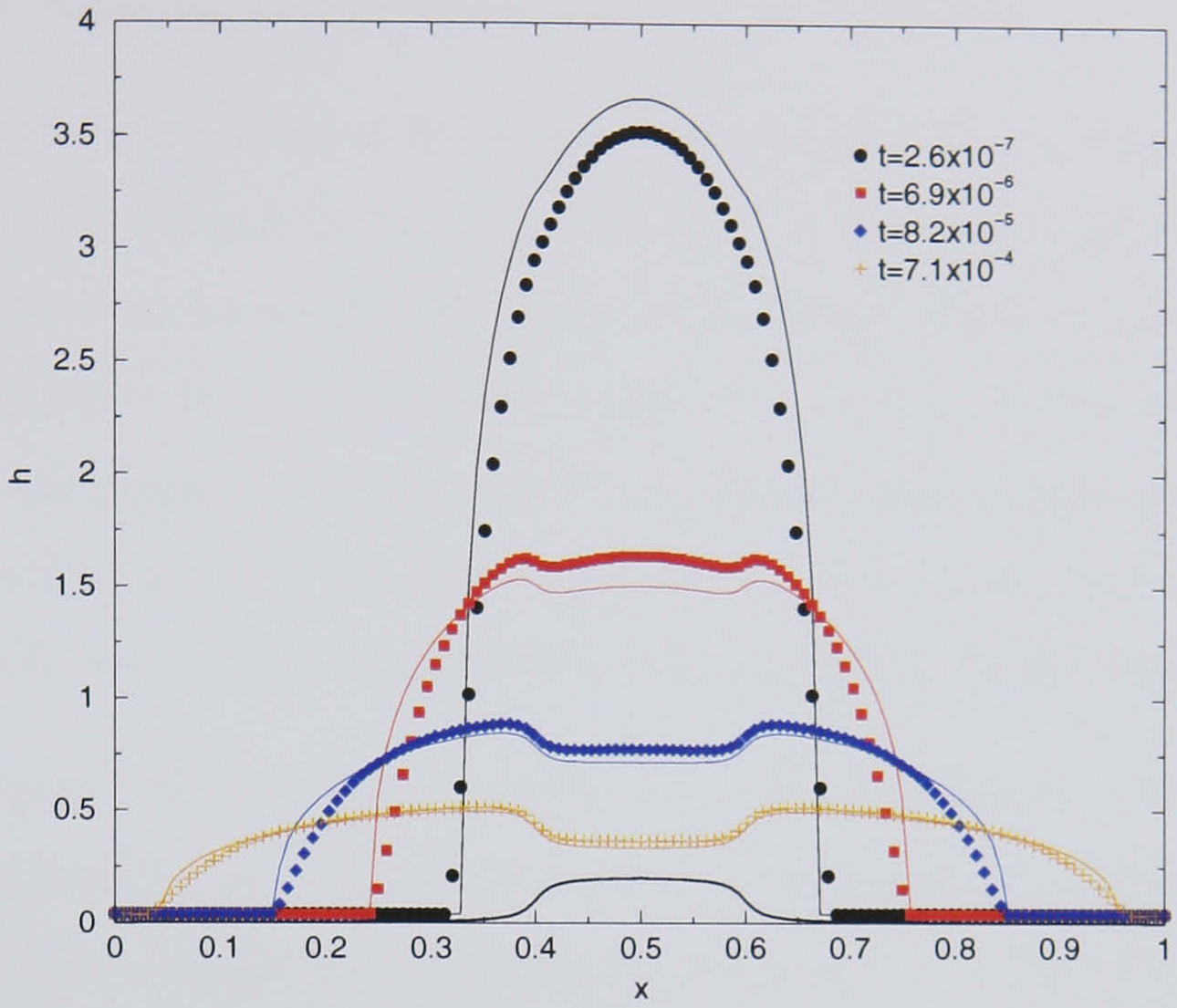

FIGURE 5.14: Cross-sectional thickness (h) profiles for a completely wetting droplet over a circular topography: comparison between numerical predictions (symbols) and the similarity solution (5.8).

ordinates, (x^*, y^*) say, with the origin at the centre of the topography and given by

$$x^* = x - x_1 - 0.5l_t;\ y^* = y - y_1 - 0.5w_t. \tag{5.12}$$

The topography $s(x, y)$ is taken as

$$s(x,y) = \frac{s_0}{b_0}\left(tan^{-1}\left(\frac{x^* - l_t/2}{l_t\gamma}\right) + tan^{-1}\left(\frac{-x^* - l_t/2}{l_t\gamma}\right)\right) \times \left(tan^{-1}\left(\frac{y^* - w_t/2}{l_t\gamma}\right) + tan^{-1}\left(\frac{-y^* - w_t/2}{l_t\gamma}\right)\right), \tag{5.13}$$

where γ controls its steepness and

$$b_0 = 4\tan^{-1}\left(\frac{1}{2\gamma}\right)\tan^{-1}\left(\frac{A}{2\gamma}\right). \tag{5.14}$$

In the results which follow the initial droplet profiles are of the same form as equation (2.36) but modified to take account of the three-dimensional topography, namely

$$h + s = max\left(5\left(1 - \frac{320}{9}r^2\right), s(x,y) + h^*\right), \tag{5.15}$$

where r is the radial distance from the centre of the substrate.

It is important to note that since the lubrication approximation is formally valid only for flows for which the free surface slope is small, its accuracy could be affected by the steep slopes of the topographies under consideration. However, previous studies that have compared the predictions of lubrication theory in such instances with experimental data and/or more detailed computations have shown that any failure of the lubrication theory is usually confined to small regions of the free surface: Peurrung and Graves (1993), Mazouchi and Homsy (2001), Gaskell *et al.* (2003(b)).

Figures 5.15 and 5.16 show the evolution of the free surface $(h + s)$ profiles and associated contours for the flow of a completely wetting droplet over a topographic peak ($s_0 = 0.5$) and trough ($s_0 = -0.5$) respectively with $l_t = 0.2$, $A = 1$, $(x_1, y_1) = (0.3, 0.3)$ and $\gamma = 0.01$. In the former case, the droplet spreads axisymmetrically until it meets the edge of the topography when it experiences an additional pressure gradient that causes it to spread preferentially from the topography to the substrate in a direction normal to the edge of the topography. Since the droplet meets the bottom left hand corner of the topography last of all, liquid in this region is the last to experience the additional pressure gradient, causing a small cusp in the contact line in this region. In the case of spreading over a trough, Figure 5.16, the edge of the topography presents an adverse pressure gradient which reduces the speed of contact line advancement across its edges and, since liquid near the bottom left hand corner is again the last to experience this adverse pressure gradient, the droplet swells slightly in its bottom left hand region.

Figures 5.17 and 5.18 show free surface profiles and associated contours for the flow of a droplet over a topography defined by $s_0 = 0.5$, $l_t = 0.5$, $A = 1$, $(x_1, y_1) = (0, 0)$ and $\gamma = 0.01$ where the wettability on the topography differs from that of the rest of the substrate. In the former case the liquid fully wets the substrate ($\Theta_0 = 0^o$) while only partially wetting the topography ($\Theta_0 = 11.5^o$). In Figure 5.17 it is evident that the droplet recedes from the topography in order to increase its contact angle towards the equilibrium value of 11.5^o whereas it advances on the substrate in order to lower its contact angle towards the equilibrium value of 0^o. Taken together these effects cause the droplet to flow off the topography, as shown in Figure 5.17(c).

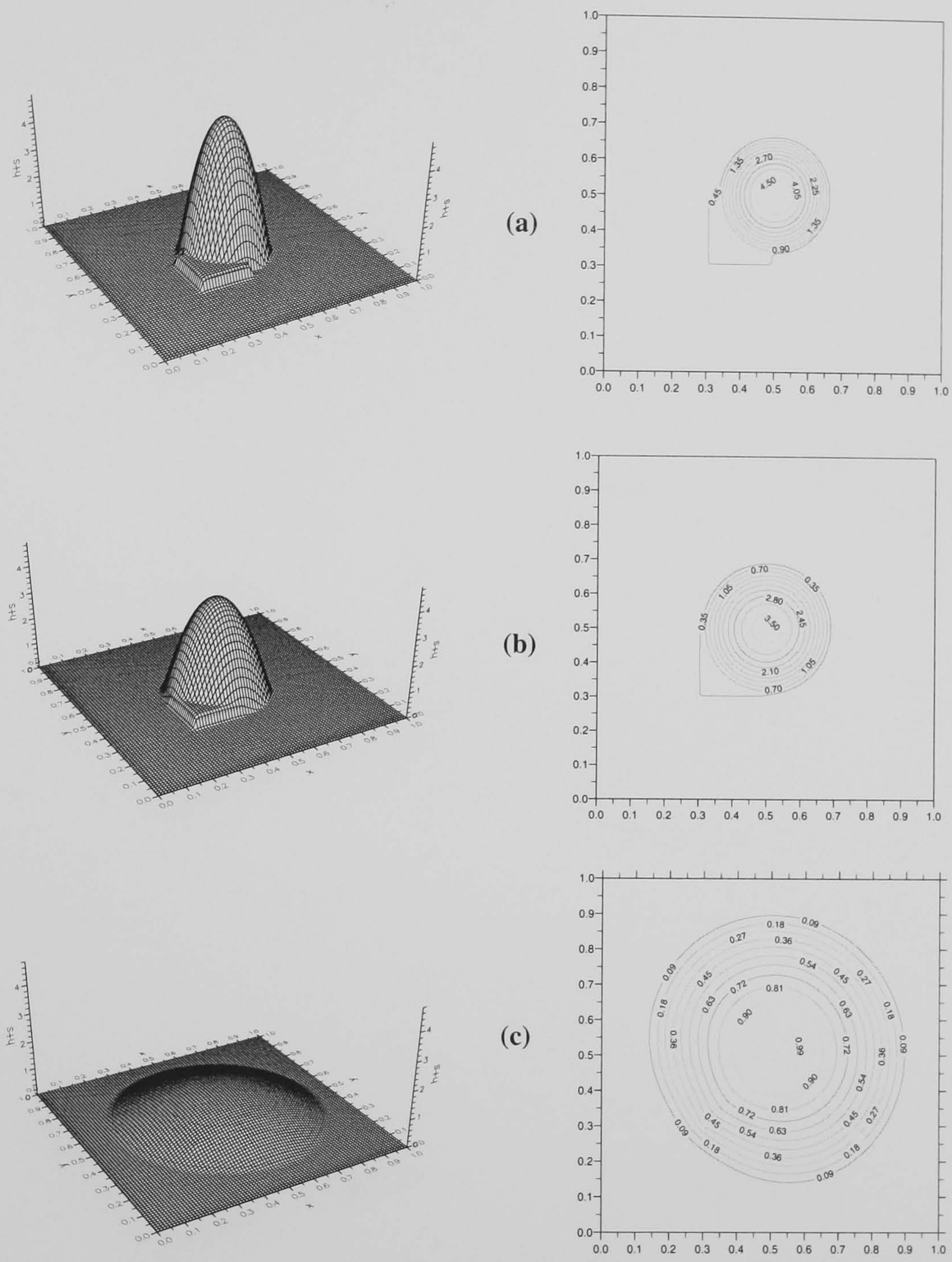

FIGURE 5.15: Free surface $(h+s)$ profiles (left) and associated contours (right) for a droplet spreading over a topographic peak with $s_0 = 0.5$, $l_t = 0.2$, $A = 1$, $(x_1, y_1) = (0.3, 0.3)$ and $\gamma = 0.01$: (a) $t = 3 \times 10^{-7}$, (b) $t = 1 \times 10^{-5}$, (c) $t = 1 \times 10^{-3}$. The density of the finest mesh is 257x257, $h^* = 0.02$ and $Tol = 10^{-4}$.

Figure 5.18 shows the effect of interchanging the wettabilities of the topography and substrate. In this case the contact line on the topography advances further across it so as to reduce the contact angle towards the equilibrium value of 0^o, while that on the substrate recedes, the net effect of which is to cause the droplet to flow up (climb) onto the topographic peak, Figure 5.18(c).

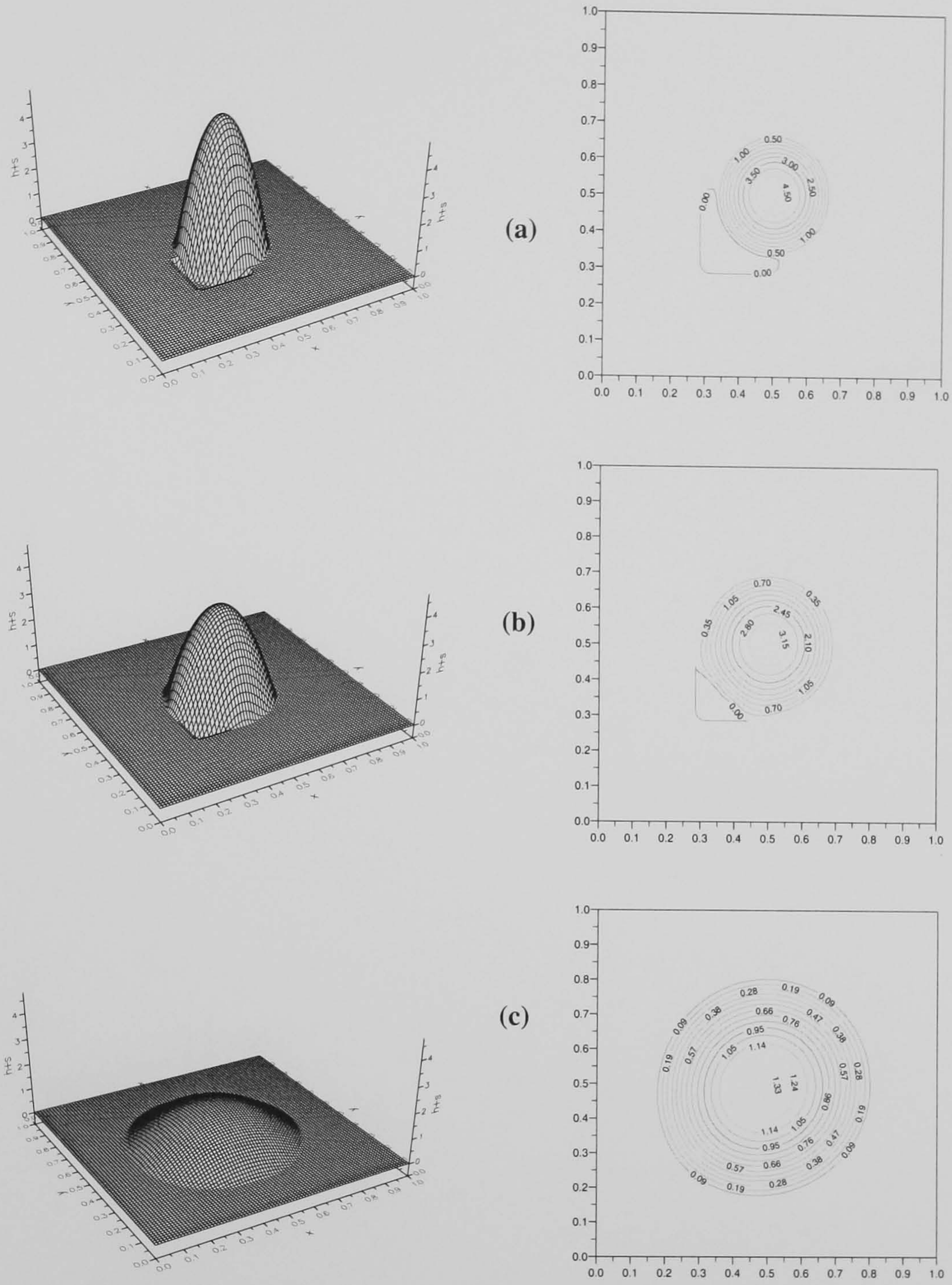

FIGURE 5.16: Free surface $(h+s)$ profiles (left) and associated contours (right) for a droplet spreading over a topographic trough with $s_0 = -0.5$, $l_t = 0.2$, $A = 1$, $(x_1, y_1) = (0.3, 0.3)$ and $\gamma = 0.01$: (a) $t = 3 \times 10^{-7}$, (b) $t = 1 \times 10^{-5}$, (c) $t = 1 \times 10^{-3}$. The density of the finest mesh is 257x257, $h^* = 0.02$ and $Tol = 10^{-4}$.

The final figure, Figure 5.19, considers the flow of a fully wetting droplet down a plane inclined at 28.6^o to the horizontal over a topographic peak defined by $s_0 = 0.5$, $l_t = 0.2$, $A = 1$, $(x_1, y_1) = (0.6, 0.4)$ and $\gamma = 0.01$. As expected, the gravitational force causes the droplet to spread over and eventually engulf the topography. The

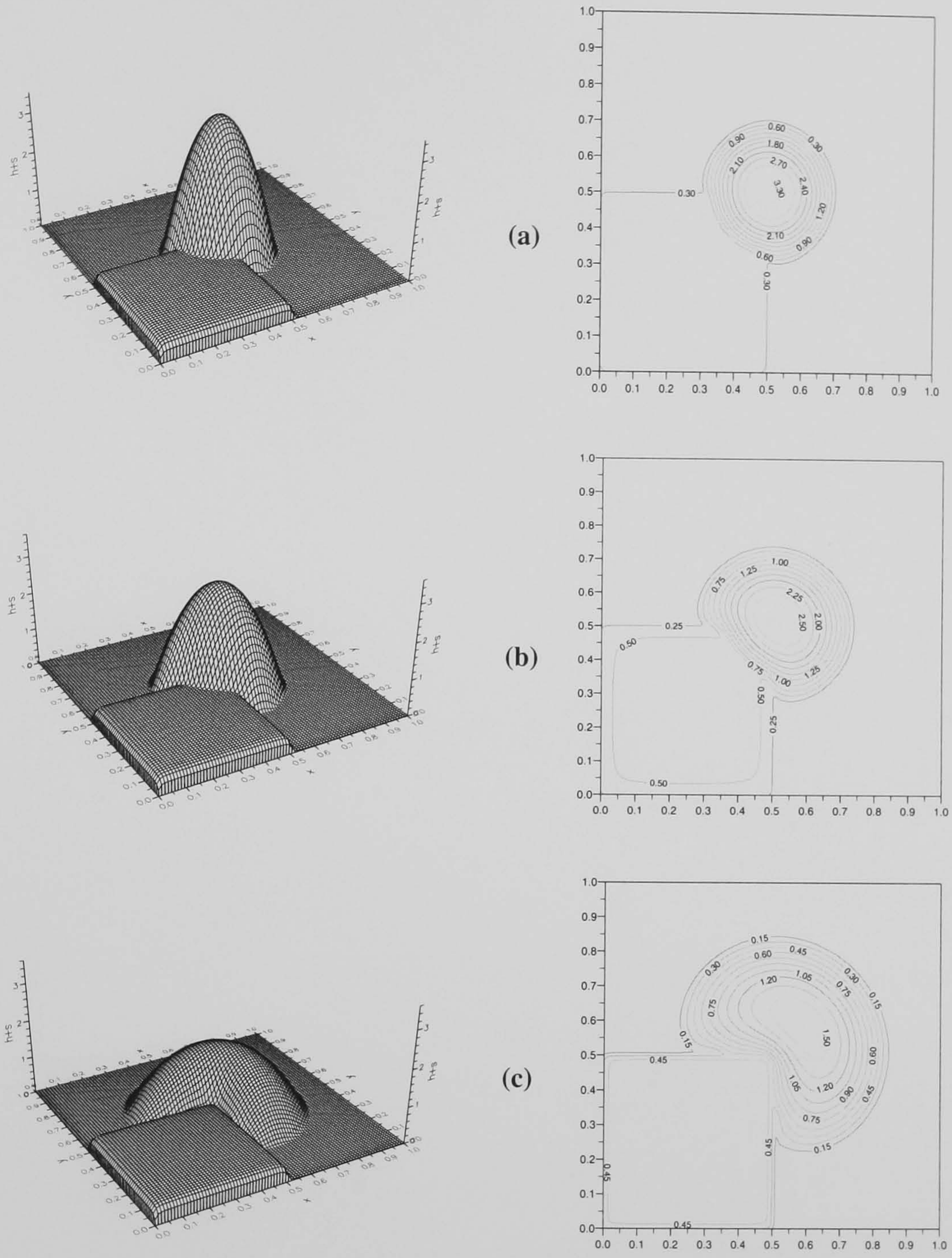

FIGURE 5.17: Free surface $(h+s)$ profiles (left) and associated contours (right) for a droplet spreading over a topographic peak with $d = 0.5$, $w = 0.5$, $A = 1$, $(x_1, y_1) = (0.0, 0.0)$ and $\gamma = 0.01$, with $\Theta_0 = 11.5^o$ on the topography and $\Theta_0 = 0^o$ on the rest of the substrate: (a) $t = 1.2 \times 10^{-5}$, (b) $t = 5 \times 10^{-5}$, (c) $t = 5 \times 10^{-4}$. The density of the finest mesh is 257x257, $h^* = 0.02$ and $Tol = 10^{-4}$.

results also show that the droplet spreads more quickly along the edges of the topography causing the contact line downstream of it to become heart-shaped, Figure 5.19(b). Indeed similar behaviour has been reported in recent experiments on gravity-driven flows over fully-submerged topographies by Decré and Baret (2003).

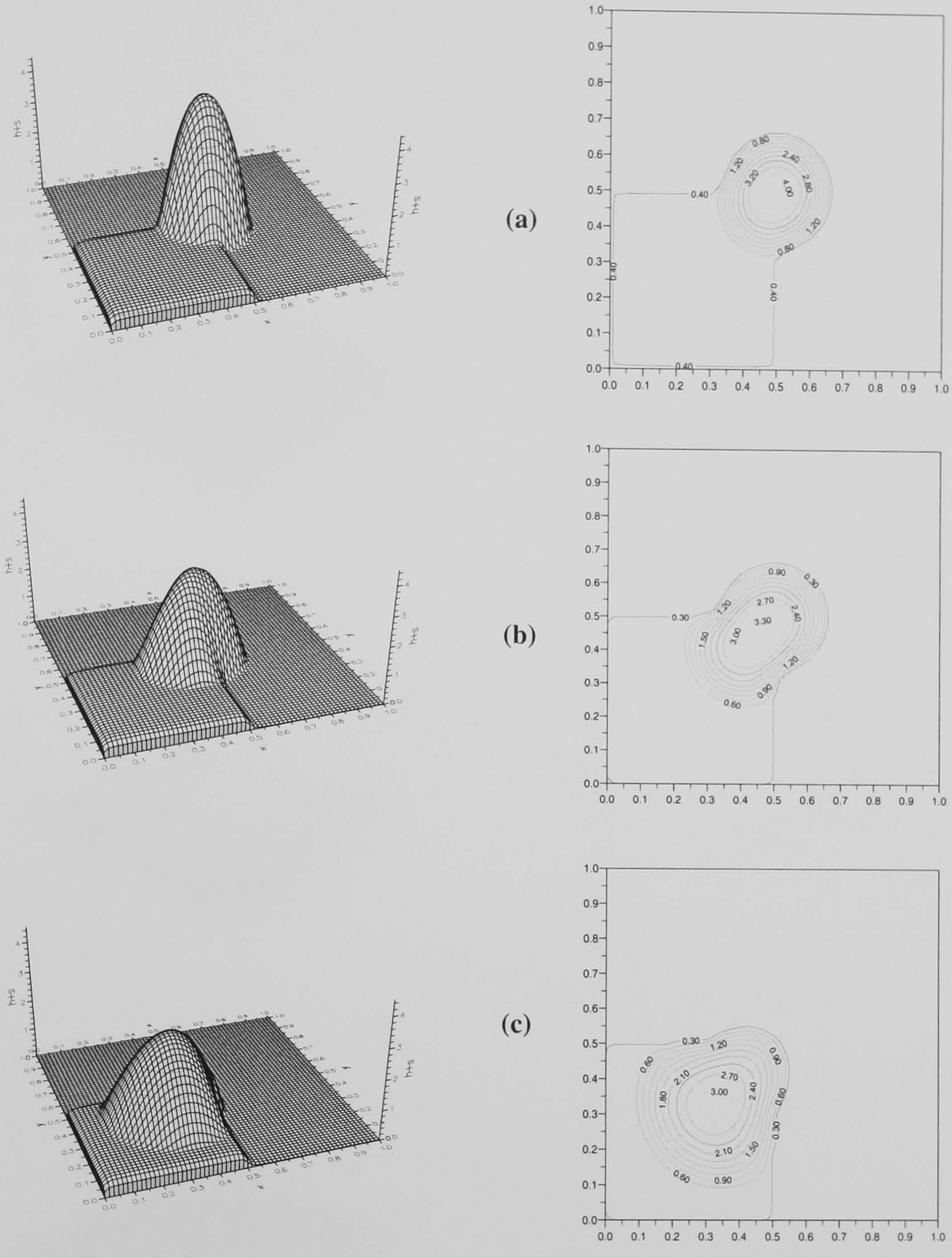

FIGURE 5.18: Free surface ($h+s$) profiles (left) and associated contours (right) for spreading of a droplet over a topographic peak with $s_0 = 0.5$, $l_t = 0.5$, $A = 1$, $(x_1, y_1) = (0.0, 0.0)$ and $\gamma = 0.01$, with $\Theta_0 = 0^o$ on the topography and $\Theta_0 = 11.5^o$ on the rest of the substrate: (a) $t = 1.2 \times 10^{-5}$, (b) $t = 1 \times 10^{-4}$, (c) $t = 5 \times 10^{-4}$. The density of the finest mesh is 257x257, $h^* = 0.02$ and $Tol = 10^{-4}$.

At later times the branches of the contact line behind the topography coalesce and form a straight contact line perpendicular to the direction of spreading, Figure 5.19(c).

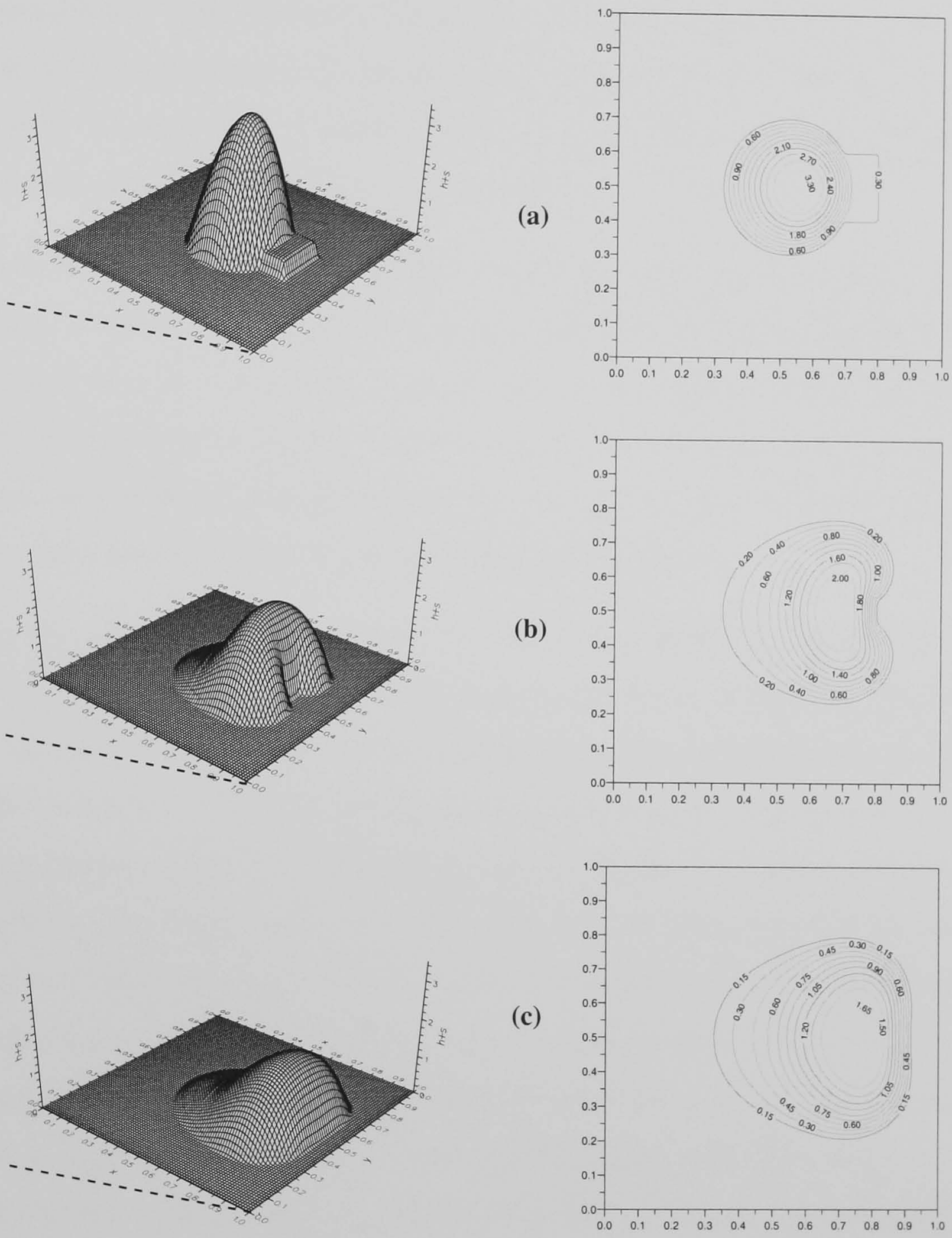

FIGURE 5.19: Free surface $(h + s)$ profiles (left) and associated contours (right) for the motion of a fully-wetting droplet, down a plane inclined at 28.6^o to the horizontal, over a topographic peak with $s_0 = 0.5$, $l_t = 0.2$, $A = 1$, $(x_1, y_1) = (0.6, 0.4)$ and $\gamma = 0.01$. Dotted lines indicate the inclination of the substrate with respect to the horizontal: (a) $t = 1.3 \times 10^{-5}$, (b) $t = 1.6 \times 10^{-4}$, (c) $t = 2.6 \times 10^{-4}$. The density of the finest mesh is 257x257 and $Tol = 10^{-4}$.

5.7 Concluding remarks

The numerical solution of the time-dependent lubrication equations for the case of droplet spreading is complicated by the need to overcome, in an efficient way, the severe restrictions encountered in relation to the use of permissible time increments consequent on two main factors: stiffness introduced by surface tension and the need to resolve short length scales close to wetting lines.

The answer here, has been to develop and employ an efficient, fully implicit, multigrid solver embodying adaptive time-stepping selection, the latter optimising the choice of time step in a controlled manner subject to a specified temporal error tolerance. A variety of previously reported analytical and numerical results, together with a series of new ones concerning the motion of droplets on heterogeneous substrates, have been used to validate successfully the approach.

Moreover, the present work found that the choice of spatial discretisation is important when simulating flows over topographies and, more specifically, that it is better to use the $\mathcal{PPS}$ scheme when the contact line moves perpendicular to a dry topographic boundary since the $\mathcal{SS}$ scheme may yield negative film thickness. For example, in Figures 5.15, 5.16 and 5.19 (but not in Figures 5.17 and 5.18) the $\mathcal{SS}$ scheme fails for this reason when the contact line tries to move over the dry topographic corners. The experience of the present work suggests that a possible reason for this behaviour could be due to the fact that in such instances the effective spatial resolution in the direction of motion of the contact line, $\Delta^{'}$ say, may be closer to a value of $\Delta^{'} = \Delta/\cos\delta$ where Δ is the actual spatial resolution and δ is the angle that the face of the topography makes with the horizontal. Consequently, as suggested by Bertozzi (1998), the effective spatial resolution for steep topographies with δ close to $\frac{\pi}{2}$ may be insufficient to prevent the occurrence of negative film thicknesses when the $\mathcal{SS}$ scheme is used. In light of the above, the present work suggests that the $\mathcal{PPS}$ scheme is preferable for flows over topographies since the additional computational overhead is negligible and no discernible differences with results from the $\mathcal{SS}$ scheme have been found for flows when the latter scheme is also effective.

The technological requirement for the simulation of flows past ever smaller topographic and wetting heterogeneities, and combinations of the same, makes the efficiency of such a numerical formulation extremely attractive, particularly where high resolution and hence fine meshes are essential. Firstly, time-step selection is efficient and enables the relatively small time steps required, for example, at the beginning of a simulation or when the flow is evolving quickly to be increased in a controlled and accurate manner when conditions permit. Second, the benefit of the multigrid solver is such that its fully implicit nature ensures that the larger time step estimates given by the adaptive time-stepping selection procedure can actually be used in practice, while also offering the attractive feature that the CPU time taken to solve the discretised equation set, at each time step, is simply 0(N) where N is the number of unknowns.

Chapter 6

Gravity-driven flow of continuous thin liquid films on substrates with topography

Contents

6.1 Introduction

The behaviour of thin liquid films, whether forced to spread or deposited as a distinct pattern on the surface of a non-porous substrate, is of enormous significance to many manufacturing processes. Much is known about the deposition of such films on flat homogeneous surfaces, see for example Kistler and Schweizer (1997), but considerable interest has been generated of late concerning the case of thin liquid films that are forced (gravitationally or centrifugally) to flow over, or encounter, surfaces containing topographical features. The latter may be regular and desired (patterned) or unwanted (a random scratch or speck of dust). Similarly, many manufactured products, particularly in the electronics sector (micro-devices, sensors, printed circuits, displays, etc.) usually involve the successive deposition of several thin liquid layers, combined with photolithography at each stage. Therefore, in the subsequent formation of the desired component/surface each layer is influenced by the one deposited and cured previously which, if non-uniform, presents the current wet layer with a surface that may lead to variations in coating thickness or even instabilities. Whatever the situation, increasing demands concerning quality and finish have promoted the need for better understanding of the mechanisms leading to free-surface non-uniformities and how to control/suppress the occurrence of their attendant undesirable defects.

Most previous investigations have concerned thin film flows over two-dimensional topography. Important early examples are the combined theoretical and experimental studies of Stillwagon and Larson (1987, 1988, 1990) and Pritchard *et al.* (1992) who considered radial outflow during spin coating and gravity driven flow down an inclined plane, respectively. Both sets of authors demonstrated lubrication theory to be surprisingly accurate for modelling purposes even for cases where it is not strictly valid. Stillwagon and Larson (1990) are credited with being the first to obtain a one-dimensional analytical expression for the free surface profile over a trench by solving a linearised form of the lubrication approximation. This analytical expression was in good agreement with experiment in the two cases for which the linearity assumption is valid. In the first case, the free surface remains almost

flat and in the second, the free surface conforms to the underlying substrate. Roy and Schwartz (1997) extended the one-dimensional lubrication approach to general curved substrates by expressing the problem in an orthogonal coordinate system that naturally fits the substrate but this approach is not applicable to steep edged topographies. Following a different tack, Decré *et al.* (1999) revisited the flow studied by Stillwagon and Larson (1990) and presented a Green's function formulation to the problem. The second order term contained therein has the effect of locating the capillary ridge further upstream of the topography, the deeper the trench becomes.

More recently, Kalliadasis *et al.* (2000) returned to the problem of the flow over a trench under the action of an external body force, solving the assumed governing one-dimensional long wavelength, or lubrication, approximation numerically as a means of analysing further the case of trench depths comparable with, or larger than, the associated unperturbed film thickness. Their results show that deep trenches produce an asymmetry, with the step down leading to a comparatively more pronounced capillary ridge than the step up. They also explored the effect of gravity, showing that it could result in the disappearance of capillary ridges. The stability of the latter was considered in a subsequent article, Kalliadasis and Homsy (2001). The picture was essentially completed by Mazouchi and Homsy (2001) who solved the corresponding Stokes problem numerically using a boundary element method and compared the results with those obtained using lubrication theory. They demonstrated the importance of the capillary number, Ca, and in particular that increasing it leads to a diminution or flattening of the capillary ridge, with the free-surface correspondingly conforming more to the topography of the substrate.

Not surprisingly, flow over three-dimensional topography has received considerably less attention both experimentally and theoretically, each representing a significant challenge in its own right. The work of Pozrikidis and Thoroddsen (1991) is an early and important contribution in this respect for the case of gravity driven flow of full liquid films over a particle-like topography. Using a boundary element formulation to solve the governing Stokes equations numerically they showed even a small particle to result in a significant upstream and downstream disturbance to the free-surface profile of the film, in qualitative agreement with the one-dimensional cases

cited above. That is, a standing "bow wave" capillary ridge upstream of the particle together with an exponentially decaying, "horseshoe"-shaped capillary wake downstream. Other work of note is that of Peurrung and Graves (1991, 1993) for the case of spin coating over topography. Their experimental and numerical results are found to be in qualitative agreement. Hayes *et al.* (2000) formulated a Green's function for the linearised two-dimensional lubrication equations for the flow over a shallow topography which allowed the surface responses to arbitrary finite topographies to be calculated.

The motivation for the work presented in this chapter is provided by the recently reported painstaking quantitative experimental results of Decré and Baret (2003) for the case of gravity driven flow of thin water films over topography. Building on earlier work (Messé and Decré (1997); Decré *et al.* (1998, 1999); Lucéa *et al.* (1999)), they used phase-stepped interferometry to obtain detailed free-surface maps for thin films of water flowing down an inclined plate containing a range of topographies. In all cases, results compare well with those of earlier studies and, in the case of flow over three-dimensional topography, with the results of Hayes *et al.* (2000) for the linearised problem. A consequence of the latter is that linear superposition may be used to construct an approximate free surface response to a complex topography from knowledge of the responses to regular elementary topographies.

6.2 Problem specification and mathematical formulation

The case of flow of a continuous film of liquid, flux Q_0, over a plane surface (lateral extent L and span width W) inclined at an angle α to the horizontal arises as part of many manufacturing processes, with the case of flow over a smooth homogeneous surface being surely now recognised as a classical problem in fluid mechanics.

In the problems of interest here, the inclined substrate contains well-defined topographical features of amplitude S_0 and form $S(X,Y)$, with lateral extent L_T and span width W_T, centred at (X_T, Y_T). These features may completely span the do-

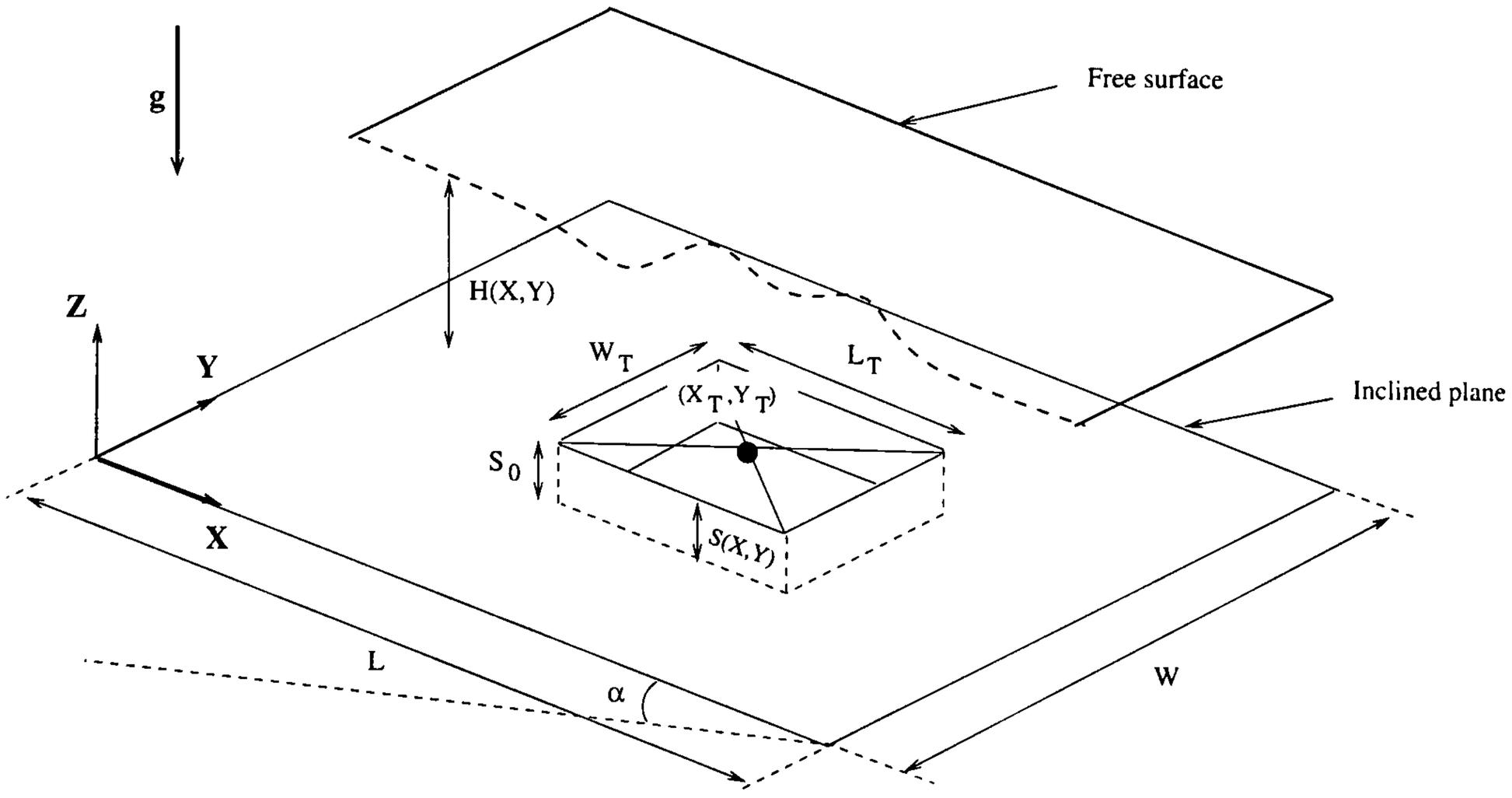

FIGURE 6.1: Schematic diagram of a three-dimensional thin film flowing over a substrate inclined at angle α to the horizontal, showing the coordinate system and parameters defining the topography.

main (in which case $W_T = W$ and $L_T \ll L$, leading to two-dimensional flow), or be localised (i.e. $W_T \ll W$ and $L_T \ll L$, giving three-dimensional flow). The former problem reduces conveniently to solving for the flow in a streamwise cross-sectional plane only, provided W_T is sufficiently large for end effects to be negligible. In both cases the topography may be a protrusion ($S_0 > 0$) or a depression ($S_0 < 0$) as sketched in Figure 6.1. These will often be referred to as "peaks" and "trenches" respectively.

6.2.1 Full-width topography

The associated two-dimensional flow is analysed by solving the steady-state counterpart of the Navier-Stokes and continuity equations (eqs. (2.1) and (2.2)) numerically, Gaskell *et al.* (2003(b)), and solutions are compared against both theoretical and experimental results of other authors, and also those obtained from solving the corresponding lubrication formulation discussed in §2.3. Apart from generating new results, this analysis is fundamental to determining the validity of the lubrication approximation as a suitable means of solving three-dimensional flow over localised steep-sided topography. Throughout this chapter, the numerical solutions to the

Navier-Stokes equations, used for comparison purposes, were performed and kindly provided by Dr M. Wilson but for completeness, the governing equations and boundary conditions are reported here.

Scaling velocities, axial coordinates and pressure with respect to U_0, H_0 as defined in §2.3 for gravity driven thin films and $\mu U_0/H_0$ respectively, and noting the absence of any Y dependence, allows equations (2.1) and (2.2) to rewritten in the form:

$$Re\,\underline{u}.\nabla\underline{u} = \nabla.\tau + St\,\underline{\hat{g}}, \tag{6.1}$$

$$\nabla.\underline{u} = 0, \tag{6.2}$$

where $\underline{u} = (u, w)$ is the non-dimensional velocity in the dimensionless $x - z$ plane, $Re = \rho U_0 H_0/\mu = 3\rho Q_0/2\mu$ is the Reynolds number, $\tau = -p\boldsymbol{I} + \nabla\underline{u} + (\nabla\underline{u})^T$ is the non-dimensional Newtonian stress tensor, and $St = \rho g H_0^2/\mu U_0 = 2/\sin\alpha$ is the Stokes number.

The boundary conditions which close the problem are shown in Figure 6.2. On the substrate the no-slip condition $u = w = 0$ is applied and at the inflow and outflow planes a fully-developed velocity profile is assumed:

$$u = \tfrac{1}{2} St \sin\alpha(2z - z^2),\ w = 0. \tag{6.3}$$

On the free surface the usual stress and kinematic conditions are imposed along with the condition that the dimensionless film thickness is equal to one, i.e the fully-developed thickness, at each end of the domain.

Full-width topographies only depends on the streamwise coordinate x. When solving the lubrication approximation, they are defined by means of a cubic function, bridging two regions of the substrate of different height, as follows,

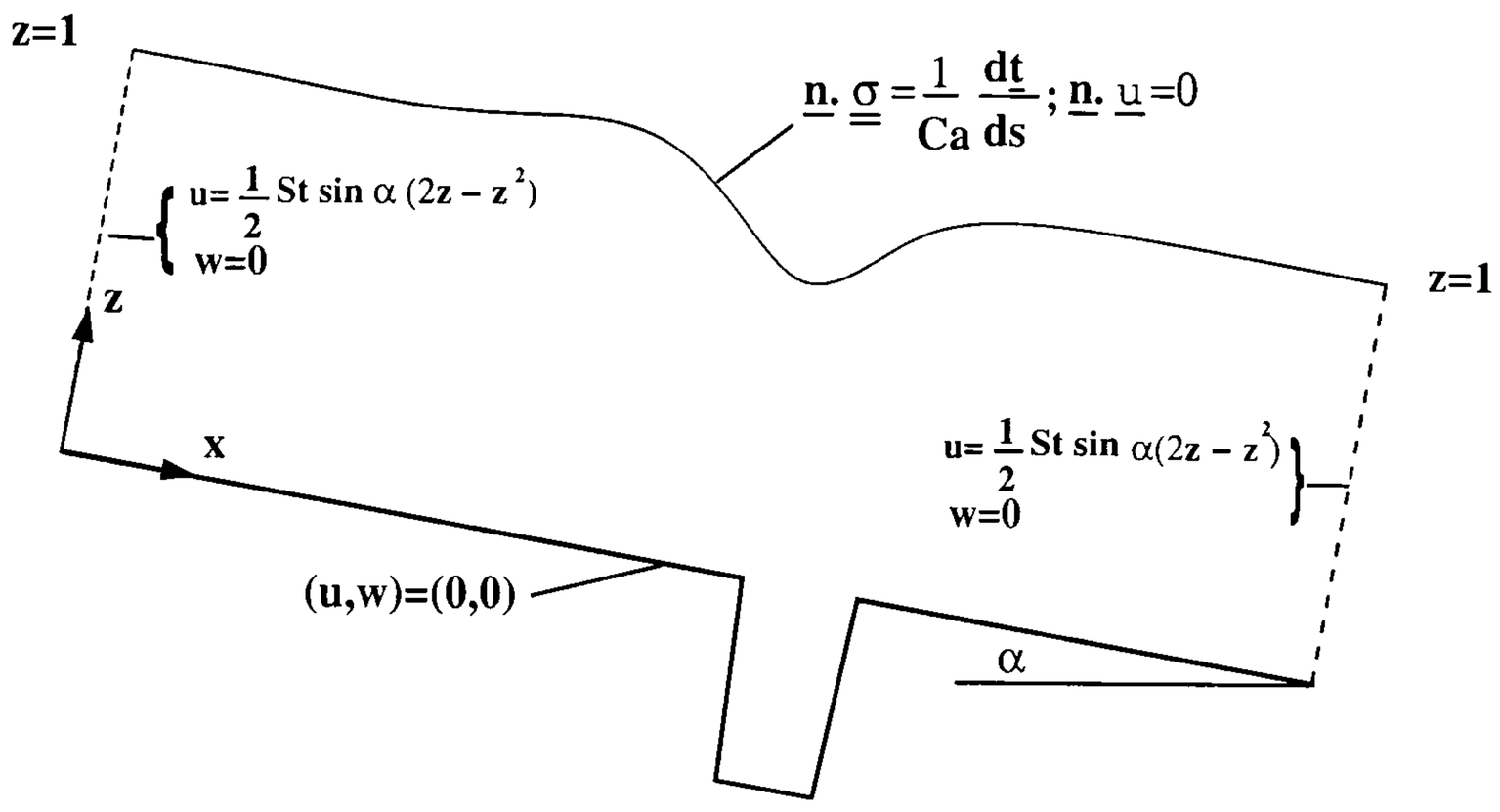

FIGURE 6.2: Schematic diagram showing the boundary conditions for finite element analysis of flow over a one-dimensional (span-wise) topography.

$$
\begin{aligned}
s(x) &= 0 \quad \text{for} \quad x < x_t - \frac{\gamma}{2}\,, \\
s(x) &= s_0 \left[-2 \left(\frac{x - (x_t - \frac{\gamma}{2})}{\gamma} \right)^3 + 3 \left(\frac{x - (x_t - \frac{\gamma}{2})}{\gamma} \right)^2 \right] \\
&\qquad \text{for} \quad x_t - \frac{\gamma}{2} < x < x_t + \frac{\gamma}{2}\,, \\
s(x) &= s_0 \quad \text{for} \quad x > x_t + \frac{\gamma}{2}\,,
\end{aligned}
\tag{6.4}
$$

where x_t is the streamwise coordinate of the topography and γ controls the steepness of the topography. The form of (6.4) ensures that the substrate function, $s(x)$, is never multivalued and approximates sharp edges in the limit of $\gamma \to 0$. Expression (6.4) defines a step-up or a step-down topography and trenches or peaks are simply defined as a combination of both.

In the framework of the Navier-Stokes equations, the definition of the substrate function is no longer an issue and therefore topographies are completely sharp. i.e. corners are perfect right angles.

6.2.2 Localised topography

Three-dimensional steady flow over localised topography is analysed using the lubrication approximation derived in §2.3 with the values of C_1, C_2, C_3 and C_4 corresponding to the gravity driven thin liquid film. Localised topography, $s(x, y)$, is defined via arctangent functions (eqs. (5.13) and (5.14)), enabling the steepness of the topography sides to be controlled easily. For comparison purposes later it is convenient to define a coordinate system $(x^*, y^*) = \beta(x - x_t, y - y_t)$ whose origin is at the centre, (x_t, y_t), of the topography and for which the norm of the unit vectors is the capillary length since $L_0 = \beta L_c$. Another coordinate system, (x^+, y^+), is used in this chapter whose origin is the same as the one for the (x, y) coordinate system but for which the norm of the unit vectors is the capillary length, i.e. $(x^+, y^+) = \beta(x, y)$. For clarity, the different coordinate systems are shown on Figure 6.3.

Moreover, to allow comparison with Decré and Baret (2003), $h^*(x^*, y^*) = [h(x^*, y^*) + s(x^*, y^*) - 1]/s_0$ is defined so that the free surface is represented in terms of the variations with respect to the asymptotic film thickness scaled with respect to the topography height. It follows that, if the absolute value of h^* is greater than 1, it means that the free surface variation is greater than the height of the topography.

6.3 Method of solution

6.3.1 Finite element formulation

The finite element (FE) method, Wilson (2003), used to solve equations (6.1) and (6.2) in two dimensions subject to the given boundary conditions is described briefly for completeness. It employs a Bubnov-Galerkin weighted residual formulation that has been applied successfully to a wide variety of incompressible flow problems. The free surface of the film is parametrised by a "spinal" algebraic mesh generation algorithm, Kistler and Scriven (1983), and the two-dimensional flow domain is tessellated using V6/P3 triangular elements (Gaskell *et al.* (1995); Summers *et al.* (2004)) giving a piecewise quadratic velocity field and a piecewise linear pressure

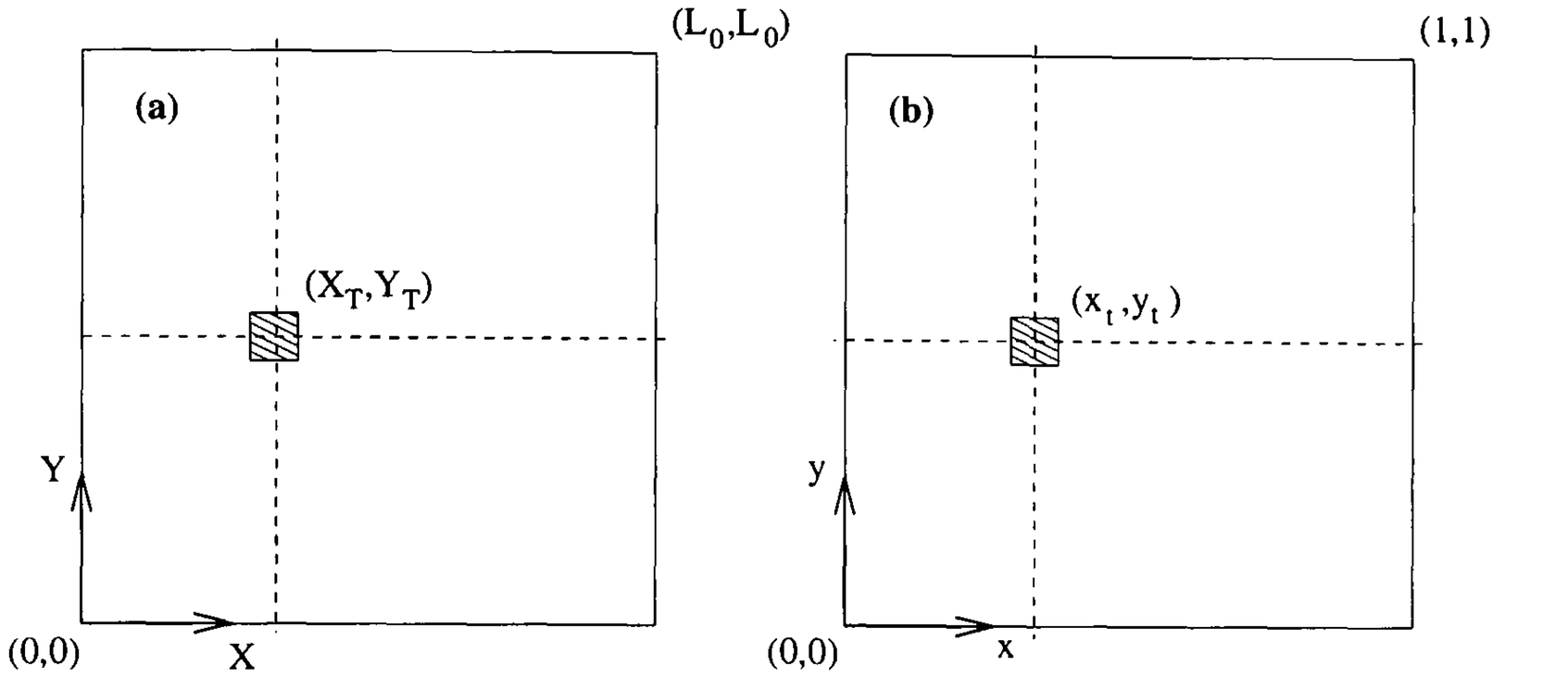

FIGURE 6.3: Square solution domain of lateral extent $L_0 = 100L_c$ with a topography (filled square) in different coordinate systems: (**a**) (X, Y), physical; (**b**) (x, y), dimensionless (computational domain) in units of L_0; (**c**) (x^*, y^*), dimensionless and centred on the topography in units of L_c; (**d**) (x^+, y^+), dimensionless in units of L_c.

field. The free surface kinematic condition $\underline{n}.\underline{u} = 0$ ($\underline{n}$ is the normal to the free surface) is used to determine the free surface location while the free surface stress conditions enter the FE formulation via a boundary integral arising in the weak form of equation (6.1) - see Kistler and Scriven (1983) for further details.

The nonlinear weighted residual equations are solved, Wilson (2003), using Newton iteration coupled to a Frontal algorithm (Hood (1976)) and is ideally suited to the long, thin nature of the computational domain. Since the film profiles are of primary interest, the accuracy of these was used as the main criterion in establishing the minimum density and extent of the computational mesh. The number of elements in the mesh was systematically doubled until the maximum change in the film profiles on consecutive meshes was less than 0.05% when measured in the way described in §6.4.1. For each mesh the locations of the inflow and outflow boundaries were checked to confirm that they had a negligible effect on the solution. The step up/down and trench problem utilised 5650 and 5900 elements, respectively; in each case 701 spines were used to parametrise the free surface position. For the Ca values used in the simulations, a computational domain extending 150 film-thicknesses upstream of the topography and 100 downstream was found to be sufficient.

6.3.2 Modifications to the multigrid algorithm

In contrast to the droplet spreading flows explored in the previous chapter, the problems of interest here are steady-state. In spite of this, for centrifugally-driven films, Stillwagon and Larson (1990) found it more convenient to obtain the quasisteady solution by integrating the time-dependent lubrication equation to steady-state using explicit time integration. A probable reason for this choice is that the effect of the nonlinearity is not as severe as in the steady-state case since at each time step, the quality of the initial guess provided by the solution at the previous time step is much better. In this work, solving the steady-state counterpart of eqs. (2.29) and (2.30) was found to be a lot less time consuming than using time marching, particularly for the mesh densities adopted. The equivalence of both approaches is illustrated in Figure 6.4 for the flow over a trench considered in §6.4.1. Starting from a flat free surface, the time-dependent solution converges exactly towards

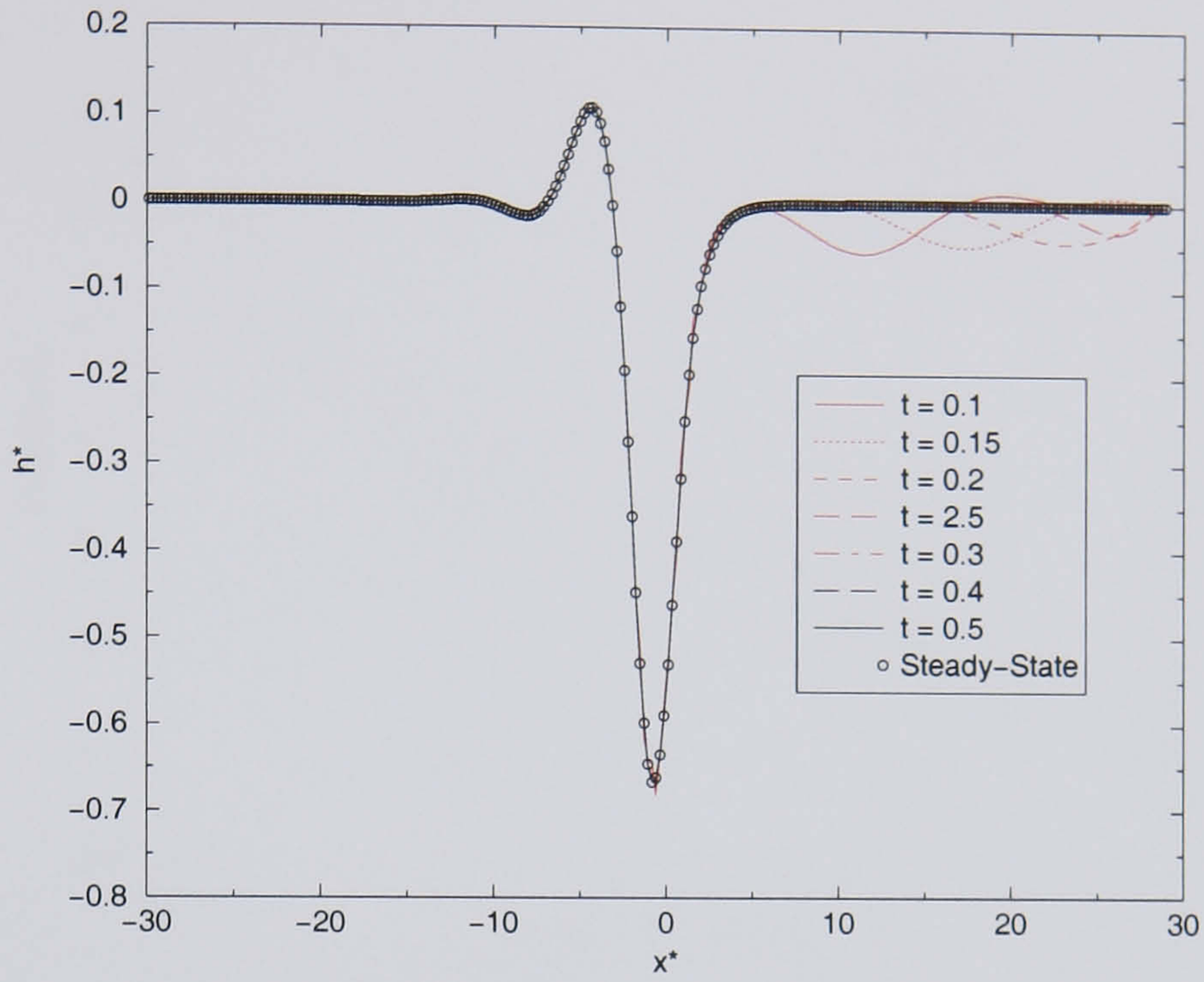

FIGURE 6.4: Free surface profile for flow over a one-dimensional trench, demonstrating the progression of the transient solution towards the solution of the steady-state equation.

the steady-state solution for large time. Interestingly, the time-dependent solution reveals that the topography sheds a wave which propagates downstream.

For two-dimensional flows, uniform 257x257 meshes were used. Beyond this mesh density, no distinction in the free surface profiles could be made. For three-dimensional flows, unless otherwise stated, the numerical solutions presented in this chapter were obtained on a uniform 1025x1025 mesh and the computational domain covers 100 capillary lengths in each direction. This choice of computational domain ensures that the mesh resolution is sufficient in the topography region and that the free surface relaxes to its undisturbed shape downstream of the topography. A total of approximately 15 V-cycles were found to be necessary to reduce residuals to within the spatial discretisation error, 10^{-6}. The number of required V-cycles is significantly larger than in the time-dependent case but as discussed above this is likely to be due to the lack of a good initial guess of the solution. The convergence history of solutions for the flow over a trench considered in §6.4.1 is shown on Figure 6.5 for various mesh densities. For all but the finest mesh density (1025x1025), the plot confirms the expected trend that the convergence rate is independent of the mesh density. For the 1025x1025 grid, the convergence rate displays a slight degradation.

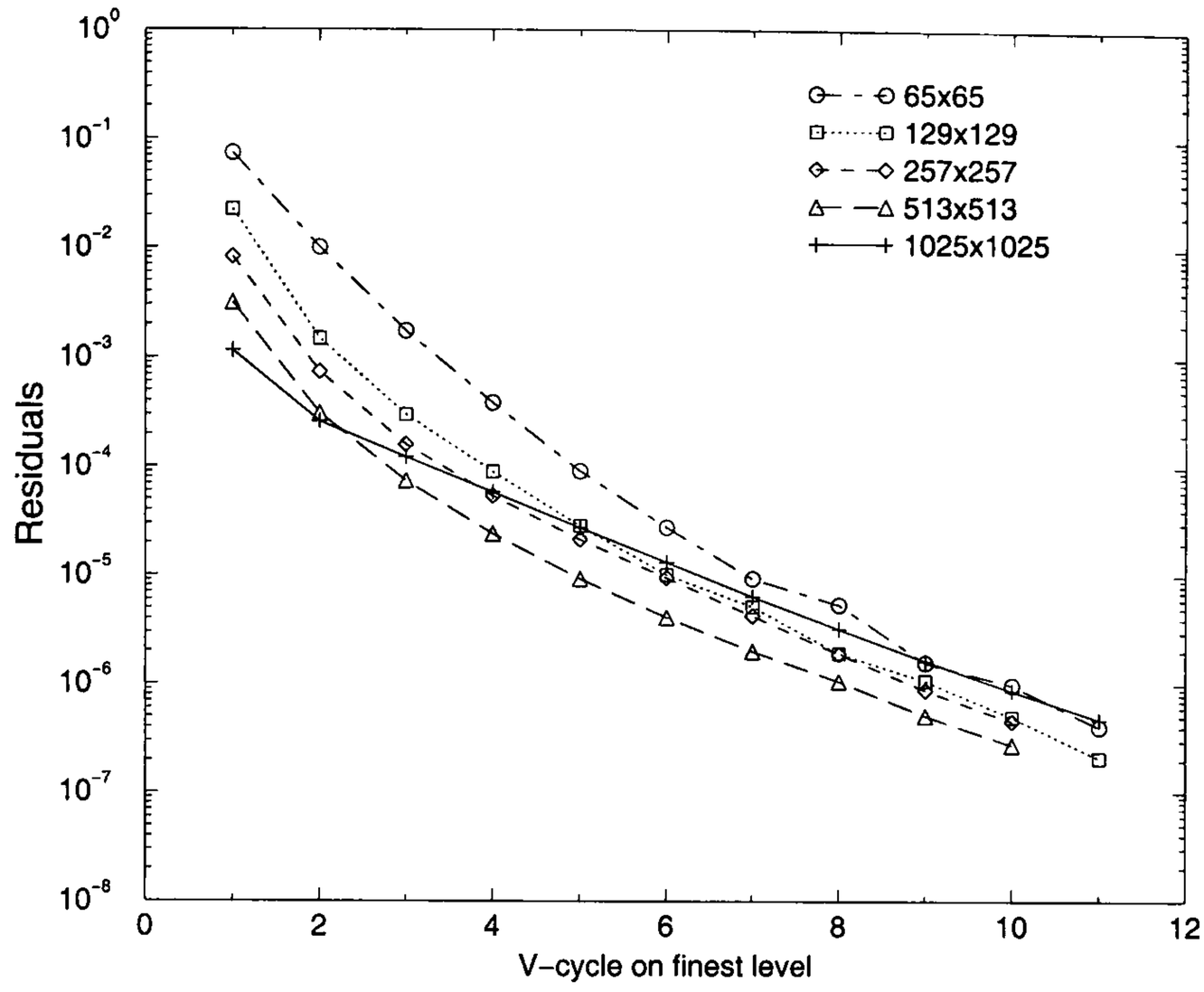

FIGURE 6.5: Convergence history of solutions for the flow over a trench considered in §6.4.1 for various mesh densities.

However, the efficiency loss is negligible in that case since no additional V-cycle is required to achieve the desired reduction in residuals compared to solutions obtained on coarser meshes. The avoidance of negative film thicknesses was not found to be an issue for the flows investigated here and therefore, the Standard Scheme was used to calculate the prefactors, equation (3.3).

6.4 Results and discussion

6.4.1 Flow over full-width spanwise topographies

First, in order to validate the FE method, comparisons are made with the theoretical predictions of Mazouchi and Homsy (2001) who used the boundary element (BE) method to study the Stokes flow of a thin liquid film over a one-dimensional trench. In fact, the trench was wide enough to ensure that the flow could be considered as that over a step down topography followed by flow over an effectively independent step up. In this case the substrate was vertical, i.e. $\alpha = 90°$. Figure 6.6 compares Mazouchi and Homsy's computed free surface profile, for $Ca = 0.005$ and 0.05, with

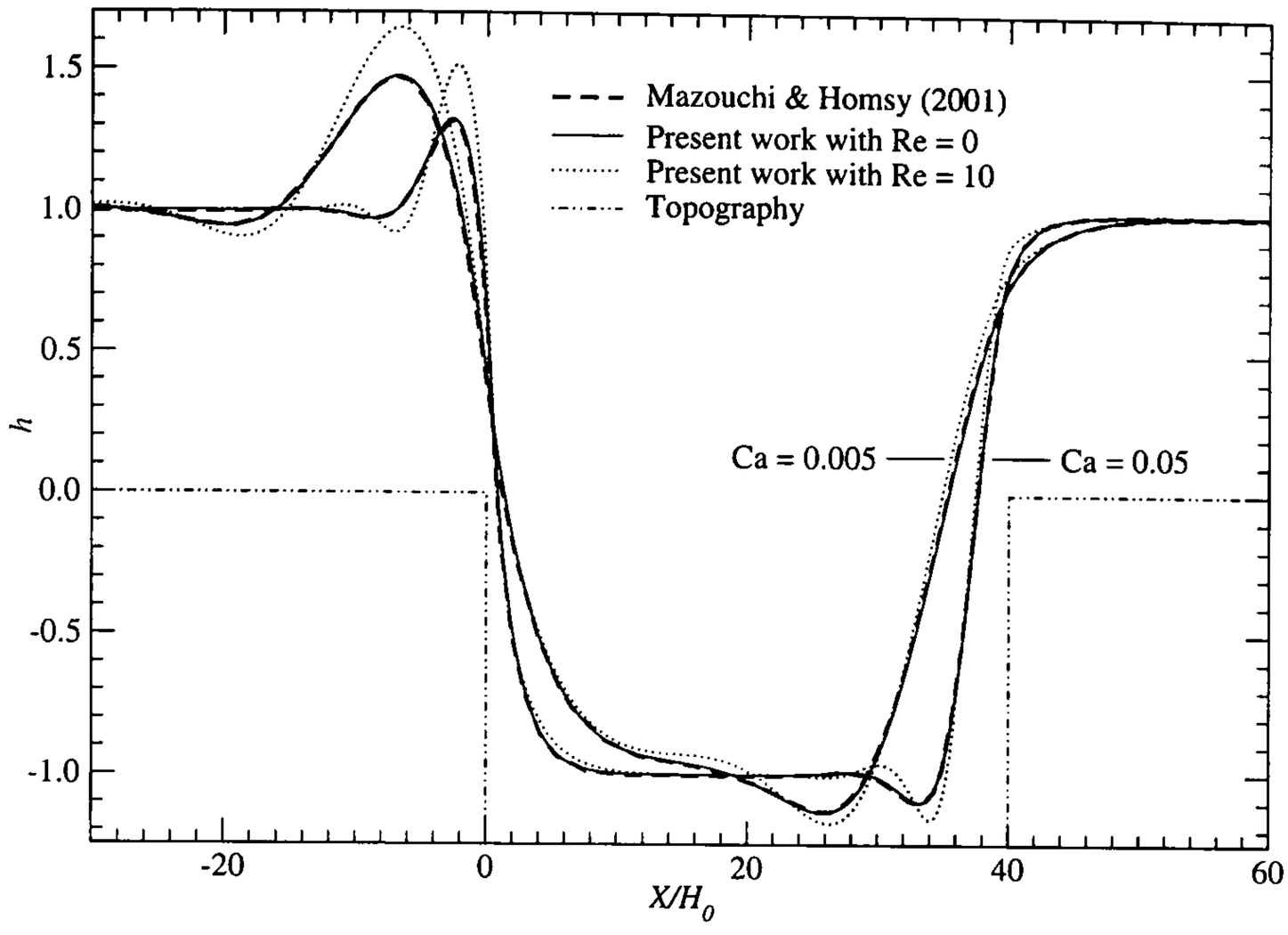

FIGURE 6.6: Comparison of film profiles calculated by the FE method, Wilson (2003), with the boundary element profiles of Mazouchi & Homsy (2001). The trench has depth $2H_0$ and width $40H_0$.

corresponding solutions found using the FE method, Wilson (2003) with Re set to 0. Note that, due to a different choice of velocity scale, the capillary number used throughout the present work is one half of that defined by Mazouchi and Homsy (2001). It is clear from the figure that excellent agreement is achieved between the FE and BE predictions when $Re = 0$.

Also shown in the Figure are two FE-generated profiles indicating the effect that increasing Re to 10 has on the free-surface shape. The most noticeable, is a significant increase in the amplitude of the capillary wave upstream of each step face, however there is also a very slight shortening of the wavelength of the disturbances.

Recently, Bielarz (2002) and Bielarz and Kalliadasis (2003) explored the effect of inertia on the free surface disturbance caused by a topography. Rather than solving the full Navier-Stokes equations, they included inertia in the form of an extra term in the lubrication approximation dependent on the film thickness and a modified Reynolds number. This approach has, of course, the benefit of fitting conveniently into the lubrication approximation framework but the range of applicability is constrained since for large value of the modified Reynolds number, the free surface blows up in finite time. As explained by Bielarz and Kalliadasis (2003), this singu-

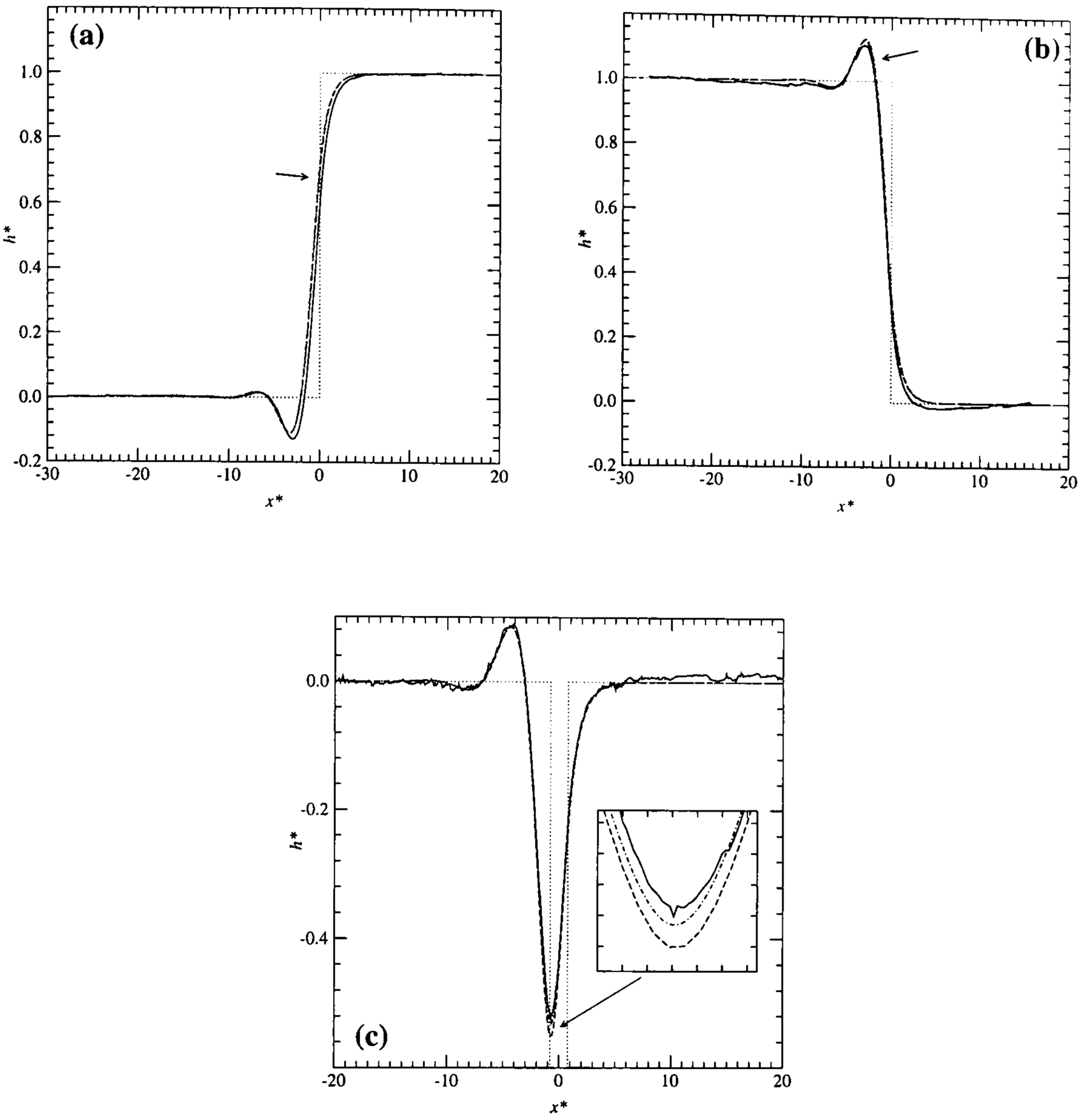

FIGURE 6.7: Comparison between numerical predictions and Decré & Baret's (2003) experimental free surface profile data for the flow of water over one-dimensional topographies: (**a**) flow over a step up with $H_0 = 100$ μm, $s_0 = 0.2$, and $Re = 2.45$; (**b**) flow over a step down with $H_0 = 100$ μm, $s_0 = 0.2$, and $Re = 2.45$; (**c**) flow over a trench with $H_0 = 105$ μm, $s_0 = 0.19$, width 1.2 mm, and $Re = 2.84$. Legend: —— experimental data of Decré & Baret (2003); – – – lubrication theory; - · - · - finite elements; · · · topography.

larity formation is due to the fact that the long-wave approximation breaks down for large values of the modified Reynolds number. The results reported in Bielarz (2002) and Bielarz and Kalliadasis (2003) focused on the flow over a mound and revealed that inertia increases the maximum height of the ridge which confirms the trend observed here.

Decré and Baret's (2003) recent experimental study of thin water films flowing down an inclined plane with topographies is another valuable source of data to compare numerical predictions against. Figure 6.7 presents a comparison of FE and

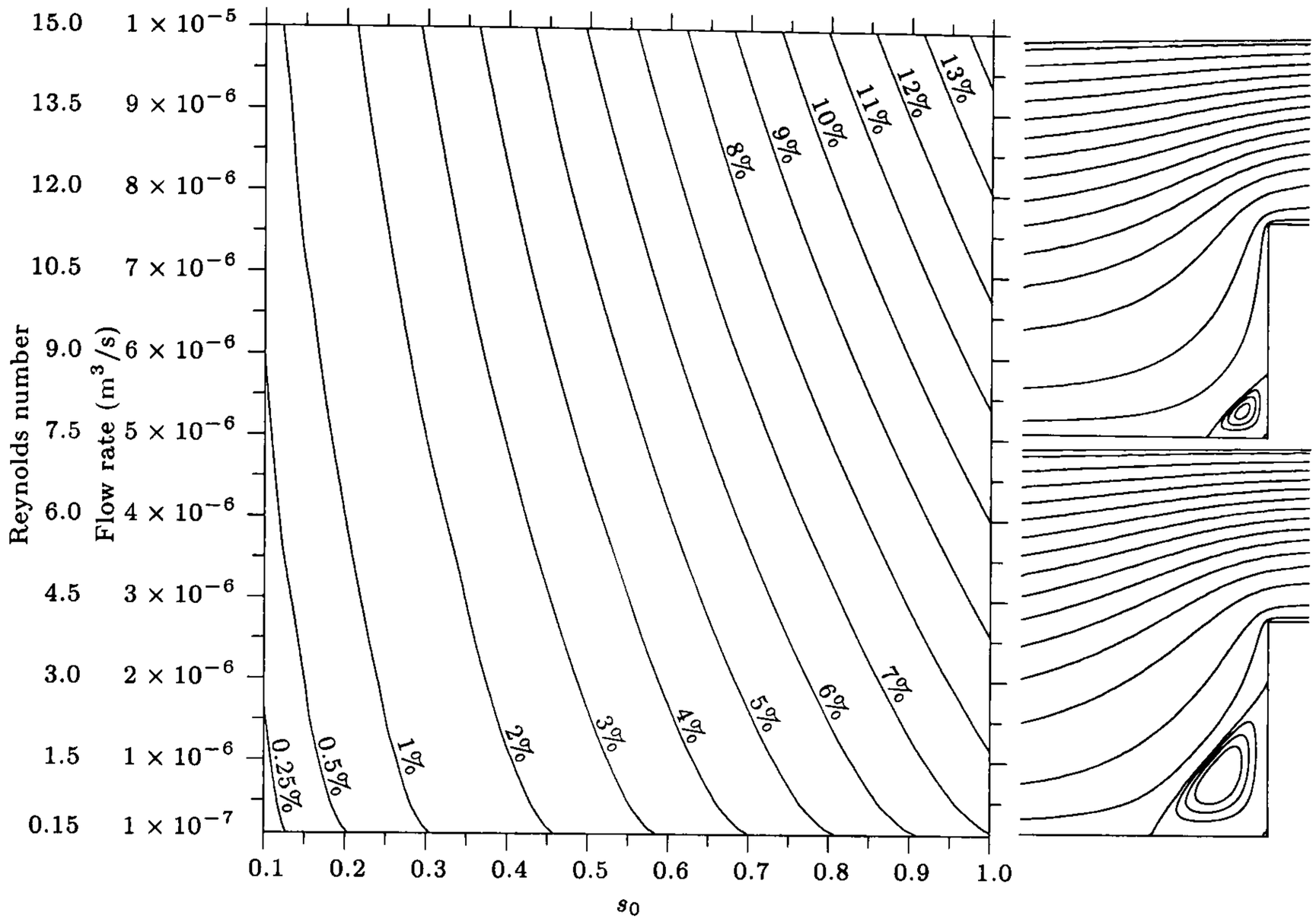

FIGURE 6.8: Contours illustrating the maximum error between the lubrication theory and Navier-Stokes film profiles for a range of step heights and flow rates in flow over a step up topography. Example flow structures for $s_0 = 1$ are presented on the right. The upper picture corresponds to a flow rate of 10^{-5} m^3 s^{-1} ($H_0 = 180$ μm), where the lubrication results have an error of 14%, and the lower to $Q_0 = 10^{-7}$ m^3 s^{-1} ($H_0 = 40$ μm), where the lubrication error is 7%.

lubrication solutions for free surface profiles with those found experimentally by Decré and Baret (2003) for the cases of flow over a small one-dimensional step down, a step up and a trench, Gaskell *et al.* (2003(b)). The Reynolds number was 2.45 for the steps and 2.84 for the trench. Note that in this and all subsequent comparisons, liquid properties are taken as $\mu = 0.001$ Pa s, $\rho = 1000$ kg m^{-3} and $\sigma = 0.07$ N m^{-1}, and, unless otherwise stated, the inclination angle is set to $\alpha = 30°$. In all three cases the FE and lubrication solutions are seen to be practically indistinguishable (see below), to agree well with experiment and to reproduce accurately the main features of the film thickness profiles, such as the characteristic free surface trough and capillary ridge just upstream of the step topographies and the free surface depression characteristic of flow over the trench. These free surface variations result from the competition between the pressure generated by the topography which tends to conform the free surface to the underlying substrate and the surface tension which tends to reduce the overall curvature of the free surface.

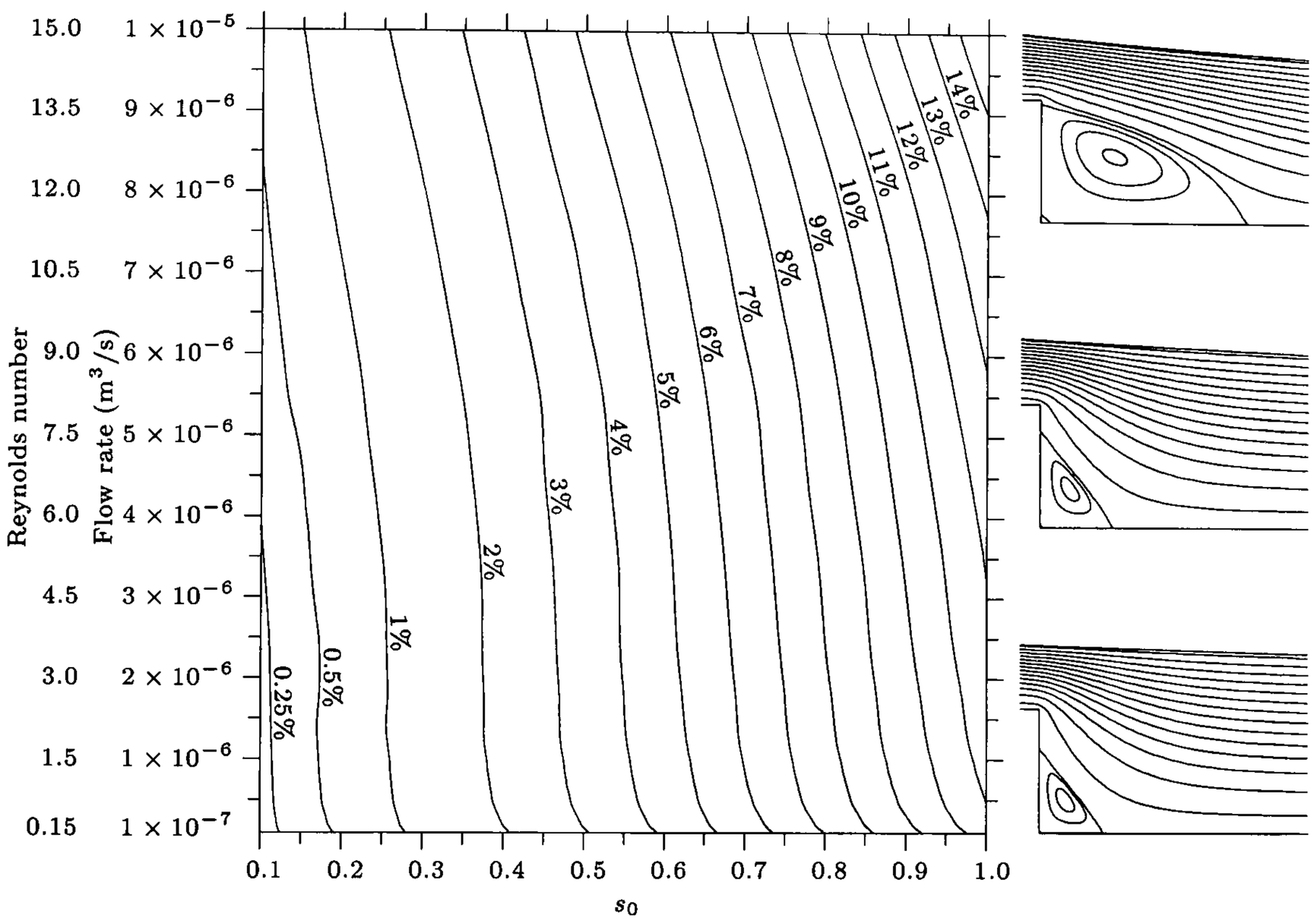

FIGURE 6.9: Contours illustrating the maximum error between the lubrication theory and Navier-Stokes film profiles for a range of step heights and flow rates in flow over a step down topography. Example flow structures for $|s_0| = 1.0$ are presented on the right. The upper picture corresponds to a flow rate of 10^{-5} m^3 s^{-1} ($H_0 = 180$ μm), where the lubrication results have an error of 15-16%, and the lower to $Q_0 = 10^{-7}$ m^3 s^{-1} ($H_0 = 40$ μm), where the lubrication error is 10-11%.

Since the FE solutions do not have the inherent limitations of those based on lubrication theory, they can be used to assess the accuracy of the long-wave approximation in relation to flow over topography. These limitations include, for example, the slope of the free surface which needs to be small for the lubrication approximation to be valid. Hence, one would expect that the lubrication approximation breaks down in the immediate vicinity of a sharp step. However, as mentioned by Mazouchi and Homsy (2001), for small capillary flows the free surface is so strong that it mitigates the free surface response to the pressure gradients produced by the step, leading to a solution that in fact has a small slope. Figures 6.8 and 6.9 show contours which quantify the discrepancy between the the FE and lubrication theory solutions as step height and flow rate are varied for flow over both step up and step down topography. The difference is defined as the maximum distance between the predicted lubrication film thickness and its Navier-Stokes counterpart, measured normal to the lubrication profile. This measure is preferred to one based on a r.m.s. distance since both profiles satisfy the same boundary conditions far upstream and downstream of the topography so that the latter measure would be unduly influenced by the long asymptotic regions of the domain where the two profiles are practically indistinguishable. For both step up and step down topography the position of the maximum difference between corresponding profiles is near the top of the steeply sloping part of the profile, as indicated by the arrows in Figures 6.7(**a**) and (**b**). The difference in the predictions of the height (depth) of the capillary ridge (trough) is typically much smaller, roughly 1/4 of the maximum difference. Note that the vertical scales in Figures 6.8 and 6.9 indicate both the value of the Reynolds number and corresponding flow rate; Ca therefore also varies (from 5.4×10^{-5} to 1.2×10^{-3}) as the flow rate increases.

In both cases the contours are as expected; they show that as the step height increases, the maximum flow rate (and Re) for a given error decreases. There are, however, interesting differences between the two configurations. When the step height is a small fraction of the asymptotic film thickness, for a given error a larger flow rate can be achieved over a step down topography than over a step up. However, for a given flow rate, the difference between lubrication theory and the FE

analysis generally increases more rapidly in the flow over a step down topography. Interestingly, no lubrication solution beyond $|s_0| = 0.8$ were obtainable for the step-down case using the steady-state multigrid lubrication solver; equilibrium solutions for $|s_0| > 0.8$ were determined using the time-dependent variant of the method detailed in Chapter 3. A final noteworthy difference is that for flow over a step up topography, fluid inertia has only a minor influence on the extent of the eddy region, while it has a much more pronounced effect for flow over a step down — see the streamline plots in Figures 6.8 and 6.9.

6.4.2 Flow over localised topography

The comparison of results obtained with the lubrication theory and with Dr M. Wilson's FE code support the consensus that lubrication theory provides remarkably good solutions to "thin film" problems, even when it is applied to situations where it is strictly-speaking not valid - such as the flow over steep topographies considered here. The lubrication formulation is now used to explore free-surface responses to localised peaks and trenches with reference to Decré and Baret (2003) experimental measurements for the trench cases.

An asymptotic film thickness $H_0 = 100$ μm gives $Ca = 3.5 \times 10^{-4}$, $N = 0.12$ and $L_c = 0.78$ mm as shown in §2.4. The small value of N indicates that the normal component of gravity will have little effect on the free-surface shape. The topography steepness parameter in equations (5.13) and (5.14) is set to $\gamma = 0.05$, a value below which it is found to have no discernible effect on the numerical predictions. The Reynolds number for the flow is 2.45 and the topography depth is $s_0 = 0.25$. Figures 6.8 and 6.9 therefore suggest that Navier-Stokes solutions would differ only slightly from the lubrication theory predictions, Gaskell *et al.* (2003(b)).

Consider the case of flow over a square trench located at $({x^+}_t, {y^+}_t) = (30.77, 50)$ with $|s_0| = 0.25$ and $w_t = 1.54$. Decré and Baret (2003) have already demonstrated that streamwise and spanwise profiles of the free surface produced by this flow agree well with those predicted by the linear lubrication theory of Hayes *et al.* (2000). Hence it is not surprising that the experimental data is also well-matched by the

predictions of the present formulation, as demonstrated in Figures 6.10 and 6.11, which compares corresponding streamwise and spanwise profiles respectively. The agreement of the spanwise profiles appears to be poorer than for the streamwise profiles. A possible explanation provided in Decré and Baret (2003) is that the free surface profile is measured over a period of up to an hour. During that time, small fluctuations of the flow rate or unsteady variations lead to a build-up of noise in the measured profile. This is however taken into account in their error budget and does not exceed 0.3 μm.

A complete three-dimensional visualisation of the free surface is given in Figure 6.12(**a**), clearly showing the characteristic "horseshoe"-shaped "bow wave" and the deeper depression over the trench itself, followed by a peak which Decré and Baret (2003) refer to as the "downstream surge". This latter feature does not have an equivalent in the flow over one-dimensional topographies, and Decré and Baret (2003) admitted that its cause is not properly understood. A possible explanation, Gaskell *et al.* (2003(b)), is provided by considering the flow rate into and out of the trench. Since the trench is finite in length and width, fluid will enter the trench both in the streamwise direction (over the upstream wall) *and* in the spanwise direction (over the side walls). Since in a steady flow the fluid entering the trench must then leave it (over the downstream wall), the downstream surge simply rises to allow the fluid to exit the trench across a shorter width than that across which it entered. In the one-dimensional case there is no difference in the widths over which fluid enters and leaves the trench and therefore no cause for a downstream ridge.

Figure 6.12(**b**) gives the view corresponding to flow over an "equal-but-opposite" square peak topography, where the free surface appears to be a straightforward inversion of that over the trench. Decré and Baret (2003) did not consider peak-type topographies, but the plot in Figure 6.12(**b**) is very similar to Figure 3 in Hayes *et al.* (2000) which gives the free surface produced in response to a Dirac delta peak topography. Note that the downstream surge is now replaced by a depression (though this is not visible from the viewpoint in Figure 6.12(**b**)). The above flow-rate argument can explain this feature too: fluid which passes over the top of the topography ascends the peak in the streamwise direction over the upstream wall,

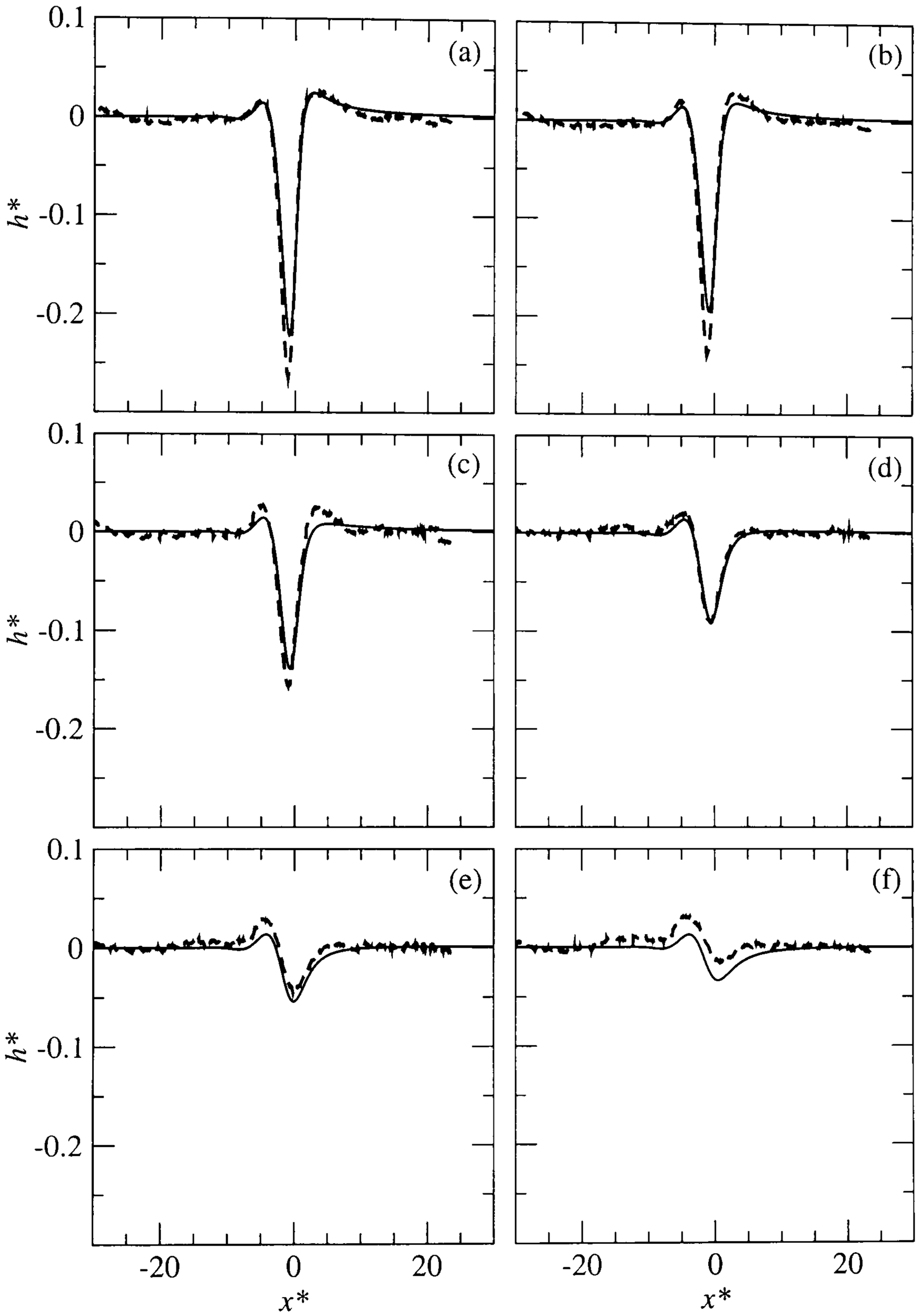

FIGURE 6.10: Comparison of numerical (full line) and experimental (dashed line) streamwise free surface profile at different spanwise locations: (**a**) $y^* = 0$; (**b**) $y^* = L_c/2$; (**c**) $y^* = L_c$; (**d**) $y^* = 3L_c/2$; (**e**) $y^* = 2L_c$; (**f**) $y^* = 5L_c/2$.

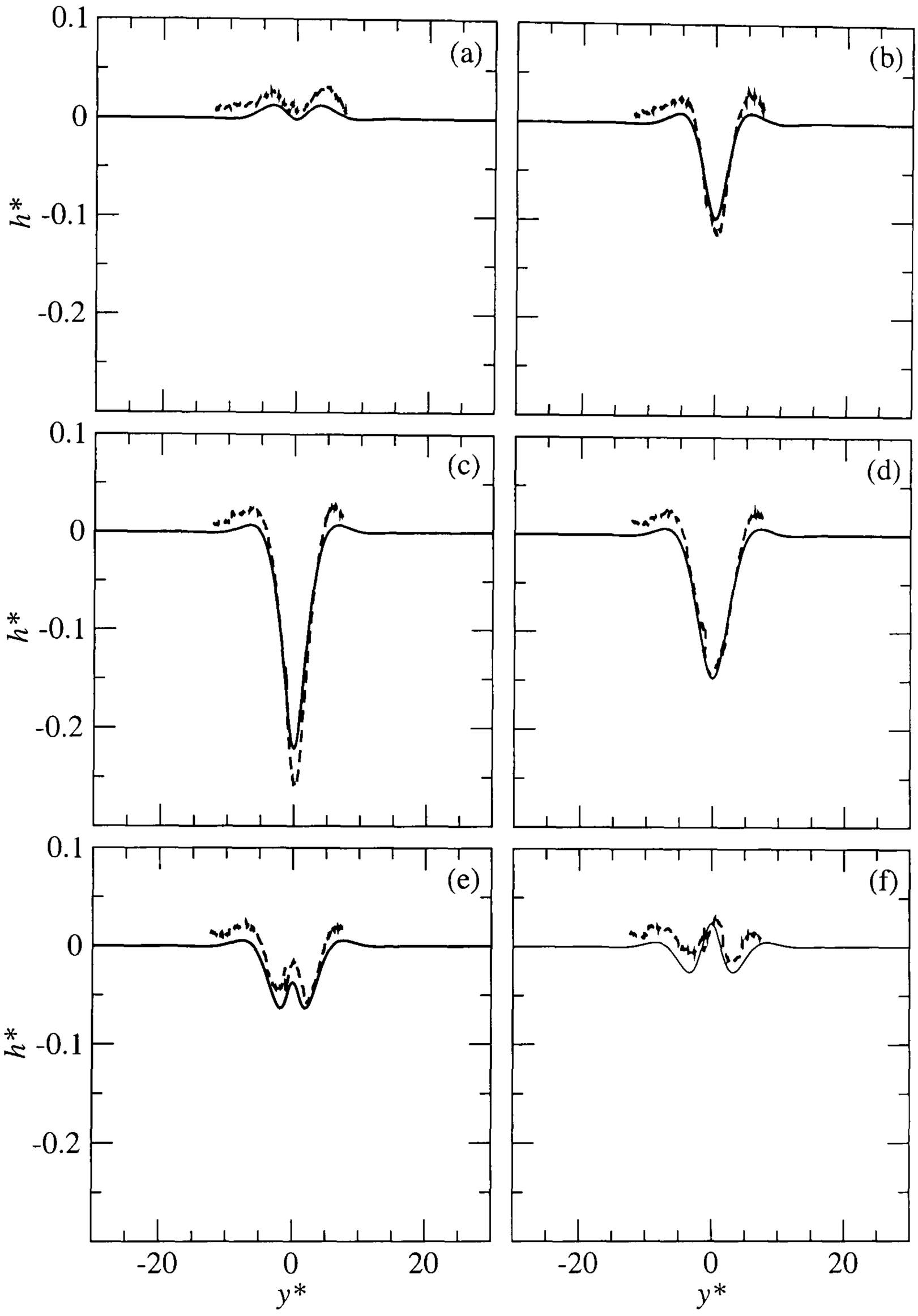

FIGURE 6.11: Comparison of numerical (full line) and experimental (dashed line) spanwise free surface profile at different streamwise locations: **(a)** $x^* = -5L_c/2$; **(b)** $x^* = -3L_c/2$: **(c)** $x^* = -L_c/2$; **(d)** $x^* = 0$; **(e)** $x^* = L_c/2$; **(f)** $x^* = 3L_c/2$.

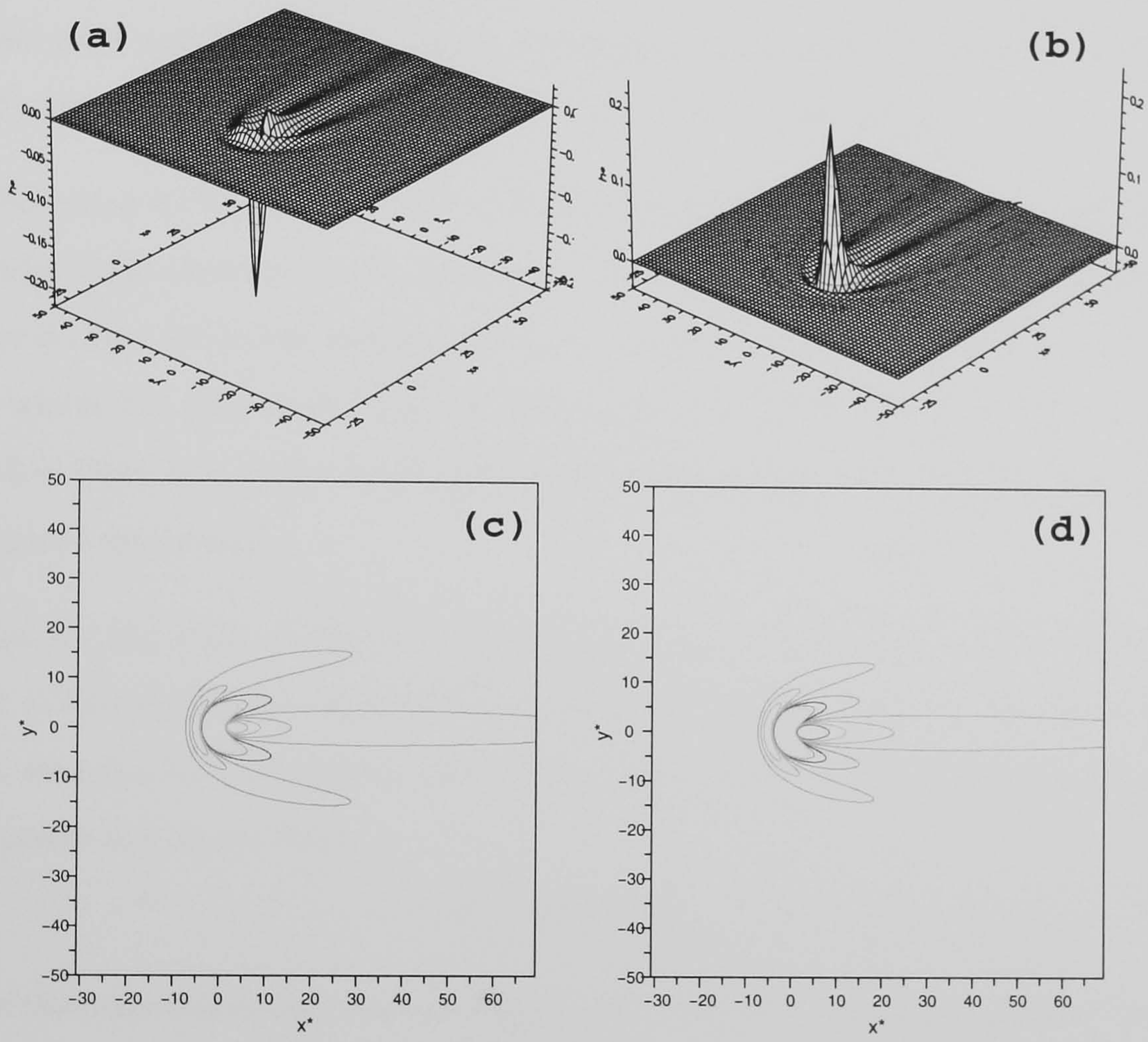

FIGURE 6.12: Flow of a thin water film over square topographies with $l_t = 1.54$, $A = 1$, $|s_0| = 0.25$ and $Re = 2.45$. In the three-dimensional views, the flow is from bottom-left to top-right: (**a**) trench; (**b**) peak. In the contour plots, flow is from left to right and the contours show free surface height. Contour values are chosen to be equal in magnitude but opposite in sign: (**c**) trench; (**d**) peak.

but is shed off the topography symmetrically by spanwise components over the side walls, leading to a reduced flow rate per unit width over the middle of the downstream wall and the consequent reduction in film thickness there.

Figures 6.12(**c**) and (**d**) show contour plots of free-surface height for the two topographies. The contour values are chosen to be equal in magnitude but opposite in sign, and show that the patterns produced are indeed very similar, but the surfaces are not quite mutual inverses. Again, the figures compare well with Decré and Baret (2003) Figure 7 and Figure 8 in Hayes *et al.* (2000) respectively.

The flows can be explored in more quantitative detail by examining the positions of spanwise local extrema in film thickness calculated by finding where $\partial h^*/\partial y^* = 0$. Figure 6.13(**a**) shows the extrema from the trench and peak flows on the same plot, from which it is easy to see that the patterns produced are extremely close in shape but that there is a slight downstream shift between the two. This feature will be considered again later.

Guided by the form of Hayes *et al.*'s (2000) linear lubrication theory, Decré and Baret (2003) noted the self-similar behaviour of the film thickness far downstream of the topography. As a result, the downstream spread of the extrema can be fitted by a power-law of the form

$$y^* = K(x^*)^{0.25}. \tag{6.5}$$

While this expression does indeed describe the behaviour far enough downstream of the topography, it is of course not valid close to the origin (i.e. the topography) and can not describe the shape of the bow wave upstream of the topography. Computations suggest an alternative fitting function which takes the form

$$y^+ = \pm A_1 \cosh^{-1}\left(\frac{(x^+) - A_2}{A_0}\right) + {y^+}_t, \tag{6.6}$$

where x^+ and y^+ are the unshifted coordinates with origin as shown in Figure 6.3. For the case of flow over a square trench, Figure 6.13(**b**) shows the location of the spanwise free surface extrema together with fitting curves following equation (6.6). The fitting parameters are given in Table 6.1 and, as can be seen, the curves fit

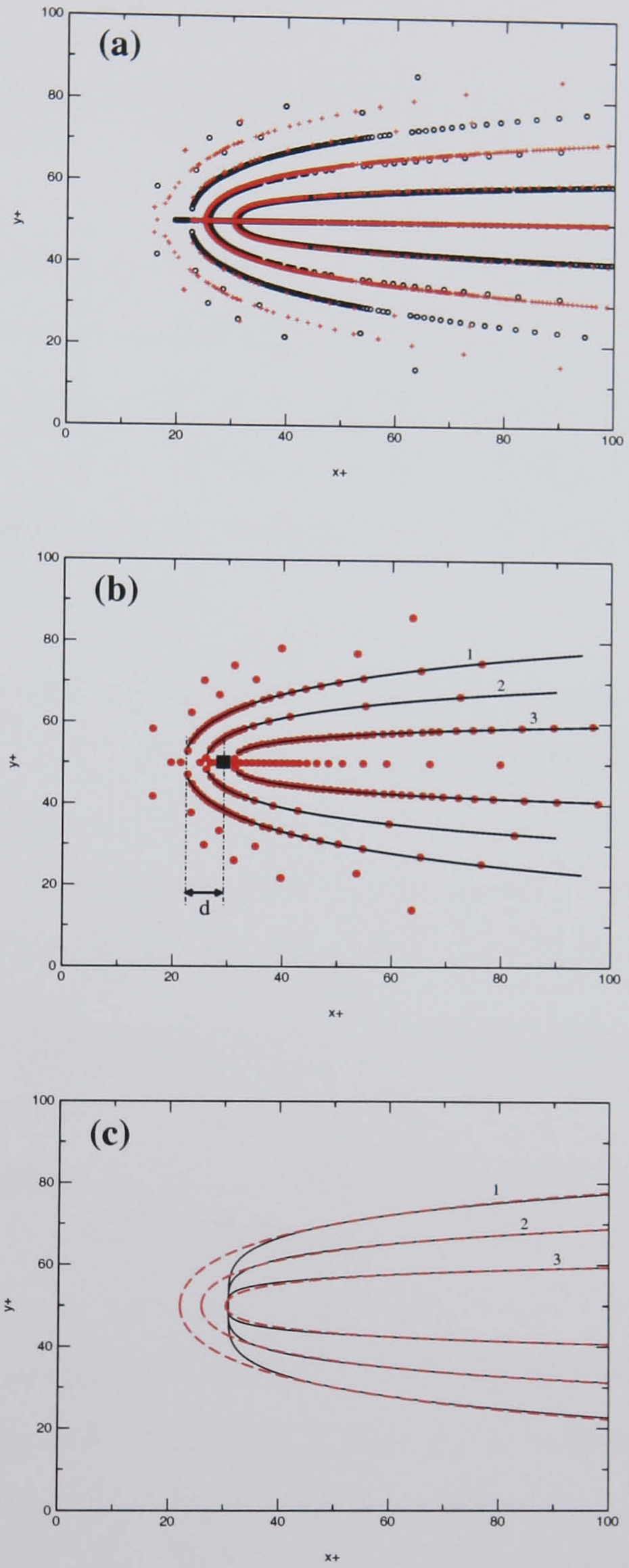

FIGURE 6.13: (**a**) Positions of extrema in film thickness for the flow past the square trench (∘) and square peak (+) of Figure 6.12; (**b**) extrema for the trench case fitted using equation (6.6) with constants given in Table 6.1; (**c**) comparison of curves fitted using equation (6.5), shown as solid lines, and equation (6.6), shown as dashed lines. Fitting constants are given in Table 6.1.

Curve	A_0	A_1	A_2	K
1	7.0	8.7	15.0	9.50
2	4.5	5.3	21.4	6.50
3	2.4	2.3	27.9	3.28

TABLE 6.1: Curve fitting parameters for equations (6.5) and (6.6) corresponding to the curves labelled in Figure 6.13

the data extremely well over the entire solution domain, $0 \leq x^+, y^+ \leq 100$. Note that in this figure, curves 1 and 3 correspond to spanwise local minima and curve 2 to the spanwise maxima of the upstream capillary ridge (cf Figure 6.12(**a**)). The data points to the left of curve 1 in Figure 6.13(**a**,**b**) correspond to very slight ridges and depressions which cannot be resolved in Figure 6.12(**a**) and are not considered further.

The two expressions (6.5) and (6.6) are compared in Figure 6.13(**c**). From approximately 10 capillary lengths downstream of the topography, the two sets of curves are practically indistinguishable. However, the clear distinction between the plots is that the proposed inverse function, (6.6), describes the positions of the spanwise extrema upstream of the topography and thus over the entire flow domain.

The function (6.6) provides useful insight into the behaviour of the capillary waves since the latter are predicted to meet the centreline $y^+ = {y^+}_t = 50$ at $x^+ = A_0 + A_2$ or, in physical coordinates, $X_0 = (A_0 + A_2)L_c$. As the topography is centred at $(X_T, Y_T) = (30.77, 50)L_c$, it follows that the distance, d say - see Figure 6.13(**b**) - between the point where the capillary wave intersects the centreline and the topography will be proportional to the capillary length and is given by $d = L_c|30.77 - (A_0 + A_2)|$. This means that waves upstream of the topography are shifted further upstream when L_c increases while those downstream of it are shifted further downstream. The former prediction is consistent with Mazouchi and Homsy's (2001) finding, for one-dimensional topographies, that as the capillary number decreases (i.e. L_c increases via equation (2.18)) the capillary ridge moves further upstream.

While providing a very good description of wave spread, it should be noted that the function (6.6) does, however, have the disadvantage of requiring three parameters

rather than one to provide a fit, and of course it does not predict the streamwise decay in amplitude available from the self-similar asymptotics.

Kalliadasis *et al.* (2000) demonstrated that for the flow over one-dimensional steps up and down, increasing the normal component of gravity could reduce or even suppress entirely the capillary trough/ridge, making the free surface conform much more closely to the topography. In the present formulation, the parameter controlling the relative strength of this gravity component is $N = Ca^{1/3} \cot \alpha = H_0 \cot \alpha / (6^{1/3} L_c)$, which is of course most strongly influenced by the inclination angle. Figure 6.14 shows, via three-dimensional views and streamwise profiles of the free surface, the effect of increasing N on the response to the above square trench. Consistent with Kalliadasis *et al.* (2000), increasing N reduces and eventually eliminates the curved upstream capillary ridge, and dramatically reduces the depth of the depression over the trench itself. However, the size of the downstream surge is not reduced by increasing N: in fact this peak in the free surface is higher for intermediate values of N. This behaviour is consistent with the flow-rate argument above since increasing N does not change the fact that fluid is pouring into the trench from three sides but must exit via a single side, Gaskell *et al.* (2003(b)).

Returning to the $\alpha = 30°$, $N = 0.12$ flow, Figure 6.15 demonstrates the effect of increasing the aspect ratio, A, of the trench by extending its spanwise length. The viewpoint chosen for these visualisations is on the opposite side of the topography to that in Figures 6.12 and 6.14, giving a reverse view of the free surface disturbance. When A is increased to 5 (Figure 6.15(**b**)), the depth of the depression over the trench is greatly increased and the height of the curved capillary ridge upstream of the topography is also increased. The central downstream surge is still clearly present, though it decays in amplitude more slowly than that following the square trench. Increasing A to 8.33 widens the upstream ridge, and introduces a bifurcation in the downstream surge such that two smaller surges lie either side of the centreline of the topography, see Figure 6.15(**c**). As A increases further, the free surface appears to become flat in the central region just downstream of the trench; coupled with the flattening of the top of the upstream ridge (Figure 6.15(**d**)), this shows that the flow near to the centreline $y^* = 0$ approximates closely that over a one-

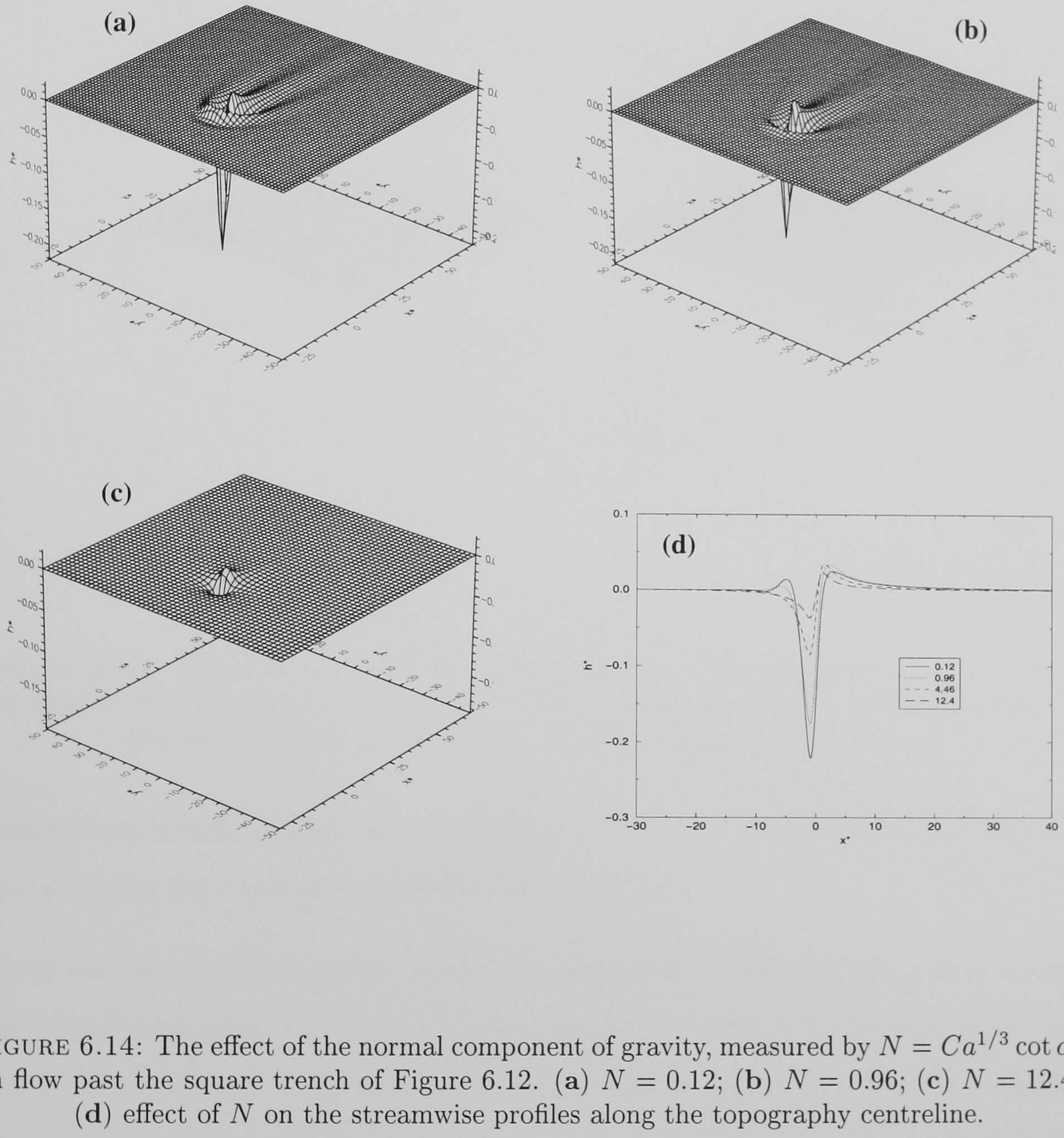

FIGURE 6.14: The effect of the normal component of gravity, measured by $N = Ca^{1/3} \cot \alpha$, on flow past the square trench of Figure 6.12. (**a**) $N = 0.12$; (**b**) $N = 0.96$; (**c**) $N = 12.4$; (**d**) effect of N on the streamwise profiles along the topography centreline.

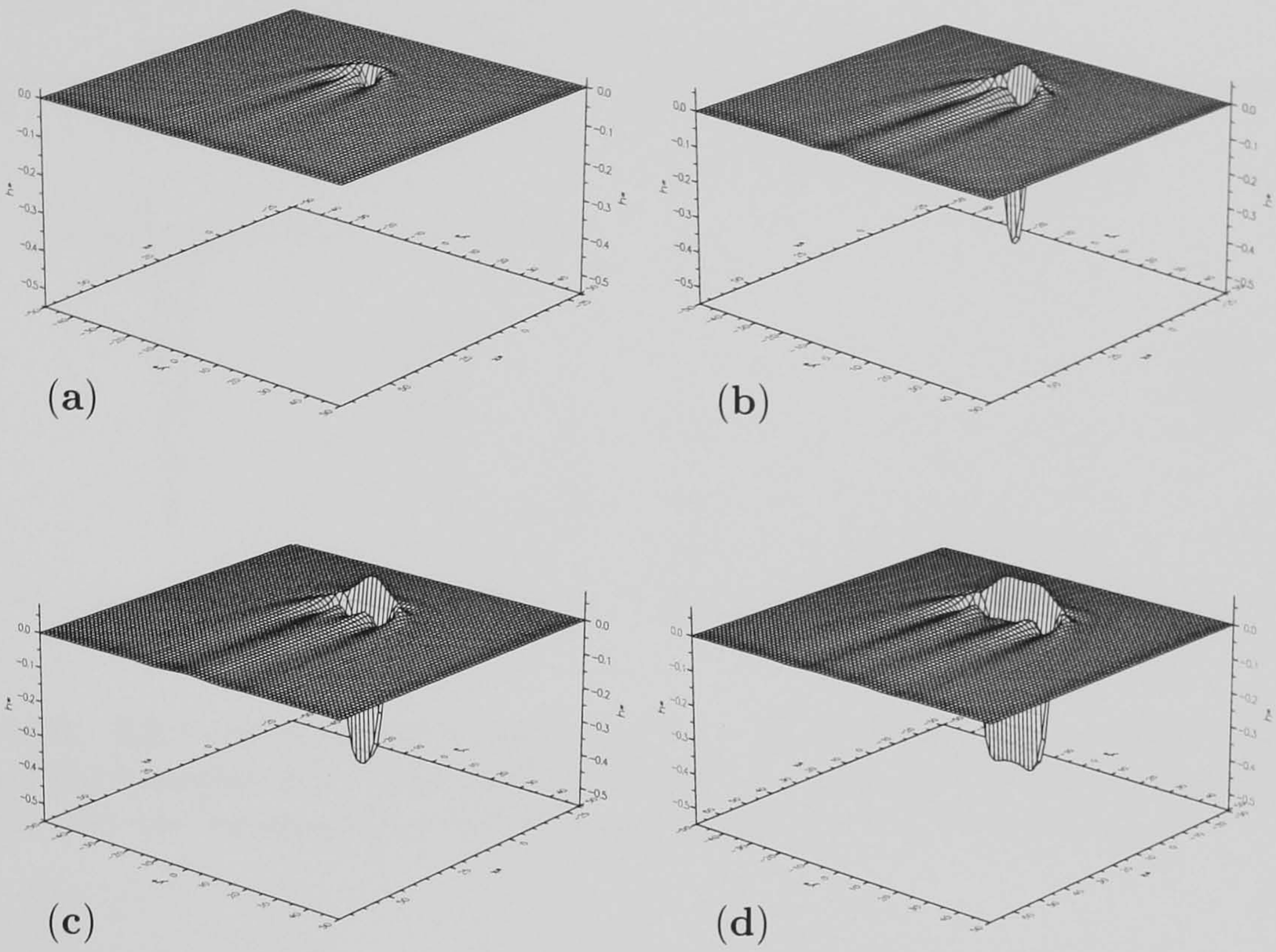

FIGURE 6.15: Three-dimensional rear-view of the free surface generated by flow (from top-right to bottom-left) over trenches, showing the effect of trench aspect ratio on the downstream surge. (**a**) $A = 1$; (**b**) $A = 5$; (**c**) $A = 8.33$; (**d**) $A = 15$.

dimensional trench, Gaskell *et al.* (2003(b)). The above observations are clarified by overlaying the centreline profiles as in Figure 6.16.

Decré and Baret (2003) showed that their measured profiles for the square trench agreed well with linear lubrication theory, but tested the linearity of their results further by comparing the measured profile for the trench of aspect ratio 5 with a linear superposition of five suitably-shifted square-trench profiles. The result was that the superposition profile approximated fairly well the measured profile, indicating that nonlinear effects are small. The same test can be made using numerical solutions, and the result is given in Figure 6.17, which also includes the experimental data for comparison purposes. The plot shows that the linear superposition of numerical solutions is indeed very close to the direct solution for the $A = 5$ trench, except in the bottom of the trench where it over-predicts the depth of the depression. In

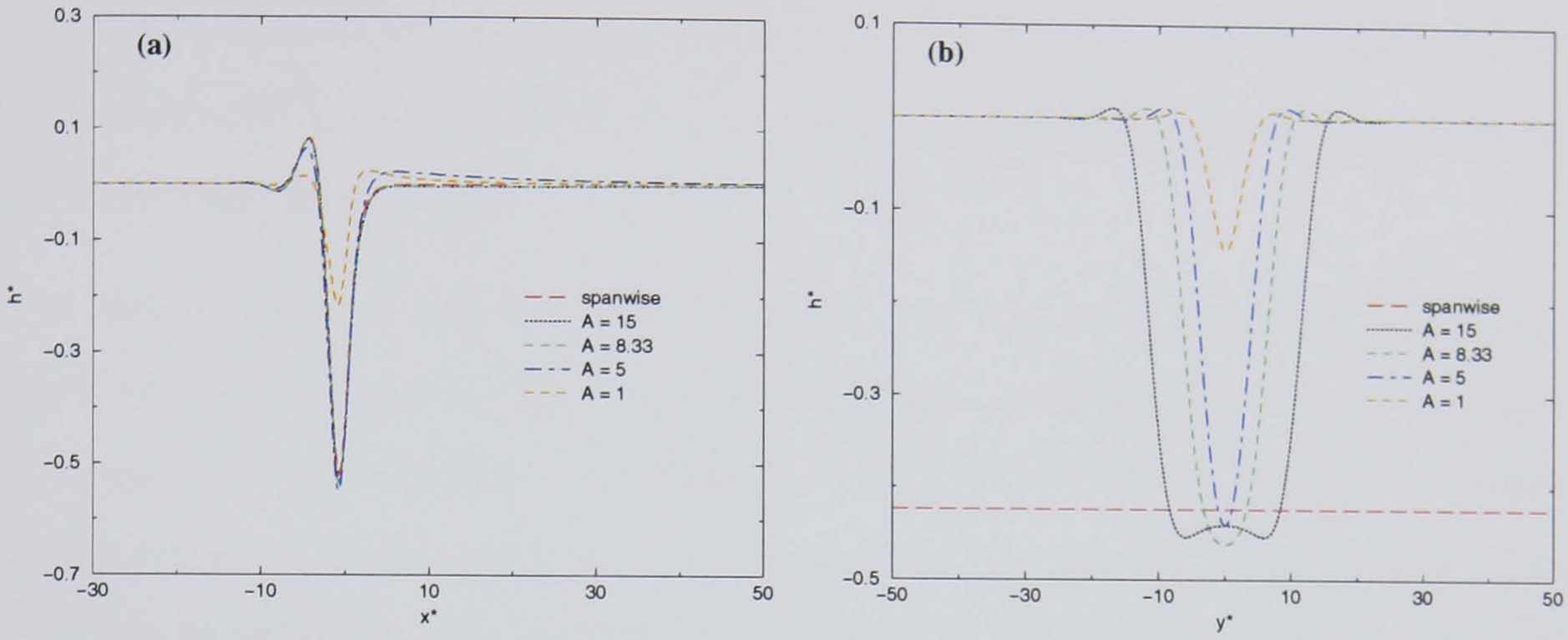

FIGURE 6.16: Effect of topography aspect ratio on (**a**) streamwise free surface profiles $y^* = 0$, and (**b**) spanwise free surface profiles along $x^* = 0$. For comparison, the profiles for flow over the corresponding one-dimensional spanwise trench are also given.

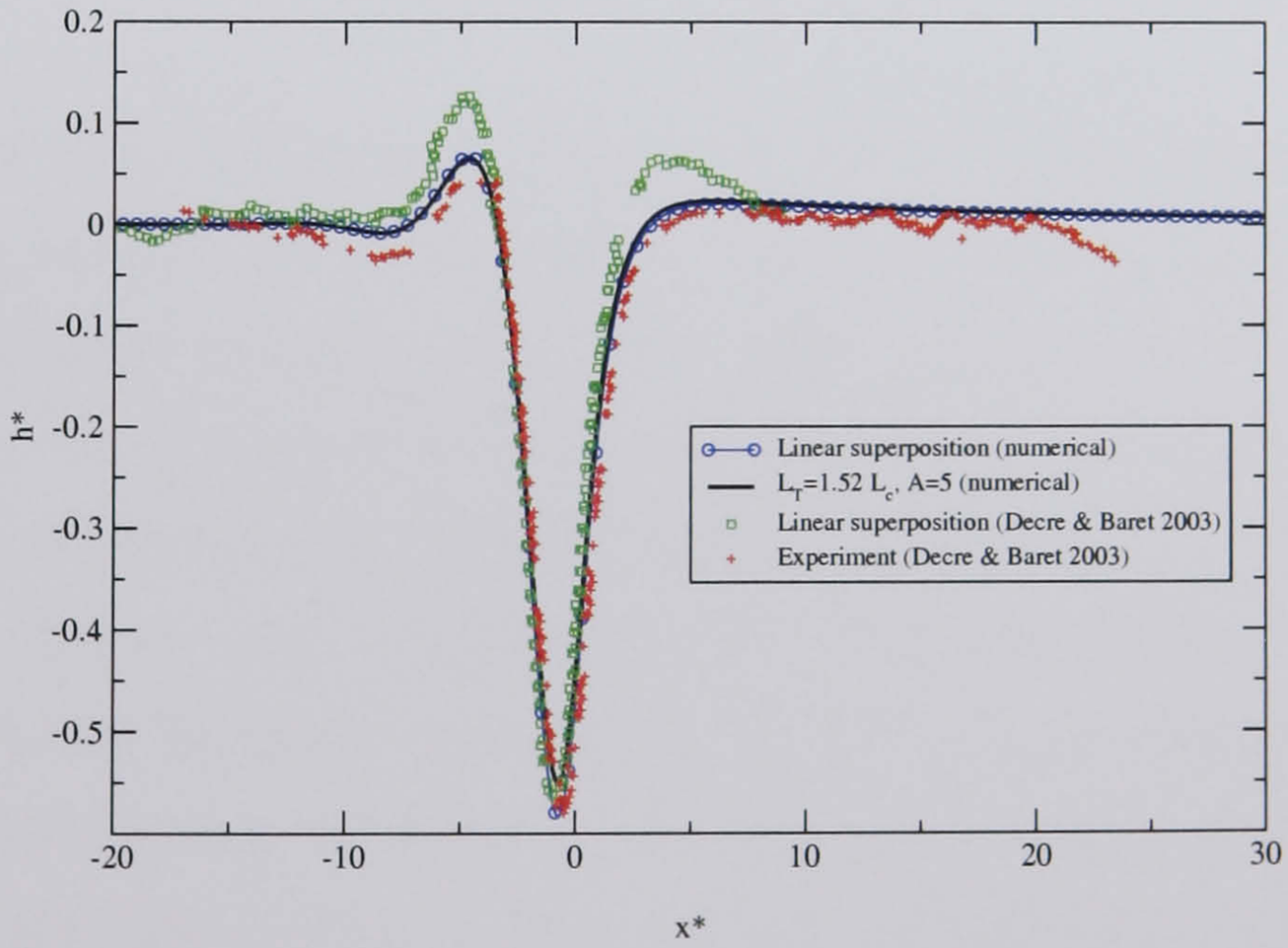

FIGURE 6.17: Streamwise free surface profiles for a spanwise trench of aspect ratio 5: comparison between the full numerical solution and a linear superposition of five suitably-shifted solutions for flow over a square trench. Also shown are the direct experimental measurements and corresponding superposition of square-trench measurements from Decré and Baret (2003).

contrast, the superposition of the experimental data agrees very well with the measured profile in terms of the depression depth, but is not so close near the walls of the trench. Note that while they exhibit a discrepancy in the trough depth, the full numerical solution and the numerical superposition are both still in good agreement with the experimental data.

The near-linearity of the results in Figure 6.17 and in Decré and Baret (2003) supports the observation by those authors that linear superposition of the responses to elementary topographies can reliably construct the response to more complex topographies — at least for flow conditions similar to those considered here. The accuracy of the linear superposition is perhaps most rigorously tested by adding together the solutions corresponding to a pair of equal but opposite topographies, i.e. a trench and a peak, since if the response of the free surface to topographic features is linear, the resulting surface should be planar, Gaskell *et al.* (2003(b)). From the analysis of Stillwagon & Larson (1990), such a linear response is to be expected in the limits of very small Ca, when the free surface is almost planar, or larger Ca if the height (depth) of the topography is much smaller than the film thickness (i.e. $|s_0| \ll 1$).

Figure 6.18(**a**) shows the surface constructed by adding together the two surfaces in Figure 6.12(**a**) and (**b**), i.e. the responses to equal but opposite square topographies located at the same position. Recall that in this case $s_0 = 0.25$. It has already been noted in the discussion of the results in Figures 6.12 and 6.13 that, although these two free surfaces are very close to being inverses of each other, there are slight differences in features such as the positions of the spanwise extrema. Hence it is not surprising that the surface in Figure 6.18(**a**) is not planar. However, the three-dimensional visualisation does not give a true impression of the scale of the features remaining in the surface; Figure 6.18(**b**) shows the streamwise profiles through the centreline for the two topographies together with their sum. From this it can be seen that although there is still a disturbance in the surface, its amplitude is only about 7% of that in the original profiles. By way of comparison, Figure 6.18(**c**) shows the streamwise profiles and their sum when s_0 is reduced to 0.1. In this case, where the response is expected to be more linear, the variation in the constructed

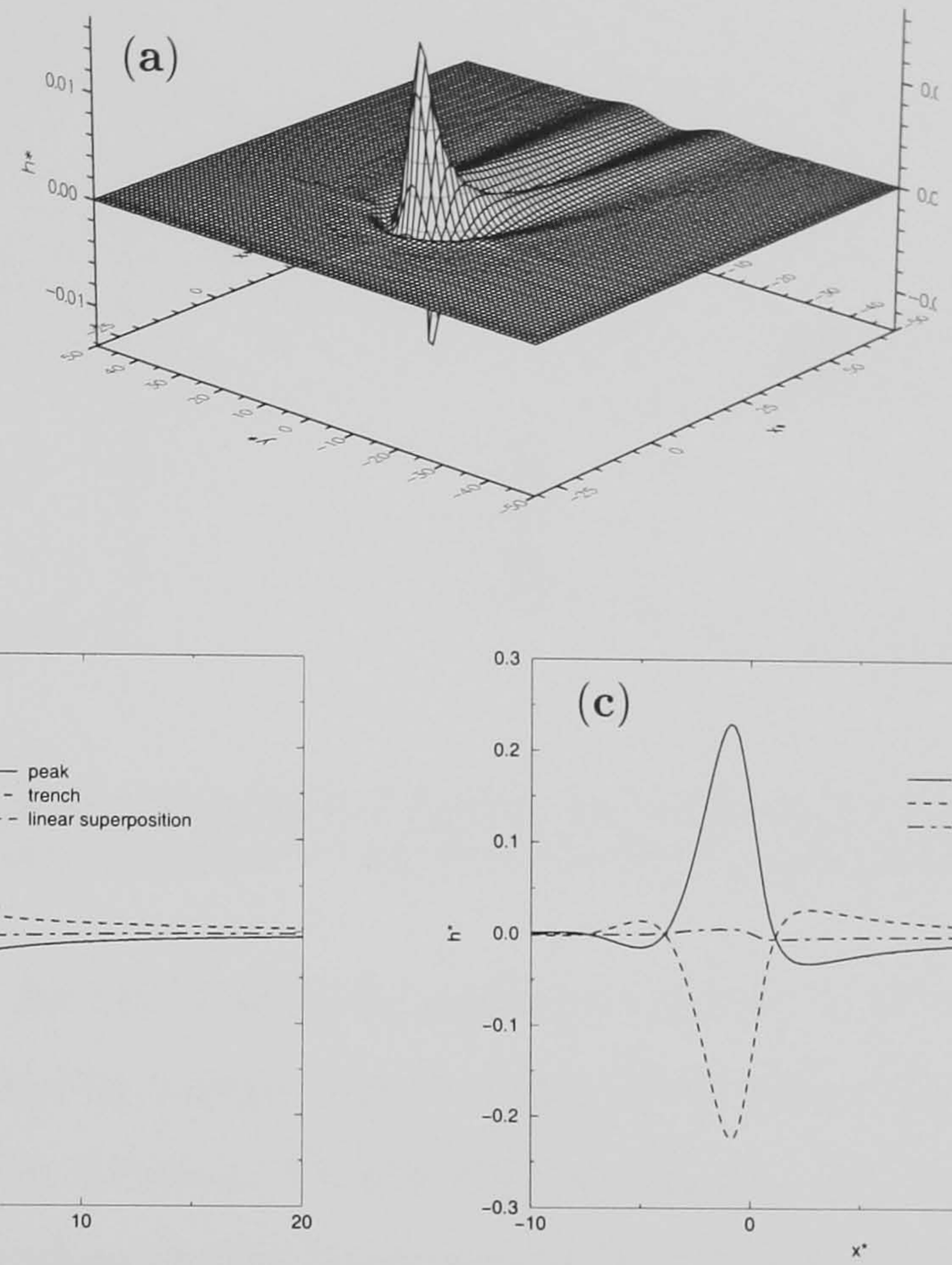

FIGURE 6.18: Superposition of the free surfaces generated by flows over equal but opposite square topographies with $w = 1.54$. (**a**) Three-dimensional view of the constructed surface when $|s_0| = 0.25$; (**b**) streamwise free surface profiles along $y^* = 0$ compared against those of the individual flows with $|s_0| = 0.25$; (**c**) same plot with $s_0 = 0.1$.

profile is indeed reduced — to below 2%.

The linearity was further tested for the flow over topography with a more complex geometry. The topography considered is illustrated on Figure 6.19(**a**) and has a **T** shape. It effectively corresponds to the superposition of 8 elementary topography blocks. These elementary blocks are square trenches of lateral extent 1.54 L_c and depth 0.25 H_0 as in the previous results. The free surface contours, shown in Figure 6.19(**b**), obtained numerically for the union of all the elementary topographies, reveal that the **T**-shaped topography still generates a "horse-shoe" capillary wave despite its much larger spanwise extent of the topography. The contours also highlight the tendency of the free surface to conform to the underlying topography since they form a distinct **T**. The linearity is assessed by comparing the streamwise free

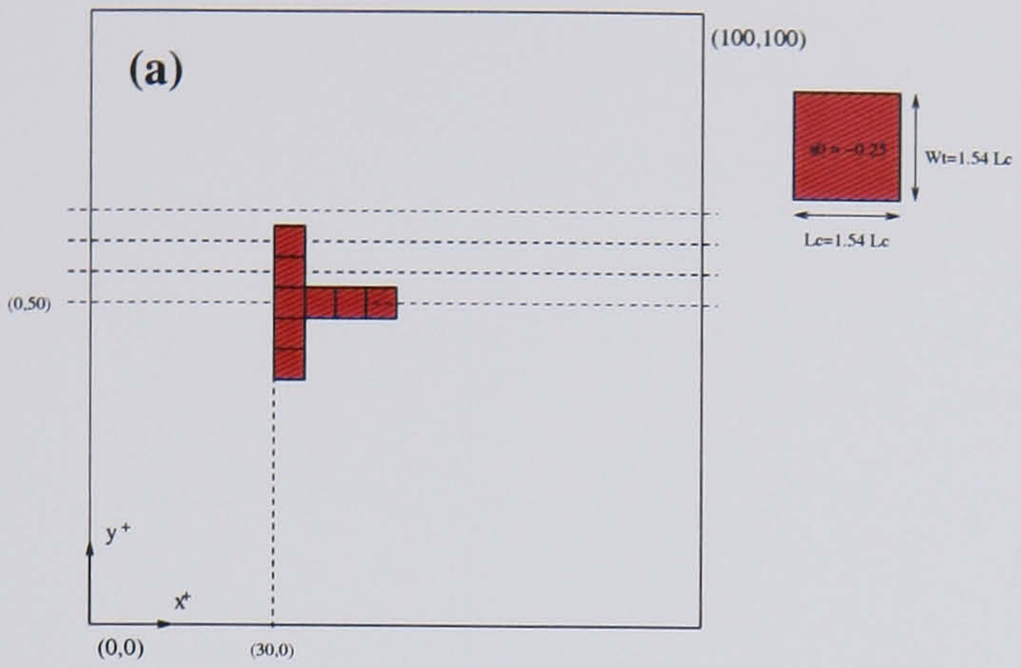

FIGURE 6.19: **(a)**: sketch of the computational domain and the **T**-shaped topography (not to scale); **(b)**: Free surface contours for the flow over the **T**-shaped topography

surface profile obtained for the **T**-shaped topography (union of all the elementary topography blocks) and by superposing the response of each of the elementary blocks at a given spanwise location. Figures 6.20(**a**), (**b**), (**c**) and (**d**) representing the streamwise free surface profiles for increasing distance from the topography centreline (dashed lines on Figure 6.19(**a**)) confirm the ability of the linear superposition principle to capture accurately the free surface features. In fact close to the topography centreline (Figures 6.20(**a**) and (**b**)), the profiles are barely distinguishable. The agreement between the profiles decays for spanwise locations further away from the topography centreline but still remains in an acceptable range (approximately 7.5% of the maximum film thickness variation). The discrepancy associated with linear superposition occurs in the corners delimited by the **T** where the slope of the free surface changes rapidly.

Finally in this section, an example is given in Figure 6.21 of an attempt to reduce the free surface disturbance caused by a square peak topography by modifying the topography surrounding the peak, Gaskell *et al.* (2003(b)). In this case, a simple shallow ditch is created around the peak; the topography sizes are given in the figure. The streamwise profile along the centreline (Figure 6.21(**b**)) shows that although the composite topography produces a deeper depression in the free surface, the overall disturbance is smaller (the r.m.s. deviation over the whole domain is 0.62% for the peak alone and 0.26% for the peak with a ditch). In addition, the film thickness relaxes more quickly to equilibrium downstream of the ditch. The contour plots

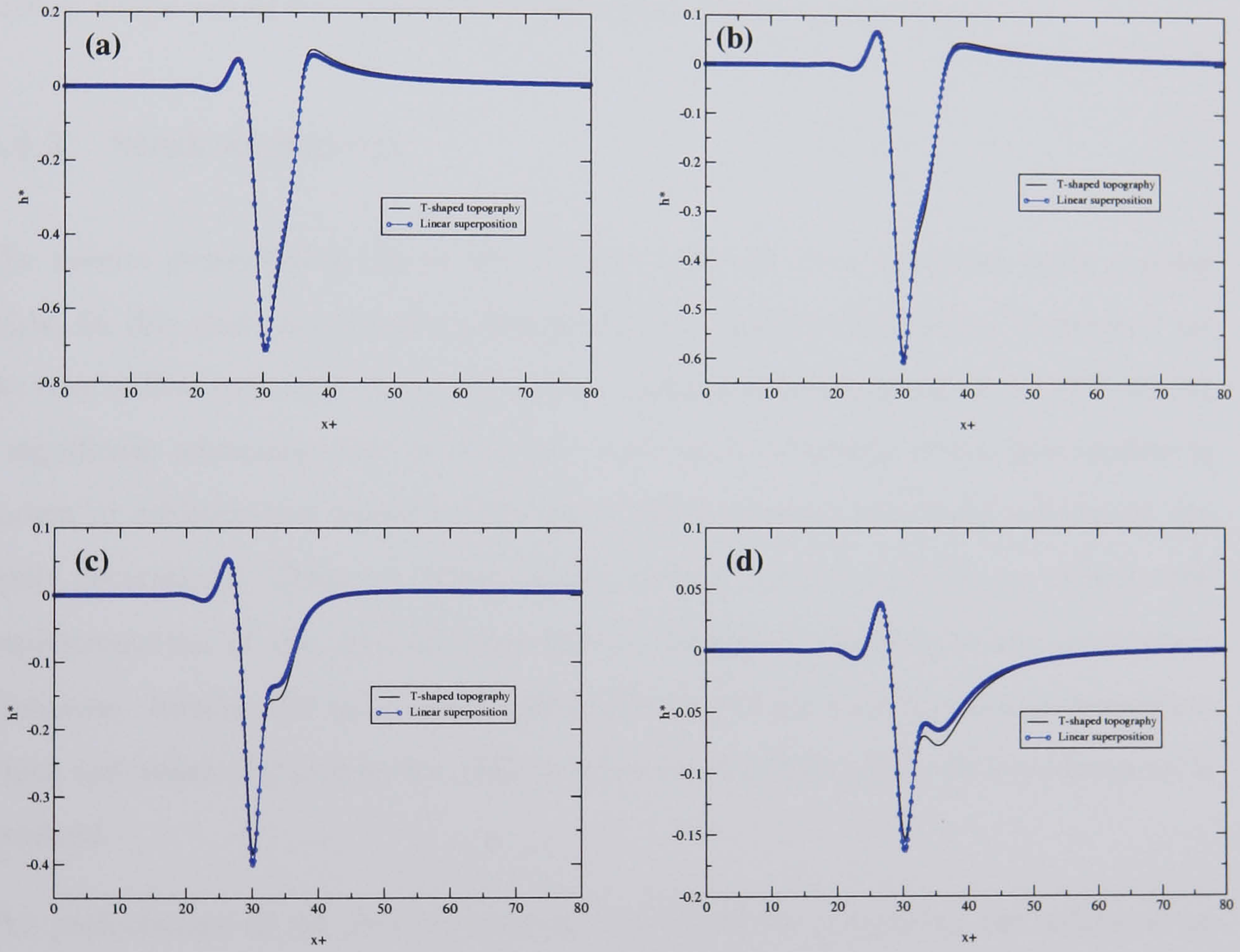

FIGURE 6.20: **(a),(b),(c),(d)**: comparison of the streamwise free surface profile obtained numerically and by superposing the response of each elementary topography blocks at $y^* = 0$, $y^* = 0.77$, $y^* = 2.31$ and $y^* = 3.85$ respectively (dashed lines on Figure 6.19(**a**).

(Figure 6.21(**c**),(**d**) also show that the region of maximum disturbance is smaller for the composite topography, despite its greater lateral extent.

The minimisation of free-surface disturbances is of great interest in the manufacturing processes mentioned in §6.1, and the modification of base-layer topographies may offer a useful alternative to other means of free-surface control such as localised heating (Gramlich *et al.* (2002)). This emphasises Decré and Baret (2003)'s closing remarks that the inverse problem of determining topographies given a desired free surface shape would be a useful and interesting future research area.

6.4.3 Mesh adaptivity

The results presented so far in this chapter have all been obtained using regular grids. In this short section the potential of local mesh refinement is illustrated for the case of flow over step down and square topographies discussed above. Of course, a significant advantage here is that the qualitative behaviour of the free surface is known in advance and therefore the parts of the domain requiring refinement are easily determined. Thus, the intent of the present section is merely to validate the implementation of the $\mathcal{MLAT}$ discussed in Chapter 3 applied to the lubrication equations. Ideally, the local mesh refinement should be coupled with an algorithm which automatically locates the regions of strong gradient (say) where refinement is required.

The performance of the $\mathcal{MLAT}$ scheme is assessed by comparing the solutions on various composite grids with the solution on a uniform grid, G^4, having 257 mesh points in either direction for the flow over a step down. The composite grids are generated so that the mesh density at the finest grid level is identical to to that of the uniform grid. The coarsest grid level, G^0, is a 17x17 grid and the local refinement delimited by the dashed lines on Figure 6.22(**a**) is performed on G^1, G^2, G^3 so that the composite grids are $\widehat{G}^{1+3}$, $\widehat{G}^{2+2}$ and $\widehat{G}^{3+1}$ respectively according to the notation introduced in Chapter 3. For clarity, the streamwise variations of the mesh density for the various grids are plotted on Figure 6.22(**b**). The streamwise free surface profiles obtained on the uniform and composite grids are seen to be indistinguishable

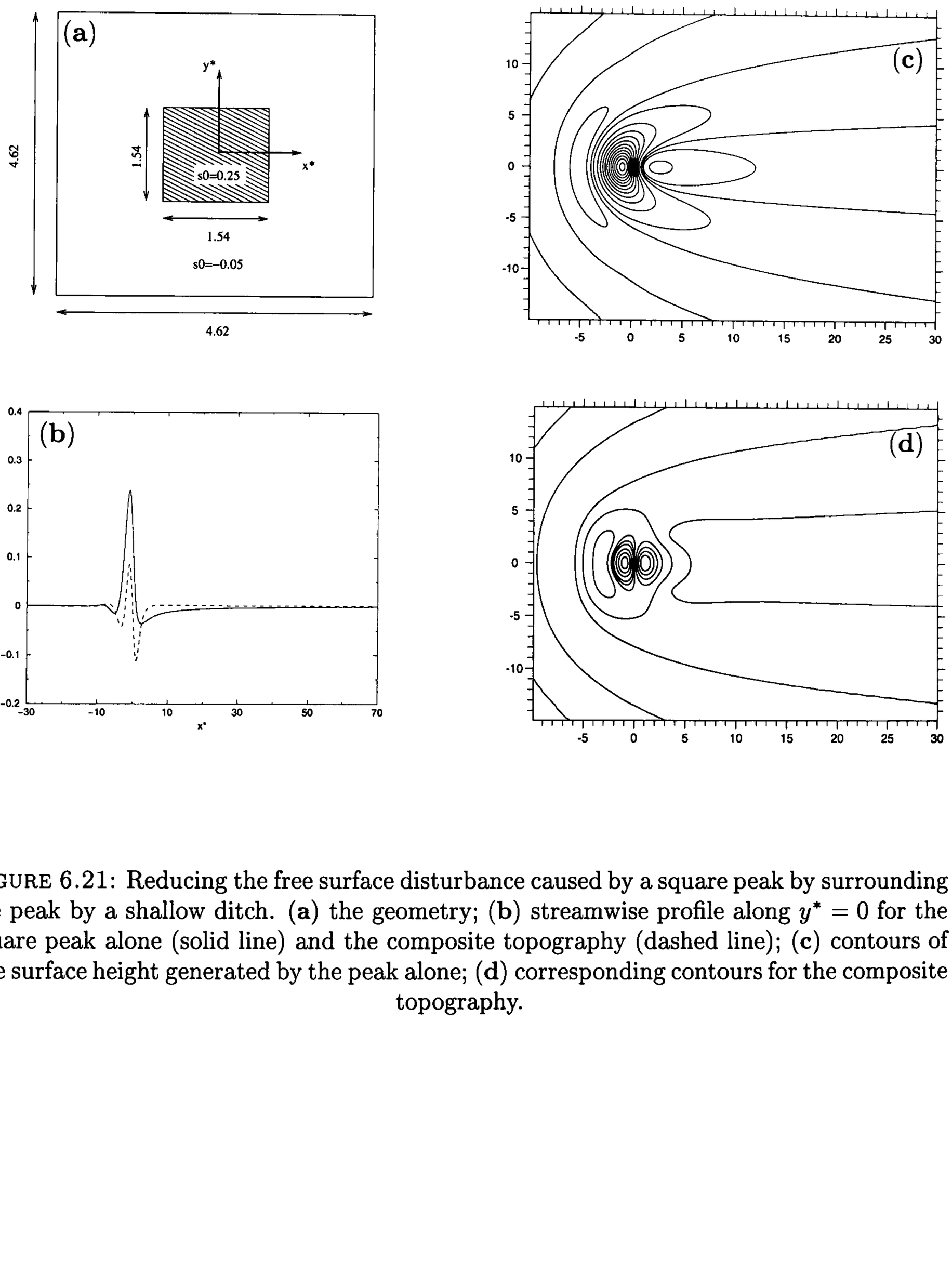

FIGURE 6.21: Reducing the free surface disturbance caused by a square peak by surrounding the peak by a shallow ditch. (**a**) the geometry; (**b**) streamwise profile along $y^* = 0$ for the square peak alone (solid line) and the composite topography (dashed line); (**c**) contours of free surface height generated by the peak alone; (**d**) corresponding contours for the composite topography.

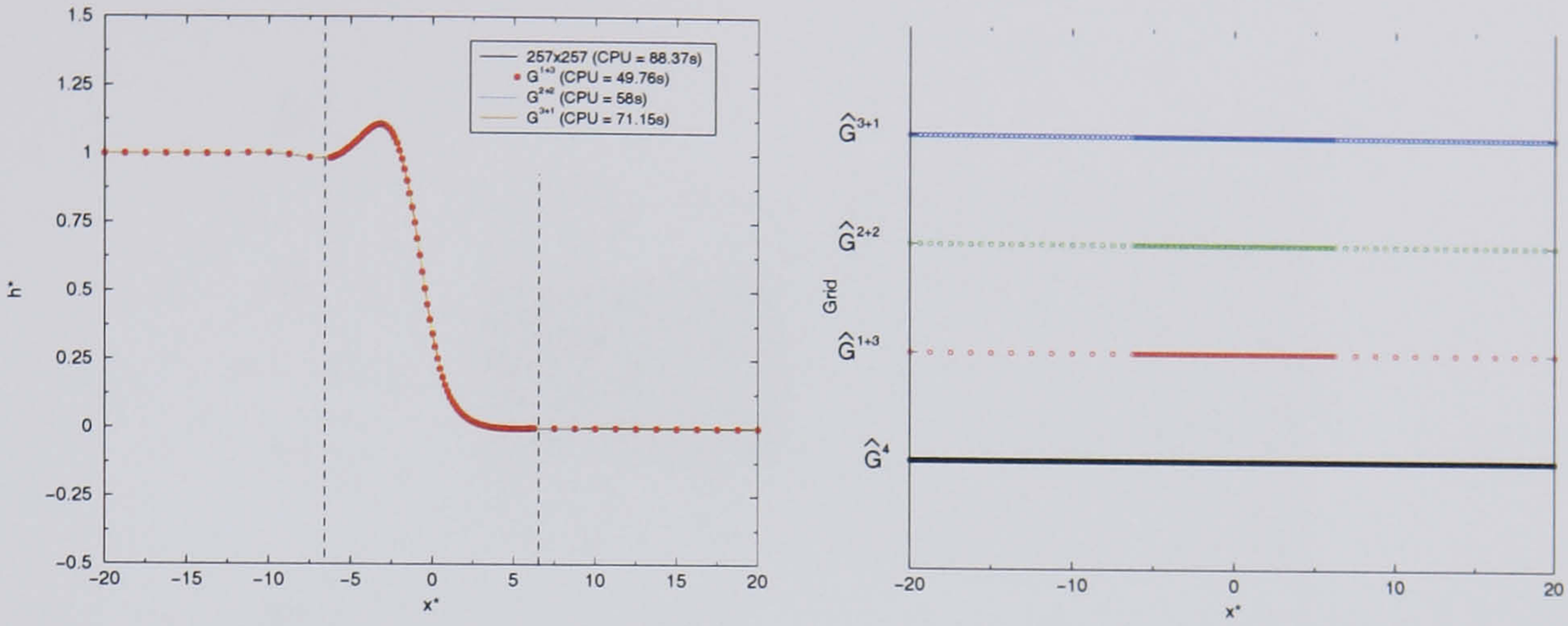

(**a**) Streamwise profile obtained on the uniform grid G^4 and the composite grids, $\widehat{G}^{1+3}$, $\widehat{G}^{2+2}$ and $\widehat{G}^{3+1}$. The dashed lines delimits the refined region.

(**b**) Mesh densities in the streamwise direction of the uniform grid, G^4, and the composite grids, $\widehat{G}^{1+3}$, $\widehat{G}^{2+2}$ and $\widehat{G}^{3+1}$.

FIGURE 6.22: Performance of the $\mathcal{MLAT}$ applied to the step down topography considered in §6.4.1.

on Figure 6.22(**a**). The total CPU time required to reach convergence, shown in the legend of Figure 6.22(**a**), confirms that substantial computational time can be saved without observable loss of accuracy. The most favourable case is for grid $\widehat{G}^{1+3}$, for which the computational time is reduced by almost a factor two with respect to the uniform grid.

The flow over a step down topography is particularly well suited to mesh adaption because the film thickness is uniform in a rather large portion of the computational domain. The flow over the localised trench explored in §6.4.2 presents a greater challenge since the capillary wave triggered by the topography expands downstream of the topography in the spanwise direction. For that reason, numerical solutions were sought on a composite grid having the two refinement patches shown in Figure 6.23. Again, the coarsest grid level, G^0, is 17x17. The first refinement is applied on the 65x65 grid, G^2, and covers a domain ranging from upstream of the topography to the downstream end of the computational domain in order to capture accurately the capillary wave. The second mesh refinement, performed at the next grid level, covers the topography region delimited by the red dashed lines on Figure 6.23 where the steepest variations of the free surface are expected. At the finest grid level, the spatial increment, Δ, is equal to 1/512. Using the notation introduced previously,

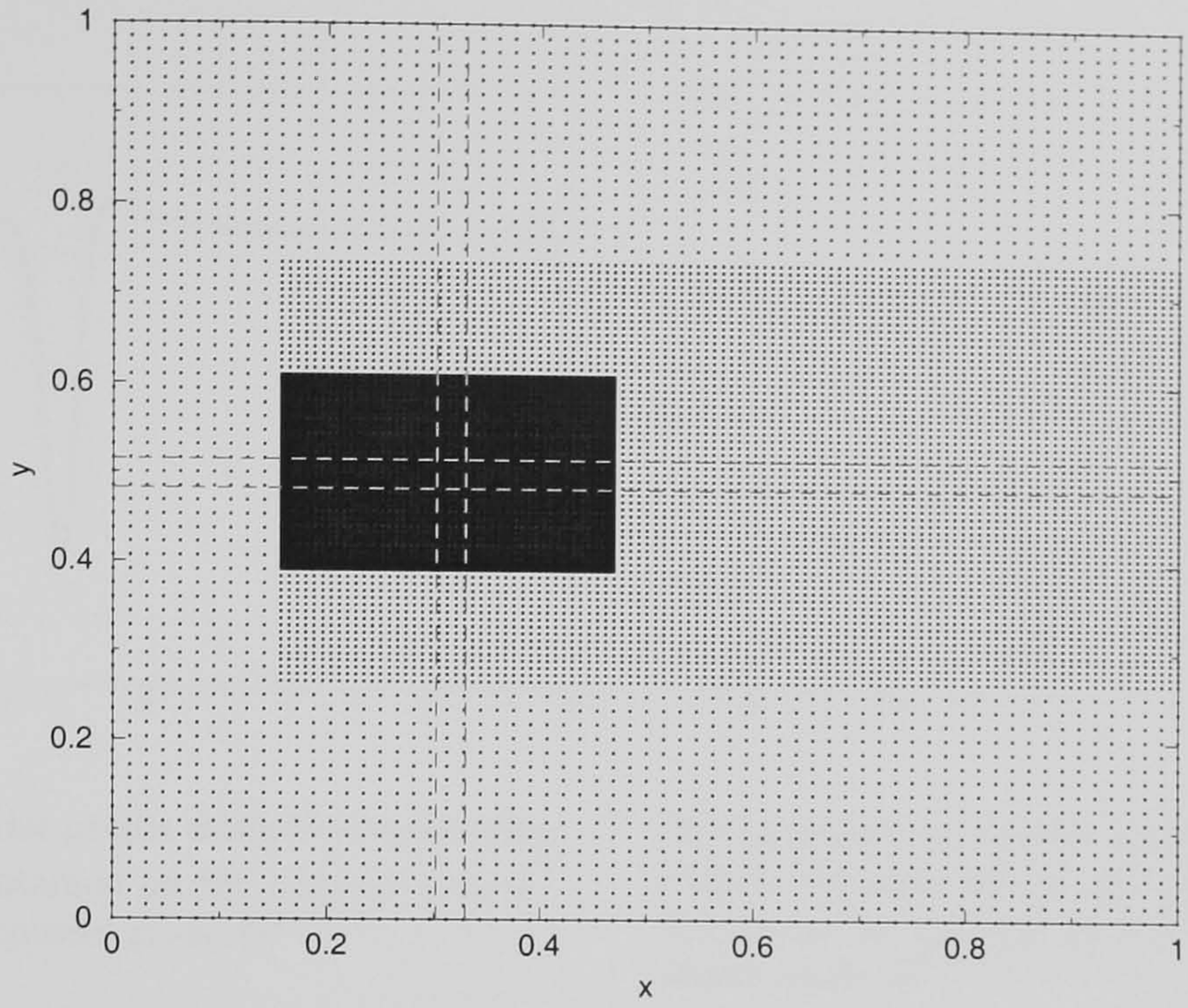

FIGURE 6.23: Mesh density of the composite grid, $\widehat{G}^{2+1+2}$ used to solve the flow over a square trench described in §6.4.2. The red dashed line delimit the topography

the composite grid is therefore denoted, $\widehat{G}^{2+1+2}$. The streamwise free surface profiles along the topography centreline shown on Figure 6.24(**a**) obtained on the uniform and locally refined mesh appear to match perfectly but the spanwise profiles shown on Figure 6.24(**b**) reveal a slight discrepancy at $y^* = 0$. This difference between the two profiles is however smaller than 1% of the maximum film thickness variation and is put into perspective when it is taken into account that calculations on the locally refined grid only took a third of the computational time required on the uniform grid.

In this section, the potential of $\mathcal{MLAT}$ has been highlighted. However, much more work is required to achieve an automatic and robust spatially adaptive algorithm.

6.4.4 Time-dependent inlet flow rate

As pointed out by Bertozzi and Brenner (1997), the fingering instability for moving contact-line problems is linked to the presence of the capillary ridge. This is due to the response of the free surface to pressure build-up in the vicinity of the contact line as a result of the kinematic requirement that the streamwise velocity gradually

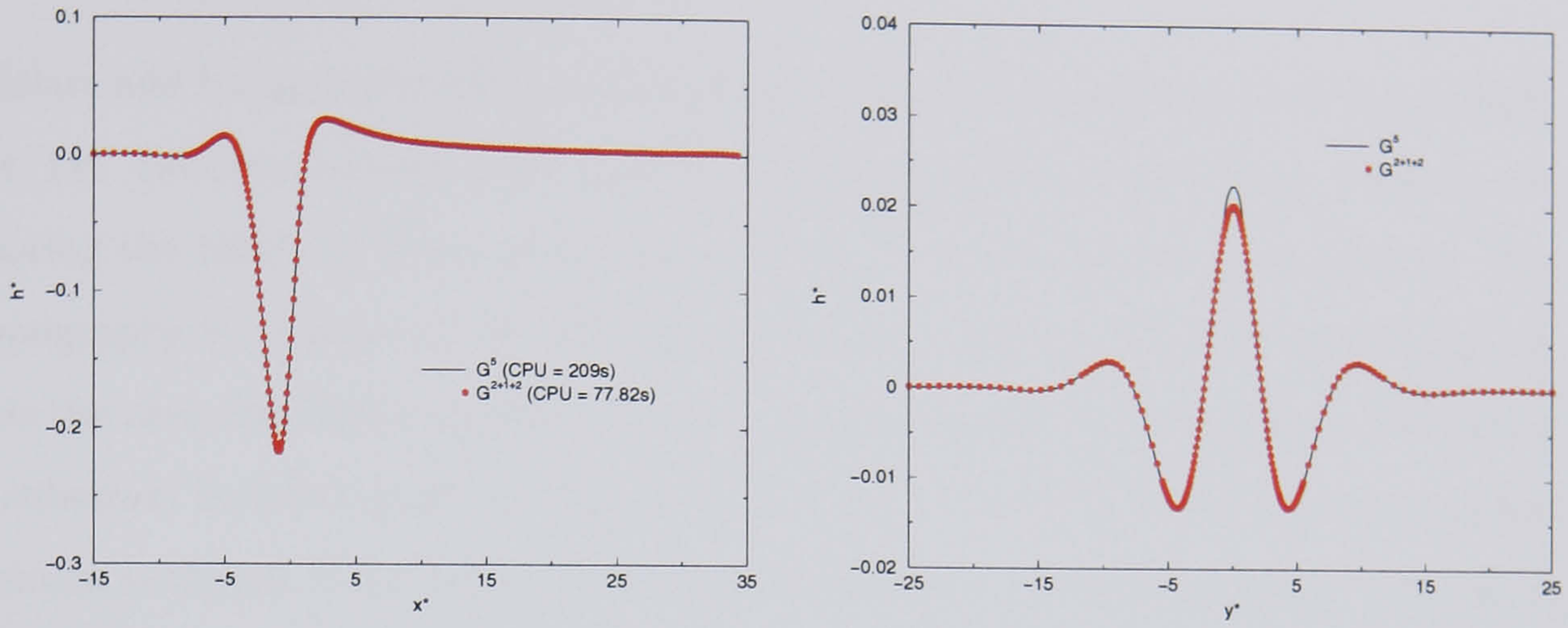

(**a**) Streamwise profile along the topography centreline obtained on the uniform grid G^5 and the composite grids, $\widehat{G}^{2+1+2}$.

(**b**) Spanwise free surface profile 10 capillary lengths downstream of the topography obtained on the uniform grid G^5 and the composite grids, $\widehat{G}^{2+1+2}$.

FIGURE 6.24: Comparison of the streamwise and spanwise free surface profiles for the flow over a square trench described in §6.4.2 obtained on the uniform 513x513 grid (G^5) and the composite grid $\widehat{G}^{2+1+2}$ shown on Figure 6.23.

decays as the contact point is approached and then reverses as fluid leaves the contact region, Goodwin and Homsy (1991). Because of the presence of this capillary ridge for thin film flows over step down topographies, Kalliadasis and Homsy (2001) suggested an analogy with moving contact line problems and analysed the linear stability of the ridge with respect to disturbance in the spanwise direction. Their main result was that the topography-driven ridge is stable for a wide range of pertinent parameters. In a recent study, Bielarz and Kalliadasis (2003) explored further the interaction of free surface disturbances with topographies in an attempt to identify possible unstable regimes. They solved numerically the time-dependent lubrication problem using a semi-implicit $\mathcal{ADI}$ scheme and introduced disturbances to the free surface of various kind; including, step change of the inlet film thickness ("impulse response"), periodic forcing of the film thickness, or adding a drop of liquid on the top of the capillary ridge. The study confirms that flows over topographies are remarkably stable and that the free surface ultimately recovers its undisturbed shape even when inertia effects are included through a modified Reynolds number in the lubrication equation. Only for extremely large value of long-range attractive Van der Waals interaction and large disturbances can the film become unstable. This instability takes the form of a point rupture at the pinch where the deviation height

of the steady-state free surface is a minimum.

Bielarz and Kalliadasis (2003) concentrate mainly on full-width spanwise topographies, i.e. two-dimensional flows and the following results extend their work by exploring the effects of fluctuating flow rate on flows over localised topography. The topography is a square cavity of lateral extent $5L_c$ and depth $0.25H_0$. As previously was the case, the fluid considered is water with asymptotic film thickness 100 μm on a substrate inclined at 30^o so that $L_c = 0.78$ mm. The extent of the computational domain is chosen to be $100L_c$. The time-dependent computations are performed on a 257x257 mesh.

The fluctuating flow rate is represented by a sinusoidal variation of the inlet film thickness: $h(x = 0, y) = 1 + 0.2 \sin\left(\frac{2\pi t}{L_t}\right) \sin\left(\frac{2\pi y}{L_y}\right)$ where $f = 1/L_t$ is the frequency of the perturbation and L_y is the wave length in the spanwise direction. The amplitude of the fluctuation is 0.2 and equation (2.17) implies that the corresponding flow rate variation is $\sim 73\%$. The flow rate is only allowed to fluctuate when the free surface has reached a steady state so that the results do not depend on the choice of initial conditions.

First, fluctuations uniform in the spanwise direction are considered and results are presented for two values of the frequency: $f = 5$ Hz and $f = 20$ Hz in Figure 6.25. This figure shows, as expected, that the high frequency fluctuations ($f = 20$ Hz) are damped much quicker than the low frequency ones ($f = 5$ Hz). The surface tension is responsible for this feature as high frequency fluctuations generate high curvature regions which are quickly smoothed by surface tension (Orchard (1962)).

Fig. 6.25 (**d**), (**f**) and (**h**) illustrate how the cavity may act as an amplifier of the film thickness variations for low frequency of the perturbation. The peaks of the travelling wave upstream and downstream of the topography clearly exceed the inlet amplitude of the film thickness variations (straight solid lines in the figures). Analogous results were found by Kondic and Bertozzi (1999) where small perturbations of the precursor film thickness were found to be largely amplified by an advancing contact line although the value of the amplification factor were found to be much larger in that case. Furthermore, for low frequency of the perturbation, the shape

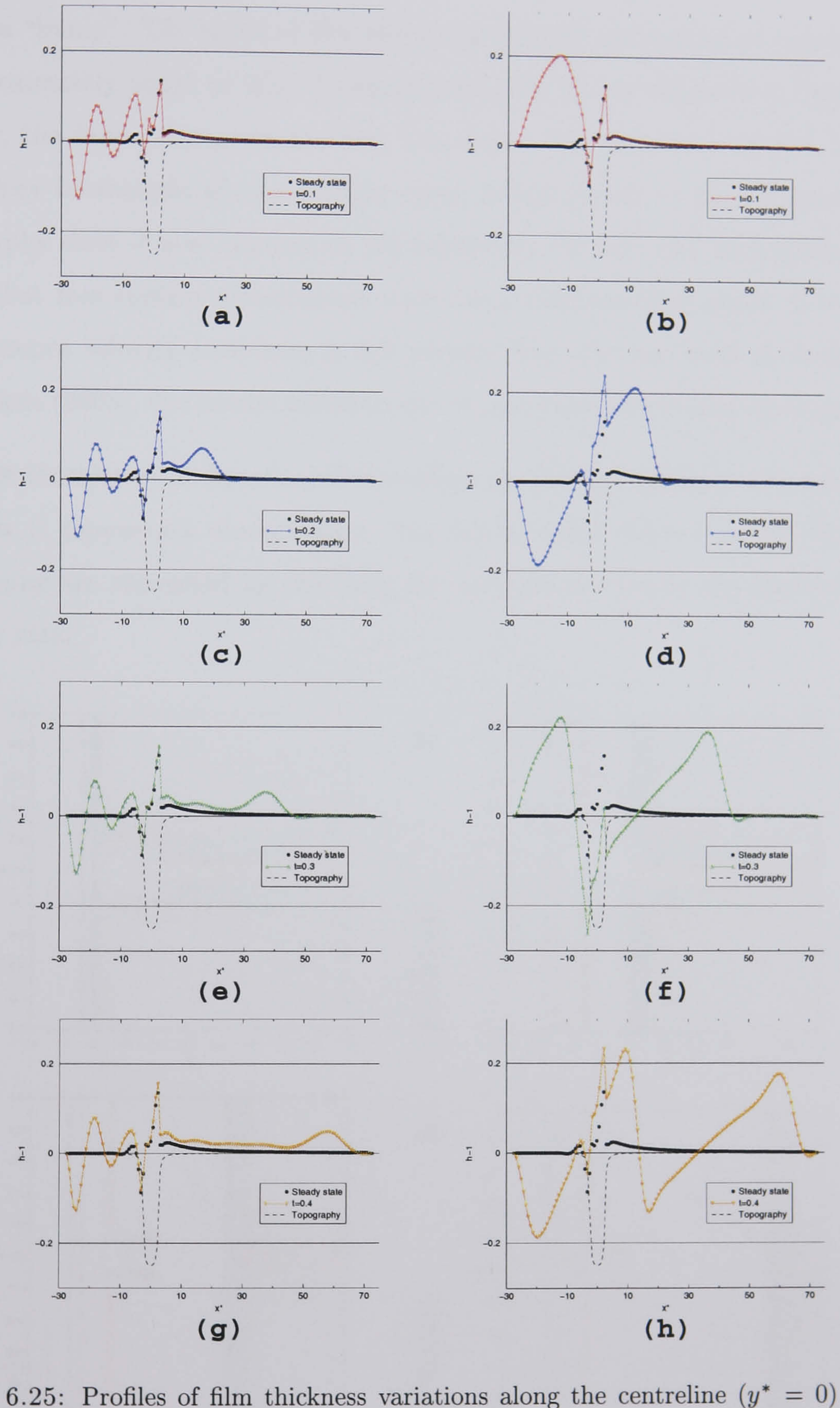

FIGURE 6.25: Profiles of film thickness variations along the centreline ($y^* = 0$) for two different frequencies ($f = 20$ Hz for the figures on the left and $f = 5$ Hz for the figures on the right) at different times for the flow over localised topography: **(a)** and **(b)**: t=0.1, **(c)** and **(d)**: t=0.2, **(e)** and **(f)**: t=0.3, **(g)** and **(h)**: t=0.4.

of the initial sine wave is strongly distorted downstream of the topography.

Another feature which can be observed from fig. 6.25 **(c)**, **(e)** and **(g)** is the forma-

tion of a "bump". The speed of this advancing "bump" appears to be constant and is approximately equal to $2U_0$. Remembering that U_0 corresponds to the surface velocity, the front propagates at twice this value. The formation of this "bump", which may be thought of as a solitary wave, is not related to the presence of the topography since it also appears on flat substrates. Bielarz and Kalliadasis (2003) found that free surface disturbances travel at a dimensionless speed of 3. Since the reference velocity used here is 3/2 greater than the one used in Bielarz and Kalliadasis (2003), the results obtained are in agreement with their findings.

Fig. 6.26 illustrates the structure of the advancing "bump" (indicated by the arrow) and how it propagates downstream. The disturbances created by the finite size topography are convected by the front far downstream due to the fluctuations in the flow rate.

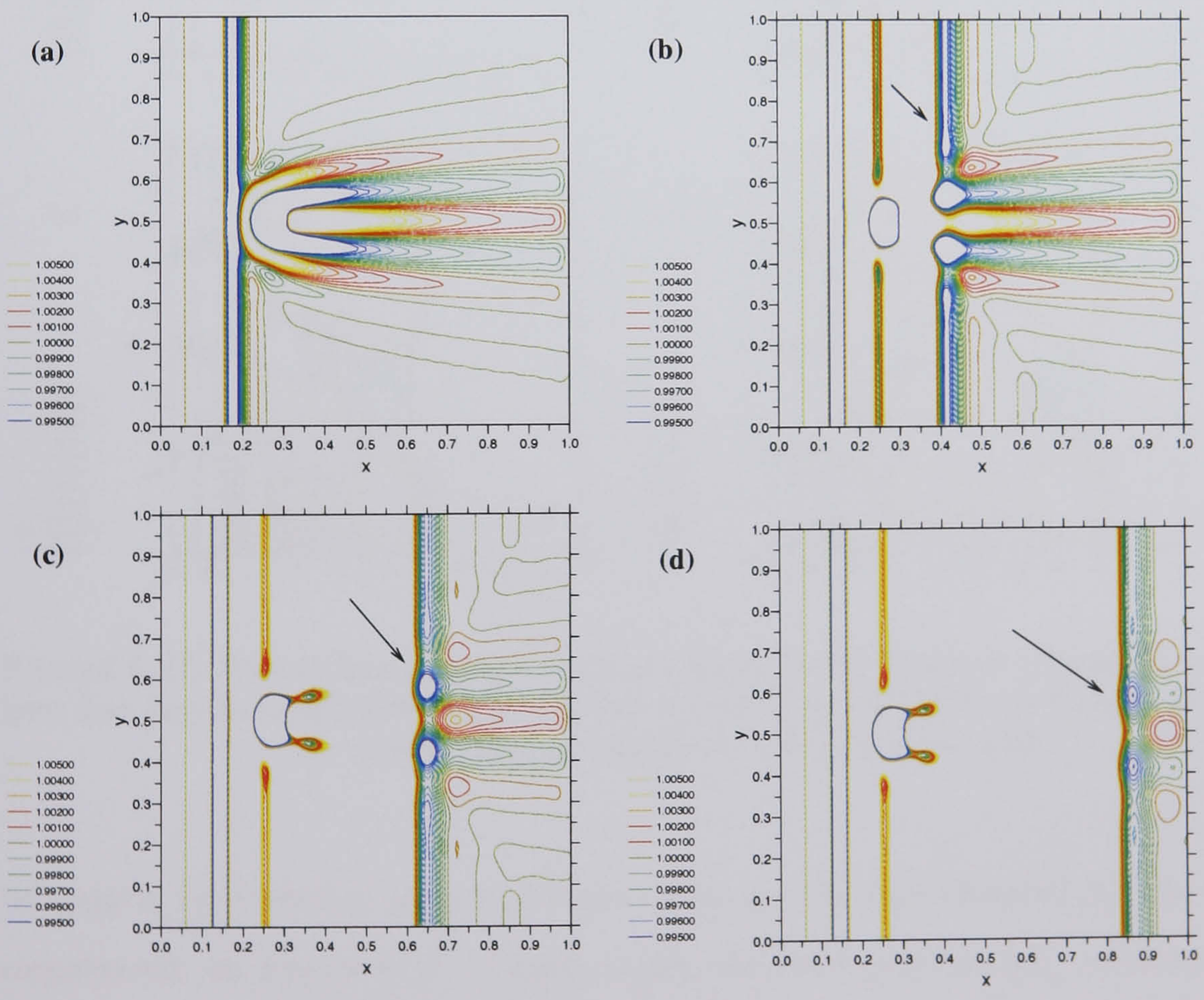

FIGURE 6.26: Free surface contours at various times for the flow over a localised trench and inlet flow rate fluctuating at $f = 20$ Hz: **a**: t=0.05, **b**: t=0.15, **c**: t=0.25 and **d**: t=0.35. Range considered: $0.995 < h + s < 1.005$. The arrow indicates the advancing front.

The addition of a spanwise component in the disturbance yields a rather complex free surface structure as can be seen from Figure 6.27. The flow rate varies again at a 20 Hz frequency and the wave length of the spanwise variation is 0.5. This spanwise perturbation is particularly interesting because in the absence of a perturbation, the free surface is symmetric with respect to the topography centreline in the streamwise direction and the imposed perturbation is antisymmetric with respect to this line. The analysis of the complete sequence on Figure 6.27 is tedious but insight can

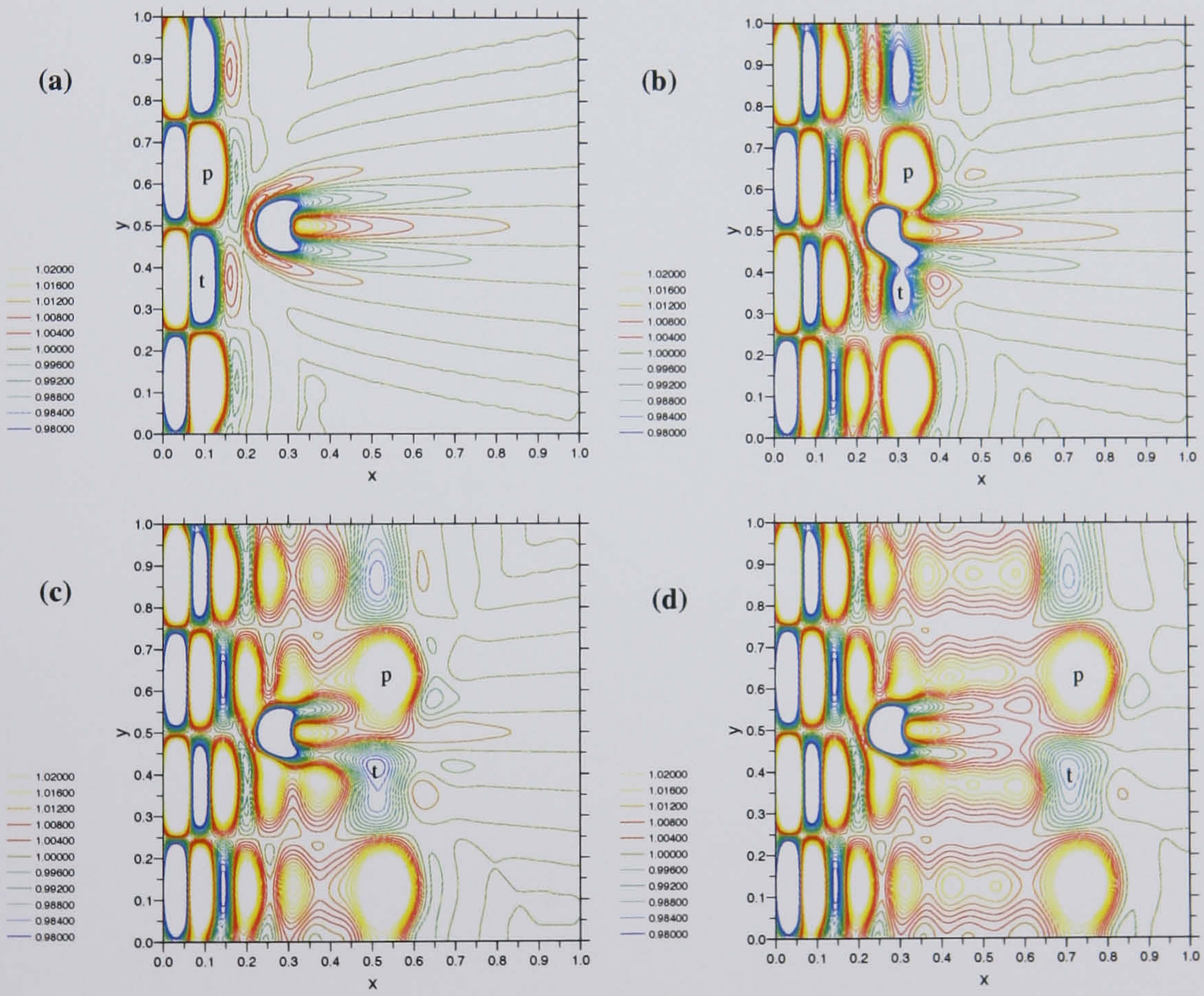

FIGURE 6.27: Free surface contours at various times for the flow over a localised trench and inlet flow rate fluctuating at $f = 20$ Hz and $L_y = 0.5$: **a**: t=0.05, **b**: t=0.15, **c**: t=0.25 and **d**: t=0.35. Range considered: $0.98 < h + s < 1.02$

be gained by focusing on a particular peak and trough denoted by (**p**) and (**t**) respectively on Figure 6.27. Clearly when the peak and trough, advected by the mean flow, collide with the capillary ridge, their response is quite different. The peak (**p**) appears to expand in the streamwise direction as it passes the topography while the trough (**t**) is contracted as can be seen on Figure 6.27(**b**). Despite this contrast in behaviour no phase change is observed in the sense that perturbations

initially aligned in the spanwise direction are still aligned in the spanwise direction far downstream of the topography (see Figure 6.27(**d**)). The appearance of a front discussed in the previous case without spanwise variations can also be seen on Figure 6.27(**d**).

Chapter 7

Evaporating thin films and droplets

Contents

7.1 Introduction

In many coating processes, the liquid deposited is composed of a resin which contains the functional coated material dissolved in a volatile solvent. The evaporation of the solvent and the associated increase in viscosity of the liquid ultimately leaves a solid resin film adhering to the substrate. The main reason why a solvent is used is therefore to increase the coatability of the resin. Typical examples of solvent-based liquids are paints or photoresistent films used in the lithographic stages of microelectronic manufacturing. Solvent evaporation affects the dynamics of thin films and the quality of the coating in many ways because fluid properties generally depend on the solvent fraction. For example, Overdiep's experiment (Overdiep (1986)) reveal that the free surface of some solvent-based high-gloss alkyd paints unexpectedly undergo *reversal* after the levelling of disturbances; that is initial peaks in the free surface become troughs and vice-versa. This result clearly contradicts Orchard's theory of levelling (Orchard (1962)) which predicts that disturbances of the free surface should decay under the action of constant surface tension until complete flatness of the film is reached. To explain this apparent discrepancy in the theory, Overdiep suggested that surface tension gradients induced by solvent concentration variations are responsible for the observed reversal. Based upon this idea Overdiep developed an improved model for the free surface levelling and derived an equation for the optimal choice of parameters to achieve perfect levelling. Eres *et al.* (1999) tackled the reversal problem by solving numerically the lubrication with concentration-dependent surface tension and confirmed Overdiep's suggestion, as their numerical results compared favourably with experiments.

As mentioned previously, the solvent concentration also has a direct effect on the viscosity of the resin/solvent mixture and much work has been done in the context of spin coating to quantify this effect. Meyerhofer (1978) is credited with the first attempt to model the effects of solvent evaporation and variable viscosity on the thickness of dried films during spin coating. The model is effectively one-dimensional since it relies on the assumption that the film thickness and solvent concentration are uniform across the entire substrate and only vary with time. Meyerhofer's

main conclusion is that the thinning of thin films occurs in two stages. The first stage is convection dominated and the effect of evaporation is negligible, but during the second stage only evaporation is responsible for the thinning of the film. By considering these two stages separately, Stillwagon and Larson (1990) computed the free surface profiles of dried film during spin coating over topographies. Meyerhofer's approach was later improved by Bornside *et al.* (1989) who considered variation of the solvent concentration across the film. However, they limited their analysis to one-dimensional flows.

Solvent evaporation can also affect the motion of the contact line. Despite its industrial importance, until the recent work of Parisse and Allain (1996, 1997), little effort was directed towards the fundamental understanding of the shape and composition changes due to solvent evaporation during the spreading of a droplet. Their study revealed that after an initial expansion, the radius of the contact base between the drop and the solid plate remained constant. As soon as evaporation begins, the resin deposits and adheres to the plate leading to a strong anchoring of the wetting line. This phenomenon is known as contact line pinning and a common consequence of it is the brown ring left when a drop of coffee dries on a counter top. This ring formation is due, according to Deegan *et al.* (1997) and Deegan (2000), to the capillary flow in which pinning of the contact line of the drying drop ensures that liquid evaporating from the edge is replenished by liquid from the the bulk of the droplet. The resulting outward flow carries all the dispersed material to the edge.

For modelling purposes, a key parameter is the diffusivity of the solvent as pointed out by Howison *et al.* (1997). If the diffusion of solvent is sufficiently rapid the leading-order distribution of solvent across the film is uniform, leading to the so-called *well-mixed* assumption. This assumption fits naturally in the lubrication formalism for which all quantities are depth averaged and has been used successfully to predict reticulations such as hole formation in drying films (Schwartz *et al.* (2000) and Evans *et al.* (2000)). If the *well-mixed* assumption breaks down then variations of the solvent concentration across the film need to be taken into account and so remaining in the framework of the lubrication approximation is impossible unless the fluid parameters (viscosity, surface tension) are assumed constant across the

film, see van de Fliert (2001).

In this chapter, an evaporation model based on the well-mixed assumption is first described. The governing equations are then solved in the context of a gravity-driven, evaporating thin film assuming that composition variations affect the viscosity only and therefore Marangoni effects can be ignored. An analytical solution is derived for the long-time behaviour of the film on a flat substrate when a steady-state is reached. This analytical solution is used to validate the numerical results and to confirm the assumption made by previous authors (Stillwagon and Larson (1990), Lawrence (1988)) that the presence of a full-width spanwise topography does not affect the composition of the resin/solvent mixture. Results are presented for the case of evaporating flow over localised topographies for which, in contrast to full-width spanwise topographies, composition variation can be observed downstream of the topography leading to possible defects in the dried film. Finally, the model is applied to fully-wetting droplet spreading with results capturing the pinning of the wetting line for high values of the evaporation rate.

7.2 Description of the evaporation model

In this section, the model described in Chapter 2 is extended to account for composition changes in the solvent/resin mixture. Although for results presented subsequently only the viscosity varies with the solvent concentration, modifications to the lubrication approximation (2.29) and (2.30) are presented in the more general form for which surface tension is also a function of the solvent concentration. The effect of surface tension gradient is introduced in the lubrication approximation through the continuity of the shear stress at the free surface. Accordingly, eqs. (2.24) are modified as follows,

$$\frac{\partial u}{\partial z} = \frac{C_5}{\tilde{\mu}} \frac{\partial \tilde{\sigma}}{\partial x} \quad \text{and} \quad \frac{\partial v}{\partial z} = \frac{C_5}{\tilde{\mu}} \frac{\partial \tilde{\sigma}}{\partial y} \quad \text{on} \quad z = \psi(x, y, t) \,, \tag{7.1}$$

where $\tilde{\sigma}$ and $\tilde{\mu}$ are the dimensionless surface tension and viscosity respectively, scaled with the reference surface tension σ_0 and viscosity μ_0. The constant C_5 is scaling

dependent: for droplet spreading flows $C_5 = 1/\epsilon^2$; while for gravity driven films $C_5 = \epsilon/Ca$. The velocity profiles as given by eqs. (2.27) and (2.28) now have the following form,

$$u = \frac{1}{\tilde{\mu}}\left(\frac{\partial p}{\partial x} - C_1\right)(z-s)\left(\frac{1}{2}(z-s) - h\right) + \frac{C_5}{\tilde{\mu}}\frac{\partial \tilde{\sigma}}{\partial x}(z-s)\,, \tag{7.2}$$

$$v = \frac{1}{\tilde{\mu}}\left(\frac{\partial p}{\partial y}\right)(z-s)\left(\frac{1}{2}(z-s) - h\right) + \frac{C_5}{\tilde{\mu}}\frac{\partial \tilde{\sigma}}{\partial y}(z-s)\,. \tag{7.3}$$

The corresponding components of the flux vector, $\underline{Q}$, defined as $(Q_x, Q_y)^T = \int_s^\psi (u, v)^T \, dz$ are:

$$Q_x = -\frac{h^3}{3\tilde{\mu}}\left(\frac{\partial p}{\partial x} - C_1\right) + C_5\frac{h^2}{2\tilde{\mu}}\frac{\partial \tilde{\sigma}}{\partial x}\,, \tag{7.4}$$

$$Q_y = -\frac{h^3}{3\tilde{\mu}}\left(\frac{\partial p}{\partial y}\right) + C_5\frac{h^2}{2\tilde{\mu}}\frac{\partial \tilde{\sigma}}{\partial y}\,, \tag{7.5}$$

which when combined with the conservation of mass equation, modified to account for the mass loss due to evaporation, yield the lubrication approximation in its general form,

$$\frac{\partial h}{\partial t} = \frac{\partial}{\partial x}\left[\frac{h^3}{3\tilde{\mu}}\left(\frac{\partial p}{\partial x} - C_1\right) - C_5\frac{h^2}{2\tilde{\mu}}\frac{\partial \tilde{\sigma}}{\partial x}\right] + \frac{\partial}{\partial y}\left[\frac{h^3}{3\tilde{\mu}}\left(\frac{\partial p}{\partial y}\right) - C_5\frac{h^2}{2\tilde{\mu}}\frac{\partial \tilde{\sigma}}{\partial y}\right] - e\,. \tag{7.6}$$

In (7.6) $e = E/(\epsilon U_0)$ is the constant dimensionless evaporation rate. This restricting assumption could be improved by using a composition dependent evaporation rate as in Weidner *et al.* (1996) and Schwartz *et al.* (2000). The pressure across the film is unchanged in this model and is still given by eq. (2.30). Note however that the values of C_1, C_2, C_3 and C_4 are now defined in terms of the reference values of the viscosity, μ_0, and surface tension, σ_0.

An additional equation is required to describe the evolution of the solvent concentration, c_s. Howison *et al.* (1997) showed that the well-mixed approximation is valid providing the solvent diffusion, D, satisfies $D \gg \epsilon^2 L_0 U_0$. In the following, it will be assumed that this condition holds. At leading order, the conservation of mass of solvent (Howison *et al.* (1997)) reads:

$$\frac{\partial (hc_s)}{\partial t} + \nabla.\left(c_s \underline{Q}\right) = -e + d\nabla.\left(h\nabla c_s\right)\,, \tag{7.7}$$

where $d = D/L_0U_0$ is the dimensionless solvent diffusion. Making the additional assumption that lateral diffusion in eq. (7.7) is largely dominated by convection, which is true if $D \ll L_0U_0$, and combining eqs. (7.7) and (7.6) yields,

$$\frac{\partial c_s}{\partial t} = \left[\frac{h^2}{3\tilde{\mu}}\left(\frac{\partial p}{\partial x} - C_1\right) - C_5\frac{h}{2\tilde{\mu}}\frac{\partial \tilde{\sigma}}{\partial x}\right]\frac{\partial c_s}{\partial x} + \left[\frac{h^2}{3\tilde{\mu}}\left(\frac{\partial p}{\partial y}\right) - C_5\frac{h}{2\tilde{\mu}}\frac{\partial \tilde{\sigma}}{\partial y}\right]\frac{\partial c_s}{\partial y} + e\frac{(c_s - 1)}{h}. \tag{7.8}$$

For gravity driven thin liquid films, a fixed solvent concentration, c_0, is imposed at the inlet ($x = 0$) and the initial solvent concentration profile is uniform, also equal to c_0, in the entire computational domain. In the case of droplet spreading, the gradient of the solvent concentration across the boundary is set to zero and initial solvent concentration is constant and equal to c_0. Equations (7.6), (2.30) and (7.8) constitute the governing equation bearing in mind that Marangoni effects resulting from surface tension gradients are not considered here.

7.3 Solution methodology

The multigrid algorithm described in Chapter 3 is extended to solve the additional solvent concentration equation. An advantage of the multigrid method is that providing the relaxation scheme and coarse grid solver are suitably modified, the algorithm remains essentially unchanged. The following subsection describes the discretisation scheme adopted.

7.3.1 Discretisation scheme

Solutions are sought on a square computational domain with $(x, y) \in \Omega = (0, 1) \times (0, 1)$ using a uniform mesh having $(2^{k_f} + 1)$ nodes in each direction. The discrete analogue of eq. (7.6) is the intuitive extension of eq. (3.1) since the only difference, apart from the additional evaporation term, is the presence of the composition-

dependent viscosity in the prefactor; that is $\Gamma(h) = \frac{h^3}{3\tilde{\mu}}$. Thus,

$$\frac{\partial h_{i,j}}{\partial t} = \frac{1}{\Delta^2}\left[\frac{h^3}{3\tilde{\mu}}|_{i+\frac{1}{2},j}\left(p_{i+1,j} - p_{i,j}\right) - \frac{h^3}{3\tilde{\mu}}|_{i-\frac{1}{2},j}\left(p_{i,j} - p_{i-1,j}\right) + \frac{h^3}{3\tilde{\mu}}|_{i,j+\frac{1}{2}}\left(p_{i,j+1} - p_{i,j}\right) - \frac{h^3}{3\tilde{\mu}}|_{i,j-\frac{1}{2}}\left(p_{i,j} - p_{i,j-1}\right)\right] - \frac{C_1}{\Delta}\left(\frac{h^3}{3\tilde{\mu}}|_{i+\frac{1}{2},j} - \frac{h^3}{3\tilde{\mu}}|_{i-\frac{1}{2},j}\right) - e + O(\Delta^2)\ , \tag{7.9}$$

for any interior point (i,j) in the computational domain where, as mentioned previously, $\Delta = 2^{-k_f}$ is the spatial increment. The Standard Scheme described in §3.2 was implemented for the mid-point interpolation of the prefactors leading to,

$$\frac{h^3}{3\tilde{\mu}}|_{i\pm\frac{1}{2},j} = \frac{1}{2}\left(\frac{h^3}{3\tilde{\mu}}|_{i\pm1,j} + \frac{h^3}{3\tilde{\mu}}|_{i,j}\right)\ , \tag{7.10}$$

with analogous expressions for $\frac{h^3}{3\tilde{\mu}}|_{i,j\pm\frac{1}{2}}$. The discretisation of eq. (2.30) is unchanged and given by eq. (3.2) while the discrete form of the solvent concentration equation (eq. 7.8) is obtained using central differences, viz

$$\frac{\partial c_{si,j}}{\partial t} = \frac{h_{i,j}^2}{12\tilde{\mu}_{i,j}\Delta^2}\left[\left(p_{i+1,j} - p_{i-1,j}\right)\left(c_{si+1,j} - c_{si-1,j}\right) + \left(p_{i,j+1} - p_{i,j-1}\right)\left(c_{si,j+1} - c_{si,j-1}\right)\right] - C_1\frac{h_{i,j}^2}{6\tilde{\mu}_{i,j}\Delta}\left(c_{si+1,j} - c_{si-1,j}\right) + e\frac{\left(c_{si,j} - 1\right)}{h_{i,j}} + O(\Delta^2)\ , \tag{7.11}$$

for any interior point (i,j) in the computational domain.

The adaptive time-stepping scheme described in §3.3 is employed for the results, concerning droplet spreading, presented subsequently to march the solution forward in time. Note however that, because the time derivative now appears in both eqs. (7.9) and (7.11), the time step selection is based on the equation having the largest estimated truncation error. This ensures that both equations are solved with the same prescribed error tolerance.

7.3.2 Relaxation scheme and coarse grid solver

The relaxation scheme adopted here consists of a non-linear Gauss-Seidel scheme with a single local Newton iteration for each update. It is most clearly described by rewriting the discrete system of governing equations (7.9), (3.2) and (7.11) at the finest grid level L in the following condensed form:

$$\mathcal{L}_L^h\left(\underline{h}_L^{n+1}, \underline{p}_L^{n+1}, \underline{c_s}_L^{n+1}\right) = f_L^h\left(\underline{h}_L^n, \underline{p}_L^n, \underline{c_s}_L^n\right), \tag{7.12}$$

$$\mathcal{L}_L^p\left(\underline{h}_L^{n+1}, \underline{p}_L^{n+1}\right) = 0, \tag{7.13}$$

$$\mathcal{L}_L^{c_s}\left(\underline{h}_L^{n+1}, \underline{p}_L^{n+1}, \underline{c_s}_L^{n+1}\right) = f_L^{c_s}\left(\underline{h}_L^n, \underline{p}_L^n, \underline{c_s}_L^n\right), \tag{7.14}$$

where f_L^h and $f_L^{c_s}$ correspond to the right-hand side of eq. (3.8) with $\Theta_t = \frac{1}{2}$ when $F = \frac{\partial h_{i,j}}{\partial t}$ and $F = \frac{\partial c_{s\,i,j}}{\partial t}$ respectively.

This nonlinear system of equations is linearised by computing the local Jacobian, $\underline{\underline{J}}$, only: i.e. for a particular grid level k,

$$\underline{\underline{J}} = \frac{\partial\left(\mathcal{L}_k^h, \mathcal{L}_k^p, \mathcal{L}_k^{c_s}\right)}{\partial\left(h_{i,j}^{n+1}, p_{i,j}^{n+1}, {c_s}_{i,j}^{n+1}\right)}. \tag{7.15}$$

Thus, given an initial guess $({h_0}_{i,j}^{n+1}, {p_0}_{i,j}^{n+1}, {c_{s0}}_{i,j}^{n+1})$ to the solution, the Newton iteration proceeds by solving

$$\underline{\underline{J}}\begin{pmatrix}\Delta h\\ \Delta p\\ \Delta c_s\end{pmatrix} = \begin{pmatrix} f_k^h - \mathcal{L}_k^h\left({h_0}_{i,j}^{n+1}, {p_0}_{i,j}^{n+1}, {c_{s0}}_{i,j}^{n+1}\right)\\ f_k^p - \mathcal{L}_k^p\left({h_0}_{i,j}^{n+1}, {p_0}_{i,j}^{n+1}\right)\\ f_k^{c_s} - \mathcal{L}_k^{c_s}\left({h_0}_{i,j}^{n+1}, {p_0}_{i,j}^{n+1}, {c_{s0}}_{i,j}^{n+1}\right)\end{pmatrix}, \tag{7.16}$$

for $(\Delta h, \Delta p, \Delta c_s)$. Hence a new approximation to the solution is given by: $\widetilde{{h_0}_{i,j}}^{n+1} = {h_0}_{i,j}^{n+1} + \Delta h$, $\widetilde{{p_0}_{i,j}}^{n+1} = {p_0}_{i,j}^{n+1} + \Delta p$ and $\widetilde{{c_{s0}}_{i,j}}^{n+1} = {c_{s0}}_{i,j}^{n+1} + \Delta c_s$. The local Jacobian matrix $\underline{\underline{J}}$ is 3x3 and its inversion is eased by the fact that the equation governing the pressure across the film, (3.2), does not explicitly depend on the solvent concentration.

In order to find the exact solution at the coarsest grid level the approach described

in §3.4, for which the complete Jacobian matrices were computed, becomes too computationally expensive. To give an idea, for a 17x17 coarsest grid level, this would involve handling nine 287x287 matrices. For this reason, it was found to be preferable to apply the previously described relaxation scheme until the norm of the residuals becomes smaller than 10^{-10}, an arbitrary small number.

7.4 Results and discussion

The evaporation model described in the previous section is applied to the two different types of flow investigated in the previous chapters: droplet spreading and gravity-driven thin films.

7.4.1 Gravity-driven, evaporating thin liquid films

Continuous, evaporating film over a flat substrate

The problem of a pure liquid film draining down a flat, inclined plane in the constant flux configuration is trivial in the absence of evaporation, yielding a liquid film of uniform thickness. This behaviour can no longer be expected when the composition of the resin/solvent mixture induces viscosity variations. Because of the increasing solvent loss and associated increase in viscosity when the fluid travels further and further downstream, intuition suggests that, faced with a greater viscous resistance, the free surface should rise. Making the same assumptions as Huppert (1982) who investigated the fingering instability in gravity-driven thin films down a slope, a simple analytical solution for the film thickness, the solvent concentration and therefore the viscosity can be found providing a convenient way to validate the numerical results. Huppert (1982) assumed that the effects of the surface tension and the component of the gravity normal to the substrate could be neglected so that the fluid motion is dictated by a balance between the tangential component of the gravity driving the liquid and viscous stresses. In that case, Huppert derived a simple similarity solution which describes the evolution of the free surface as a function of time.

While Huppert considered the evolution of a constant amount of liquid leading necessarily to a time-dependent problem, a steady-state solution can be expected in the present configuration since the film is fed by a constant flux at the inlet. Taking these assumptions into account, eqs. (7.6) and (7.8) reduce to:

$$-C_1 \frac{d}{dx}\left[\frac{h^3}{3\tilde{\mu}}\right] - e = 0\,, \tag{7.17}$$

$$-C_1 \frac{h^2}{3\tilde{\mu}} \frac{dc_s}{dx} + e\frac{(c_s - 1)}{h} = 0\,, \tag{7.18}$$

where the constant C_1 is equal to 2 for gravity-driven thin film (see Chapter 2) and the partial derivatives can be replaced by total derivatives since, on a flat substrate, the film thickness and solvent concentration no longer vary in the spanwise direction. The first equation (eq. (7.17)) is trivial to integrate yielding,

$$\frac{h^3}{3\tilde{\mu}} = -e\frac{x}{2} + K_1\,, \tag{7.19}$$

and given that upstream, $h(x = 0) = \tilde{\mu}(x = 0) = 1$, the constant of integration K_1 is easily determined and equal to 1/3. Combining eqs. (7.19) and (7.18) gives the following ODE:

$$\left(ex - \frac{2}{3}\right)\frac{dc_s}{dx} + e(c_s - 1) = 0\,. \tag{7.20}$$

The solution of this ODE is also easily found and has the following form:

$$c_s = \frac{K_2}{ex - \frac{2}{3}} + 1\,, \tag{7.21}$$

where the integration constant, K_2, is imposed by letting $c_s(x = 0) = c_0$, giving

$$c_s = \frac{\frac{2}{3}(1 - c_0)}{ex - \frac{2}{3}} + 1\,. \tag{7.22}$$

For a given dependence of the viscosity on the solvent concentration ($\tilde{\mu}(c_s)$), the film thickness is obtained through eq. (7.19),

$$h = \left(3\tilde{\mu}\left(-e\frac{x}{2} + \frac{1}{3}\right)\right)^{1/3}\,. \tag{7.23}$$

Equation (7.22) reveals that the solvent evaporates completely ($c_s = 0$) at $x = \frac{2}{3}\frac{c_0}{e}$

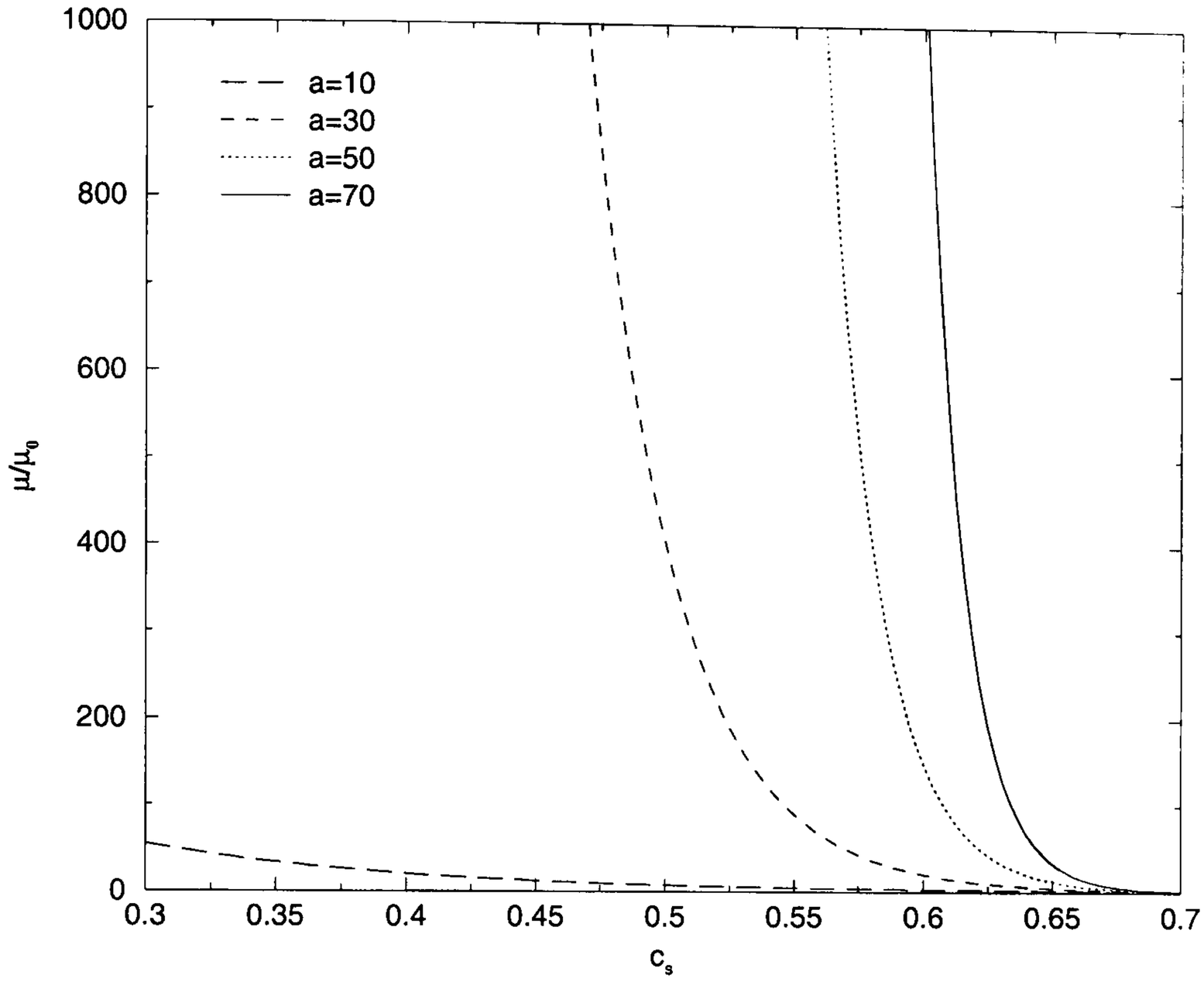

FIGURE 7.1: Variation of the viscosity with the solvent concentration for different values of a.

or $X = \frac{Q_0 c_0}{E}$ in terms of dimensional quantities. This result simply asserts the conservation of the solvent, since $Q_0 c_0$ is the inlet flux of solvent and EX is the amount of solvent lost through evaporation. The film thickness at this location is $h = (\tilde{\mu}(c_s = 0)(1 - c_0))^{1/3}$ and tends to infinity since, in the absence of solvent, the resin is solid and therefore has an infinite viscosity. Following Schwartz *et al.* (2000), the viscosity is assumed to depend exponentially on the solvent fraction, obeying:

$$\mu = \mu_0 e^{a(c_0 - c_s)} , \tag{7.24}$$

so that the viscosity is effectively infinite for small solvent concentrations. The parameter a, chosen to be equal to 70 for the present case, as in Schwartz *et al.* (2000), and controls the sensitivity of the viscosity to solvent concentration variations.

The viscosity is plotted on Figure 7.1 as a function of the solvent concentration for different values of a and $c_0 = 0.7$. Note that, in this model, the viscosity depends on the variation of the solvent concentration from its initial value. The graph shows that

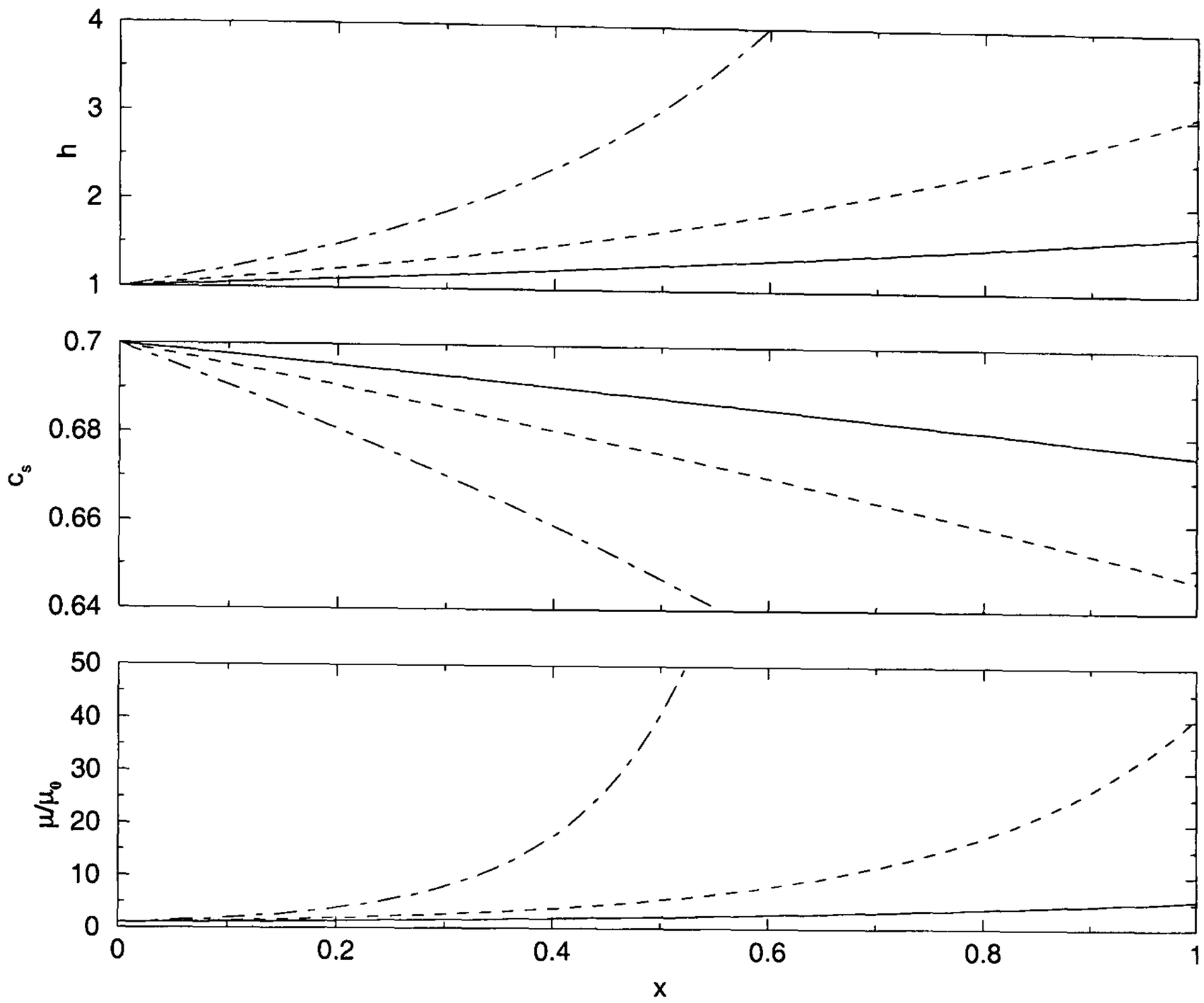

FIGURE 7.2: Theoretical streamwise profiles of film thickness, solvent concentration and viscosity (eqs. (7.23), (7.22) and (7.24)) for a gravity-driven film on a flat substrate with various evaporation rates (—— : e=0.05; - - - : e=0.1; – - –: e=0.2).

for $a = 70$, a small decrease in the solvent concentration leads to a sharp increase of the viscosity. The theoretical profiles of film thickness, solvent concentration and viscosity given by eqs. (7.23), (7.22) and (7.24) respectively are plotted on Figure 7.2 for different values of the evaporation rate, $c_0 = 0.7$ and $a = 70$. As expected, the decrease of solvent concentration induces an increase of the resin/solvent mixture viscosity which in turn leads to a rise in the film thickness as the film flows further and further downstream. For the largest value of the evaporation rate ($e = 0.2$), the film thickness increases dramatically and of course, in practice, the formation of a solid plug would stop the flow and induce instabilities not encompassed in the simple analysis given above.

The analytical solutions for an evaporation rate of 0.05 shown in Figure 7.2 are compared with numerical results for an evaporating thin film down a plane inclined at an angle of 30^o to the horizontal. Following on from previous work, the base

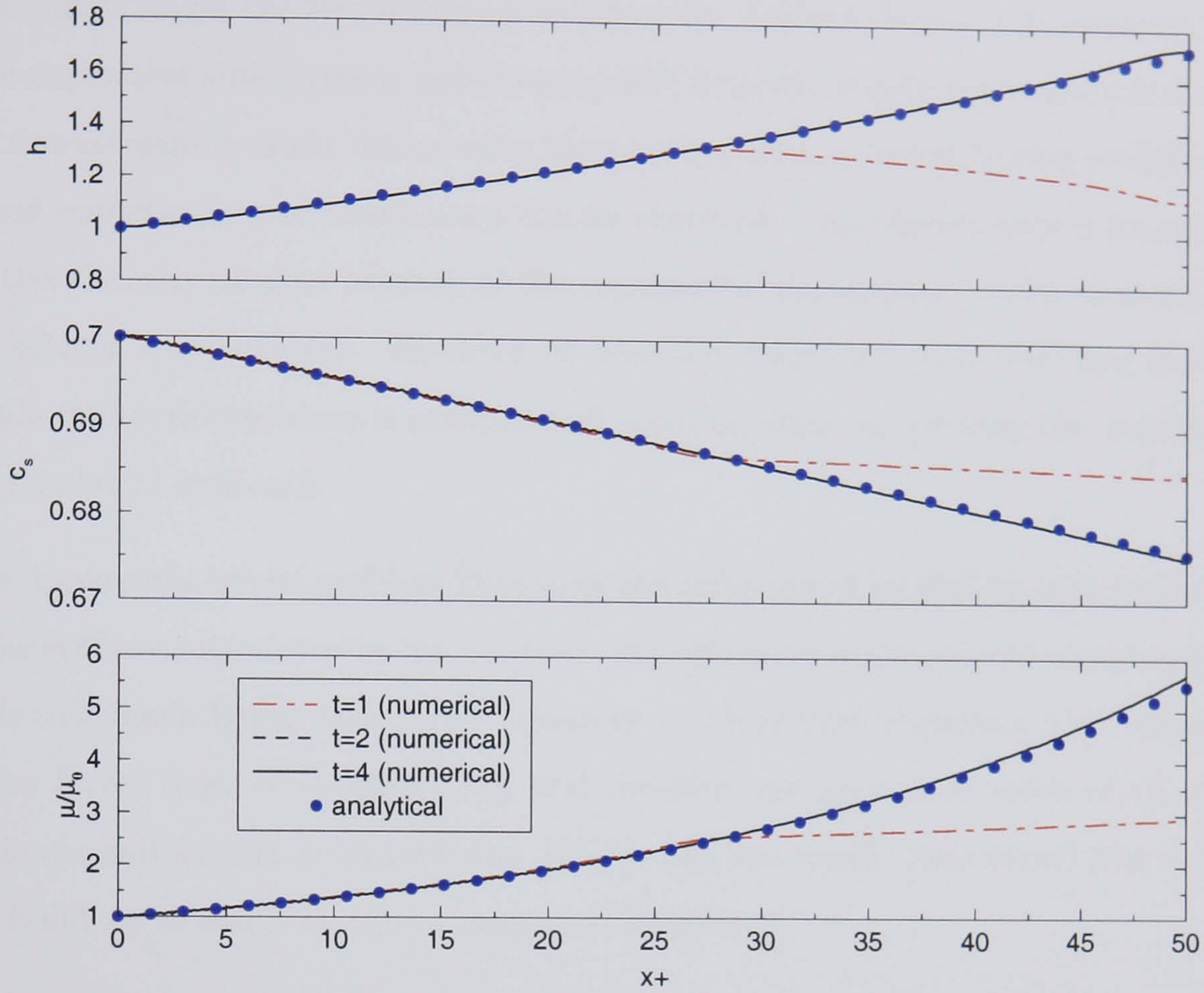

FIGURE 7.3: Comparison the streamwise profiles of film thickness, solvent concentration and viscosity obtained numerically at $t = 1$, $t = 2$ and $t = 4$ and analytically (eqs. (7.23), (7.22) and (7.24)) for a gravity-driven film on a flat substrate.

property are those of water, i.e. $\mu_0 = 0.001$ Pa s, $\rho = 1000$ kg m^{-3}, $\sigma = 0.07$ N m^{-1}. The inlet flow rate is imposed so that the asymptotic film thickness, H_0, is effectively equal to 100 μm according to eq. (2.17). Numerical simulations are obtained on a computational domain that is 50 capillary lengths long, using a finest grid level of 257x257 and a coarsest one of 9x9. Fixed time-steps equal to 5×10^{-3} are used along with the Crank-Nicholson scheme described in §3.3. The use of the adaptive time-stepping scheme was not found to be necessary because of the possibility to use large time-steps. The initial conditions are a film of uniform thickness ($h(x, t = 0) = 1$) and uniform solvent concentration ($c_s(x, t = 0) = c_0 = 0.7$). Unless stated otherwise, these flow conditions and numerical parameters are used to obtain the results which follow for the case of gravity-driven thin liquid films.

Figure 7.3 shows the profiles of film thickness, solvent concentration and viscosity obtained at different times ($t = 1$, $t = 2$ and $t = 4$) and confirms that, after a tran-

sient initial stage, the film reaches a steady-state. Indeed, from $t = 2.$ onwards, the time-dependent simulation is indistinguishable from the steady-state analytical one. Far downstream, a slight discrepancy between the solvent concentration profiles obtained numerically and analytically can be observed. This discrepancy is magnified for the viscosity profiles because of the exponential dependence of the viscosity on the solvent concentration. However, it does not cause the numerical free surface profile to deteriorate since it matches well the analytical one proving the validity of the numerical approach.

This apparently trivial problem illustrates the difficulty of modelling such flows due to the stiffness introduced by the viscosity. A slight error in the solvent concentration leads to a much larger error in the viscosity which in turn induces a poor estimate of the fluxes (eqs. (7.4) and (7.5)), and therefore an inaccurate value of the film thickness and solvent concentration. Hence, one can easily understand how errors can build up to result in a poor numerical solution.

Continuous, evaporating film over a full-width spanwise topography

The previous chapter revealed that flow over step-up topographies without solvent evaporation produce a depression in advance of the step followed by a film thickness increase and an exponential recovery downstream of the step. On the other hand, trenches of small extent create a capillary ridge ahead of the free surface depression over the trench. The question of interest in this section is whether these disturbances of the film thickness will be amplified by the solvent evaporation. The goal is to validate the assumption made by previous authors that the evolution of the film profile can be divided into two stages, with fluid flow dominating the first stage and solvent evaporation the second (Stillwagon and Larson (1990), Lawrence (1988)). In the first, or flow, stage of the model, the film profile over a feature is assumed to be controlled by a balance of the driving force and the capillary force within the lubrication approximation. This stage persists until solvent evaporation makes the film viscous enough that fluid rearrangement over a substrate feature is no longer possible. In the second, or shrinkage, stage, the film shrinks without flow by further evaporative drying. The transition between the two stages is assumed

to occur abruptly at a given solvent concentration. This two stage decomposition necessarily implies that during the first stage, the topography and associated free surface disturbance does not affect the composition of the resin/solvent mixture.

The flow over a step up is considered first. Numerical results are obtained for a step height of 0.5 (half the asymptotic film thickness) and $\gamma = 0.05$ in eq. (6.4). The profile of the topography can be seen on Figure 7.4. The flow conditions and numerical parameters are identical to those described in the previous section. As in the related case without topography, Figure 7.4 shows that, as the viscosity increases, the film thickness increases with downstream location. Despite this increase in the film thickness, the same free surface features can be observed as in the case without evaporation. These features appear to be simply shifted vertically.

Figure 7.4 also displays the fictitious "resin/solvent interface" defined by $h_r + s$ where $h_r = (1 - c_s)h$. This interface, which represents the dried film profile if all the solvent evaporated instantaneously, is fictitious since the resin and solvent phase are mixed and therefore not delimited by an interface. Nevertheless it still provides insight about the effect of the topography on the composition of the resin/solvent mixture. Because this interface displays the same characteristic features as the free surface, the effect of the topography on the composition of the mixture can be anticipated as small. A more quantitative picture can be achieved by comparing the numerical results with the analytical solutions for a flat substrate (eqs. (7.23), (7.22) and (7.24)) derived above. Although this analytical solution can not be expected to be valid in the topography region, significant differences far from the topography would reveal that the topography has an effect on the composition of the mixture. In other words, for the flow over a step-up topography, the film thickness only departs from the film thickness for the flow over a flat substrate in the step region. Hence, any differences between the solvent concentration profile for the flow over the step-up and the flow over a flat substrate could be attributed to the presence of the step-up. The good match for the solvent concentration and viscosity shown in Figure 7.5 confirms that the presence of the step-up does not have any observable influence on the composition of the resin/solvent mixture. It is therefore not surprising that the film thickness obtained numerically and analytically also agree well away from the

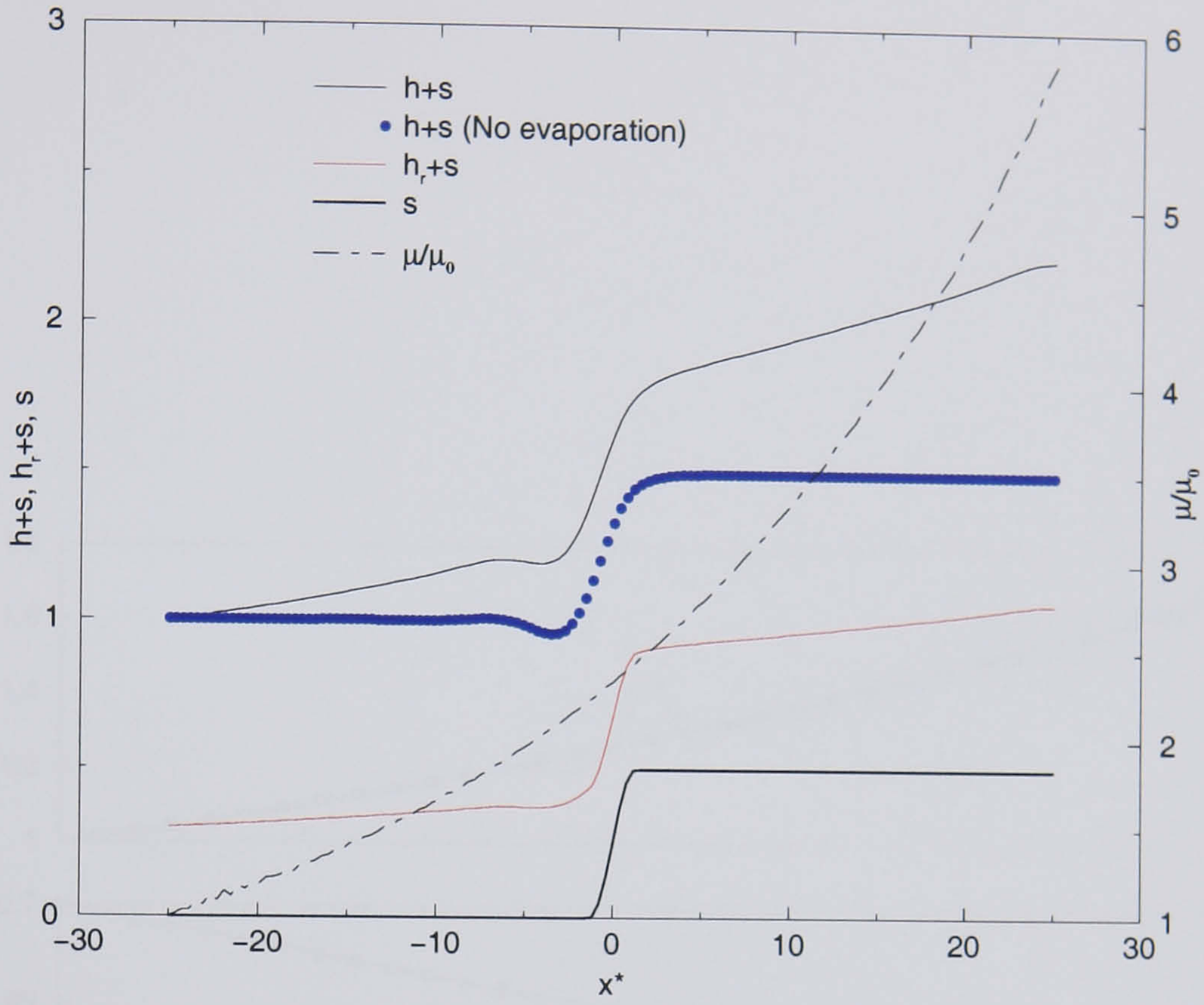

FIGURE 7.4: Streamwise profile of the free surface, the "resin/solvent interface", the topography and the viscosity for the flow over a step-up.

step region.

The analysis performed for the step-up is next applied to a span-wise trench topography of lateral extent four capillary lengths and depth equal to $0.7H_0$. The profile of the topography can be seen in Figure 7.6 along with the computed free surface profile and the resin/solvent interface. The free surface reveals the exact same features as highlighted in Chapter 6 (the case without evaporation) although they are shifted vertically because of the increasing viscous resistance as the fluid flows further downstream. The expected dried film profile given by the resin/solvent interface in Figure 7.6 conforms much more to the substrate feature than the free surface although a slight ridge can still be seen upstream of the topography.

The good agreement of the solvent concentration and viscosity profiles with the corresponding analytical ones for a flat substrate gives further evidence that, for two-dimensional flows, the topography does not affect noticeably the composition of the resin/solvent mixture (see Figure 7.7).

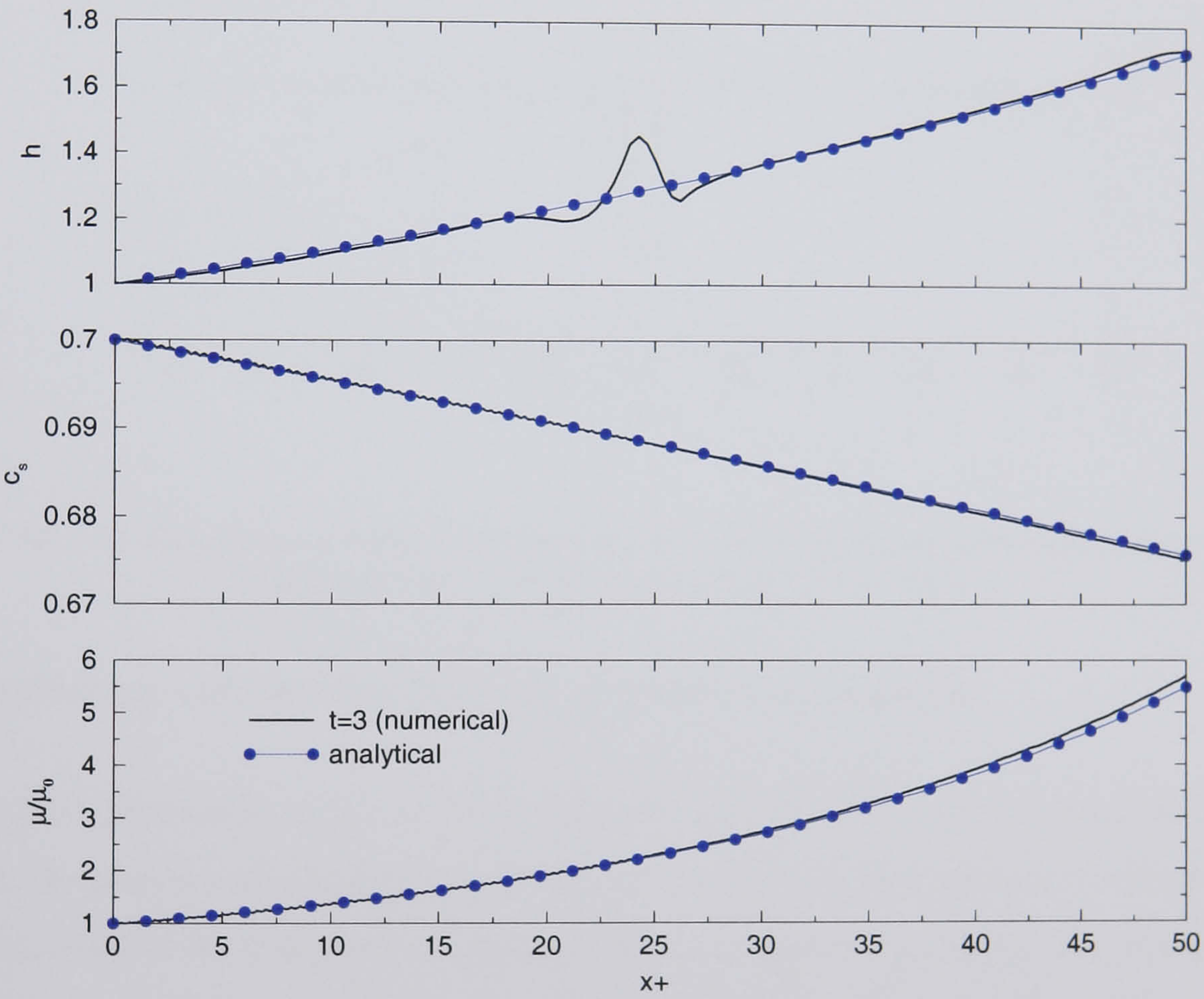

FIGURE 7.5: Comparison the steady-state streamwise profiles of film thickness, solvent concentration and viscosity obtained numerically and analytically (eqs. (7.23), (7.22) and (7.24)) for a gravity-driven film over a step-up topography.

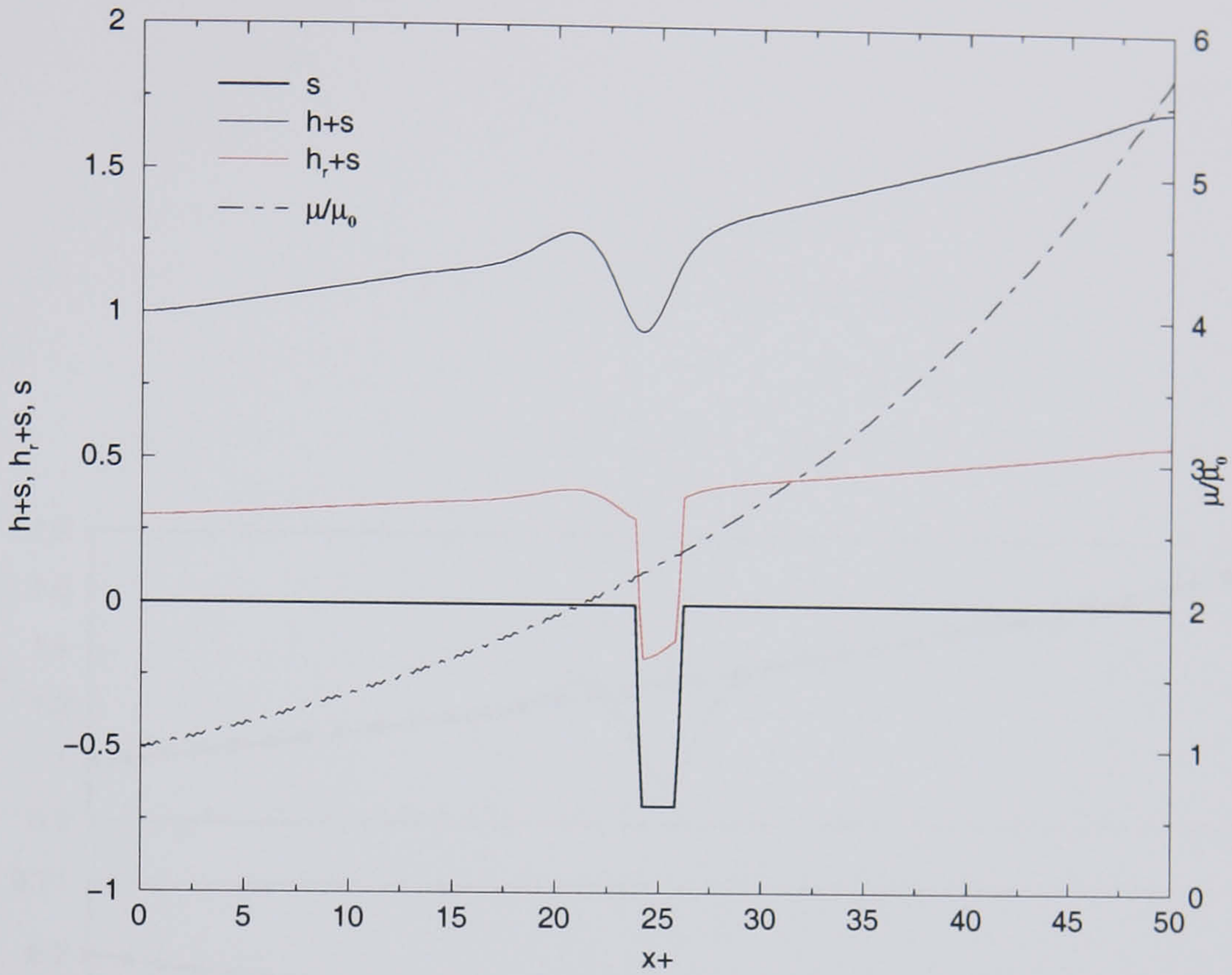

FIGURE 7.6: Streamwise profile of the free surface, the "resin/solvent interface", the topography and the viscosity for the flow over a trench.

Continuous, evaporating film over a localised topography

The key observation of the previous subsection is that for a two-dimensional flow field, the presence of a topography (a step-up or a trench) does not seem to affect the composition of the resin/solvent mixture. For a localised topography, the results of Chapter 6 show that the associated free surface profile is more complex, developing a series of capillary waves. How these modify the map of the solvent concentration is clearly the question of interest.

The topography considered is a square trench of extent 5 capillary lengths ($l_t = w_t = 0.1$ since the computational domain is $50L_c \times 50L_c$) and the same depth as the asymptotic film thickness ($s_0 = -1$). It is centred at $(x_t, y_t) = (0.35, 0.5)$. The topography steepness parameter in equations (5.13) and (5.14) is set to $\gamma = 0.05$.

Numerical results, after reaching steady-state, are shown in Figure 7.8 for $e = 0.01$. The free surface (7.8 (**a**)) displays similar features to its non-evaporating

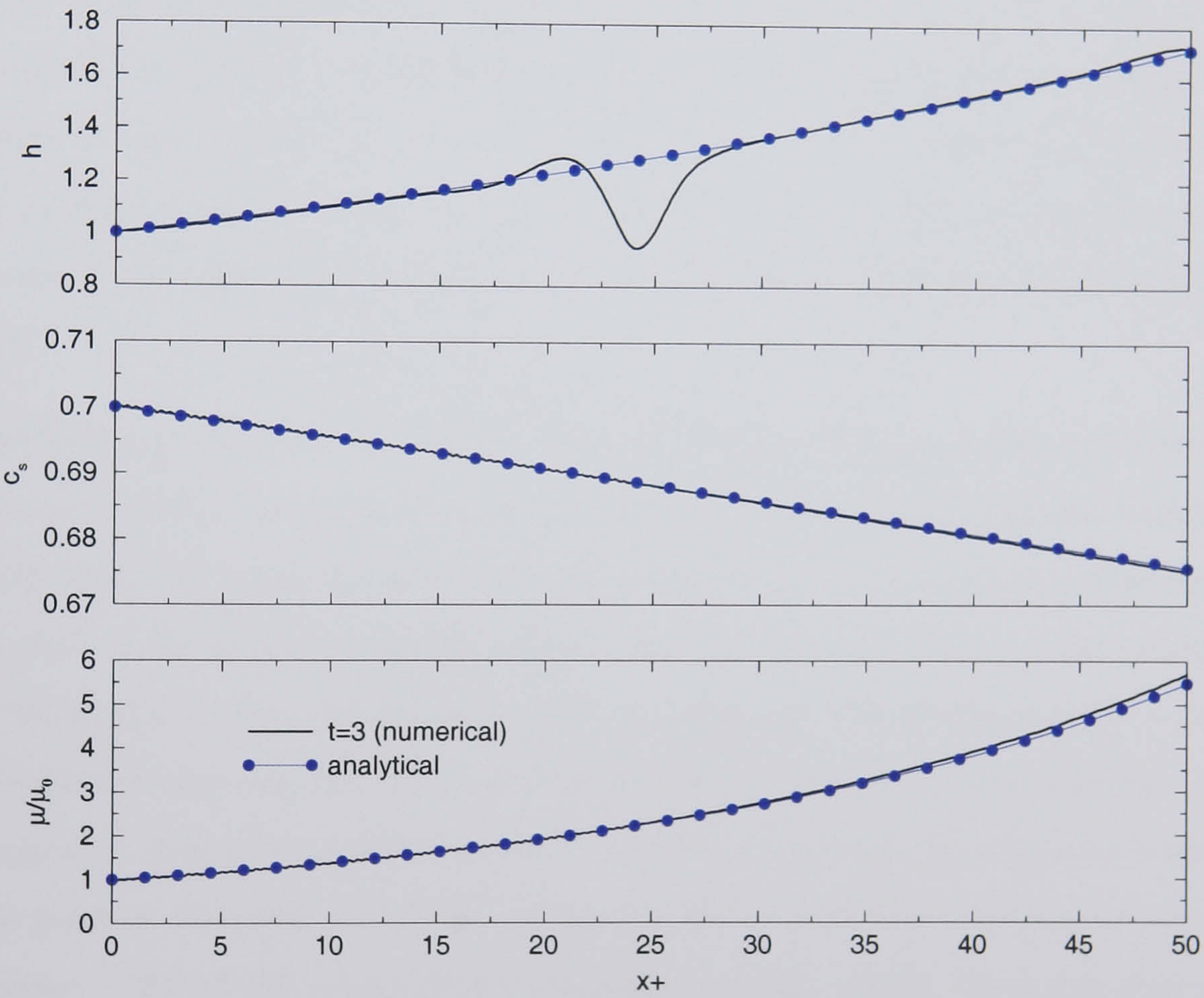

FIGURE 7.7: Comparison the steady-state streamwise profiles of film thickness, solvent concentration and viscosity obtained numerically and analytically (eqs. (7.23), (7.22) and (7.24)) for a gravity-driven film over a trench.

counterpart: the upstream ridge, the tails on each side of the topography and the downstream surge in the middle. The pressure, on the other hand, forms two steep peaks on the upstream and downstream walls of the topography separated by a pressure drop across it (Figure 7.8 (**c**)). In the same way that the pressure gradients induced by the topography deform the free surface, they also affect the solvent transport. This is clearly seen in Figure 7.8 (**d**) showing a rear-view of the solvent concentration. As well as an expected solvent concentration decrease further and further away from the inlet, two grooves initiated by the side walls of the topography develop downstream of the topography. The solvent concentration between these two grooves is higher than the asymptotic value away from the topography centreline. The pattern of the viscosity shown in Figure 7.8 (**d**) reveals an opposite trend because of the chosen dependence of the viscosity on the solvent concentration (eq. (7.24)).

Considering the spanwise profiles downstream of the topography in Figure 7.9 provides a more quantitative picture. The amplitudes of film thickness and pressure variation clearly decay for larger distances from the topography. This decay is accompanied by a shift of the extrema towards larger spanwise locations. This is what produces the "horseshoe" shape. In contrast, the shape of the grooves observed in the solvent concentration and viscosity profiles seem invariant in the streamwise direction and no spanwise shift of the extrema is seen. Moreover the spanwise distance between these grooves, between 5 and 10 capillary lengths, appears to be dictated by the spanwise width of the topography (5 capillary length). While full-width spanwise topography did not appear to affect the composition of the resin/solvent mixture, the presence of a localised topography produces significant variations of the solvent concentration. These can lead to undesirable defects in the remaining solid coating.

The dried film free surface defined by the "resin/solvent interface", as before, is shown in Figure 7.10. It clearly shows a depression downstream of the topography delimited by two grooves in the resin layer due to the non-uniformity of the solvent concentration. As highlighted in Chapter 6, trenches and peaks have opposite (but not symmetric) effects on the free surface. Hence, it comes as no surprise that the depression in the dried film layer shown in Figure 7.10 for the flow over a square

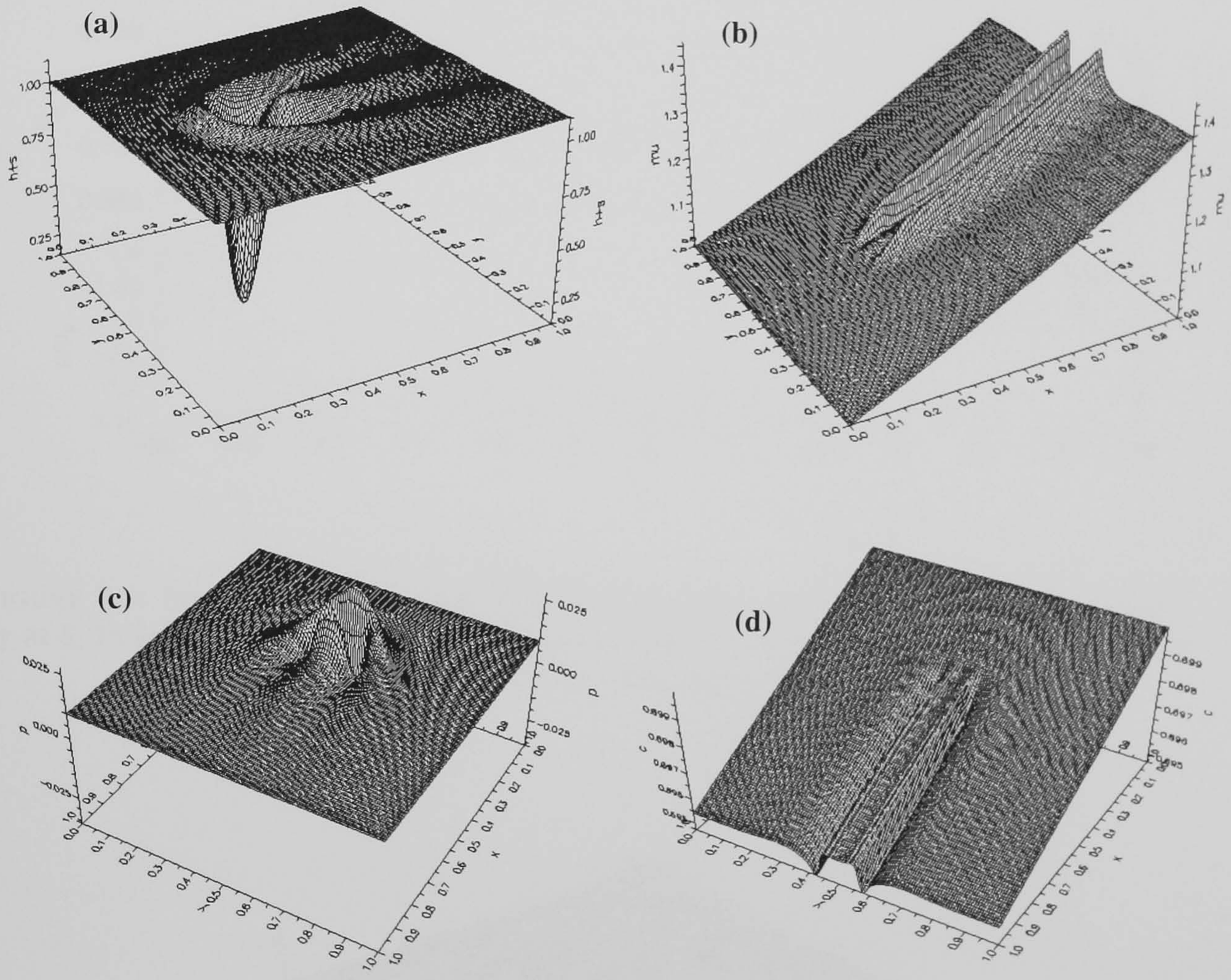

FIGURE 7.8: Equilibrium free surface (**a**), viscosity (**b**), pressure across the film: rear-view (**c**) and solvent concentration: rear-view (**d**) for the flow of an evaporating thin film over a square trench for an evaporation rate of 0.01.

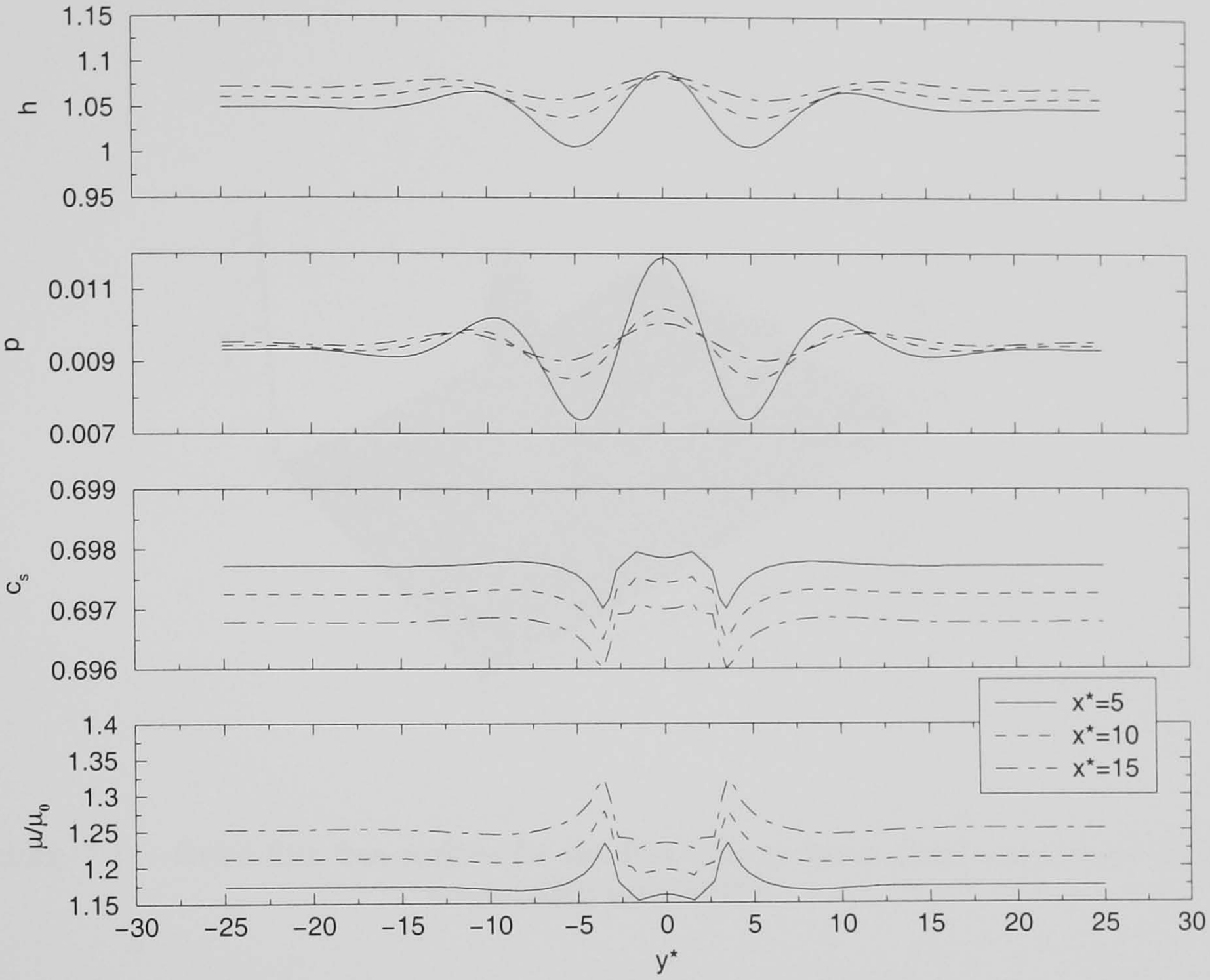

FIGURE 7.9: Spanwise profiles of film thickness, pressure, solvent concentration and viscosity at 5, 10 and 15 capillary length downstream of the topography for the flow over a square trench topography and an evaporation rate of 0.01.

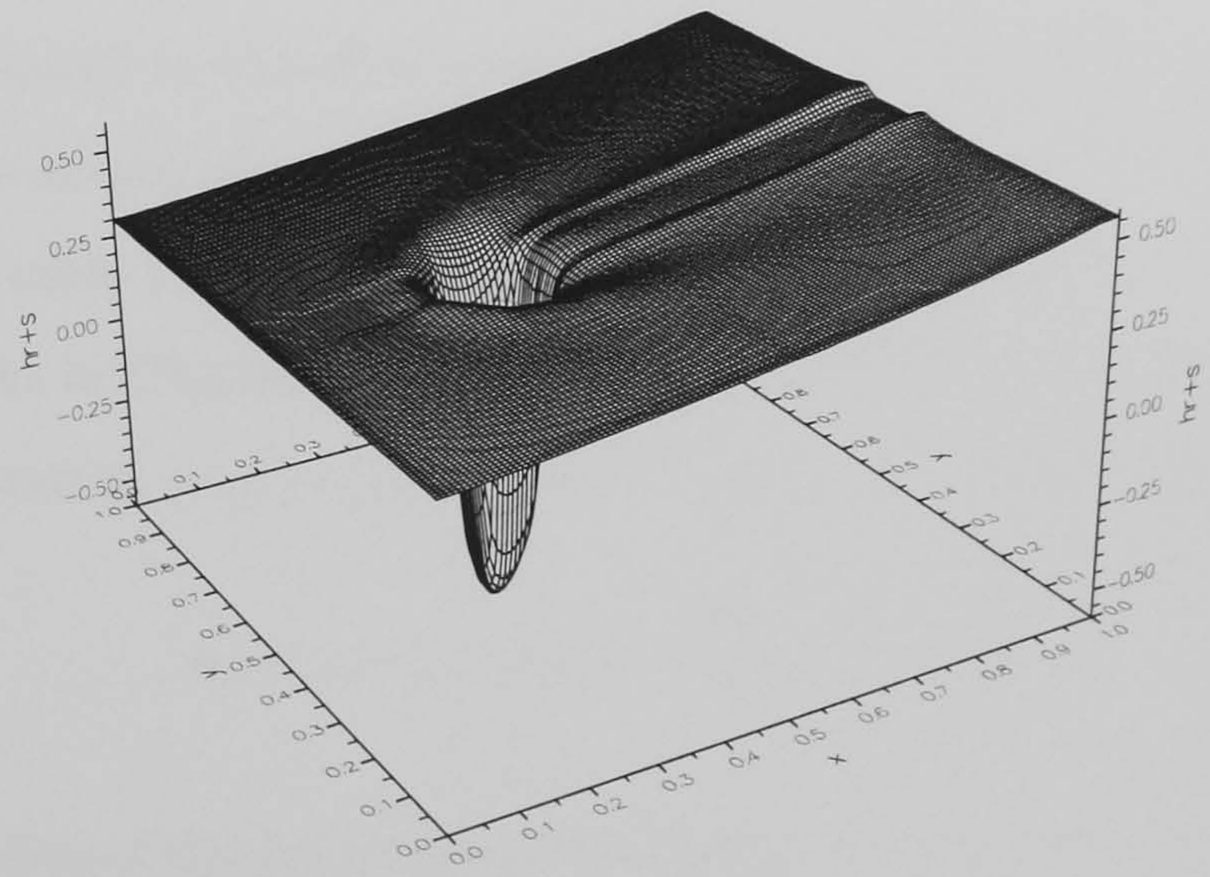

FIGURE 7.10: Dried film free surface for the flow over a square trench topography and an evaporation rate of 0.01.

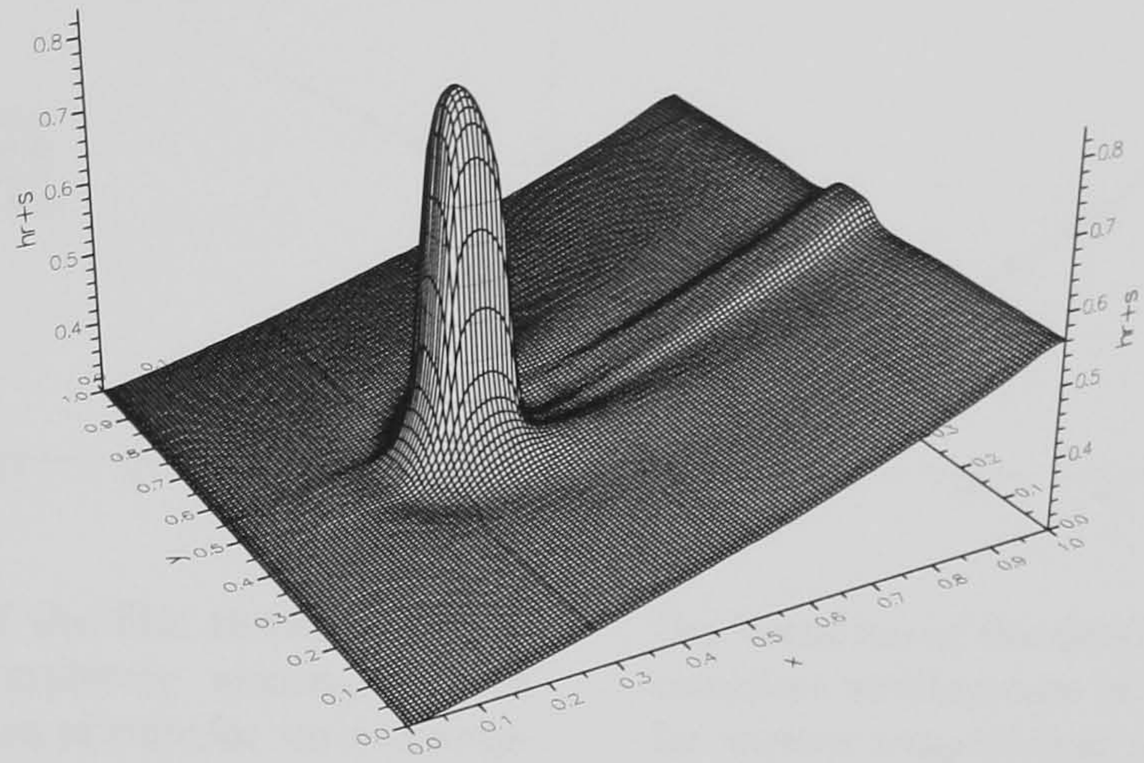

FIGURE 7.11: Dried film free surface for the flow over a square peak topography and an evaporation rate of 0.01.

trench is replaced by a surge in Figure 7.11 when flow over a peak is considered instead. The dimension and steepness of the peak are the same as for the trench and its height is half the asymptotic film thickness.

7.4.2 Evaporating droplet spreading

The results presented in this section are restricted to fully-wetting droplets ($\Theta_0 = 0$) for which the action of gravity can be neglected ($Bo = 0$). This implies that $C_1 = C_2 = 0$ in table 2.1 and that the lubrication approximation is effectively free of parameters. As in Chapter 5, the initial profile of the droplet is an axisymmetric paraboloid, centred at $(x, y) = (0.5, 0.5)$, satisfying the following equation,

$$h(r) = max\left(5\left(1 - \frac{320}{9}r^2\right), h^*\right) , \tag{7.25}$$

where r is the radius of the footprint of the droplet on the surface of the substrate and the precursor film thickness, $h^* = 0.01$. The initial solvent concentration is assumed uniform across the droplet with $c_0 = 0.7$. The viscosity follows the exponential law given by eq. (7.24) with $a = 70$. Numerical results are obtained on a finest grid

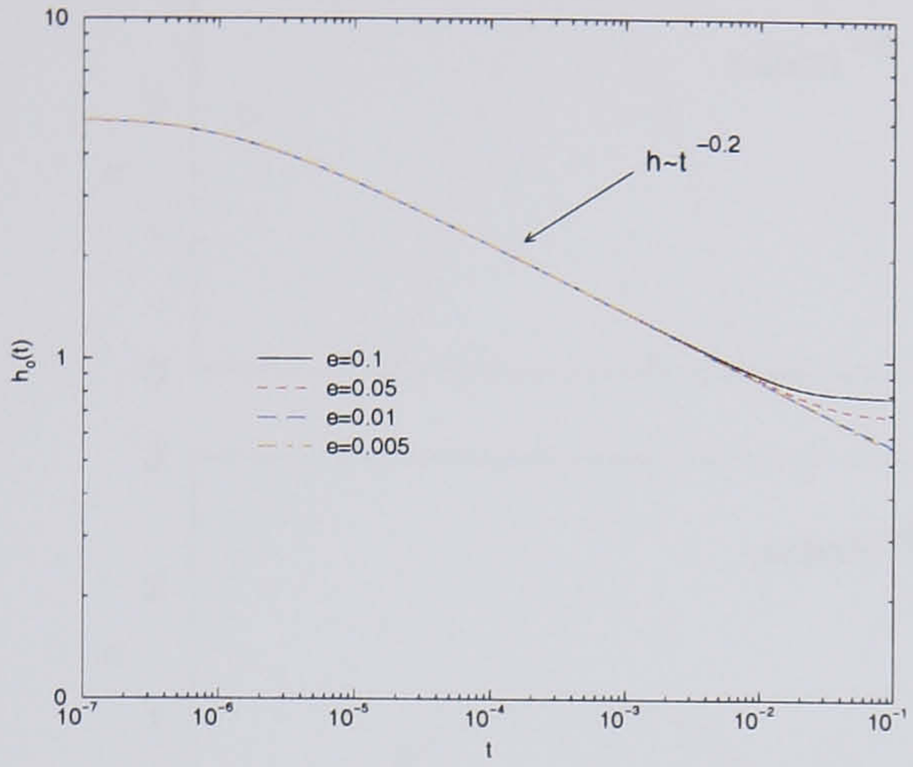

(**a**) Variation of the film thickness at the centre of a completely wetting droplet $h_0(t)$ as a function of time for various evaporation rates.

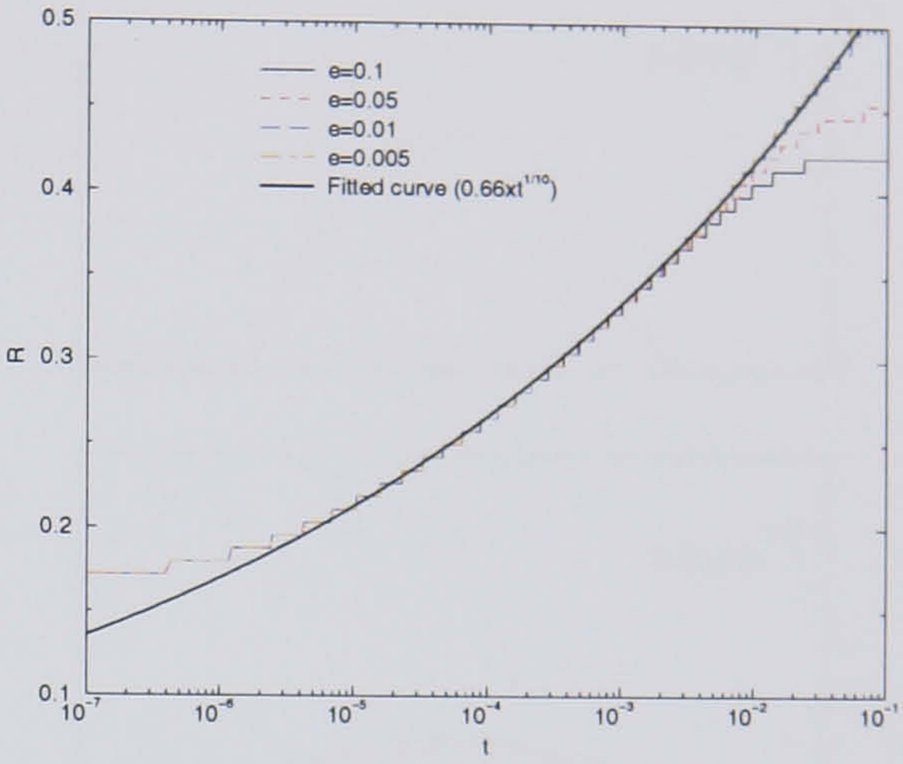

(**b**) Variation of the droplet radius R in the complete wetting case as a function of time for various evaporation rates.

FIGURE 7.12: Variation of the droplet thickness $h_0(t)$ and radius R as a function of time and comparison with the expected behaviour for pure liquids (Tanner's law).

level having 129 nodes in each direction and a 9x9 coarsest grid level. The adaptive time-stepping scheme is used with $Tol = 10^{-3}$.

The effect of solvent evaporation is best illustrated by comparing the numerical result with Tanner's predictions for the evolution of pure liquid droplets (Tanner (1979)). For all values of the evaporation rate Figure 7.12(**a**) shows that, up to $t = 3 \times 10^{-3}$, the film thickness at the centre of the droplet, $h_0(t)$, follows a power law. A closer analysis reveals that, in this range, the film thickness is inversely proportional to $t^{0.2}$ as predicted by Tanner's law (eq. (5.1)). Moreover, the fitted curve in Figure 7.12(**b**) confirms that the droplet radius, R, expands as $t^{0.1}$ for $t < 3 \times 10^{-3}$, which is also in agreement with Tanner's analysis. The initial discrepancy between the fitted curve and the numerical results is representative of the time it takes for the dynamics of the droplet to be no longer affected by the initial conditions. The droplet radius curves on Figure 7.12(**b**) are not smooth (they have a saw tooth appearance) because the wetting line, defined as the point where the film thickness first becomes greater than the precursor film thickness, always corresponds to a node on a discrete mesh. The radius can be defined without ambiguity because the three-dimensional calculations conserve the initial axisymmetry of the droplet. For $t > 3 \times 10^{-3}$, solvent evaporation effects become more important leading to a departure from the

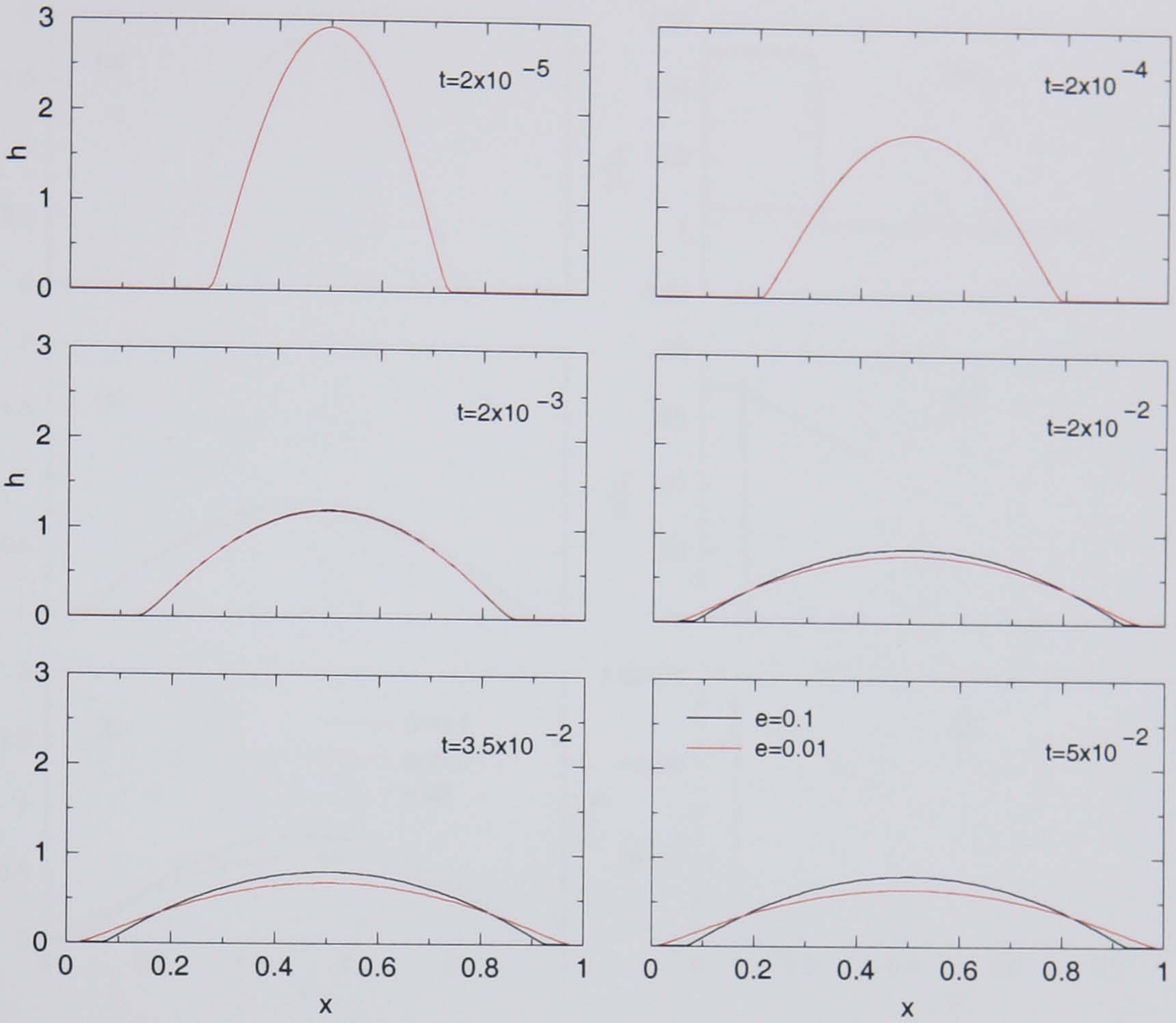

FIGURE 7.13: Droplet free surface profiles at different times for $e = 0.1$ and $e = 0.01$.

power laws for the two largest values of the evaporation rate ($e = 0.1$ and $e = 0.05$). The droplet thickness and radius reach a plateau; reminiscent of the spreading of partially wetting droplets shown in Chapter 5. This interruption of the spreading corresponds to contact line pinning mentioned in the introduction of this chapter. It can be anticipated that this pinning of the wetting line would also occur for smaller values of the evaporation rate but for radii of the droplet too large to be captured in the computational domain. Comparing the evolution of the droplet free surface profiles for $e = 0.1$ and $e = 0.01$ Figure 7.13 emphasises the behaviour contrast induced by solvent evaporation. The droplet profiles match for both evaporation rates up to $t = 2 \times 10^{-3}$. After this time, they can clearly be distinguished. While the contact line motion slows down and eventually stops for $e = 0.1$, the droplet carries on spreading for $e = 0.01$.

Intuitively, the contact line pinning is easily understood. Evaporation, which dominates in the contact line region, induces solvent loss and therefore an increase in the

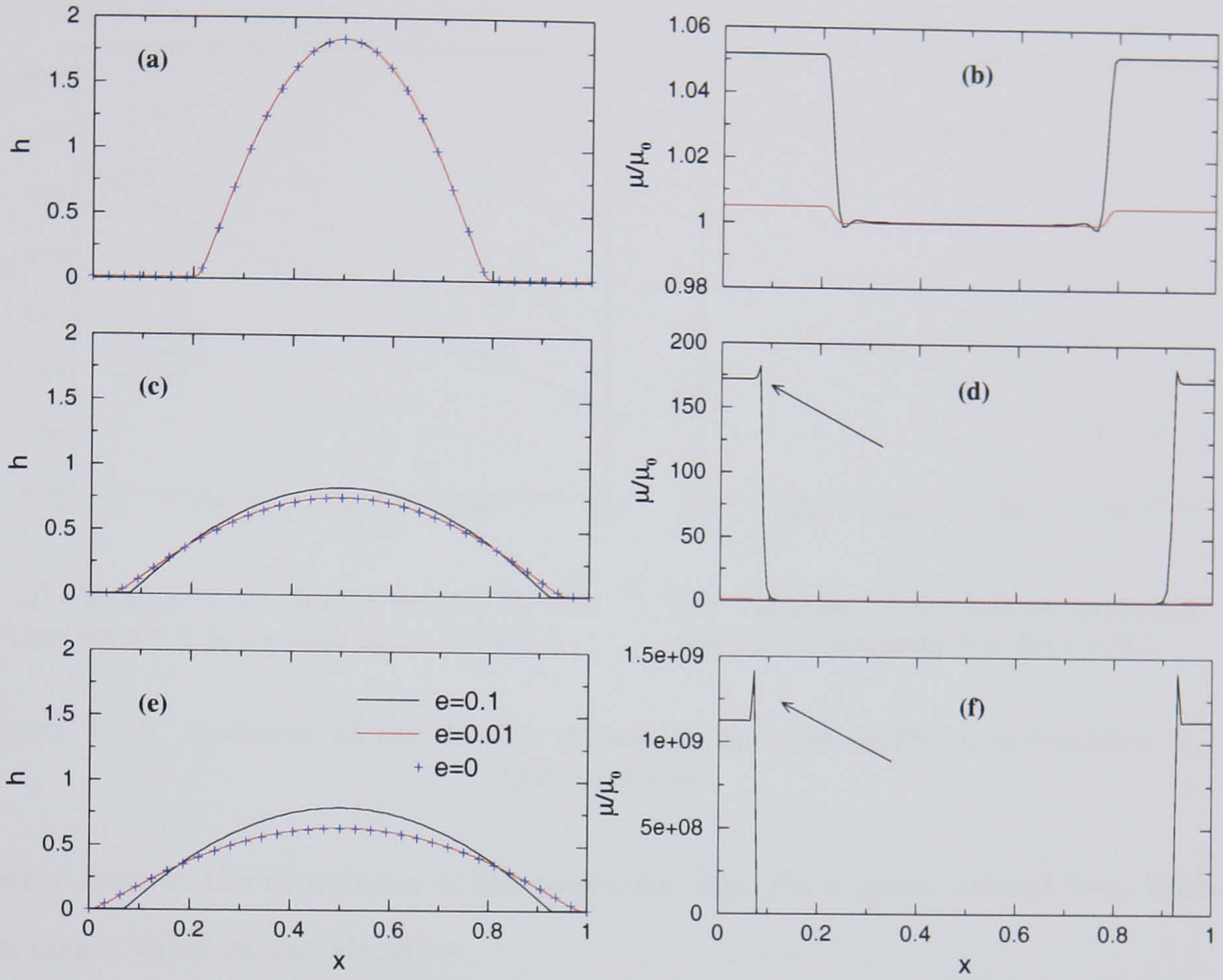

FIGURE 7.14: Droplet free surface and viscosity profiles at $t = 2 \times 10^{-4}$ (Figures (**a**) and (**b**)), $t = 2 \times 10^{-2}$ (Figures (**c**) and (**d**)) and $t = 5 \times 10^{-2}$ (Figures (**e**) and (**f**)) for $e = 0.1$, $e = 0.01$ and no evaporation.

viscosity. This viscosity rise is responsible for the pinning of the contact line. This reasoning is confirmed when looking at Figure 7.14 which shows the free surface and viscosity profiles at different times and various evaporation rates. The free surface profiles for $e = 0.01$ and no evaporation are indistinguishable in Figures 7.14 (**a**), (**c**), (**e**) because the small evaporation rate does not induce substantial variations in the viscosity.

On the other hand, for $e = 0.1$ the viscosity is seen to increase dramatically in the contact line region and in the precursor film from Figure 7.14 (**b**), (**d**) and (**f**). At the latest time ($t = 5 \times 10^{-2}$), the viscosity may be considered to be essentially infinite, causing the pinning of the contact line. Interestingly, the viscosity displays a sharp peak indicated by the arrows in Figure 7.14 (**d**) and (**f**). This peak is a result of the slight depression in the precursor film highlighted in Chapter 5. In this region of lower film thickness, the amplitude of the solvent fraction decrease will be

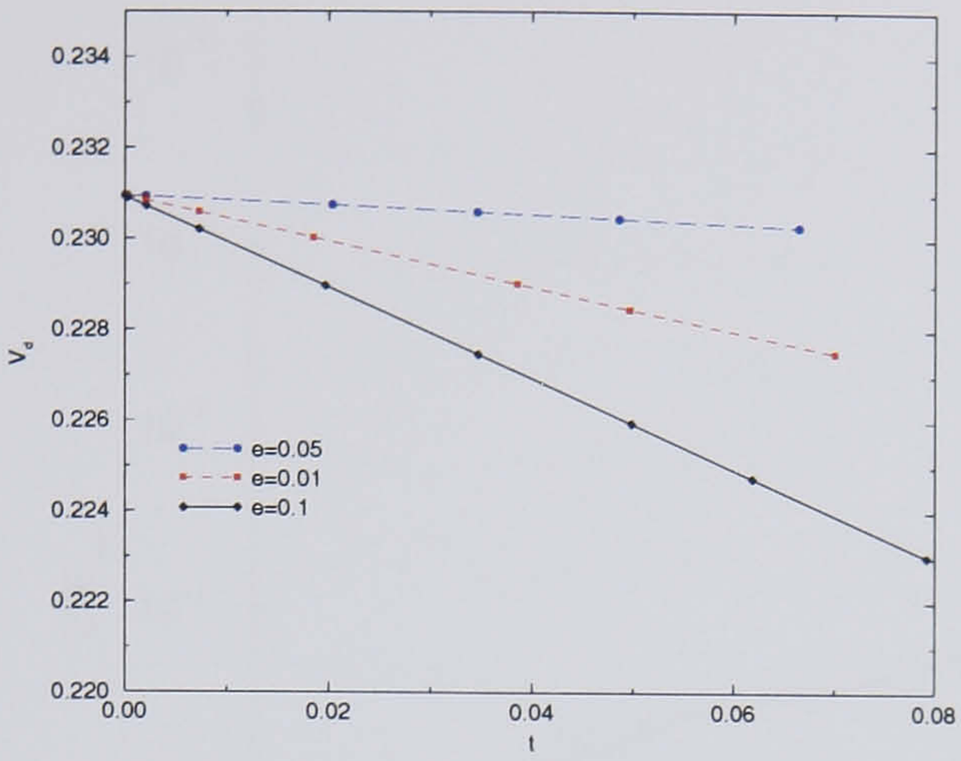

(**a**) Variation of the droplet volume V_d with time for $e = 0.1$, $e = 0.05$ and $e = 0.01$.

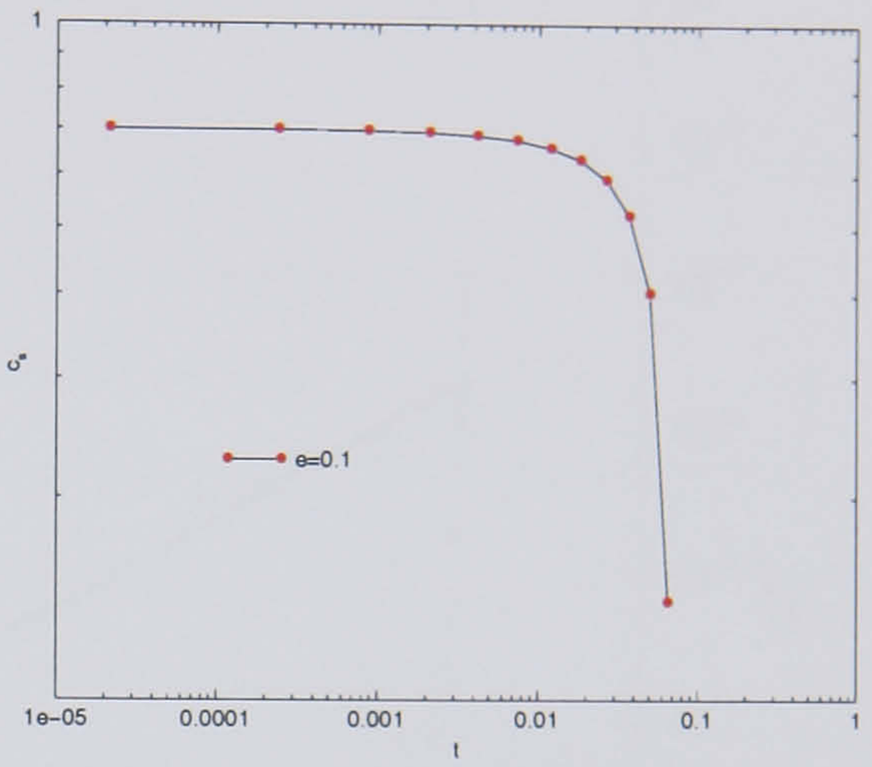

(**b**) Variation of the solvent concentration in the precursor film for $e = 0.1$.

FIGURE 7.15: Variation of the droplet volume V_d and the solvent concentration in the precursor film.

greater than in the remainder of the precursor film, for a given solvent loss, leading to a larger value of the viscosity.

Solvent evaporation is necessarily accompanied by a decrease of the overall volume of the droplet, V_d, while the volume of the resin, delimited by the "resin/solvent interface" and the substrate, should remain constant since the resin is only transported by the mean flow and not allowed to evaporate by the model. A check on the conservation of resin shows that the volume of the resin does not vary by more that 0.04% during an entire simulation. The variation of the droplet volume is shown in Figure 7.15(**a**) for $e = 0.1$, $e = 0.05$ and $e = 0.01$. This graph shows that the droplet volume decreases linearly with time and that, as expected, the magnitude of the slope is greater for larger evaporation rates. Figure 7.15(**b**) illustrates the variation of the solvent concentration in the precursor film with time for $e = 0.1$. Two stages can clearly be distinguished. At early times, the solvent concentration decreases slowly but when $t > 5 \times 10^{-3}$, the decrease is much steeper. This reveals the limitation of the model adopted here. Since the evaporation term is assumed to be a positive constant in eqs. (7.6) and (7.8), nothing prevents the solvent concentration from becoming negative which is clearly unphysical. This shortcoming could be overcome by employing a more realistic evaporation term which tends to zero as the solvent concentration goes to zero.

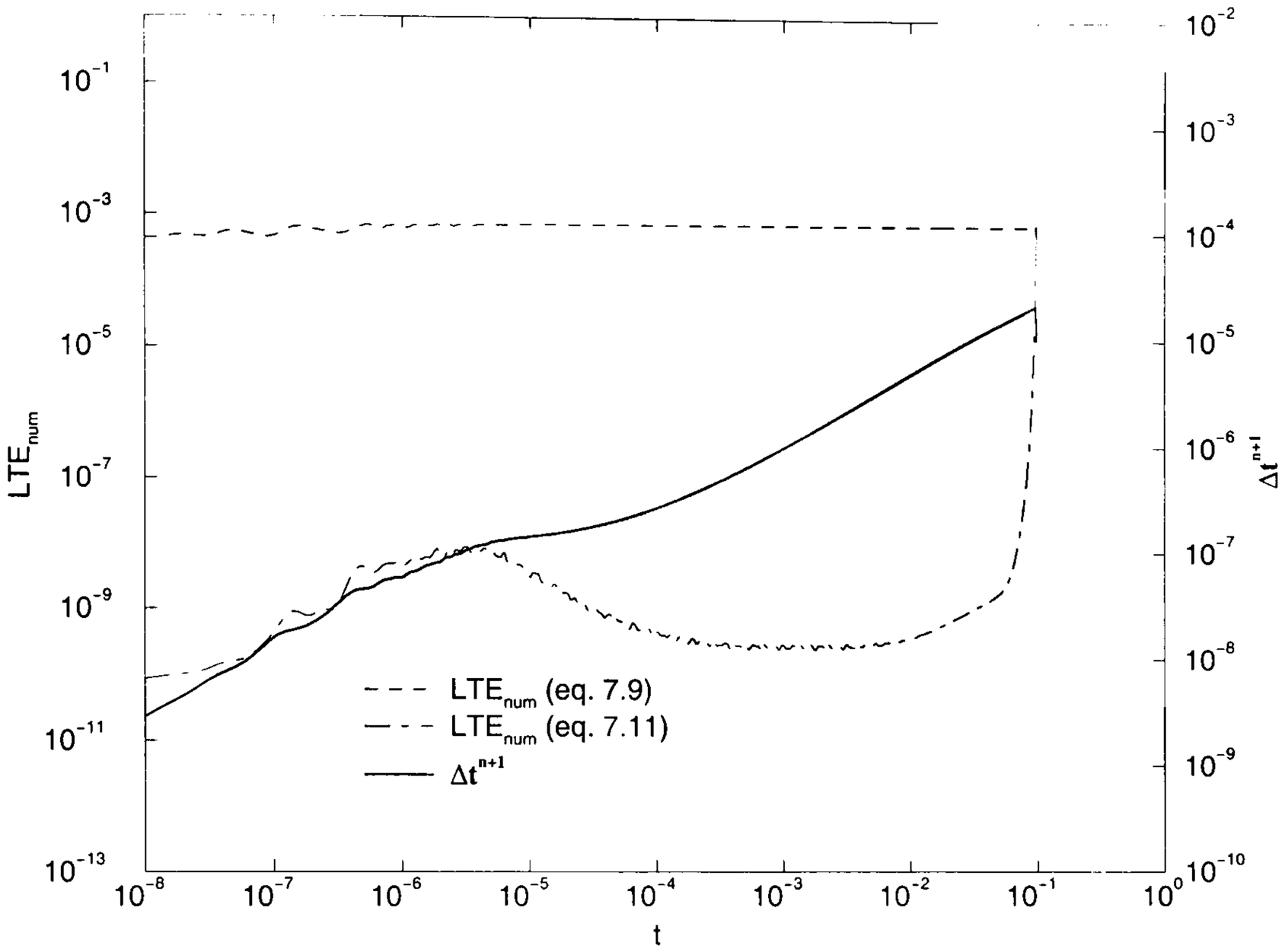

FIGURE 7.16: Variation of the time-step Δt^{n+1} and the local truncation error LTE_{num} for eqs. (7.9) and (7.11) for the droplet spreading with $e = 0.1$.

The presence of these two distinct stages introduces numerical difficulties which become apparent as shown in Figure 7.16. The graph reassuringly confirms that the Local Truncation Errors (LTE_{num}) for eqs. (7.9) and (7.11) are kept below the Tol equal to 10^{-3}. The LTE_{num} for the overall mass conservation equation (eq. (7.9)) dominates over the one for the solvent conservation equation (eq. (7.11)) during most of the simulation leading to a steady increase of the time-step size. However, the LTE_{num} for the solvent conservation equation rises sharply from $t \sim 5 \times 10^{-3}$ (roughly the characteristic time when evaporation effects become important) and has the same magnitude as the one for the overall mass conservation at $t \sim 0.1$. Beyond this time, the probable occurrence of negative solvent concentration in the precursor film leads to the failure of the multigrid solver to carry on the simulation. Overcoming this difficulty, in order to be able to predict the final dried profile, is left as future work.

7.5 Concluding remarks

In this chapter, evaporating thin liquid films composed of a mixture of a non-volatile resin and an evaporating solvent were considered. The model used is based on the well-mixed assumption and follows the approach of Howison *et al.* (1997). The effects of surface tension gradients and lateral diffusion of solvent are neglected in the model adopted and the evaporation rate is assumed to be constant. The latter assumption is shown to be quite restrictive and an important improvement, left as future work, would be to use a more realistic composition-dependent evaporation rate such as those described in Weidner *et al.* (1996) or Schwartz *et al.* (2000). The additional partial differential equation governing the solvent concentration is successfully implemented in the multigrid algorithm as shown by the good agreement between the numerical and analytical results for the flow of a thin film over an inclined, flat substrate. The numerical results confirmed the assumption made implicitly by other authors (Stillwagon and Larson (1990), Lawrence (1988)) that full-width spanwise topographies giving rise to two-dimensional flows did not affect the composition of the resin/solvent mixture. The solvent evaporation and associated viscosity rise was seen to induce an increase of the film thickness for larger and larger downstream locations. This film thickness increase did not however remove the free surface features characteristic of the flow of non-evaporating thin films over full-width spanwise topographies. These appeared to be simply shifted vertically. In contrast, localised square trenches or peaks triggered important non-uniformities of the solvent concentration in the wake of the topography. These non-uniformities persist far downstream of the topography and result in defects of the final dried profile in the form of a depression for the trench and a surge for the peak. Finally, the effect of solvent evaporation on the spreading of droplets was investigated. Numerical results showed that after an initial stage during which the spreading obeys Tanner's (1979) predictions, the contact line slows down and eventually pins for large values of the evaporation rate. This contact line pinning is caused by the solvent evaporation in the contact line region yielding large values of the viscosity.

Chapter 8

Conclusion

Contents

8.1 Summary

The key outcomes of this thesis are twofold:

1. A new numerical approach for the solution, in an efficient, robust and accurate manner, of both transient and steady-state forms of the nonlinear lubrication equations, both with and without the effects of evaporation.

2. Application of the above to industrially relevant thin film flow over heterogeneous substrates. More specifically:

   - droplet spreading over substrates containing topographic and wetting heterogeneities;
   - the gravity-driven flow of continuous thin liquid film over topography.

The underpinning governing equations, together with important flow parameters, issues concerning the modelling of contact lines and boundary conditions are presented in Chapter 2. This is followed, Chapter 3, by a comprehensive description of the numerical approach used to solve these equations which, in brief, is a fully-implicit Full Approximation Storage (FAS) Mutligrid algorithm which has embedded within it an adaptive time-stepping scheme that enables the same to be optimised in a controlled manner subject to a specific error tolerance.

The validity and correct implementation of the numerical method was first assessed, Chapter 4, by considering a number of problems, described by ordinary and partial differential equations, with known analytical solutions.

Applied to a first order ODE, (4.1), with constant coefficients the adaptive time-stepping scheme and associated two-stages solution process (explicit predictor stage and implicit solution stage) proved successful in estimating the Local Truncation Error (LTE) for small enough values of the prescribed error tolerance. As a consequence, the time-step selection was shown to be optimal taking the largest possible value while guaranteeing control of the LTE.

The transient two-dimensional heat equation was solved next. The presence of spatial truncation error implies that the value of the prescribed error tolerance

needs to be chosen carefully in order to balance it and the (temporal) LTE. With an appropriate choice of the tolerance, the adaptive time-stepping scheme is found to outperform the backward Euler scheme (fixed time-steps) in terms of required CPU time and accuracy.

In Chapter 5, the efficiency and accuracy of the numerical method was explored further by solving the lubrication equations for the case of droplet spreading, in some cases for which corresponding analytical solutions are available for validation purposes.

Droplet height at the centre of a partially wetting droplet, spreading over an homogeneous, flat substrate, was found to satisfy the power law predicted by Tanner (1979). Moreover, the value of the coefficient in this power-law matched well those found by Schwartz and Eley (1998). For the spreading of a fully wetting droplet driven by gravity, the self-similar solution first derived by Nakaya (1974) proved a valuable source for validation purposes. Again, droplet profiles obtained numerically were found to be in good agreement, over the bulk of the droplet, with the corresponding analytical ones.

In addition, for the first time, the spreading of a droplet over a substrate with topographic and wettability features was solved numerically. Results include the spreading of a fully wetting droplet over a square trench and peak and the wetting and dewetting of a square peak by a droplet due to contrast in wettability between the topography and the rest of the surrounding substrate. The flow of a fully wetting droplet down an inclined plane and over a square peak was also considered. Of course, in the absence of possible comparison with experimental data, estimating to what extent these results match reality is difficult. It may be anticipated, however, that the over large value of the precursor film thickness used in the computations will over predict the spreading rate as discussed by Schwartz and Eley (1998). Nevertheless, these solutions provide useful qualitative insight.

Although direct comparison, with existing schemes such as $\mathcal{ADI}$, of the performance of the numerical method utilised, is difficult due to the lack of reported data, the evidence suggests it possesses the following benefits:

1. The efficiency of the scheme is optimal in the sense that the CPU time taken to solve a discretised equation set, at each time step, is simply $O(N)$ where N is the number of unknowns. This allows unprecedented (to the best of the author's knowledge) fine mesh densities to be used for the solution to the two-dimensional lubrication approximation.

2. The adaptive time-stepping scheme allows optimal selection of the time-step, taking the largest possible value while guaranteeing the control of the LTE. The scheme also "follows the physics". This is most clearly demonstrated when solving the transient two-dimensional heat equation – the rapid fluctuations of the diffusivity is mirrored by the time-step variations. It is also clear for the case of a droplet spreading over a cross of poorly wetting material. The break-up of the droplet into four satellite droplets, in the four quadrants, delimited by the cross is seen to coincide with episodes of a decrease in the time-step.

3. The fully-implicit nature of the multigrid ensures that the larger time-step estimates given by the adaptive time-stepping selection procedure can actually be used in practice.

4. A significant improvement in robustness was achieved by using the $\mathcal{PPS}$ developed by Zhornitskaya and Bertozzi (2000). This scheme proved to be essential in order to solve droplet spreading over topographies. A possible explanation for the necessity of using this scheme, based on the effective spatial resolution, is also provided.

5. Local mesh refinement is fully compatible with the multigrid algorithm. The potential of the $\mathcal{MLAT}$ is illustrated for the two-dimensional heat equation with a step-change in the diffusivity, and for the flow of a thin film over a step-down topography and a localised square trench as discussed later.

6. A further useful attribute is that further physics and additional equations can be incorporated in the multigrid solver without requiring modifications to the algorithm. For example, the addition of a solvent concentration equation into the multigrid solver, as reported in Chapter 7, illustrates this desirable feature.

The flow of a gravity-driven thin liquid film was explored in depth in Chapter 6. Step up and step down geometries were used to test the accuracy of the lubrication analysis, relative to corresponding Navier-Stokes calculations, over a range of step heights and flow rates (and hence Reynolds number). Contours of constant error revealed that even when the step height is equal to the film thickness and the flow rate is such that $Re = 15$ (with $Ca \approx 10^{-3}$), the maximum error between the predicted profiles is only about 15%. This lends support to the general experience that lubrication theory can provide good predictions even when topographies are steep.

The discussion of three-dimensional flow focused mainly on that over a square trench, calculated using lubrication theory. The predicted free surface shapes agree well with the experiments of Decré and Baret (2003), and particular thought was given to the cause of the "downstream surge" which is not present in the flow over one-dimensional topographies. A simple explanation for the elevated surface behind the trench is that fluid flows into the trench across a greater width (i.e. over the upstream and side walls) than that across which it must exit. The normal component of gravity was shown to suppress the upstream free-surface disturbance, as expected from the one-dimensional analysis of Kalliadasis *et al.* (2000), but it does not inhibit the downstream surge. Three-dimensional rear-view visualisations of the free surface show how the downstream surge separates into two as the aspect ratio of the trench is increased and how the flow over the centre of the trench approaches the one-dimensional case.

The positions of the spanwise local extrema in film thickness produced by flow past a square trench and an equal but opposite square peak were plotted as a function of the lateral coordinates, and an inverse hyperbolic cosine function was demonstrated to fit these loci extremely well even upstream of the topography. This gives a complete description of the spread of the bow wave, but does not capture the rate of decay in amplitude. The equal square peak and trench were used to test the linearity of the free surface responses by superimposing their individual responses to see if the surface produced was planar. While not being perfectly so, there is only a slight deviation of the order of 7% of the individual disturbances when the

topography depth is a quarter of the film thickness. Reducing the relative depth of the topography to 0.1 resulted in an even smaller deviation of the order of 2%.

The superposition principle was further tested for a more complex, **T**-shaped topography. Even in that case, where nonlinear effects might be expected to be more important, free surface profiles obtained by linear superposition were still in good agreement with those obtained numerically. An example was also given of a modification to a square peak topography which substantially reduces the free-surface disturbance. Such modifications of essential topographic features may help to minimise troublesome free-surface features at later stages in manufacturing processes.

Chapter 6 concludes with results exploring the effect of perturbations at the inlet boundary. These perturbations, produced by imposing periodic variations of the inlet film thickness, propagate downstream at a velocity found to be approximately equal to twice the free surface velocity, in agreement with Bielarz and Kalliadasis (2003). High frequency perturbations are found to be damped more rapidly than low frequency ones and produced a solitary wave of almost constant amplitude that travels far downstream, propagating free surface defects produced by the topography.

Finally, evaporating thin liquid films were considered in Chapter 7 in the context of droplet spreading and gravity-driven films. The former reveal that the increase in viscosity induced by the solvent evaporation in the contact line region lead to a decrease of the droplet base expansion rate and eventually the pinning of the contact line in a way reminiscent of partially wetting droplets of pure liquids. The latter emphasised the contrast between the response of the flow to full-width spanwise and localised topographies. The presence of a step-up or a trench leading to a two-dimensional flow field did not appear to affect the composition of the resin/solvent mixture. Nevertheless, the solvent loss as the fluid travels further and further downstream leads to a viscosity increase and as a consequence a rise of the free surface. This rise is more and more pronounced for large values of the evaporation rate. Localised topographies, on the other hand, were found to produce two distinct grooves in the solvent concentration downstream of the topography. This nonuniformity of the solvent concentration was shown to induce defects in the final dried profile for

a trench and a peak topography.

8.2 Suggestions for future work

Several aspects of the work reported above would benefit from further investigation. The first relates to the accurate modelling of wetting lines and closure of the gap between the macroscopic description of the droplet and the molecular scale of the contact line region. Due to the requirement that the mesh resolution should be of the same order as the precursor film thickness, it was impossible to use realistic values of the latter. To emphasise this difficulty, consider the following example. The largest values of the precursor film thickness are generally thought to be in the range of 100 nm. For a droplet of typical thickness 1 mm, the above requirement imposes that the mesh resolution should be of $O(10^{-4})$. The bulk of the results for droplet spreading presented in Chapter 5 were obtained on a 257x257 mesh having a mesh resolution of 3.9×10^{-3}. Hence, a more than one order of magnitude increase in the mesh resolution still needs to be gained. A means of achieving this would be to parallelise the multigrid solver in order to share the computational workload on several processors, since a number of stages in the multigrid algorithm can be suitably performed independently on different processors, for example the pointwise relaxation procedure or the evaluation of the residuals. One can anticipate that large amount of computational time might be saved allowing finer mesh resolution to be used. An alternative, which would undoubtedly require more work but could be the answer to the multiple-scale physics involved in dynamic wetting, would be to optimise the local mesh refinement algorithm so that regions of fine mesh resolution are restricted to the contact line. Allied with adaptive time-stepping, much greater efficiency could be achieved and realistic values of the precursor film thickness used in computations.

In this work, spreading driven by gravity and by surface tension were essentially explored independently. However, depending on the droplet volume, the two regimes can coexist during the spreading. It would be an interesting study to investigate the transition between the initial surface tension-driven stage and the final gravity-

driven one. Moreover, the effect of topographic features on the speed of droplets sliding down an inclined plane could be explored further as a potential means to slow the sliding motion down.

The validity of the lubrication approximation has been quantified for two-dimensional flow over a step-up and a step-down topography for a range of step heights and flow rates. A useful extension would be to perform a similar analysis for localised topographies giving rise to three-dimensional flows. The necessity to compute accurately the three-dimensional free surface shape using the Navier-Stokes equations is, however, still an obstacle in realising this goal.

The inverse problem, mentioned by Decré and Baret (2003), consisting of optimising the topography shape in order to reduce the free surface disturbance is also a problem deserving further attention. Performing numerical simulations would require an efficient algorithm to reduce the penalty function (measure of how flat the free surface is for a given topography) since each takes a large amount of computational time to execute.

Much more work still remains to be done in the area of evaporating and drying of thin films. In industrial applications, much of the interest usually concerns the ultimate profile of the dried film. The pinning of the contact line due to solvent evaporation was successfully reproduced in Chapter 7 but it would be interesting to be able to predict the next stage when the thinning of the droplet is essentially due to the mass loss caused by solvent evaporation. Parisse and Allain (1996) observed that during the latter, a solid foot forms near the contact line and with time its size increases. However, it is arguable that solvent diffusion and solutal Marangoni effects become important and should therefore be included in the governing equations.

Appendix A: Force balance in the contact line region at equilibrium

A diagram of the edge of a drop at static equilibrium is shown on figure 1.

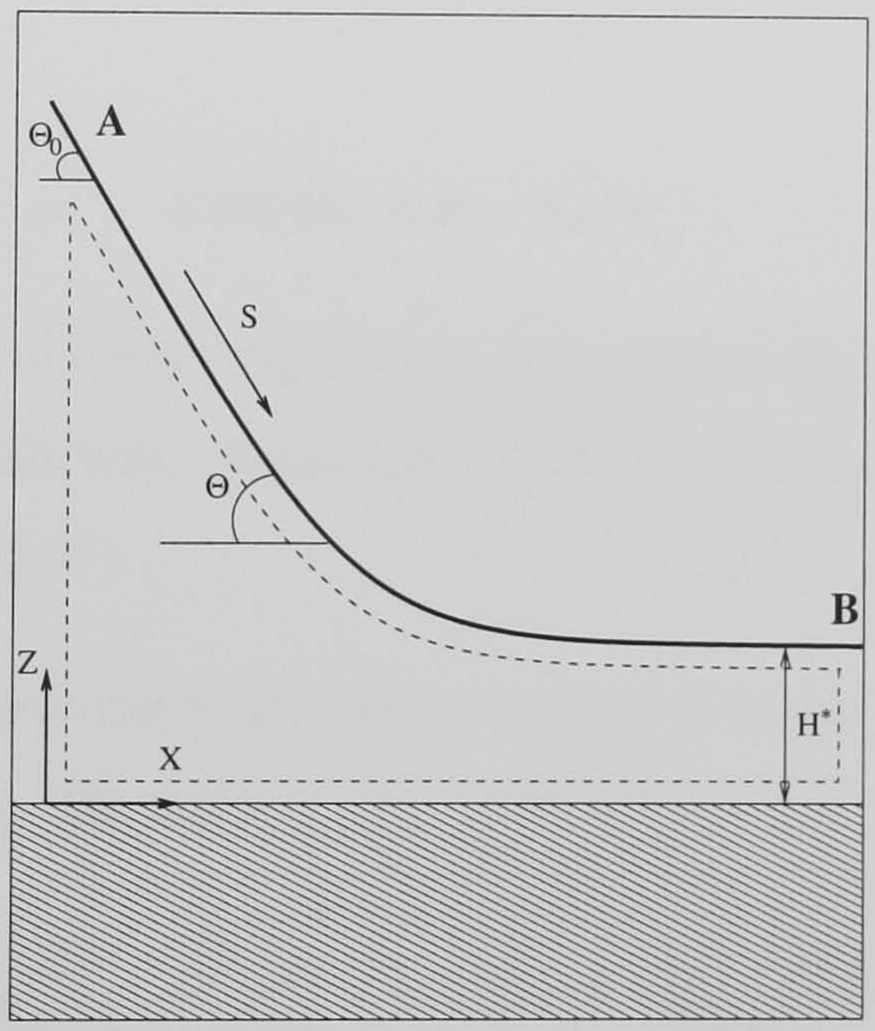

FIGURE 1: Contact region, at the edge of the drop, at equilibrium

Following the same approach as Schwartz (1998), it is useful to review the basic force balance and its relationship to the equivalent line tensions using the disjoining pressure model described in §2.5.2. Because the analysis is local to the drop edge, only a 2-dimensional problem needs to be considered. The point labelled A in fig. 1 is assumed to be sufficiently far from the substrate that its height H when measured

in units of H^*, is effectively infinite and $\Pi(H)$ is zero there. The inclination at A has become constant at the equilibrium contact angle Θ_0; thus the pressure jump caused by the curvature of the surface is also zero. Therefore, the total pressure at A is zero. Similarly, at point B on the precursor film, the inclination Θ and its rate of change are both zero, and $\Pi(H)$ is also zero there.

Performing an integrated force balance in the X direction on the region enclosed by the dashed line on figure 1 and recognising that the total pressure is zero on the vertical faces at A and B, we have

$$0 = \int_{H^*}^{\infty} P(H)dH = \sigma \int_{H^*}^{\infty} \frac{d\Theta}{dS} dH - \int_{H^*}^{\infty} \Pi(H)dH \ , \tag{1}$$

where S is the arc length measured along the free surface. But $\frac{dH}{dS} = \sin\Theta$; thus,

$$0 = \sigma \cos\Theta|_0^{\Theta_0} - \int_{H^*}^{\infty} \Pi(H)dH \ , \tag{2}$$

or

$$\sigma \cos\Theta_0 = \sigma - E_d(\infty) \ , \tag{3}$$

where $E_d(H)$ is the local disjoining energy density and $E_d(\infty)$ is equivalent to the so-called spreading coefficient. Equation (3) is the disjoining-model equivalent of the Young's equation (2.37).

Using the two-term disjoining model, the constant B in eq. (2.43) may be replaced in favour of Θ_0 using eq. (2) and

$$B = \frac{(n-1)(m-1)}{H^*(n-m)}\sigma(1-\cos\Theta_0) \approx \frac{(n-1)(m-1)}{2H^*(n-m)}\sigma{\Theta_0}^2 \tag{4}$$

where the small-argument approximation to $\cos\Theta_0$ is used for the approximate equality.

Appendix B: Equivalence of the differential and integral forms of the kinematic boundary condition

The integral form of the kinematic boundary condition at the film free surface requires that

$$\frac{\partial H}{\partial T} + \frac{\partial}{\partial X}\left(\int_S^\Psi U dZ\right) + \frac{\partial}{\partial Y}\left(\int_S^\Psi V dZ\right) = 0\,. \tag{5}$$

Using Liebnitz' Rule (see Chapter 2), the second term of this equation may be rewritten as

$$\frac{\partial}{\partial X}\left(\int_S^\Psi U dZ\right) = \int_S^\Psi \frac{\partial U}{\partial X} dZ - \left(U\frac{\partial S}{\partial X}\right)|_{Z=S} + \left(U\frac{\partial \Psi}{\partial X}\right)|_{Z=\Psi}\,, \tag{6}$$

Similarly, for the third term,

$$\frac{\partial}{\partial Y}\left(\int_S^\Psi V dZ\right) = \int_S^\Psi \frac{\partial V}{\partial Y} dZ - \left(V\frac{\partial S}{\partial Y}\right)|_{Z=S} + \left(V\frac{\partial \Psi}{\partial Y}\right)|_{Z=\Psi}\,. \tag{7}$$

Noting that,

$$0 = \int_S^\Psi \frac{\partial W}{\partial Z} dZ - W|_{Z=\Psi} + W|_{Z=S}\,, \tag{8}$$

and dropping terms involving U, V and W at $Z = S$ from eqs. (6), (7) and (8) because of the no-slip boundary condition (eq. (2.3)), eq. (5) is equivalent to:

$$\frac{\partial H}{\partial T} + \int_S^{\Psi} \left(\frac{\partial U}{\partial X} + \frac{\partial V}{\partial Y} + \frac{\partial W}{\partial Z} \right) dZ - W|_{Z=\Psi} + \left(U \frac{\partial \Psi}{\partial X} \right) |_{Z=\Psi} + \left(V \frac{\partial \Psi}{\partial Y} \right) |_{Z=\Psi} \ . \quad (9)$$

Because of the incompressibility assumption, the integral term in eq. (9) vanishes so that finally, we obtain

$$\frac{\partial H}{\partial T} + U \frac{\partial \Psi}{\partial X} + V \frac{\partial \Psi}{\partial Y} = W \quad \text{on} \quad Z = \Psi(X, Y, T) \ , \quad (10)$$

which is precisely the differential form of the kinematic boundary condition at the film free surface given in Chapter 2. Hence, the equivalence of the differential and integral forms of the kinematic boundary condition is proven.

Appendix C: Derivation of the adaptive time-stepping scheme and Local Truncation Error estimate

For the sake of simplicity and clarity, the adaptive time-stepping scheme and LTE estimate are derived for the following ODE,

$$\frac{du}{dt} = F(u,t) \ . \tag{11}$$

The derivation is readily applicable to equations of the form of eq. (3.1). The solution of eq. (11) is sought at the discrete times $t^1, t^2, \ldots, t^n$ defined recurrently by $t^{n+1} = t^n + \Delta t^{n+1}$ as seen on Figure 2. In order to obtain the explicit predictor

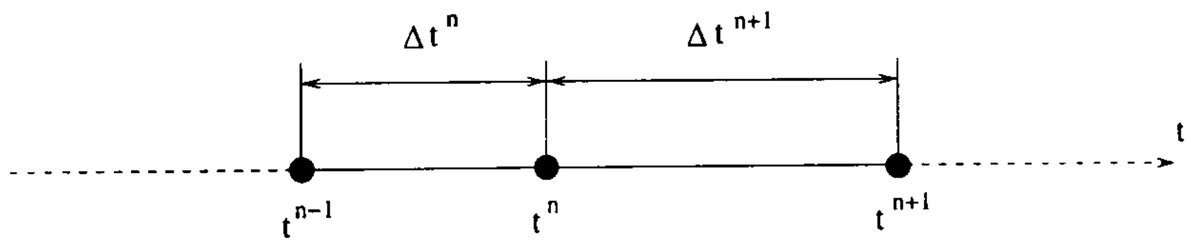

FIGURE 2: Discrete time points and time intervals.

(eq. (3.9)), $u^{n+1}{}_{Predict}$, to the solution u at $t = t^{n+1}$, eq. (11) is expanded in Taylor series in the neighbourhood of t^n leading to

$$u^{n+1} = u^n + \Delta t^{n+1}\frac{\partial u}{\partial t}|_{t^n} + \frac{\left(\Delta t^{n+1}\right)^2}{2}\frac{\partial^2 u}{\partial t^2}|_{t^n} + \frac{\left(\Delta t^{n+1}\right)^3}{6}\frac{\partial^3 u}{\partial t^3}|_{t^n} + O\left(\Delta t^{n+1^4}\right) \quad (12)$$

$$u^{n-1} = u^n - \Delta t^n\frac{\partial u}{\partial t}|_{t^n} + \frac{\left(\Delta t^n\right)^2}{2}\frac{\partial^2 u}{\partial t^2}|_{t^n} - \frac{\left(\Delta t^n\right)^3}{6}\frac{\partial^3 u}{\partial t^3}|_{t^n} + O\left(\Delta t^{n4}\right) \ . \quad (13)$$

The second order derivatives are eliminated from eqs. (12) and (13) by calculating $\left(\Delta t^n\right)^2 \times$ eq. (12)-$\left(\Delta t^{n+1}\right)^2 \times$ eq. (13) and after rearrangement, the following second-order accurate explicit scheme is obtained:

$$u^{n+1}{}_{Predict} = \beta^2 u^{n-1} + \left(1-\beta^2\right)u^n + \Delta t^{n+1}(1+\beta)F\left(u^n, t^n\right) + O\left(\Delta t^2\right) \ , \quad (14)$$

with the associated LTE,

$$LTE_{Predict} = \frac{\left(\Delta t^{n+1}\right)^2 \Delta t^n(1+\beta)}{6}\frac{\partial^3 u}{\partial t^3}|_{t=t_p} \ , \ t_p \in (t_n, t_{n+1}) \ , \quad (15)$$

where β is the ratio of successive time steps. The solution stage uses the Θ_t-scheme described in Chapter 3 with $\Theta_t = \frac{1}{2}$ (implicit, $O((\Delta t^{n+1})^2)$), defined as

$$u^{n+1} = u^n + \frac{\Delta t^{n+1}}{2}\left(F\left(u^n, t^n\right) + F\left(u^{n+1}, t^{n+1}\right)\right) + O\left(\Delta t^2\right) \ , \quad (16)$$

for which the LTE is equal to (Chapra and Canale (1998))

$$LTE = \frac{-1}{12}(\Delta t_{n+1})^3\frac{\partial^3 u}{\partial t^3}|_{t=t_c} \ , \ t_c \in (t_n, t_{n+1}) \ . \quad (17)$$

Hence, given the true solution to eq. (11) at $t = t^n$, the solution at $t = t^{n+1}$ will be given by

$$u\left(t^{n+1}\right) = u^{n+1}{}_{Predict} + \frac{\left(\Delta t^{n+1}\right)^2 \Delta t^n(1+\beta)}{6}\frac{\partial^3 u}{\partial t^3}|_{t=t_p} \ , \quad (18)$$

$$u\left(t^{n+1}\right) = u^{n+1} - \frac{1}{12}(\Delta t_{n+1})^3\frac{\partial^3 u}{\partial t^3}|_{t=t_c} \ . \quad (19)$$

Assuming negligible variation of the third order derivative for $t \in (t_n, t_{n+1})$, this can be estimated using eqs. (18) and (19) leading to

$$\frac{\partial^3 u}{\partial t^3}|_{t\in(t_n,t_{n+1})} = \frac{u^{n+1} - u^{n+1}{}_{Predict}}{\frac{\Delta t_{n+1}{}^3}{12} + \frac{(\Delta t^{n+1})^2 \Delta t^n (1+\beta)}{6}} \,. \tag{20}$$

Finally, replacing eq. (20) in eqs. (15) and (17) gives an estimate for the LTE for the solution stage:

$$LTE = -\frac{u^{n+1} - u^{n+1}{}_{Predict}}{1 + 2\frac{\beta+1}{\beta}} \,, \tag{21}$$

and the predictor stage:

$$LTE_{Predict} = \frac{u^{n+1} - u^{n+1}{}_{Predict}}{1 + \frac{\beta}{2(1+\beta)}} \,. \tag{22}$$

An interesting corollary result is that the estimate for the LTE of the predictor stage is proportional to the estimate for the LTE of the solution stage according to,

$$LTE_{Predict} = -\frac{2(1+\beta)}{\beta} LTE \,. \tag{23}$$

Therefore, for fixed time steps, the magnitude of the LTE for the predictor stage is 4 times greater than the one for the solution stage.

Appendix D: Analytical solution to the transient, two-dimensional heat diffusion equation

The solution to the transient two-dimensional heat diffusion equation, namely

$$\frac{\partial u}{\partial t} = \frac{\partial}{\partial x}\left(k\frac{\partial u}{\partial x}\right) + \frac{\partial}{\partial y}\left(k\frac{\partial u}{\partial y}\right) \ , \tag{24}$$

for $(x, y) \in \Omega = (0, 1) \times (0, 1)$, $t > 0$ and constant k is sought using separation of variables. Equation (24) is solved subject to the following initial and boundary conditions

$$\begin{aligned} u(x, 0, t) &= u(x, 1, t) = 0 \ , \\ u(0, y, t) &= u(1, y, t) = 0 \ , \\ u(x, y, 0) &= xy(x - 1)(y - 1) \ . \end{aligned}$$

Letting $u(x, y, t) = X(x)Y(y)T(t)$ and replacing into eq. (24) yields

$$\frac{T'}{kT} - \frac{Y''}{Y} = \frac{X''}{X} \ . \tag{25}$$

Both side of eq. (25) must equal the same constant, which we will call $-\lambda$. Then:

$$\frac{X''}{X} = -\lambda \,,$$
$$\frac{T'}{kT} - \frac{Y''}{Y} = -\lambda \,.$$

The last equation may be rewritten as $\frac{T'}{kT} + \lambda = \frac{Y''}{Y}$ and again, both sides of this equation must equal the same constant, $-\mu$. Hence,

$$\frac{Y''}{Y} = -\mu \,,$$
$$\frac{T'}{kT} + \lambda = -\mu \,.$$

Having separated the variables, solving eq. (24) is equivalent to solving

$$X'' + \lambda X = 0 \,,\; Y'' + \mu Y = 0 \,,\; T' + (\lambda + \mu)kT = 0 \,. \tag{26}$$

Considering now the boundary conditions. Since $u(0, y, t) = X(0)Y(y)T(t) = 0$, we conclude $X(0) = 0$ and similarly, using other boundary conditions, we obtain $X(1) = Y(0) = Y(1) = 0$.

The problems for X and Y are therefore:

$$X'' + \lambda X = 0 \quad ; \quad X(0) = X(1) = 0 \,, \tag{27}$$
$$Y'' + \mu Y = 0 \quad ; \quad Y(0) = Y(1) = 0 \,, \tag{28}$$

which admit respectively the following eigenvalues and eigenfunctions:

$$\lambda_n = n^2\pi^2 \quad ; \quad X_n(x) = \sin(n\pi x) \quad \text{for} \quad n = 1, 2, ...$$
$$\mu_m = m^2\pi^2 \quad ; \quad Y_m(y) = \sin(m\pi y) \quad \text{for} \quad m = 1, 2, ...$$

The equation for T is:

$$T' + k(m^2\pi^2 + n^2\pi^2)T = 0 \,, \tag{29}$$

and its solutions are constant multiples of $e^{-k\alpha_{nm}t}$ in which $\alpha_{nm} = m^2\pi^2 + n^2\pi^2$ for $n, m = (1, 2, ...)$.

We can now form functions

$$u_{nm} = C_{nm} \sin(n\pi x) \sin(m\pi y) e^{-k\alpha_{nm} t} \ , \tag{30}$$

which satisfy eq. (24) and its boundary conditions for any m and n positive integers. In order to satisfy the initial condition, a linear superposition is tried,

$$u(x,y,t) = \sum_{n=1}^{\infty} \sum_{m=1}^{\infty} C_{nm} \sin(n\pi x) \sin(m\pi y) e^{-k\alpha_{nm} t} \ .$$

The initial condition requires that

$$u(x,y,0) = xy(x-1)(y-1) = \sum_{n=1}^{\infty} \sum_{m=1}^{\infty} C_{nm} \sin(n\pi x) \sin(m\pi y) \ ,$$

which is the Fourier sine expansion of $u(x,y,0)$ on the domain $\Omega = (0,1) \times (0,1)$. The coefficients of such an expansion are

$$C_{nm} = 4 \int_0^1 \int_0^1 xy(x-1)(y-1) \sin(n\pi\kappa) \sin(m\pi\eta) d\kappa d\eta \ ; n,m = 1,2,...$$

Performing this integration yields,

$$C_{nm} = \frac{16}{n^3 m^3 \pi^6} \left[1-(-1)^n\right] \left[1-(-1)^m\right] \ . \tag{31}$$

Finally, the solution to eq. (24) with initial and boundary conditions is:

$$u(x,y,t) = \frac{16}{\pi^6} \sum_{n=1}^{\infty} \sum_{m=1}^{\infty} \frac{\left[1-(-1)^n\right]}{n^3} \frac{\left[1-(-1)^m\right]}{m^3} \sin(n\pi x) \sin(m\pi y) \exp(-k\alpha_{nm} t) \ . \tag{32}$$

Bibliography

ADAMSON, A.W. (1982) *Physical Chemistry of Surface, fourth edition.* Wiley, New York.

AKSEL, N. (2000) Influence of the capillary on a creeping film flow down an inclined plane with an edge. *Arch. Appl. Mech.* **70**, 81–90.

BERTOZZI, A.L. (1995) Loss and gain of regularity in a lubrication equation for thin viscous films. In: *Pitman Research Notes in Mathematics Series, vol. 323 (proceedings of the International Colloquium on Free Boundary Problems Toledo, Spain, June 1993)* pp. 72–85.

BERTOZZI, A.L. (1998) The mathematics of moving contact lines in thin liquid films. *Notices of the AMS* **45**(6), 689–697.

BERTOZZI, A.L. AND BRENNER, M.P. (1997) Linear stability and transcient growth in driven contact lines. *Phys. Fluids* **9**(3), 530–539.

BIELARZ, C. (2002) Free surface thin film flows over topography. PhD thesis, University of Leeds.

BIELARZ, C. AND KALLIADASIS, S. (2003) Time-dependant free-surface thin film flows over topography. *Phys. Fluids* **15**(9), 2512–2524.

BLAKE, T.D. AND HAYNES, J.M.J. (1969) Kinetics of liquid/liquid displacement. *J. Colloid Interface Sci.* **30**, 421–423.

BORNSIDE, D.E., MACOSKO, C.W. AND SCRIVEN, L.E. (1989) Spin coating - one-dimensional model. *J. Appl. Phys.* **66**(11), 5185–5193.

BRAKKE, K. (1992) The surface evolver. *Exp. Math.* **1**, 141–165.

BRANDT, A. (1977) Multi-level adaptive solutions to boundary-value problems. *Math. Comput.* **31**(138), 333–390.

BRANDT, A. (1982) Guide to multigrid development. In: W. Hackbush and U. Trottenberg (eds.), *Multigrid methods: Lecture notes in Mathematics 960.* Springer-Verlag, Berlin, pp. 220–312.

BRETHERTON, F.P. (1961) The motion of long bubbles in tubes. *J. Fluid Mech.* **10**, 166–188.

BRIANT, A.J., PAPATZACOS, P. AND YEOMANS, J.M. (2002) Lattice boltzmann simulations of contact line motion in a liquid-gas system. *Phil. Trans. R. Soc. Lond. A* **360**, 485–495.

CHAPRA, S.C. AND CANALE, R.P. (1998) *Numerical methods for engineers.* McGraw-Hill.

CHOU, M-H. (2000) A multigrid difference approach to steady flow between eccentric rotating cylinders. *Int. J. Numer. Meth. Fluids* **34**, 479–494.

CHRISTOV, C.I., PONTES, J., WALGRAEF, M.G. AND VELARDE, M.G. (1997) Implicit time splitting for fourth-order parabolic equations. *Comput. Methods Appl. Mech. Eng.* **148**, 209–224.

CHURAEV, N.V. AND SOBOLEV, V.D. (1995) Prediction of contact angle on the basis of the frumkin-derjaguin approach. *Adv. Colloid Interface Sci.* **61**, 1–16.

CUBAUD, T. (2001) Mouillage et démouillage de surface hétérogènes. PhD thesis, Université Paris XI Orsay.

DANIELS, N., EHRET, P., GASKELL, P.H., THOMPSON, H.M. AND DECRÉ, M. (2000) Multigrid methods for thin liquid film spreading flows. In: *Proc. 1st International Conference on Computational Fluid Dynamics (ed. N. Satofuka)* Kyoto, Japan, pp. 279–284.

DARHUBER, A.A., TROIAN, S.M. AND WAGNER, S. (2001) Physical mechanisms governing pattern fidelity in microscale offset printing. *J. Appl. Phys.* **90**(7), 3602–3609.

DE GENNES, P.G. (1985) Wetting: statics and dynamics. *Rev. Mod. Phys.* **57**(3), 827–863.

DECRÉ, M., FERNANDEZ-PARENT, C. AND LAMMERS, J.H. (1998) Flow of a gravity driven thin liquid film over one-dimensional topographies. Technical report, Philips Research, Unclassified Report NL-UR 823/98.

DECRÉ, M., FERNANDEZ-PARENT, C. AND LAMMERS, J.H. (1999) Flow of a gravity driven thin liquid film over one-dimensional topographies: a tripartite approach. In: *Proc. 3rd European Coating Symposium (ed. F. Durst and H. Raszillier)* pp. 151–156.

DECRÉ, M.J. AND BARET, J-C. (2003) Gravity driven flows of viscous liquids over two-dimensional topographies. *J. Fluid Mech.* **487**, 147–166.

DEEGAN, R.D. (2000) Pattern formation in drying drops. *Phys. Rev. E* **61**(1), 475–485.

DEEGAN, R.D., BAKAJIN, O., DUPONT, T.F., HUBER, G., NAGEL, S.R. AND WITTEN, T.A. (1997) Capillary flow as the cause of ring stains from dried liquid drops. *Nature* **389**, 827–829.

DERYAGIN, B.V. (1955) *Kolloidn. Zh.* **17**, 191.

DIEZ, J.A. AND KONDIC, L. (2002) Computing three-dimensional thin film flows including contact lines. *J. Comp. Phys.* **183**, 274–306.

DIEZ, J.A., KONDIC, L. AND BERTOZZI, A. (2000) Global models for moving contact lines. *Phys. Rev. E* **63**(1), 011208:1–13.

DORMAND, J.R. (1996) *Numerical methods for differential equations - a computational approach.* CRC press.

DUPUIS, A., BRIANT, A.J., POOLEY, C.M. AND YEOMANS, J.M. (2003) Droplet spreading on heterogeneous surfaces using a three-dimensional lattice boltzmann model. *Lect. Notes Comp. Sc.* **2657**, 1024–1033.

DUSSAN V., E.B. (1979) On the spreading of liquids on solid surfaces: static and dynamic contact lines. *Annu. Rev. Fluid Mech.* **11**, 371–400.

EHRET, P., DOWSON, D., TAYLOR, C.M. AND WANG, D. (1997) Analysis of isothermal elastohydrodynamic point contacts lubricated by newtonian fluids using multigrid methods. *Proc. Instn. Mech. Engrs., Part C* **211**(7), 493.

EHRHARD, P. AND DAVIS, S.H. (1991) Non-isothermal spreading of liquid drops on horizontal plates. *J. Fluid Mech.* **229**, 365–388.

ERES, M.H., SCHWARTZ, L.W. AND ROY, R.V. (2000) Fingering phenomena for driven coating films. *Phys. Fluids* **12**(6), 1278–1295.

ERES, M.H., WEIDNER, D.E. AND SCHWARTZ, L.W. (1999) Three-dimensional direct numerical simulation of surface-tension-gradient effects on the leveling of an evaporating multicomponent fluid. *Langmuir* **15**, 1859–1871.

EVANS, P.L., SCHWARTZ, L.W. AND ROY, R.V. (2000) A mathematical model for crater defect formation in drying paint layer. *J. Colloid Interface Sci.* **227**. 191–205.

FEDORENKO, R.P. (1964) The speed of convergence of one iterative process. *USSR Comput. Math. and Math. Phys.* **4**(3), 227–235.

FULTON, S.R. (1997) A comparison of multilevel adaptive methods for hurricane track prediction. *Electron. Trans. Numer. Anal.* **6**, 120–132.

GASKELL, P.H., JIMACK, P.K., SELLIER, M. AND THOMPSON, H.M. (2003) Efficient and accurate time adaptive multigrid simulations of droplet spreading. *To appear in Int. J. Num. Meth. Fluids* .

GASKELL, P.H., JIMACK, P.K., SELLIER, M., THOMPSON, H.M. AND WILSON, M.C.T. (2004) Gravity-driven flow of continuous thin liquid films on non-porous substrates with topography. *To appear in J. Fluid Mech.* .

GASKELL, P.H., SAVAGE, M.D., SUMMERS, J.L. AND THOMPSON, H.M. (1995) Modelling and analysis of meniscus roll coating. *J. Fluid Mech.* **298**, 113–137.

GLASNER, K.B. (2003) Spreading of droplets under the influence of intermolecular forces. *Phys. Fluids* **15**(7), 1837–1842.

GOODWIN, R. AND HOMSY, G.M. (1991) Viscous-flow down a slope in the vicinity of a contact line. *Phys. Fluids A* **3**(4), 515–528.

GOODYER, C.E. (2001) Adaptive numerical methods for elastohydrodynamic lubrication. PhD thesis, University of Leeds.

GRAMLICH, C.M., KALLIADASIS, S., HOMSY, G.M. AND MESSER, C. (2002) Optimal levelling of flow over one-dimensional topography by marangoni stresses. *Phys. Fluids* **14**, 1841–1850.

GREENSPAN, H.P. (1978) On the motion of a small viscous droplet that wets a surface. *J. Fluid Mech.* **84**, 125–143.

GREENSPAN, H.P. AND MC CAY, B.M. (1981) On the wetting of a surface by a very viscous-fluid. *Stud. Appl. Maths* **64**(2), 95–112.

GRESHO, P. AND KAY, D. (2002) Analysis of numerical method for incompressible fluid dynamics. url: www.ma.umist.ac.uk/djs/epsrc-x.pdf. Technical report, EPSRC.

GRUN, G. AND RUMPF, M. (1998) 'Nonnegativity preserving numerical schemes for the thin film equation'.

GU, Y. AND LI, D. (1998) A model for a liquid drop spreading on a solid surface. *Colloids Surf. A* **142**, 243–256.

HACKBUSCH, W. (1981) On the convergence of a multi-grid iterations. *Beit. Numer. Math.* **9**, 231–329.

HAYES, M., O'BRIEN, S.B.G. AND LAMMERS, J.H. (2000) Green's function of steady flow over a two-dimensional topography. *Phys. Fluids* **12**, 2845–2858.

HIRASAKI, G.J. AND YANG, S.Y. (2000) Interpretation of the dynamic contact line with disjoining pressure, large capillary numbers, large angles, and pre-wetted or entrained films. In: *AIChe Annual Meeting* Los Angeles.

HOCKING, L.M. (1992) Rival contact-angle models and the spreading of drops. *J. Fluid Mech.* **239**, 671–680.

HOOD, P. (1976) Frontal solution program for unsymmetric matrices. *Int. J. Num. Meth. Eng.* **10**, 379–399.

HOWISON, S.D., MORIARTY, J.A., OCKENDON, J.R. AND TERRILL, E.L. (1997) A mathematical model for drying paint layers. *J. Eng. Math.* **32**(4), 377–394.

HUH, C. AND SCRIVEN, L.E. (1971) Hydrodynamic model of steady movement of a solid/liquid/fluid contact line. *J. Colloid Interface Sci.* **35**, 85–101.

HUPPERT, H.E. (1982) Flow and instability of a viscous current down a slope. *Nature* **300**, 427–429.

KALLIADASIS, S., BIELARZ, C. AND HOMSY, G.M. (2000) Steady free-surface thin film flow over two-dimensional topography. *Phys. Fluids* **12**, 1889–1898.

KALLIADASIS, S. AND HOMSY, G.M. (2001) Stability of free surface thin-film flows over topography. *J. Fluid Mech.* **448**, 387–410.

KISTLER, S.F. AND SCHWEIZER, P.M. (1997) *Liquid Film Coating.* Chapman and Hall.

KISTLER, S.F. AND SCRIVEN, L.E. (1983) Coating flows. In: *Computational Analysis of polymer processing.* Pearson, J.R.A and Richardson, S.M., chapter 8, pp. 243–299.

KONDIC, L. AND BERTOZZI, A.L. (1999) Nonlinear dynamics and transient growth of driven contact lines. *Phys. Fluids* **11**(11), 3560–3562.

KONDIC, L. AND DIEZ, J. (2001) Pattern formation in the flow of thin film down an inclined plane: constant flux configuration. *Phys. Fluids* **13**(11), 3168–3184.

LANDAU, L. AND LEVICH, B. (1942) Dragging of a liquid by a moving plate. *Acta Physico-Chim. USSR* **17**, 42–54.

LAW, B.M. (2001) Wetting, adsorption and surface critical phenomena. *Prog. Surf. Sci.* **66**, 159–216.

LAWRENCE, C.J. (1988) The mechanics of spin coating of polymer films. *Phys. Fluids* **31**(10), 2786–2795.

LELAH, M.D. AND MARMUR, A.M. (1981) Spreading kinetics of drops on glass. *J. Colloid Interface Sci.* **82**, 518–525.

LIAO, S-J. AND MASHAYEK, F. (2001) A multigrid approach for steady state laminar viscous flow. *Int. J. Numer. Meth. Fluids* **37**, 107–123.

LUCÉA, M., DECRÉ, M.M.J. AND LAMMERS, J.H. (1999) Flow of a gravity driven thin liquid film over topographies. Technical report, Philips Research, Unclassified Report NL-UR 833/99.

MAZOUCHI, A. AND HOMSY, G.M. (2001) Free surface stokes flow over topography. *Phys. Fluids* **13**(10), 2751–2761.

MESSÉ, S. AND DECRÉ, M.M.J. (1997) Experimental study of a gravity driven water film flowing down inclined plates with different patterns. Technical report, Philips Research, Unclassified Report NL-UR 030/97.

MEYERHOFER, D. (1978) Characteristics of resist films produced by spinning. *J. Appl. Phys.* **49**, 3993–3997.

MITLIN, V.S. (1994) On dewetting conditions. *Colloids Surf. A* **89**. 97–101.

MITLIN, V.S. AND PETVIASHVILI, N.V. (1994) Nonlinear dynamics of dewetting - kinetically stable structures. *Phys. Lett. A* **192**, 323–326.

MORIARTY, J.A. AND SCHWARTZ, L.W. (1993) Dynamic considerations in the closing and opening of holes in thin liquid films. *J. Colloid Interface Sci.* **161**, 335-342.

MYERS, T.G. (1998) Thin films with high surface tension. *SIAM Rev.* **40**(3), 441-462.

NAKAYA, C. (1974) Spread of fluid drops over a horizontal plane. *J. Phys. Soc. Japan.* **37**, 539.

O'BRIEN, S.B.G. AND SCHWARTZ, L.W. (2002) Theory and modeling of thin film flows. In: *Encyclopedia of Surface and Colloid Science.* Marcel Dekker, Inc, pp. 5283–5297.

ORCHARD, S.E. (1962) On surface levelling in viscous liquids and gels *Appl. Sci. Res. A* **11**, 451–464.

ORON, A., DAVIS, S.H. AND BANKOFF, S.G. (1997) Long-scale evolution of thin liquid films. *Rev. Mod. Phys.* **69**(3), 931–980.

OVERDIEP, W.S. (1986) The levelling of paints. *Prog. Org. Coat.* **14**. 159–175.

PARISSE, F. AND ALLAIN, C. (1996) Shape changes of colloidal suspension droplets during drying. *J. Phys. II France* **6**, 1111–1119.

PARISSE, F. AND ALLAIN, C. (1997) Drying of colloidal suspension droplets: experimental study and profile renormaliztion. *Langmuir* **13**, 3598–3602.

PEURRUNG, L.M. AND GRAVES, B.G. (1991) Film thickness profiles over topography in spin coating. *J. Electrochemical Soc.* **138**, 2115–2124.

PEURRUNG, L.M. AND GRAVES, D.B. (1993) Spin coating over topography. *IEEE Transactions on Semiconductor Manufacturing.* **6**(1), 72–76.

PISMEN, L. AND POMEAU, Y. (2000) Nonlocal diffuse interface theory of thin films and the moving contact line. *Phys. Rev. E* **62**, 2840.

PODGORSKI, T., FLESSELLES, J.M. AND LIMAT, L. (1999) Dry arches within flowing films. *Phys. Fluids* **11**(4), 845–852.

POZRIKIDIS, C. AND THORODDSEN, S.T. (1991) The deformation of a liquid film flowing down an inclined plane wall over a small particle arrested on the wall. *Phys. Fluids A* **3**, 2546–2558.

PRITCHARD, W.G., SCOTT, L.R. AND TAVENER, S.J. (1992) Numerical and asymptotic methods for certain viscous free-surface flows. *Phil. Trans. R. Soc. Lond. A* **340**, 1–45.

QUÉRÉ, D. (2002) Rough ideas on wetting. *Physica A* **313**, 32–46.

REYNOLDS, O. (1886) On the theory of lubrication and its application to mr. beauchamp tower's experiment, including an experimental determination of the viscosity of olive oil. *Phil. Trans. R. Soc. London* **177**, 157–234.

ROY, R.V AND SCHWARTZ, L.W. (1997) Coating flow over a curved substrate. In: *Proc. 2nd European Coating Symposium (ed. P.G. Bourgin)* Université Louis Pasteur, Strasbourg, pp. 18–27.

RUSCHAK, K.J. (1985) Coating flows. *Ann. Rev. Fluid Mech.* **17**, 65–89.

SCARDOVELLI, R. AND ZALESKI, S. (1999) Direct numerical simulation of free-surface and interfacial flow. *Ann. Rev. Fluid Mech.* **31**, 567–603.

SCHWARTZ, L.W. (1989) Viscous flows down an inclined plane: Instability and finger formation. *Phys. Fluids A1* **3**, 443–445.

SCHWARTZ, L.W. (1998) Hysteretic effects in droplet motions on heterogeneous substrates: direct numerical simulation. *Langmuir* **14**, 3440–3453.

SCHWARTZ, L.W. AND ELEY, R.R. (1998) Simulation of droplet motion on low-energy and heterogeneous surfaces. *J. Colloid Interface Sci.* **202**, 173–188.

SCHWARTZ, L.W., ROY, R.V., ELEY, R.R. AND PETRASH, S. (2000) Dewetting patterns in a drying liquid film. *J. Colloid Interface Sci.* **234**, 363–374.

SHAMPINE, L.F. (1994) *Numerical Solution of Ordinary Differential Equations.* Chapman and Hall.

SPAID, M.A. AND HOMSY, G.M. (1995) Stability of newtonian and viscoelastic dynamic contact lines. *Phys. Fluids* **8**(2), 460–478.

SPITALERI, R.M. AND CORINALDESI, L. (1997) A multigrid semi-implicit finite difference method for the two-dimensional shallow water equations. *Int. J. Numer. Meth. Fluids* **25**, 1229–1240.

STILLWAGON, L.E. AND LARSON, R.G. (1987) Planarization of substrate topography by spin coating.. *J. Electrochem. Soc.* **184**, 2030–2037.

STILLWAGON, L.E. AND LARSON, R.G. (1988) Fundamentals of topographic surface levelling. *J. Appl. Phys.* **63**, 5251.

STILLWAGON, L.E. AND LARSON, R.G. (1990) Leveling of thin films over uneven substrates during spin coating. *Phys. Fluids A* **2**(11), 1937–1944.

SUMMERS, J.L., THOMPSON, H.M. AND GASKELL, P.H. (2004) Flow structure and transfer jets in a contra-rotating rigid-roll coating system. *J. Theo. Comp. Fluid Dyn.* **17**(3), 189–212.

TANNER, L.H. (1979) The spreading of silicon oil drops on horizontal surfaces. *J. Phys. D* **12**, 1473–1484.

TELETZKE, G.F. (1983) Thin liquid films: molecular theory and hydrodynamic implications. PhD thesis, University of Minnesota.

THOMAS, J.L., DISKIN, B. AND BRANDT, A. (2003) Textbook multigrid efficiency for fluid simulations. *Annu. Rev. Fluid Mech.* **35**, 317–340.

TROTTENBERG, U. (2001) *Multigrid/U. Trottenberg, C.W. Oostorbe and A. Schuller. Guest contribution by A. Brandt, P. Ooswald and K. Stuber.* San Diego Conference London: Academic.

VAN DE FLIERT, B.W. (2001) A free boundary problem for evaporating layers. *Nonlinear Anal.-Theo.* **47**(3), 1785–1796.

VERETENNIKOV, I., INDEIKINA, A. AND CHANG, H-C. (1998) Front dynamics and fingering of a driven contact line. *J. Fluid Mech.* **373**, 81–110.

WEIDNER, D.E., SCHWARTZ, L.W. AND ELEY, R.R. (1996) Role of surface tension gradient in correcting coating defects in corners. *J. Colloid Interface Sci.* **179**, 66–75.

WEIDNER, D.E., SCHWARTZ, L.W. AND ERES, M.H. (1997) Simulation of coating layer evolution and drop formation on horizontal cylinders. *J. Colloid Interface Sci.* **187**(1), 243–258.

WESSELING, P. (1992) *Introduction to Multigrid methods.* Wiley, New York.

WILLIAMS, H.A.R. (1998) Two-dimensional surfactant-driven flows of thin liquid films. PhD thesis, University of Cambridge.

WILSON, M.C.T. (2003) Private communication.

YANENKO, N.N. (1971) *The method of fractional steps.* Springer-Verlag, New York.

YARNOLD, G.D. (1938) The motion of a mercury index in a capillary tube. *Proc. R. Soc. Lond. A* **50**, 540–552.

ZHORNITSKAYA, L. AND BERTOZZI, A.L. (2000) Positivity-preserving numerical schemes for lubrication-type equations. *SIAM J. Numer. Anal.* **37**(2), 523–555.